INFORMATION TO USERS

This manuscript has been reproduced from the microfilm master. UMI films the text directly from the original or copy submitted. Thus, some thesis and dissertation copies are in typewriter face, while others may be from any type of computer printer.

The quality of this reproduction is dependent upon the quality of the copy submitted. Broken or indistinct print, colored or poor quality illustrations and photographs, print bleedthrough, substandard margins, and improper alignment can adversely affect reproduction.

In the unlikely event that the author did not send UMI a complete manuscript and there are missing pages, these will be noted. Also, if unauthorized copyright material had to be removed, a note will indicate the deletion.

Oversize materials (e.g., maps, drawings, charts) are reproduced by sectioning the original, beginning at the upper left-hand corner and continuing from left to right in equal sections with small overlaps.

Photographs included in the original manuscript have been reproduced xerographically in this copy. Higher quality 6" x 9" black and white photographic prints are available for any photographs or illustrations appearing in this copy for an additional charge. Contact UMI directly to order.

Bell & Howell Information and Learning
300 North Zeeb Road, Ann Arbor, MI 48106-1346 USA

UMI®
800-521-0600

DISSERTATION

FLUORINATION OF CLOSO-DODECAHETEROBORANE ANIONS: NEW SUPERWEAK ANIONS AND NONCLASSICAL METAL CARBONYLS: A THEORETICAL STUDY

Submitted by

Anthony John Lupinetti

Department of Chemistry

In partial fulfillment of the requirements

for the Degree of Doctor of Philosophy

Colorado State University

Fort Collins, Colorado

Fall 1999

COLORADO STATE UNIVERSITY

September 16, 1999

WE HEREBY RECOMMEND THAT THE DISSERTATION PREPARED UNDER OUR SUPERVISION BY ANTHONY JOHN LUPINETTI ENTITLED *FLUORINATION OF CLOSO-DODECAHETEROBORANE ANIONS: NEW SUPERWEAK ANIONS AND NONCLASSICAL METAL CARBONYLS: A THEORETICAL STUDY* BE ACCEPTED AS FULFILLING IN PART REQUIREMENTS FOR THE DEGREE OF DOCTOR OF PHILOSOPHY.

Committee on Graduate Work

Adviser

Department Head

ABSTRACT OF DISSERTATION

FLUORINATION OF CLOSO-DODECAHETEROBORANE ANIONS: NEW SUPERWEAK ANIONS AND NONCLASSICAL METAL CARBONYLS: A THEORETICAL STUDY

The first part of this dissertation details the synthesis and characterization of a series of very weakly basic or *superweak* anions with the form $EB_{11}H_{11-n}F_n^-$ (E = CH, As, Sb, Bi). Reaction of the unfluorinated anions with liquid anhydrous hydrogen fluoride (LAHF) at temperatures below 230°C proceeded in a stepwise manner with excellent compositional (n = 1–4) and isomeric purity for $CB_{11}H_{12}^-$: 12-$CB_{11}H_{11}F^-$, 7,12-$CB_{11}H_{10}F_2^-$, 7,9,12-$CB_{11}H_9F_3^-$, and 7,9,10,12-$CB_{11}H_8F_4^-$. Mixtures resulted at higher temperature. The target compound 7–12-$CB_{11}H_6F_6^-$ was isolated after separation using size exclusion chromatography. The $EB_{11}H_{11}^-$ clusters reacted differently; substitution occurred at the antipodal ($AsB_{11}H_{11}^-$) and lower-belt positions (E = As, Sb, Bi). The *N*-fluoro reagent F-TEDA-BF_4 also fluorinated $CB_{11}H_{12}^-$ (n = 1–6) but produced isomeric mixtures. The NMR data of $CB_{11}H_{12-n}F_n^-$ were used to provide insight about electronic structure and substitution patterns.

In the second part, high ν(CO) carbonyl complexes were examined by computational methods, and a definition for nonclassical metal carbonyls was proposed. It was found that the effect of a positive charge on a carbonyl ligand serves to make the

C–O bonds *less polar* in X^+–CO complexes and *more polar* in CO–X^+ complexes. Predicted bond dissociation energies (BDEs), geometries, and electronic structures were calculated for group-11 and group-12, d^{10} $M(CO)_n^{+/2+}$ (n = 1–6) complexes at the MP2, CCSD(T), BP86, and B3LYP levels of theory. Calculated CCSD(T)/I//MP2/I BDEs were in good agreement with experimental results, while DFT methods performed poorly for n = 1, 2. Ion-dipole coulombic attractions were found to be important in the complexes. Sequential BDEs for the group-12 complexes were more endothermic those of the group-11 complexes. Finally, the behavior of metal carbonyl complexes perturbed in one of two was monitored: adding two fluoride ions to $M(CO)_n^x$ (n = 2, 3; x = –1 to +2) cations and compressing the M–C bond of $M(CO)_n^+$ (n = 1, 2) complexes. These perturbations produced two responses in the M–C and C–O bonds and further supported the need for two classes of metal carbonyl complexes—classical and nonclassical.

Anthony John Lupinetti
Department of Chemistry
Colorado State University
Fort Collins, CO 80523
Fall 1999

"Man muß noch Chaos in sich haben, um einen tanzenden Stern gebären zu können."

–Friedrich Nietzsche, *Also sprach Zarathustra*

ACKNOWLEDGEMENTS

I would like to thank the members of the Strauss Research Group, past and present. You are my friends as well as my colleagues. I would also like to thank Professor Doctor Gernot Frenking, for his support and encouragement as my second advisor, and the Arbeitkreise Frenking in Marburg, Germany, who made my stay in Marburg a learning experience and a pleasure. My special thanks go to Dr. Sergei Ivanov, Dr. Jeff Rack, Dr. Juston Rockwell, Dr. Tom Barbarich, Dr. Kristine Gansle, Dr. Kevin Chambliss, Mr. John Hammel, Mr. Ben Nolan, Mr. Matt Havighurst, and Herr Ulrich Pidun for their valuable input, discussions, and support. I would also like to say thank Joanna Fair; without you, the final days of my graduate work would have been unbearable. You kept me grounded and sane. Thank you! And last but not least, I want to give my heartfelt appreciation to Steve Strauss for being an advisor and, more importantly, a mentor. Despite our, sometimes frequent, disagreements understand that I value your opinion immensely. Your genuine concern for me (and all of your students) is what makes you so special. Thank you!

This work was supported by U.S. National Science Foundation (CHE-9628769), the Deutsche Forschungsgemeinschaft (SFB 260 and Graduiertenkolleg Metallorganische Chemie), the Fonds der Chemischen Industrie, and Schweizerischer Nationalfonds. Computer time was provided by the Hochschulrechenzentrum of the Philipps-Universität Marburg, the HLRZ Darmstadt, the HLRZ Stuttgart, the Swiss Center for Scientific Computing (SCSC Manno), and the C4 Cluster at ETH Zürich.

Anthony (a.k.a. Lupi)

To

Mom and Dad

Thank you for teaching me that there is nothing I can't do.

TABLE OF CONTENTS

LIST OF FIGURES

PART I

Chapter 1

Chapter 2

Chapter 3

PART II

Chapter 1

Chapter 2

Chapter 3

Chapter 4

LIST OF TABLES

PART I

Chapter 1

Chapter 2

Chapter 3

PART II

Chapter 1

Chapter 2

Chapter 3

Chapter 4

LIST OF ABBREVIATIONS

PART I:

SWA	Superweak Anion
E	heteroatom in a borane cage
LAHF	liquid anhydrous hydrogen fluoride
THF	tetrahydrofuran
TMS	tetramethylsilane
MSDS	Material Safety Data Sheet
NMR	Nuclear Magnetic Resonance
NIEMS	Negative Electrospary Mass Spectrometry
δ value	NMR chemical shift value in ppm
Hz	Hertz
COSY	homonuclear two-dimensional NMR experiment
HMQC	heteronuclear magnetic quadrapole coupling (2-D NMR experiment)
F-TEDA	1-chloromethyl-4-fluoro—1,4-diazoniabicyclo[2.2.2]octane bis(tetrafluoroborate) (also F-TEDA-BF_4)
NE	neighboring atom effect (*para* effect, β effect)
RE	rhombohedral effect (*para* effect, γ effect)
AE	antipodal effect (*para* effect)

PART II:

ν(CO)	asymmetric carbon-oxygen stretching frequency
ω(CO)	symmetric carbon-oxygen stretching frequency

HOMO	highest occupied molecular orbital
ECP	effective core potential (pseudopotential)
6-31G(d)	split-valence basis set plus polarization function
TZ2P	triple-zeta basis set plus two polarization functions
MP2	second order Møller-Plesset theory
CCSD	coupled cluster singles and doubles method
CCSD(T)	coupled cluster singles and doubles (triples approximation)
DFT	density functional theory
BP86	Becke-Perdew 86 gradient-corrected functional (DFT method)
B3LYP	Becke 3-parameter hybrid functional with Lee-Young-Parr gradient correction (DFT method)
NBO	natural bond orbital (analysis)
CDA	charge decomposition anaysis
q	atomic charge
ρ_b	Electron density (e $Å^{-5}$)
$\nabla^2\rho_b$	Laplacian concentration (e $Å^{-5}$)
H_b	energy density at the bond critical point (hartree $Å^{-3}$)
ZPE	zero-point energy
D_e	sequential bond dissociation energy in kcal mol^{-1}
D_e	sequential bond dissociation energy in kcal mol^{-1} (corrected to 0 K)

PART I

Fluorination of *closo*-Dodecaheteroborane Anions: New Superweak Anions

"Blessed are the meek [weak], for they will inherit the land."

–Matthew 5:5

CHAPTER 1

Introduction to Superweak Anions

The preparation of anions that coordinate weakly to cations is an active endeavor in chemistry due to their usefulness in solving important problems in synthesis, catalysis, and materials science.[1-4] These problems include the stabilization of reactive cations such as $[Xe_2][Sb_4F_{21}]$[5] and $[C_6(CH_3)_5H_2][B(C_6F_5)_4]$[6] (Figure I.1.1), catalytic polymerization of olefins by catalysts containing anions such as $B(C_6H_5)_4^-$ and $B(C_6H_3(CF_3)_2)_4^-$,[7,8] the catalytic formation of carbon–carbon bonds (1,4 conjugate addition reactions catalyzed by $LiAl(OC(C_6H_5)(CF_3))_4$,[9] the activation of C–H bonds (by $[Pt(CH_3)(tmeda)(L)][B(C_5H_3(CF_3)_2)_4]$, for example),[10] and the manufacture of high-current-density lithium ion batteries ($N(SO_2CF_3)_2^-$ and related species incorporated into polymers).[11] In the past, these anions have simply been called weakly coordinating anions, but at the 215th National ACS Meeting in Dallas, Texas, Professor Steven H. Strauss introduced the term *superweak anion* (*SWA*) to draw attention to the conceptual connection between weakly coordinating anions and superacid media: both involve the virtual absence of basicity.[10] The term superweak anion will be used in this work, and the characteristics of an ideal superweak anion will be discussed below.

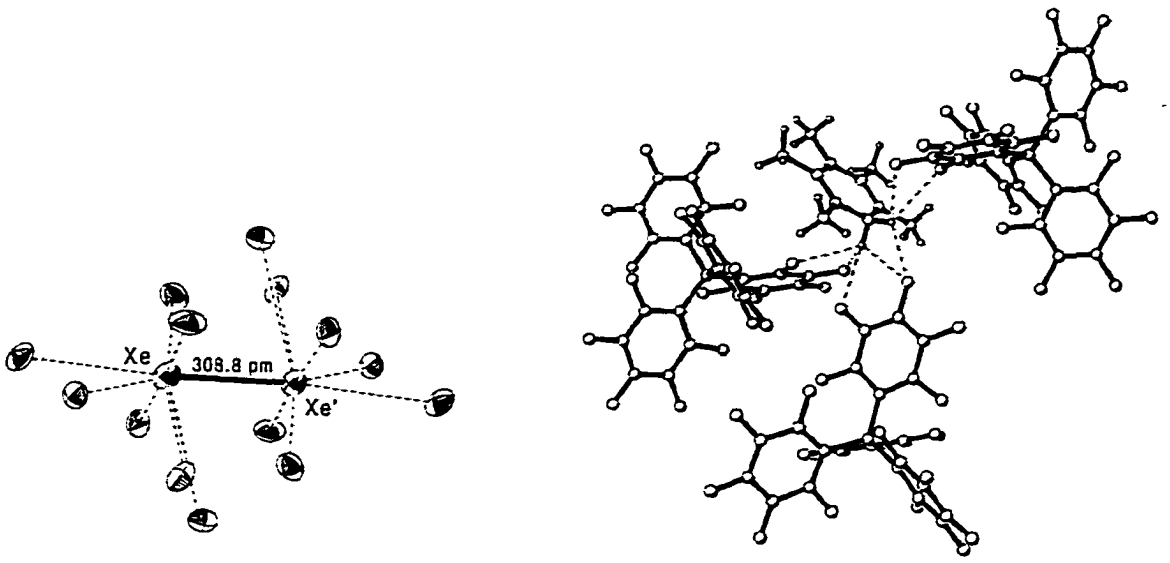

(a) (b)

Figure I.1.1. Crystal structures of two highly-reactive cations isolated using superweak anions: (a) the Xe_2^+ cation radical (50% probability ellipsoids) in $[Xe_2][Sb_4F_{21}]$. The unlabeled ellipsoids are fluorine atoms from neighboring $Sb_4F_{21}^-$ counterions; (b) the $C_6(CH_3)_5H_2^+$ cation in $[C_6(CH_3)_5H_2][B(C_6F_5)_4]$. One cation and three anions are shown to illustrate the H···F interactions between the cation and the anions.

Characteristics of the Ideal Superweak Anion

There are a number of characteristics that must be optimized in order to design the ideal *SWA*. Despite the large number of tunable parameters, there is one overriding property of a good *SWA*: low Lewis basicity. To achieve low basicity, a new *SWA* should, ideally, have an overall charge of negative one (–1) that is distributed over a large number of atoms (i.e., a large anion). One of the easiest ways to achieve a low basicity is to cover the periphery of an anion with weakly basic atoms such as hydrogen or fluorine. Peripheral atoms such as oxygen (e.g., ClO_4^- and NO_3^-) often form strong secondary bonds through available lone pairs; these basic interactions lessen the weakly

coordinating nature of an anion. Despite the presence of lone pair electrons, fluorine atoms form strong bonds but usually to only one atom at a time. This "non-stick" property of fluorine makes it perhaps the best candidate for use in *SWA*s, which is illustrated by the ever increasing number of fluorinated anions present in the literature, such as $B(C_6F_5)_4^-$,[3,12-16] $B(3,5\text{-}C_6H_3(CF_3)_2)_4^-$,[17] $B(OTeF_5)_4^-$,[18-20] $N(SO_2CF_3)_2^-$,[10] $Al(OC(C_6H_5)(CF_3)_2)_4^-$,[9] and $Nb(OCH(CF_3)_2)_6^-$.[21] Polyhalogenation of an anion with halogen atoms other than fluorine (Cl, Br, I) and polymethylation are alternative ways to achieve low basicity. In the later case, the lack of lone pair electrons on hydrogen makes bonding to electrophilic centers weak.

The size of the anion is also important. In a low dielectric solvent, cations and anions will form ion pairs instead of dissociated, solvated ions. As the size of the cation or the anion becomes increasingly larger, the electrostatic interaction holding the ion pair together becomes increasingly weaker; this force drops off as $1/r^2$, where r is the distance between the centers of charge of the ions. Therefore, the larger an anion becomes, the more weakly coordinating it becomes. Another advantage of larger anion size is that electron density (i.e., the negative charge) is distributed over a large number of atoms. As an example, a fluoride ion has a charge of negative one centered on one fluorine atom; BF_4^- has approximately 1/4 of the overall negative charge centered on each fluorine; PF_6^- has approximately 1/6 of the overall negative charge centered on each fluorine atom. As the number of fluorine atoms around a central atom of an anion increases, the basicity of each fluorine atom should decrease.

In addition to low basicity, a new *SWA* should have stability under a variety of conditions: kinetic stability, thermodynamic stability, oxidative and reductive stability, stability to ligand exchange, and stability in the presence of strong electrophiles. Table I.1.1 lists some common classes of weakly coordinating and superweak anions and includes examples of each. All of the anions listed meet at least some of the criteria for

Table I.1.1. Common Weakly Coordinating and Superweak Anions

Formula	Examples
MO_n^-	NO_3^-, ClO_4^-
MX_4^-, MX_6^-	$AlCl_4^-$, PF_6^-, SbF_6^- $B(C_6H_5)_4^-$, $B(C_6F_5)_4^-$, $B(C_6H_3(CF_3)_2)_4^-$
$M(OR_f)_4^-$, $M(OR_f)_6^-$	$Al(OC(C_6H_5)(CF_3)_2)_4^-$, $Nb(OCH(CF_3)_2)_6^-$
$M(OTeF_5)_4^-$, $M(OTeF_5)_6^-$	$Zr(OTeF_5)_4^{2-}$, $Nb(OTeF_5)_6^-$
$E(SO_2R_f)_n^-$	$N(SO_2CF_3)_2^-$, $C(SO_2CF_3)_3^-$
$CB_{11}H_{12-n}X_n^-$, $CB_9H_{10-n}X_n^-$	$CB_{11}H_6Cl_6^-$, $CB_{11}H_6I_6^-$, $CB_9H_5Br_5^-$

*SWA*s discussed above. For example, all but one of the anions are uninegative. In addition, they all have weakly basic peripheral substituents (Cl, F, CF_3, C_6F_5; NO_3^- and ClO_4^- are included for comparison). To illustrate some of the shortcomings of these commonly used weakly coordinating and superweak anions, some of the more common ones, ClO_4^-, BF_4^- and PF_6^-, $B(C_6H_3(CF_3)_2)_4^-$, $Al(OC(C_6H_5)(CF_3)_2)_4^-$, will be examined in more detail.

The perchlorate anion is one of the earliest weakly coordinating anions used. In addition to the presence of a strongly coordinating oxygen periphery, the perchlorate anion is a strong oxidizer making compounds containing it potentially explosive.[22] Related fluorinated anions of the form MF_n^- (n = 4 or 6) are more weakly coordinating than the anions with easily accessible oxygen atoms, but they still have problems.[23-26] First, these anions are thermally unstable in the temperature regime where many "normal" chemical reactions occur. For example, $LiPF_6$, a compound currently used in lithium ion batteries, decomposes to LiF and PF_5 at 70°C in the solid state.[27] Although BF_4^- and AsF_6^- are thermally more stable, they are unstable in the presence of water, forming hydroxides and oxides and hydrogen fluoride.[28,29]

The MF_n^- class of *SWA*s can be improved by the replacement of the halogen atoms with aryl groups (i.e., arylborates and arylaluminates). The prototype for this group is $B(C_6H_5)_4^-$. This anion suffers from a variety of problems including oxidative instability,[30-33] coordination of the phenyl rings to electrophiles (Figure I.1.2a),[34] metallation,[35] and phenyl abstraction.[36] Fluorination of the phenyl rings or addition of electron withdrawing $-CF_3$ groups improves on many of the problems of the parent, unfluorinated derivative. The electron withdrawing substituents serve to decrease the π electron density on the aromatic rings, thus preventing coordination to electrophiles through the aryl π system and raising the reduction potential of these anions relative to $B(C_6H_5)_4^-$.[37] Despite the decrease coordinating ability of the phenyl ligand, fluorinated aryl ligands have been shown to coordinate to

electrophilic metal centers through aryl C–F bonds (Figure I.1.2b).[38] In addition, the withdraw of π-electron density by aryl fluorine atoms and CF_3 groups has been shown, in a number of cases, to increase the possibility of aryl abstraction. In a study conducted at Los Alamos National Laboratory by Kubas et al., it was shown that the transition metal complex [*trans*-$PtMe(OEt_2)(PPh_3)_2$][$B(C_6H_3(CF_3)_2)_4$] abstracts two $C_6H_3(CF_3)_2^-$ (Ar_f^-) ligands from $B(Ar_f)_4^-$ to produce [*trans*-$Pt(Ar_f)_2(PPh_3)_2$] and other unidentified products.[10] Stability in the presence of strong electrophiles is important for salts of superweak anions that are intended for use in catalysis.

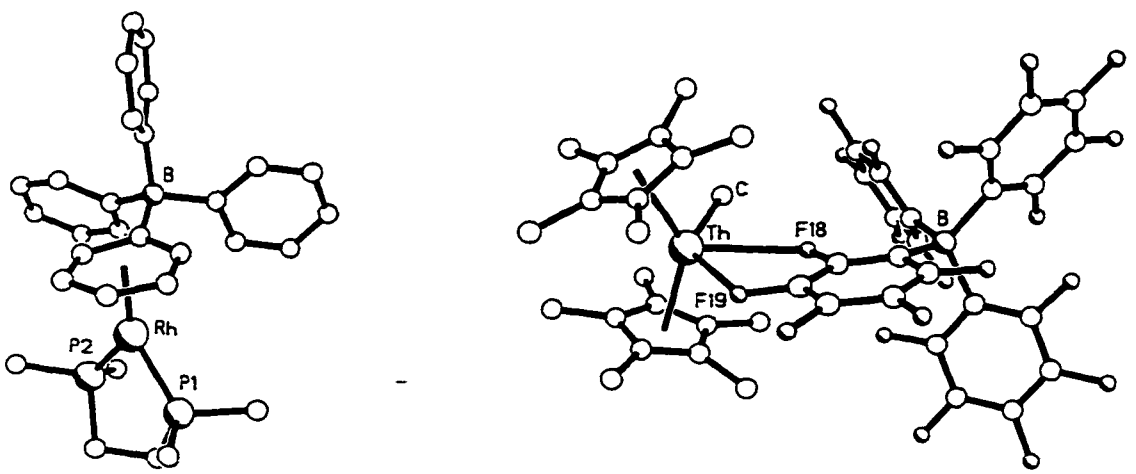

(a) (b)

Figure I.1.2. The coordination of arylborate anions to metal centers: the crystal structure of (a) $Rh(\eta^2\text{-}(P(Me)_2C_2H_4P(Me)_2))(\eta^6\text{-}(C_6H_5)BPh_3)$ and $(\eta^5\text{-}C_5Me_5)_2Th(Me)(\eta^2\text{-}(C_6F_5)B(Ar_f)_3)$.

The final class of *SWA*s to be discussed is the alkoxyborate anions, $M(OR_f)_4^-$ and $M(OR_f)_6^-$. In this class of anions, the aryl groups of anions like $B(C_6H_5)_4^-$ have been replaced by fluorinated alkoxide ligands (i.e., $OC(C_6H_5)(CF_3)_2^-$ ($HFPP^-$), $OCH(CF_3)_2^-$, $OC(CF_3)_3^-$, etc.) Despite the presence of an oxygen center on each OR_f ligand, this class of anions has been shown to be weakly coordinating.[9,39] As an example the hydrocarbon-soluble $LiAl(HFPP)_4$ salt has been shown to be an active catalyst for 1,4 conjugate additions (Figure I.1.3). The same anion is thermally stable to ca. 100°C and is stable in the presence of strong electrophiles (e.g., the system formed from $Cp_2Zr(CH_3)_2$ and $[(C_6H_5)_3C][Al(HFPP)_4]$ has shown activity as a catalyst for the polymerization of ethylene).[9,40] Despite the strongly electron-withdrawing fluorine atoms on the periphery of the anion, the oxygen atoms are still a source of basicity in the anion. This is illustrated by the coordination of Li^+ to the oxygen atoms of the anion even in those derivates where the steric bulk of the anion has been increased in order to shield the oxygen atoms (Figure I.1.3).[9,39]

The anions discussed above exhibit a number of stability problems with respect to thermolysis, hydrolysis, ligand abstraction, and oxidation. It is because of these shortcomings that the search for new, more robust superweak anions continues.

Closo-Heteroborane Anions

Some of the potentially most useful and most stable *SWA*s are the icosahedral *closo*-heteroboranes; carba-*closo*-dodecaborane(12), $CB_{11}H_{12}^-$, best typifies this class of anions.[41,42] It seems logical, based on the criteria listed above, that uninegative fluorinated *closo*-heteroborane anions might be superior to other *SWA*s for some applications. *Closo*-borane dianions, *closo*-monocarborane anions, and neutral *closo*-dicarboranes, especially those with 10 or 12 vertices, exhibit well-established thermal and

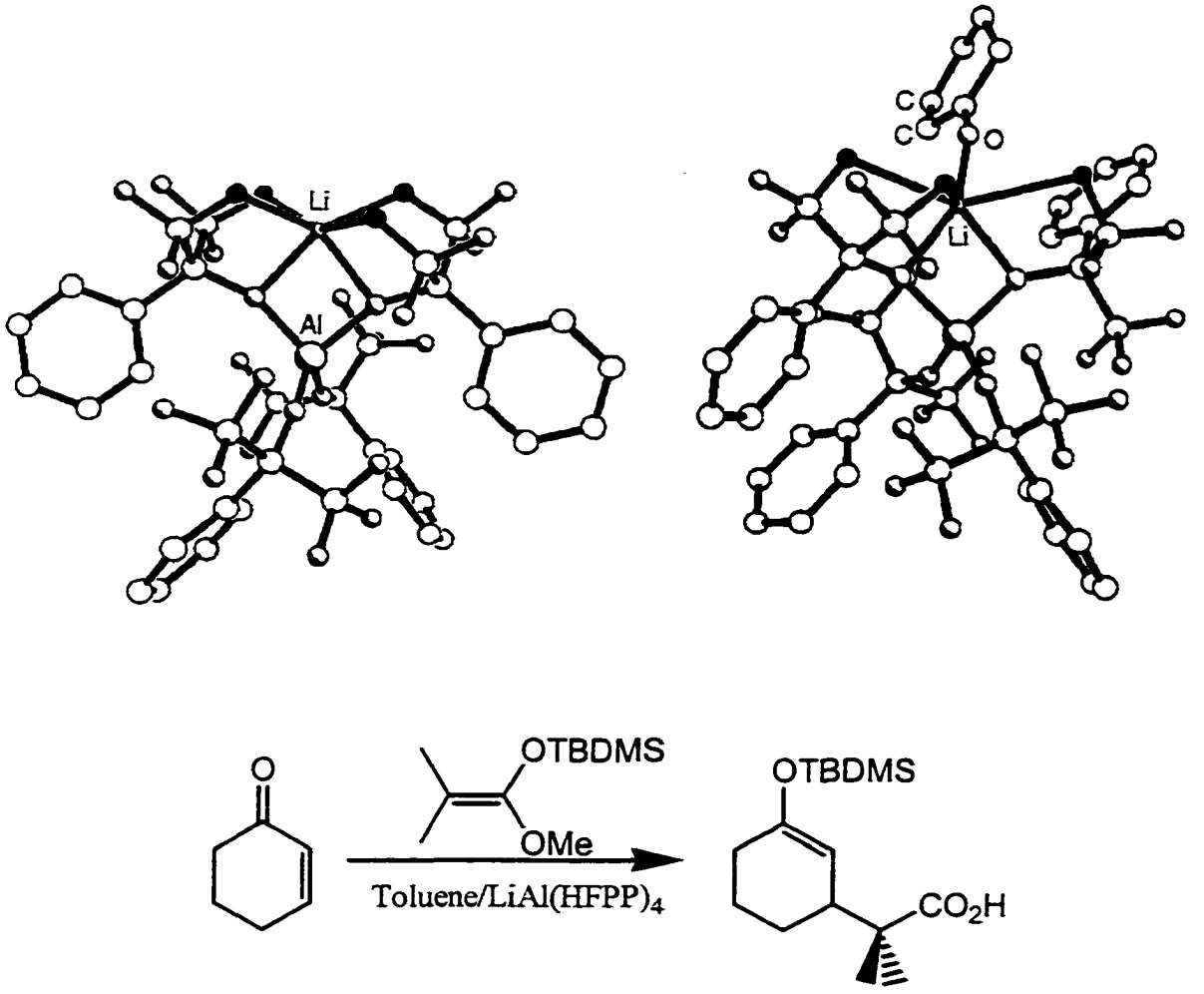

Figure I.1.3. The molecule $LiAl(OC(Ph)(CF_3)_2)_4$ (left, single crystal x-ray diffraction)[9] catalyzes the 1,4 conjugate addition reaction illustrated at the bottom of the figure in 94% yield. The complex $LiAl(OC(Ph)(CF_3)_2)_4 \cdot C_6H_8O$ (right, single crystal x-ray diffraction)[37] is assumed to be an intermediate in the reaction. The black spheres are selected fluorine atoms. The gray filled spheres represent oxygen atoms.

photochemical stability and resistance to attack by strong oxidants and by strong Brønsted acids and bases.[35] In addition, the substitution chemistry of boron-based compounds is extensive, allowing these anions to be tailored to a number of applications.[43-48]

The monocarborane anion, $CB_{11}H_{12}^-$, has been known for some time.[41,42] In addition to the stabilities mentioned above, the monocarborane anion has been shown to be a very weakly coordinating anion and a very weak nucleophile.[3,49-52] An example of the weakly coordinating nature of the *closo*-$CB_{11}H_{12}^-$ anion is provided by the work of Reed and co-workers. The structure of Fe(TPP)($CB_{11}H_{12}$)is shown in Figure I.1.4 (TPP = tetraphenylporphyrin).[50] The degree of iron atom displacement from the plane of the nitrogen atoms in $Fe(TTP)^+$ is one test of weakly coordinating ability of an anion. In comparison with the common anions I^-, ClO_4^-, and SbF_6^-, the carborane anion showed the smallest out of plane displacement (cf. 0.10 Å compared with 0.53, 0.30, and 0.15 Å, respectively) and was therefore called the weakest anion (at the time).[50]

The $CB_{11}H_{12}^-$ anion does, however, have two important limitations. First, the trityl salt of $CB_{11}H_{12}^-$ cannot be synthesized; this is presumably due to hydride abstraction from the cluster.[53] Hydride abstraction by other, stronger electrophiles (like SiR_3^+) seems likely as well. This limits the number of useful metathesis salts that can be made and therefore limits the anion's usefulness. The other limitation is the cluster's lack of oxidative stability. It has been shown that $CB_{11}H_{12}^-$ is stable to electrochemical oxidation (Pt electrode) at potentials >1.7 V (vs. NHE) in acetonitrile but is irreversibly oxidized at ~0.5 V (Pt electrode) in dichloromethane.[53]

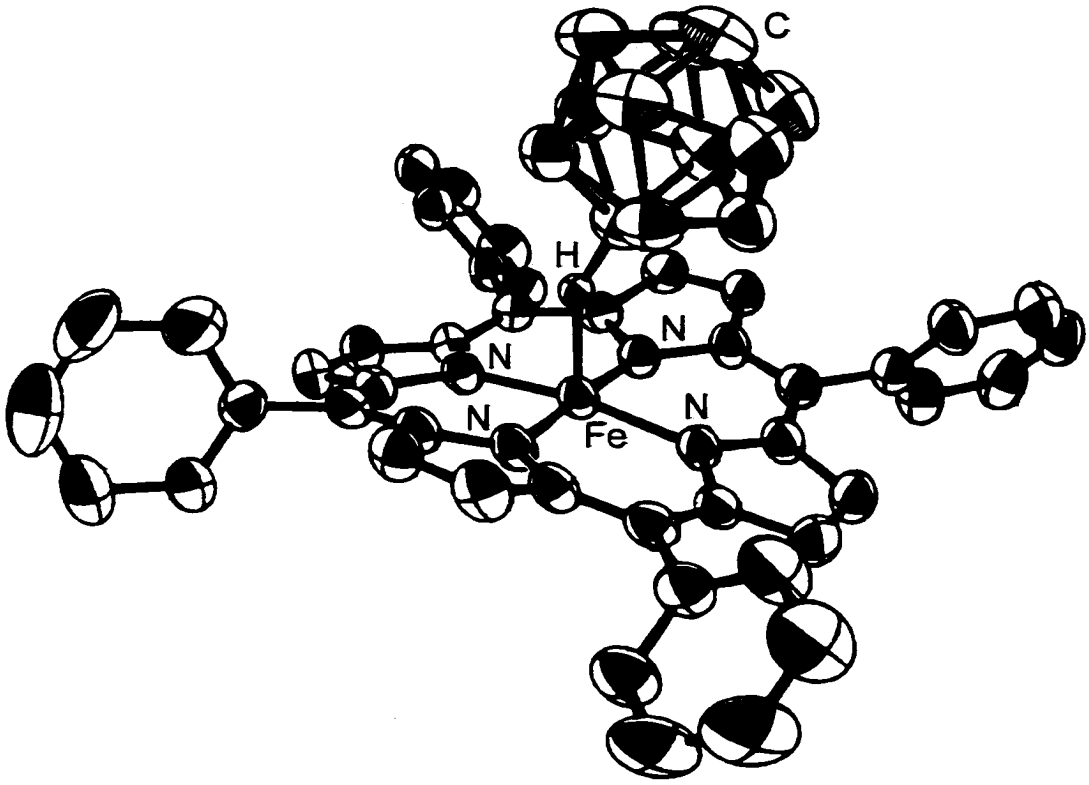

Figure I.1.4. The crystal structure of Fe(TPP)($CB_{11}H_{12}$).[50] The iron atom is nearly planar with the nitrogen atoms of the TPP. The $CB_{11}H_{12}^-$ anion is coordinated to the iron center through the H(12) atom.

Recently, derivatives of $CB_{11}H_{12}^-$ have received renewed attention as candidates for use as superweak anions.[3,49-52] Initial efforts in this area focused on the substitution of the B–H bond antipodal to the carbon atom (i.e., B(12)–H(12)) with a halogen or a halogenated group;[45,53] examples are found in the work of Reed and coworkers, who synthesized a variety of halogenated derivatives of the form $CB_{11}H_{12-n}X_n^-$ (X = Cl, Br; n = 1, 2) and 12-$CB_{11}H_{11}(C_6F_6)^-$,[53,54] and of the Czech group lead by Štíbr, who mono- and diiodinated ($CB_{11}H_{12-n}I_n^-$; n = 1, 2), polychlorinated ($CB_{11}H_{12-n}Cl_n^-$, n = 5, 6), and hexabrominated ($CB_{11}H_6Br_6^-$) the anion.[45] More recent work has extended the idea by *B*-perhalogenating the cluster:

1-H-$CB_{11}I_{11}^-$;[55] 1-CH_3-$CB_{11}X_{11}^-$ and 1-H-$CB_{11}X_{11}^-$ (X = Cl, Br, I).[56,57] Additionally, the anion has been permethylated, $CB_{11}(CH_3)_{12}^-$, and perfluoromethylated, $CB_{11}(CF_3)_{12}^-$.[58,59] By polyhalogenation and polymethylation of $CB_{11}H_{12}^-$, it was hoped that these new anions would be more oxidatively stable to electrophilic attack and more weakly coordinating. The new polyhalogenated carborane derivatives are stable in the presence of strong electrophiles; silylium salts containing the $CB_{11}H_{12-n}X_n^-$ (X = Cl, Br, I) anions are stable and have been isolated.[60,61] In addition, one member of this class of anions has even been used to synthesize new crystalline acids.[6]

Given the above improvement of the weakly coordinating ability of the carborane cluster by halogenation, it seems logical that fluorinated derivatives would be better than the corresponding chlorine, bromine, iodine, and methyl derivatives. Because of the strong electron withdrawing ability of fluorine, fluorinated carborane anions should be more resistant to oxidation. It is a long known fact that fluorinated organic compounds, such as Teflon™, are more resistant to oxidation than their unfluorinated counterparts. The fluorinated derivatives of $CB_{11}H_{12}^-$ should also be less likely to undergo halogen abstraction since B–F bonds are the strongest of the B–X bonds. Finally, these new compounds should be more weakly coordinating than the chlorinated, brominated, or iodinated analogues (vide supra; A variety of techniques have been proposed for determining the weakly coordinating ability of an anion.[50,51,60,61]), providing new and exciting possibilities for the exploration of chemistry not possible with the existing generation of superweak anions.

CHAPTER 2
Fluorination Reactions of $CB_{11}H_{12}^-$ and Related Anions

Introduction

Prior to the undertaking of this study, only one fluorinated *closo*-heteroborane, 2-$CB_{11}H_{11}F^-$, had been reported.[48] Its method of preparation was the insertion of a "BF" moiety into the *nido*-7-$CB_{10}H_{13}^-$ anion and cannot be used to produce more highly fluorinated derivatives. Therefore, the pursuit of highly fluorinated *closo*-heteroborane anions of the form $EB_{11}H_{11-n}F_n^-$ (E = CH, As, Sb, Bi) by a general method of fluorination, starting with the easily accessible precursors $CB_{11}H_{12}^-$,[41,42,62] $AsB_{10}H_{12}^-$,[63,64] $AsB_{11}H_{11}^-$,[64,65] $SbB_{11}H_{11}^-$,[65,66] and $BiB_{11}H_{11}^-$ was undertaken.[65,67] Liquid anhydrous hydrogen fluoride (LAHF) was chosen as the initial fluorinating agent. This approach to fluorinating boron clusters was pioneered by Muetterties and his group at DuPont in the 1960s[68,69] and was studied, more recently, for the $B_{12}H_{12-n}F_n^{2-}$ system, by Solntsev and co-workers[70,71] but to the author's knowledge has not been tried with any boron cluster *mono*anions. The second method examined used an organic *N*-fluoro compound. There are no reported cases of B–H to B–F bond conversion using such reagents.

The *closo*-pnictaborane anions provide a unique opportunity to study a complete class of *closo*-heteroborane anions, all of which have the same basic shape, the same geometry (i.e., C_{5v} point group, twelve cage atoms/vertices), but which contain a series of different heteroatoms in the cluster skeleton. The three *closo*-pnictaborane clusters to be examined here contain arsenic, antimony, or bismuth atoms and are isolobal with the carbon atom in $CB_{11}H_{12}^-$:

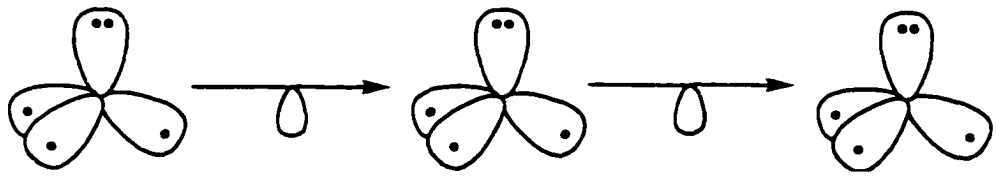

Each heteroatom has a different electron withdrawing power and each has a different amount of electron density available to provide to the cage. In addition, the bonding orbitals are different sizes and have different energies—the larger the Z number of the heteroatom, the larger the discrepancy between the boron bonding orbitals and the heteroatom orbitals becomes. These differences will cause the electron distribution within the heteroborane cage to differ between clusters, potentially altering the substitution chemistry and coordinating ability of these anions.

In addition to some of the weakness discussed in Part I, Chapter 1 for the *closo*-carborane cluster, the *closo*-pnictaborane anions have two major weaknesses that may limit their potential usefulness for superweak anion applications. First, the presence of a cluster atom capable of existing in more than one oxidation state allows for the possibility of redox chemistry with cationic electrophiles. When $AgNO_3$ was mixed with $AsB_{11}H_{11}^-$ in water, a silver mirror forms on the walls of the reaction vessel.[72] This suggests that silver(I) cations oxidized the arsenic in the cluster from As^{3+} to As^{5+}. The

second potential weakness relates to the coordinating ability of this class of anions. Unlike the *closo*-carborane anion, the *closo*-pnictaborane anions have lone pair of electron density located on the heteroatom. Two major pieces of experimental data illustrate the coordinating ability of the heteroatom lone pair electron density. First, treatment of $NB_{11}H_{11}^-$ with HBF_4 in diethyl ether followed by extraction with toluene produces the neutral cluster, 1-H-$NB_{11}H_{11}$.[73] The coordination of CH_3^+ to the $PB_{11}H_{11}^-$ cage in 1-CH_3-$PB_{11}H_{11}$ also indicates that there is significant amount of lone pair electron density on the heteroatom.[74] As in the case of $CB_{11}H_{12}^-$, halogenation is expected to make the cluster skeletal atoms (and therefore the heteroatom) more electron deficient. It is hoped that this methodology will also make the pnictaboranes less basic and, at the same time, make the heteroatom (and the cluster) more stable to oxidation. Thus fluorination is expected to make both the *closo*-carborane anions and the *closo*-pnictaborane anions better superweak anions than their respective parent clusters.

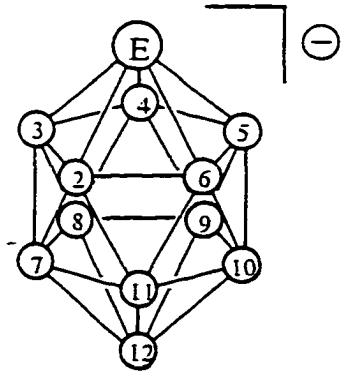

$EB_{11}H_{11}^-$

(E = CH, As, Sb, Bi)

Figure I.2.1. Numbering scheme for *closo*-heteroborane anions.

Experimental Methods

Inert Atmosphere. None of the heteroborane anions are oxygen or water sensitive. However, the silver(I) salts that were prepared are moisture sensitive. Therefore, preparations and physical measurements were carried out with rigorous exclusion of air and water whenever necessary. Schlenk, glovebox, and high-vacuum techniques were employed using purified nitrogen or argon used when an inert atmosphere was required.[75]

Solvents. All solvents used in this study were reagent grade or better. Distilled water was deionized by passage through a Barnstead Nanopure water treatment system. The following solvents were dried by distillation from the indicated drying agent: acetone (activated 4 Å molecular sieves), acetone-d_6 (activated 4 Å molecular sieves), tetrahydrofuran (Na), benzene (Na), benzene-d_6 (Na), dichloromethane (P_2O_5), dichloromethane-d_2 (P_2O_5), acetonitrile-d_3 (P_2O_5), trichlorofluoromethane (P_2O_5), and diethyl ether (Na). Liquid anhydrous HF (LAHF, Matheson) was used as received. CAUTION: HF is toxic and extremely corrosive to skin and eyes (see Appendix I.A for material safety data sheets, MSDS).

Reagents. The following compounds were used as received: KOH (Aldrich), CsOH (Aldrich), CsCl (Aldrich), $AgNO_3$ (MCB); $(CH_3)_3NHCl$ (Aldrich); Bu_4NCl (Aldrich), *n*-butyl lithium (2.5 M in hexanes, Aldrich), AsI_3 (Aldrich), As_2O_3 (Aldrich), Sb_2O_3 (Aldrich), Bi_2O_3 (Aldrich), and F-TEDA-BF_4 (Air Products).[76,77] Decaborane(14) ($B_{10}H_{14}$, Callery and Katchem) was sublimed at 70°C under vacuum CAUTION: $B_{10}H_{14}$ is toxic and is an explosion hazard if heated in air (see Appendix I.A for MSDS). The following compounds were prepared following literature

procedures: $Cs(CB_{11}H_{12})$,[41,42,62] $Cs(2\text{-}CB_{11}H_{11}F)$,[48] $Cs(7\text{-}AsB_{10}H_{12})$,[63,64] $Cs(AsB_{11}H_{11})$,[64,65] $Cs(SbB_{11}H_{11})$,[65,66] and $Cs(BiB_{11}H_{11})$.[65,67]

Spectroscopic Measurements. Samples for ^{1}H (300.0 MHz), ^{11}B (96.3 MHz), ^{13}C (75.5 MHz), and ^{19}F (282.4 MHz) NMR spectroscopy were acetone-d_6, benzene-d_6, acetonitrile-d_3, or dichloromethane-d_2 solutions in sealed 5-mm glass tubes. Spectra were recorded on a Bruker AC-300, a Bruker WP-300, or a Varian 300. Chemical shifts (δ scale) are relative to $(CH_3)_4Si$ (^{1}H and ^{13}C), external $BF_3{\cdot}OEt_2$ (^{11}B), and external $CFCl_3$ (^{19}F). Samples for negative-ion electrospray mass spectrometry (NIEMS) were solutions in water, acetonitrile, methanol, or a mixture of these three solvents. Spectra were recorded on a Fisons VG Quattro-SQ mass spectrometer. The sample cone voltage was 75 V, high enough to preclude the formation of ion clusters.[78] Control experiments with mixtures of known amounts of $Cs(CB_9H_{10})$ and $Cs(CB_9H_8F_2)$ demonstrated that mass spectral peak intensities, ^{11}B NMR peak integrals, and ^{19}F NMR peak integrals were all approximately proportional to the concentrations of the anions present.

Synthesis of Alternate Salts. All reactions using LAHF were conducted with Cs^+ salts. Cation exchange reactions have allowed Li^+, Ag^+, $(CH_3)_3NH^+$, Bu_4N^+, and $(C_6H_5)_4P^+$ salts to be isolated in quantitative yields. Transformation of cesium salts to $(CH_3)_3NH^+$ and Bu_4N^+ salts was carried out using $(CH_3)_3NHCl$ and Bu_4NCl. Addition of a slight excess of the desired metathesis reagent caused precipitation of the new trimethyl- or tetrabutylammonium salt. Lithium salts were synthesized by reacting the dry $(CH_3)_3NH^+$ salt of the desired anion with one equivalent of n-BuLi in THF. The byproducts (butane and $N(CH_3)_3$) and solvent were removed under vacuum leaving a THF adduct of the Li^+ salt. Coordinated THF was removed by heating under vacuum. The reaction of a suspension of $Cs(CB_{11}H_{12-n}F_n)$ and $AgNO_3$ in hot benzene followed by hot filtration, and removal of solvent yielded $Ag(C_6H_6)_n(CB_{11}H_{12-n}F_n)$ salts.

Synthesis of New Compounds. ***Carboranes.*** **$Cs(12\text{-}CB_{11}H_{11}F)$.** A typical reaction is as follows: 1.0023 g (3.632 mmol) of $Cs(CB_{11}H_{12})$ was placed into a 300 ml Monel reaction vessel. 60 ml LAHF was condensed into the reaction vessel at –78°C. The reaction vessel was capped under an N_2 purge. This reaction mixture was stirred at 40°C for 72 hours after which time the LAHF was removed using vacuum transfer techniques. The product was extracted with 75ml, 25 ml, and 25 ml of H_2O by rotating the aqueous mixture in the reaction vessel. The extractant was filtered leaving a clear, colorless filtrate. Removal of the solvent by rotary evaporation left a white solid. Vacuum drying yielded 0.7152 g (3.234 mmol; 89% yield) of white solid. ^{11}B NMR (acetone-d_6): δ 14.6 (s, 1 B), –14.1 (d, J_{BH} = 136, 5 B), –18.5 (d, J_{BH} = 152, 5 B); ^{19}F NMR (acetone-d_6): δ –190.4 (q, J_{BF} = 59 Hz); ^{13}C NMR (acetone-d_6): δ 36.1 (d, J_{CH} = 171 Hz, 1 C); ^{1}H NMR (acetone-d_6): δ 1.48 (q, 5 H), 1.71 (q, 5 H), 1.96 (d, CH, 1 H).

$Ag(C_6H_6)_2(12\text{-}CB_{11}H_{11}F)$. 0.300 g (1.021 mmol) of $Cs(12\text{-}CB_{11}H_{11}F)$ was dissolved in 10 ml of H_2O. A solution of $AgNO_3$ (0.1734 g; 1.021 mmol) in 10 ml of H_2O was slowly added to the above solution, and the solution was allowed to stir in darkness for 40 minutes. Benzene (35 ml) was added to the stirring solution, and the layers were separated using a separatory funnel. The water layer was again treated with 25 ml of benzene and separated. The benzene was removed from the combined, clear, colorless solution leaving a white solid.

$Cs(7,12\text{-}CB_{11}H_{10}F_2)$. A typical reaction is as follows: 0.060 g (0.217 mmol) of $Cs(CB_{11}H_{12})$ was placed into a 300 ml Monel reaction vessel, and 10 ml LAHF was condensed into the vessel at –78°C. The reaction vessel was capped under an N_2 purge. This reaction mixture was stirred at 140°C for 44 hours after which time the LAHF was removed using vacuum transfer techniques. The product was extracted with 75ml, 25 ml, and 25 ml of H_2O by rotating the aqueous mixture in the reaction vessel. The extractant

was filtered leaving a clear, colorless filtrate. Removal of the solvent by rotary evaporation left a white solid. Vacuum drying yielded the target product as a white solid. ^{11}B NMR (acetone-d_6): δ 12.3 (s, 1 B), 7.5 (s, 1 B), –15.9 (d, J_{BH} = 127, 2 B), –16.9 (d, J_{BH} = 127, 2 B), –19.9 (d, J_{BH} = 147, 2 B), –22.6 (d, J_{BH} = 156, 2 B), –26.5 (d, J_{BH} = 156, 1 B); ^{19}F NMR (acetone-d_6): δ –194.4 (q, J_{BF} = 59, 1 F), –212.0 (q, J_{BF} = 55, 1 F); ^{13}C NMR (acetone-d_6): δ 32.7 (d, 1 C); ^{1}H NMR (acetone-d_6): δ 1.17 (q, 1 H), 1.29 (q, 2 H), 1.55 (q, 2 H), 1.71 (q, 2 H), 1.80 (q, 2 H), 1.89 (d, CH, 1 H).

Cs(2,12-$CB_{11}H_{10}F_2$). 0.027 g (0.098 mmol) of Cs(2-$CB_{11}H_{11}F$)[48] was placed into a 30 ml Teflon reaction vessel. 15 ml LAHF was condensed into the vessel at –78°C. The reaction vessel was capped under an N_2 purge. This reaction mixture was stirred at 48 °C for 16 hours after which time the LAHF was removed using vacuum transfer techniques. The product was extracted with acetone leaving a clear, colorless solution. Filtration and vacuum drying yielded the target compound as a white solid. The NMR spectra showed that, although there is ca. 2% 2-$CB_{11}H_{11}F^-$ in the product, no other difluoro isomer was present in the mixture. ^{11}B NMR (acetone-d_6): δ 12.8 (s, 1 B), 1.4 (s, 1 B), –16.0 (d, 2 B), –16.9 (d, J_{BH} = 128, 2 B), –18.5 (d, 2 B), –20.8 (d, 2 B), –23.4 (d, 1 B); ^{19}F NMR (acetone-d_6): δ –193.8 (q, J_{BF} = 59, 1 F), –211.8 (q, J_{BF} = 60, 1 F); ^{13}C NMR (acetone-d_6): δ 35.8 (d, 1 C).

Cs(7,9,12-$CB_{11}H_9F_3$). Cs($CB_{11}H_{12}$) (0.060 g; 0.217 mmol) was placed into a 300 ml Monel reaction vessel, and 15 ml LAHF was condensed into the vessel at –78 °C. The reaction vessel was capped under an N_2 purge. This reaction mixture was stirred at 175°C for 59 hours after which time the LAHF was removed using vacuum transfer techniques. The product was extracted with acetone leaving a clear, colorless solution. Filtration and vacuum drying yielded the target compound as a white solid. ^{11}B NMR (acetone-d_6): δ 10.0 (s, 1 B), 5.2 (s, 2 B), –17.2 (d, 1 B), –18.4 (d, 2 B),

–23.7 (d, J_{BH} = 156, 2 B), –27.0 (d, 1 B), –28.2 (d, 2 B); ^{19}F NMR (acetone-d_6): δ –198.1 (q, J_{BF} = 61, 1 F), –216.0 (q, J_{BF} = 56, 2 F); ^{13}C NMR (acetone-d_6): δ 28.2 (d, 1 C); ^{1}H NMR (acetone-d_6): δ 1.09 (q, 1 H), 1.38 (q, 2 H), 1.56 (q, 2 H), 1.69 (q, 2 H), 1.82 (d, CH, 1 H), 1.90 (q, 1 H).

Cs(7,8,10,12-$CB_{11}H_8F_4$). Cs($CB_{11}H_{12}$) (0.073 g; 0.26 mmol) was placed into a 300 ml Monel reaction vessel, and 60 ml LAHF was condensed into the reaction vessel at –78 °C. The reaction vessel was capped under an N_2 purge. This reaction mixture was stirred at 230 °C for 64 hours after which time the LAHF was removed using vacuum transfer techniques. The product was extracted with acetone leaving a clear, colorless solution. Filtration and vacuum drying yielded the desired product as a white solid. ^{11}B NMR (acetone-d_6): δ 5.0 (s, 1 B), 0.0 (s, 3 B), –22.0 (d, J_{BH} = 139, 2 B), –29.8 (d, 2 B), –32.5 (d, 1 B), –32.9 (d, 2 B); ^{19}F NMR (acetone-d_6): δ –202.7 (q, J_{BF} = 62, 1 F), –220.3 (q, 1 F), –222.7 (q, 2 F); ^{13}C NMR (acetone-d_6): δ 22.4 (d, 1 C); ^{1}H NMR (acetone-d_6): δ 1.27 (q, 2 H), 1.38 (q, 2 H), 1.49 (q, 1 H), 1.70 (d, CH, 1 H), 1.80 (q, 2 H).

Cs(7,8,9,10,11,12-$CB_{11}H_{12-n}F_n$) (n = 5, 6, 7). Cs($CB_{11}H_{12}$) (0.500 g, 1.81 mmol) was placed into a 300 ml Monel reaction vessel, and 10 ml LAHF was condensed into the vessel at –78°C. The reaction vessel was capped under an N_2 purge. This reaction mixture was stirred at room temperature (12 h), 270°C (72 h), 360°C (24 h), and 365°C (7 d) after which time the LAHF was removed using vacuum transfer techniques. The product was rotated (15 min) in the reaction vessel with 50 ml. The clear solution was filtered and 150 mg of Me_3NHCl added. The resulting white precipitate was collected by filtration. Low-resolution NIEMS, *m/z*: 233.3 (F_5^-, 7%), 251.3 (F_6^-, 78%), 269.3 (F_7^-, 15%).

Cs(7,8,9,10,12-$CB_{11}H_7F_5$): ^{11}B NMR (acetone-d_6): δ 1.9 (s, 1 B), –2.7 (s, 4 B), –25.2 (d, 1 B), –30.7 (d, 1 B), –34.5 (d, 2 B), –36.1 (d, 2 B); ^{19}F NMR (acetone-d_6):

δ –206.8 (q, J_{BF} = 63, 1 F), –223.1 (q, 2 F), –226.9 (q, 2 F); ^{13}C NMR (acetone-d_6): δ 14.9 (d, 1 C); ^{1}H NMR (acetone-d_6): δ 1.12 (q, 2 H), 1.46 (q, 2 H), 1.56 (q, 1 H; d, CH, 1 H), 1.67 (q, 1 H).

Cs(7,8,9,10,11,12-$CB_{11}H_6F_6$): ^{11}B NMR (acetone-d_6): δ –2.0 (s, 1 B), –5.0 (s, 5 B), –37.2 (d, J_{BH} = 164, 5 B); ^{19}F NMR (acetone-d_6): δ –209.7 (q, J_{BF} = 66, 1 F), –229.9 (q, 5 F); ^{13}C NMR (acetone-d_6): δ 5.1 (d, 1 C); ^{1}H NMR (acetone-d_6): δ 1.32 (q, 5 H), 1.40 (d, CH, 1 H).

Alternate Synthesis of Carborane Anions. (n-Bu_4N)($CB_{11}H_{12-n}F_n$) (*n* =1–6). $Cs(CB_{11}H_{12})$ was dissolved in acetonitrile and treated with ten (10) equivalents of F-TEDA at 25°C, 40°C, and 100°C. At selected time intervals, samples were withdrawn, and treated as follows. The acetonitrile was removed under vacuum and all carborane-containing salts were extracted from the solid residue with acetone. Acetone was removed under vacuum, the solid residues were dissolved in 5% aqueous KOH, and (n-Bu)$_4$NCl was added to quantitatively precipitate all carborane anions as (n-Bu)$_4N^+$ salts. Reactions resulted in mixtures of fluorinated derivatives, $CB_{11}H_{12-n}F_n^-$ (*n* = 1–6). Low-resolution NIEMS, *m/z*: 25°C: 143.0 (F_0^-, 82%), 161.1 (F_1^-, 11%), 177.0 (F_2^-, 7%), 197.0 (F_3^-, trace); 40°C: 143.0 (F_0^-, 35%), 161.1 (F_1^-, 52%), 177.0 (F_2^-, 10%), 197.0 (F_3^-, 3%), 215.3 (F_4^-, trace); 100°C: 177.0 (F_2^-, 15%), 197.0 (F_3^-, 40%), 215.3 (F_4^-, 34%), 233.3 (F_5^-, 10%), 251.3 (F_6^-, 1%).

(n-Bu_4N)(7-$CB_{11}H_{11}F$): ^{11}B NMR (acetone-d_6): δ 10.2 (s, 1 B), –7.4 (d, 1 B), –14.2 (d, 2 B), –15.5 (d, 2 B), –17.4 (d, 2 B), –18.8 (d, 2 B), –24.8 (d, 1 B); ^{19}F NMR (acetone-d_6): δ –208.0 (q, 1 F).

Synthesis of New Compounds. *Arsaboranes.* Cs(2-$AsB_{11}H_{10}F$). A solution of (Me_3NH)($AsB_{10}H_{12}$) (0.5187 g, 1.535 mmol) in THF (15 ml) was treated with *n*-butyl lithium (4.0 ml, 8.0 mmol). The tan suspension was stirred for 10 minutes, at which time

half of the THF was removed using vacuum. The remaining tan, cloudy mixture was cooled to 0°C, and 3.8 ml of $BF_3{\cdot}O(C_2H_5)_2$ was added. After 3 minutes, the solution became clear and tan. This mixture was stirred overnight, after which time the solvent was removed under vacuum. The remaining tan solid was dissolved in 1 M NaOH. An excess of CsCl was added to the solution and the sample volume was reduced by rotary evaporation until 5 ml of solution remained. The resulting white precipitate was collected by filtration and dried on a vacuum line. ^{11}B NMR (acetone-d_6): δ 15.8 (s, 1 B), 4.6 (d, J_{BH} = 134, 1 B), –6.9 (d, 2 B), –8.7 (d, 4 B), –11.3 (d, 2 B), –17.8 (d, J_{BH} = 134, 1 B); ^{19}F NMR (acetone-d_6): δ –192.7 (q, J_{BF} = 78, 1 F).

$Cs(AsB_{11}H_{11-n}F_n)$ (n = 0, 1, 2). 0.0275 g (0.814 mmol) of $Cs(AsB_{11}H_{11})$ was placed into a 300 cc Monel reaction vessel. To this, 30 ml of liquid anhydrous hydrogen fluoride (LAHF) was added. This reaction mixture was rotated at 25°C for 40 hours after which time the LAHF was removed via vacuum transfer techniques. After drying for 12 hours in the reaction vessel to remove HF, the product was extracted with 2 x 20 mL of acetone and filtered. Acetone was removed from the clear, colorless filtrate on a rotary evaporatory leaving a white solid. This sample was dried on a vacuum line. Low-resolution NIEMS, *m/z*: 205.2 (F_0, 26%), 223.2. (F_1, 67%), and 239.2 (F_2, 7%).

$Cs(12\text{-}AsB_{11}H_{10}F)$: ^{11}B NMR (acetone-d_6): δ 21.6 (s, 1 B), –10.2 (s, 5 B), –12.3 (d, 5 B, J_{B-H} = 162 Hz); ^{19}F NMR (acetone-d_6): δ –158.9 (q, J_{BF} = 62, 1 F). Other ^{19}F NMR signals: δ –193.6 (q) and –196.5 (q)

$Cs(AsB_{11}H_{11-n}F_n)$ (n = 4, 5). 0.0200 g (0.0592 mmol) of $Cs(AsB_{11}H_{11})$ was placed into a Monel reaction vessel containing a Teflon coated stirring bar. To this, 7 ml of LAHF was added. This reaction mixture was stirred at 200°C for 64 hours after which time the LAHF was removed via vacuum transfer techniques. The resulting white solid

was dried on a vacuum line. Low-resolution NIEMS, *m/z*: 205.2 (F_0, 10%), 277.2 (F_4, 70%), and 295.2 (F_5, 20%).

Synthesis of New Compounds. ***Stibaboranes.*** **$Cs(7,9\text{-}SbB_{11}H_9F_2)$.** 0.0188 g (0.0489 mmol) of $Cs(SbB_{11}H_{11})$ was placed into a Teflon reaction vessel containing a Teflon coated stirring bar. To this, 9 ml of LAHF was added. This reaction mixture was stirred at room temperature (25°C) for 44 hours after which time the LAHF was removed using vacuum transfer techniques. The resulting white solid was dried on a vacuum line. Low-resolution NIEMS, *m/z*: 252.2 (F_0^-, 1%), 269.2 (F_1^-, 1%), 287.3 (F_2^-, 97%), and 305.3 (F_3^-, 1%). ^{11}B NMR (acetone-d_6): δ 13.1 (s, 2 B), 7.7 (d, 1 B), –11.2 (d, 3 B), –14.1 (d, 2 B), –17.3 (d, 1 B), –19.0 (d, 2 B); ^{19}F NMR (acetone-d_6): δ –194.1 (q, J_{BF} = 63, 2 F); ^{1}H NMR (acetone-d_6): δ 4.31 (q, 1 H), 3.10 (q, 1 H), 2.79 (q, 2B), 1.64 (q, 2 H), 1.47 (q, 2 H), 1.17 (q, 1 H).

Synthesis of New Compounds. ***Bismaboranes.*** **$Cs(7,9\text{-}BiB_{11}H_9F_2)$.** 0.0235 g (0.0498 mmol) of $Cs(BiB_{11}H_{11})$ was placed into a Teflon reaction vessel containing a Teflon coated stirring bar. To this, 10 ml of LAHF was added. This reaction mixture was stirred at 0°C for 40 hours after which time the LAHF was removed using vacuum transfer techniques. The resulting tan solid was dried on a vacuum line. Low-resolution NIEMS, *m/z*: 339.4 (F_0^-, 57%), 356.5 (F_1^-, 6%), 375.5 (F_2^-, 34%), and 393.4 (F_3^-, 3%). ^{11}B NMR (acetone-d_6): δ 18.9 (s, 2 B), 12.3 (d, J_{BH} = 130, 1 B), –10.6 (d, 3 B), –12.5 (d, 2 B), –15.9 (d, 1 B), –16.9 (d, J_{BH} = 144, 2 B); ^{19}F NMR (acetone-d_6): δ –190.8 (q, J_{BF} = 57, 2F).

$Cs(BiB_{11}H_{11-n}F_n)$ (n = 1–4). 0.0226 mg (0.0479 mmol) of $Cs(BiB_{11}H_{11})$ was placed into a Teflon reaction vessel containing a Teflon coated stirring bar. To this, 10 ml LAHF was added. This reaction mixture was stirred at room temperature (25°C) for

44 hours after which time the LAHF was removed using vacuum transfer techniques. The resulting tan solid was dried on a vacuum line. Low-resolution NIEMS *m/z*: 339.4 (F_0^-, 23%), 357.5 (F_1^-, 31%), 375.5 (F_2^-, 13%), 392.5 (F_3^-, 15%), and 410.5 (F_4^-, 17%).

Results

The following shorthand notation will be used for the heteroborane anions. For a given anion: X_0^- = parent (i.e., unhalogenated) cluster, X_1^- = monohalogenated derivative, X_2^- = dihalogenated derivative, etc. A numerical prefix before the shorthand notation indicates the vertex to which the halogen atom is bound. For example, 12-Br_1^- means that the cluster is a monobromo derivative with the bromine atom bonded to B(12), and 7,9-F_2^- means that the cluster is a difluoro derivative with fluorine atoms boned to both B(7) and B(9). When necessary, the *X*-notation will be augmented with the heteroatom of the cluster to be considered: 7-AsF_1^- represents 7-$AsB_{11}H_{10}F^-$.

Fluorination Using LAHF[79]

It was previously found that salts of $B_{12}H_{12}^{2-}$ could be fluorinated by treatment with liquid anhydrous hydrogen fluoride (LAHF) at temperatures from –20°C to 600°C to give $B_{12}H_{12-n}F_n^{2-}$ (n = 1–12).[70,71,80] These anions were fully characterized by ^{11}B and ^{19}F NMR spectroscopy and, in some cases, by X-ray crystallography.[70,71] These fluorination reactions occurred with high regio- and stereospecificity. In this work, it was found that LAHF will selectively fluorinate salts of $CB_{11}H_{12}^-$ and 2-$CB_{11}H_{11}F^-$ in a stepwise manner at a given temperature to produce salts of the form $CB_{11}H_{12-n}F_n^-$ (n = 1–4) that have high compositional purity and excellent isomeric purity.

$CB_{11}H_{12}^-$

Treatment of one gram of $Cs(CB_{11}H_{12})$ with LAHF (60 ml) for 72 hours at 25°C produced a single pure solid in 89% yield as well as one equivalent of a noncondensable gas (H_2):

$$Cs(CB_{11}H_{12}) + HF \xrightarrow[25\ °C,\ 72\ h]{} Cs(12\text{-}CB_{11}H_{11}F) + H_2$$

The ^{11}B and ^{19}F NMR spectra of the unrecrystallized product are shown in Figure I.2.2 (there is no detectable $CB_{11}H_{12}^-$ or difluoro derivative), and the ^{11}B, ^{1}H, ^{13}C, and ^{19}F NMR chemical shifts and coupling constants are listed in Table I.2.1. These NMR spectra are consistent with monofluoro substitution and C_{5v} symmetry, and they support the assertion that the hydrogen atom farthest removed from the carbon atom (i.e., the antipodal hydrogen atom) was replaced by a fluorine atom.

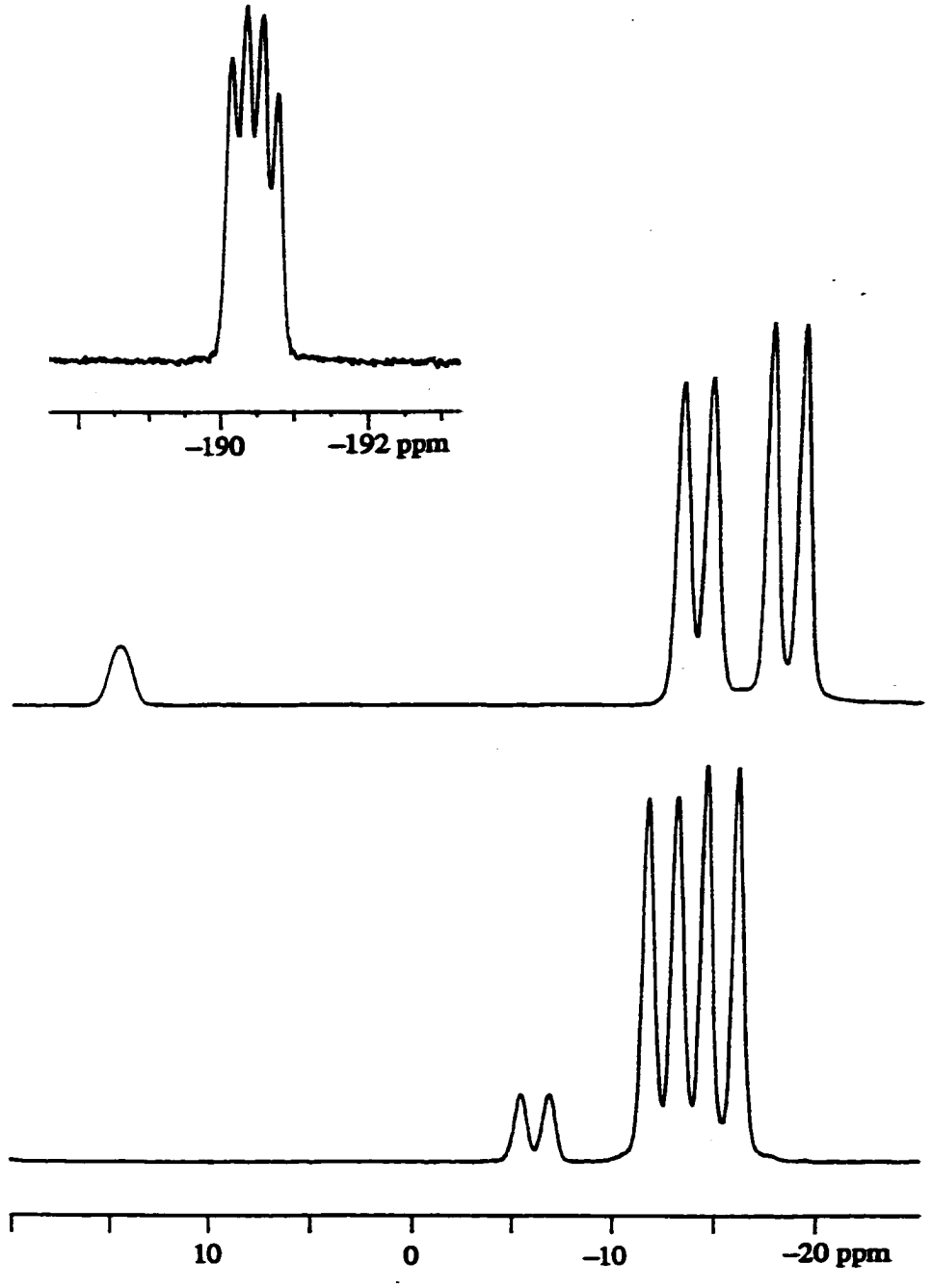

Figure I.2.2. ^{11}B NMR spectra (acetone-d_6) of Cs(12-$CB_{11}H_{11}F$) (top) and Cs($CB_{11}H_{12}$) (bottom). Inset: ^{19}F NMR spectrum of Cs(12-$CB_{11}H_{11}F$).

Table I.2.1. NMR Spectral Data for $CB_{11}H_{11-n}F_n^-$ Anions in Acetone-d_6

anion	atom #	$\delta(^{13}C)^a$	$^1J_{CH}{}^b$	$\delta(^{11}B)^{a,c}$	$^1J_{BH}{}^b$	$\delta(^{19}F)^{a,d}$	$^1J_{BF}{}^b$	$\delta(^1H)^a$
$CB_{11}H_{12}^-$	1	51.4						2.35
	12			–5.9				1.59
	7–11			–12.3				1.46
	2–6			–15.4				1.61
12-$CB_{11}H_{11}F^-$	1	36.1	171					1.96
	12			14.6		–190.4	59	
	7–11			–14.1	136			1.71
	2–6			–18.5	152			1.48
7-$CB_{11}H_{11}F^-$	1							
	7			10.2		–208.0		
	12			–7.4				
	8,11			–14.2				
	9,10			–15.5				
	2,3			–17.4				
	4,6			–18.8				
	5			–24.8				
7,12-$CB_{11}H_{10}F_2^-$	1	32.7						1.89
	12			12.3		–194.4	59	
	7			7.5		–212.0	55	
	8,11			–15.9	**127**[e]			1.80
	9,10			–16.9	**127**[e]			1.55
	2,3			–19.9	**147**[e]			1.71
	4,6			–22.6	156			1.29
	5			–26.5	156			1.17
2,12-$CB_{11}H_{10}F_2^-$	1	35.8						
	12			12.8		–193.8	59	
	2			1.4		–211.8	60	
	7,11			–16.0				
	8,10			–16.9	128			
	3,6			–18.5				
	4,5			–20.8				
	9			–23.4	143			

Table I.2.1. NMR Spectral Data for $CB_{11}H_{11-n}F_n^-$ Anions in Acetone-d_6 (*continued*)

anion	atom #	$\delta(^{13}C)^a$	$^1J_{CH}{}^b$	$\delta(^{11}B)^{a,c}$	$^1J_{BH}{}^b$	$\delta(^{19}F)^{a,d}$	$^1J_{BF}{}^b$	$\delta(^1H)^a$
7,9,12-$CB_{11}H_9F_3^-$	1	28.2						1.82
	12			10.0		-198.1	61	
	7,9			5.2		-216.0	56	
	8			–17.2				1.90
	10,11			–18.4	**137**[e]			1.69
	3,4			–23.7	156			1.56
	6			–27.0	**156**[e]			1.09
	2,5			–28.2	**156**[e]			1.38
7,9,10,12-$CB_{11}H_8F_4^-$	1	22.4						1.70
	12			5.0		–202.7	62	
	7			0.0		–220.3		
	9,10			0.0		–222.7		
	8,11			–22.0	139			1.80
	4,6			–29.8	**147**[e]			1.38
	5			–32.5				1.49
	2,3			–32.9	**161**[e]			1.27
7–10,12-$CB_{11}H_7F_5^-$	1	14.9						1.56
	12			1.9		–206.8	63	
	7,10			–2.7		–223.1		
	8,9			–2.7		–226.9		
	11			–25.2				1.67
	4			–30.7				1.56
	3,5			–34.5				1.46
	2,6			–36.1				1.12
7–12-$CB_{11}H_6F_6^-$	1	5.1						1.40
	12			–2.0		-209.7	66	
	7–12			–5.0		-229.9		
	2–6			–37.2	164			1.32

[a] δ values are in ppm from TMS (^{13}C, ^1H), $BF_3{\cdot}OEt_2$ (^{11}B), and $CFCl_3$ (^{19}F). [b] ^1J units = Hz. [c] All ^{11}B signals for B–F boron atoms are broad singlets, all B–H signals are doublets. [d] ^{19}F signals are quartets due to ^{11}B splitting. [e] Estimated values, due to partial signal overlap: 2 x (one coupled peak, Hz – the decoupled peak, Hz).

Two difluoro derivatives of $CB_{11}H_{12}^-$ were prepared using higher reaction temperatures. Treatment of $Cs(CB_{11}H_{12})$ with LAHF for 44 h at 140 °C produced $Cs(7,12\text{-}CB_{11}H_{10}F_2)$ in high compositionally purity. Boron-11 and ^{19}F NMR spectra indicate that the product also contained ca. 1% $12\text{-}CB_{11}H_{11}F^-$ and ca. 3% $7,9,12\text{-}CB_{11}H_9F_3^-$ (to be discussed below). The 7,12-assignment (C_s symmetry) is based on the 2D ^{11}B–^{11}B COSY NMR coupling pattern (Table I.2.1 and Figure I.2.3 top) and the 1:1 ^{19}F NMR intensity pattern (Table I.2.1 and Appendix I.B).[13,18] Significantly, no other difluoro isomer was detected in the NMR spectra (ignoring CF-containing isomers, there are six possible $CB_{11}H_{10}F_2^-$ isomers). The second difluoro derivative, the C_s-symmetry $2,12\text{-}CB_{11}H_{10}F_2^-$ isomer, was formed regioselectively when $Cs(2\text{-}CB_{11}H_{11}F)$[10] was treated with LAHF for 16 h at 42°C. This difluoro isomer exhibited a 1:1:2:2:2:2:1 ^{11}B and a 1:1 ^{19}F NMR intensity pattern similar to, but clearly different than, those of the 7,12-isomer (Table I.2.1 and Figure I.2.3 bottom).[13,18] The NMR spectra clearly show that, although there is ca. 2% $2\text{-}CB_{11}H_{11}F^-$ in the product, there is no other difluoro isomer.

A comparison of the 2D ^{11}B–^{11}B COSY NMR spectra of the 7,12- and 2,12-isomers is shown in Figure I.2.3. The peak intensities and order are the same for both isomers. This similarity is a result of the related degeneracy of the vertices; both anions have C_s symmetry. There is, however, a clear difference between the coupling patterns. Because weak of a weak signal no B(F)–B(F) coupling is seen in the $7,12\text{-}F_2^-$ isomer but B(F) coupling to B(8,11) is seen. This supports the 7,12-assignment. For the $2,12\text{-}F_2^-$ isomer, no B(F)–B(F) coupling is seen, as expected. Coupling of the B(2) boron atom to B(7,11) and to B(3,6) is seen, supporting the 2,12-assignment. In addition, the atom antipodal to the B(2)–F(2) vertex (Appendix I.C), B(9), should have the most negative δ value (see Part I, Chapter 3). This peak is coupled to the other fluorinated vertex (i.e., not B(2)) supporting the idea that fluorination of $2\text{-}CB_{11}H_{11}F^-$ occurs at B(12).

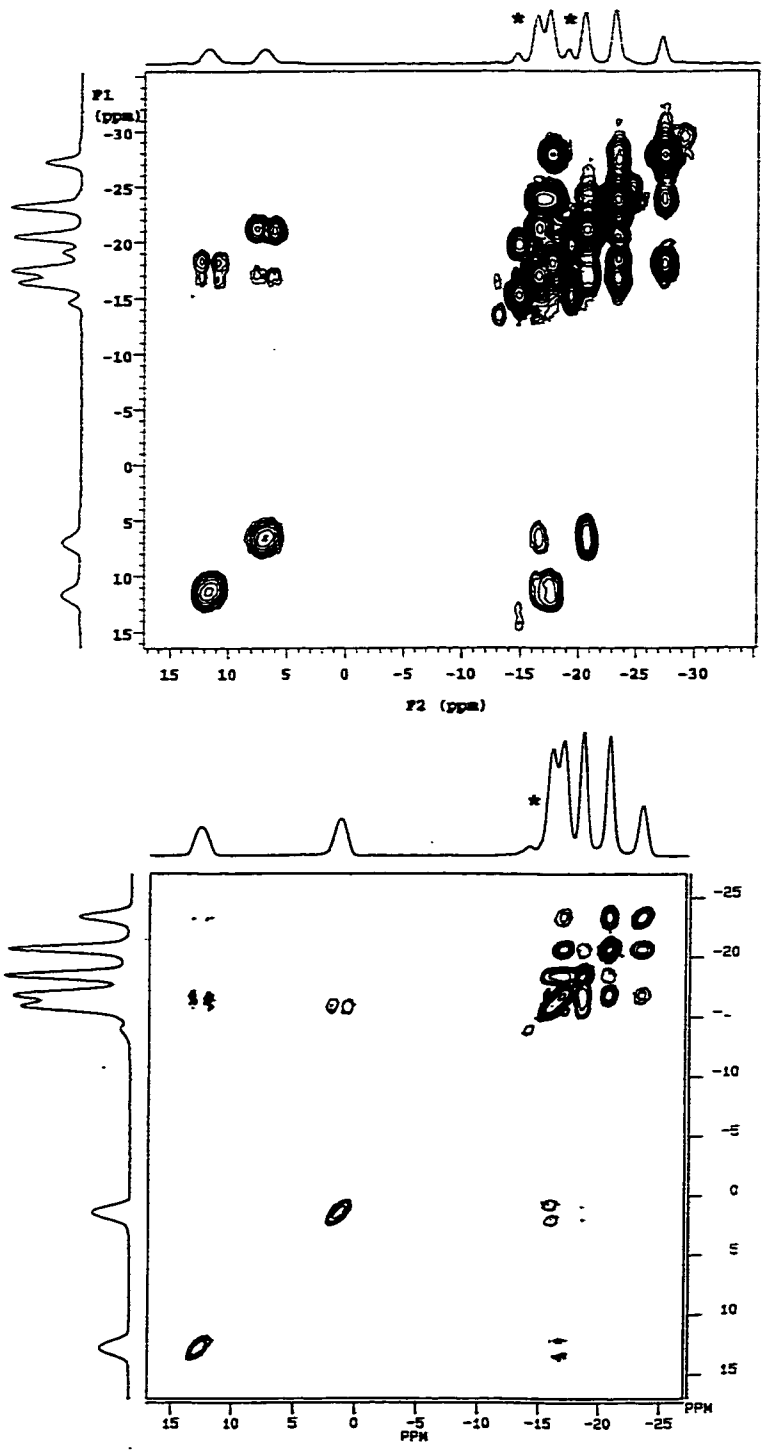

Figure I.2.3. Two-dimensional ^{11}B–^{11}B COSY NMR spectra (acetone-d_6) of the two $CB_{11}H_{10}F_2^-$ isomers: 7,12-$CB_{11}H_{10}F_2^-$ (top) and 2,12-$CB_{11}H_{10}F_2^-$ (bottom). Impurities are denoted with an astrick (*).

The reaction of $Cs(CB_{11}H_{12})$ with LAHF at 180°C for 70 hours produced $Cs(7,9,12\text{-}CB_{11}H_9F_3)$ in excellent compositional and isomeric purity. The 7,9,12-assignment (C_s symmetry) was based on the 1:2:1:2:2:1:2 ^{11}B NMR intensity pattern, the 1:2 ^{19}F NMR intensity pattern, and the ^{11}B–^{11}B NMR coupling pattern of the compound (Table I.2.1 and Figure I.2.4).[13,18] The NMR spectra are inconsistent with any other isomer, including the C_s-symmetry 7,8,12-isomer (ignoring CF-containing isomers, there are 34 possible $CB_{11}H_9F_3^-$ isomers). One or two percent of an unknown BF-containing impurity was present; therefore, the regioselectivity of this reaction is at least 98%. Higher reaction temperatures resulted in mixtures of $7,9,12\text{-}CB_{11}H_9F_3^-$ and what appears to be a single isomer of $CB_{11}H_8F_4^-$. When the reaction temperature was raised by 50°C to 230°C, $CB_{11}H_8F_4^-$ was formed exclusively. The 1:2:1 intensity ration of the ^{19}F NMR peaks and the 2D ^{11}B–^{11}B NMR coupling pattern (Figure I.2.5) allowed for the assignment of the isomerically pure derivative as the $7,9,10,12\text{-}CB_{11}H_8F_4^-$ isomer (Table I.2.1).

A summary of the reactions of $CB_{11}H_{12}^-$ with neat LAHF up to 230°C is shown in Figure I.2.6. As illustrated, varying the reaction temperature formed compositionally and isomerically pure derivatives containing one to four fluorine atoms, and the substitution reactions proceeded in a stepwise manner. When temperatures above 230°C were used, mixtures resulted. For example when 0.500 g of $Cs(CB_{11}H_{12})$ was reacted with 5 mL of LAHF at 390°C in a sealed Monel vessel, a mixture of derivatives with $n = 5$–7 was formed (Figure I.2.7). A NIEMS of the reaction mixture, shown in Figure I.2.7a, indicated that the predominant composition formed was $CB_{11}H_6F_6^-$. The predominant one-to-five ratio of peaks in the ^{19}F NMR spectrum of the mixture, also shown in Figure I.2.7b, indicated that $7\text{–}12\text{-}CB_{11}H_6F_6^-$ was the predominant hexafluoro isomer formed.

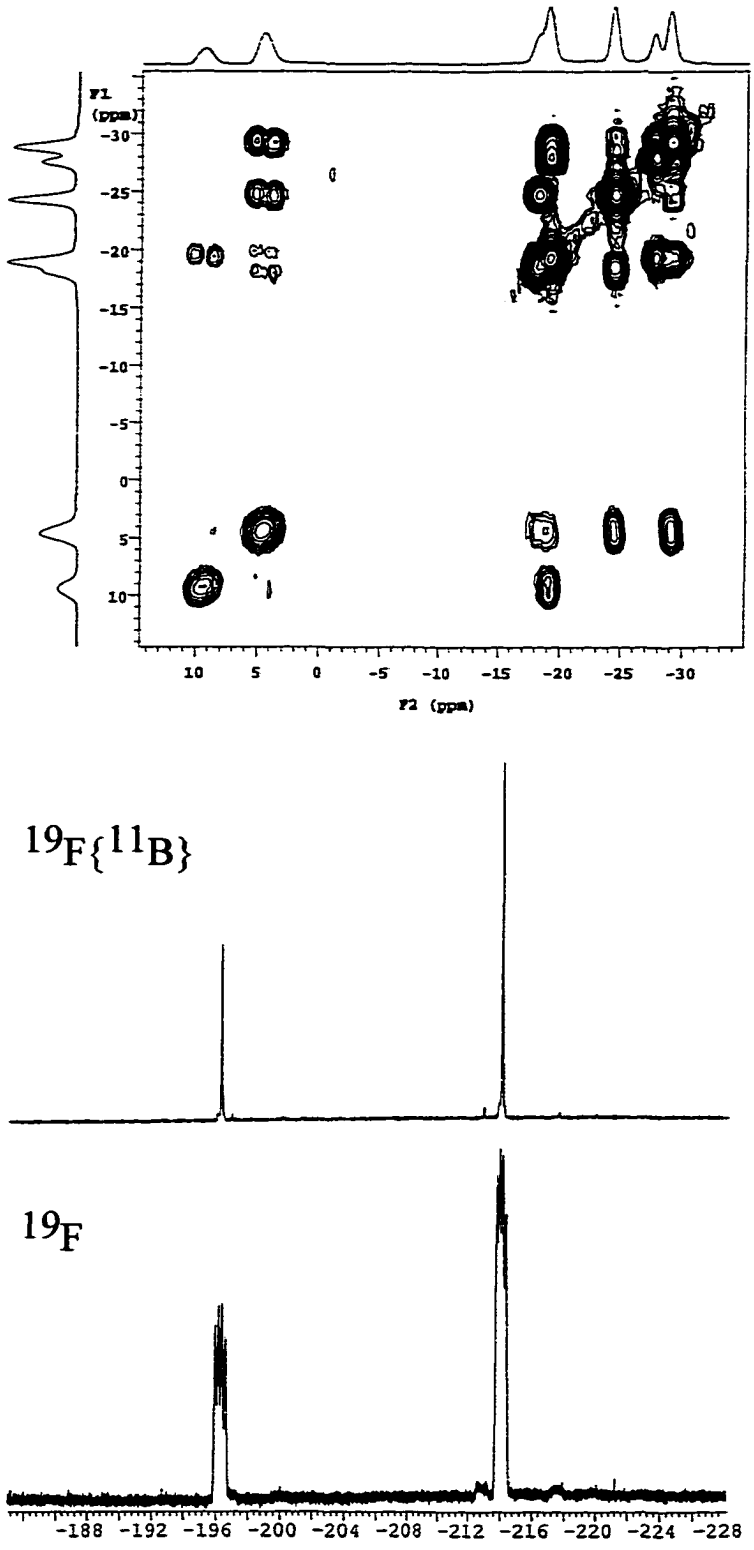

Figure I.2.4. Two-dimensional ^{11}B–^{11}B NMR spectrum (top) and ^{19}F NMR spectra (bottom) of Cs(7,9,12-$CB_{11}H_9F_3$) in acetone-d_6.

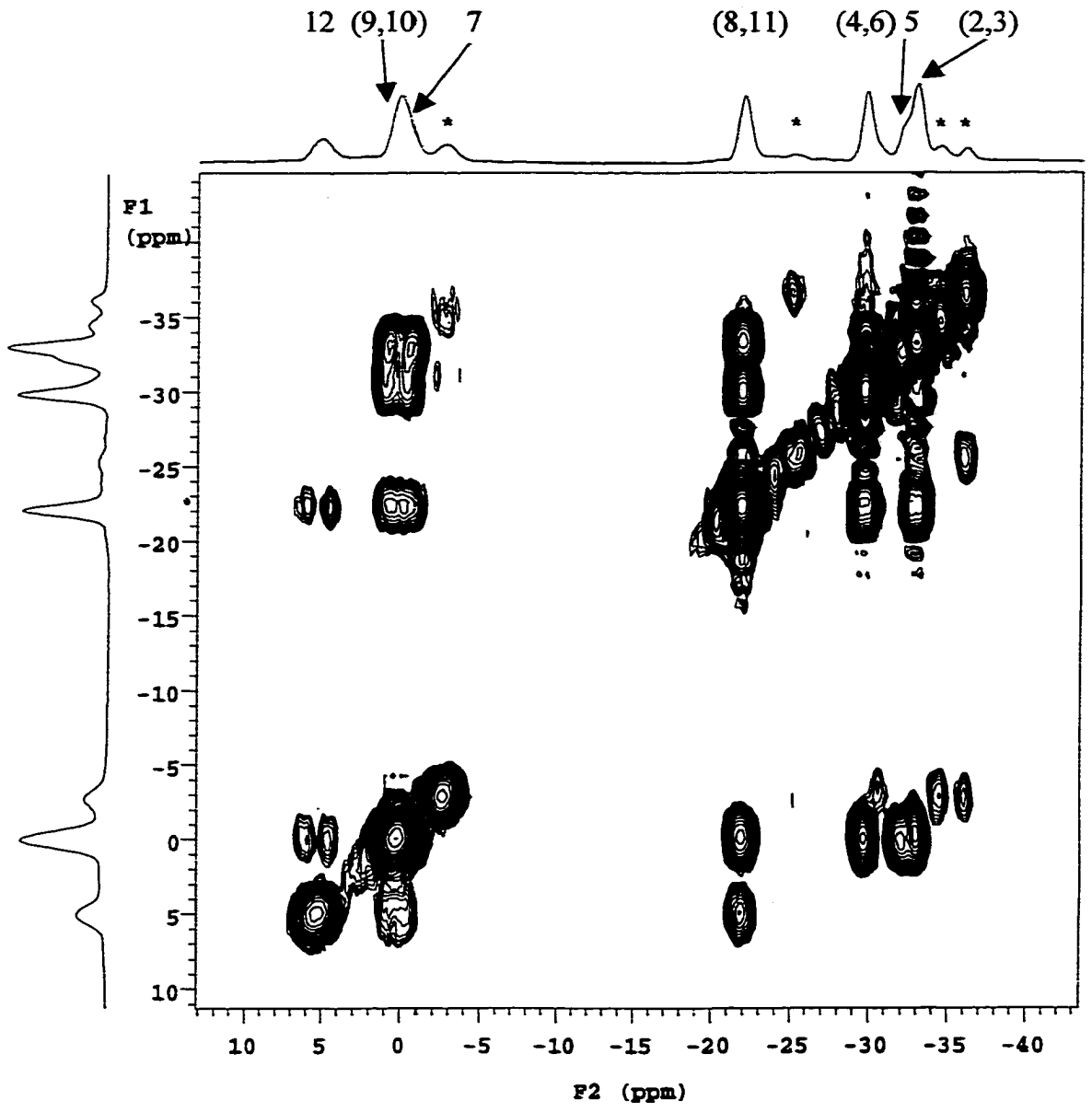

Figure I.2.5. Two-dimensional ^{11}B–^{11}B NMR spectrum for Cs(7,9,10,12-$CB_{11}H_8F_4$) in acetone-d_6. The peak assignments are above the peaks on the F2 axis. Expected Couplings (observed couplings in bold): B(12)→**B(7), B(9,10), B(8,11);** B(7)→**B(12), B(8,11), B(2,3)**; B(9,10)→**B(12), B(8,11), B(4,6), B(5)**; B(8,11)→**B(12), B(7), B(9,10), B(4,6), B(2,3)**; B(4,6)→**B(9,10), B(8,11)**, B(5), **B(2,3)**; B(5)→**B(9,10)**, B(4,6); B(2,3)→**B(7), B(8,11), B(4,6)**. Impurities are denoted with an astrick (*).

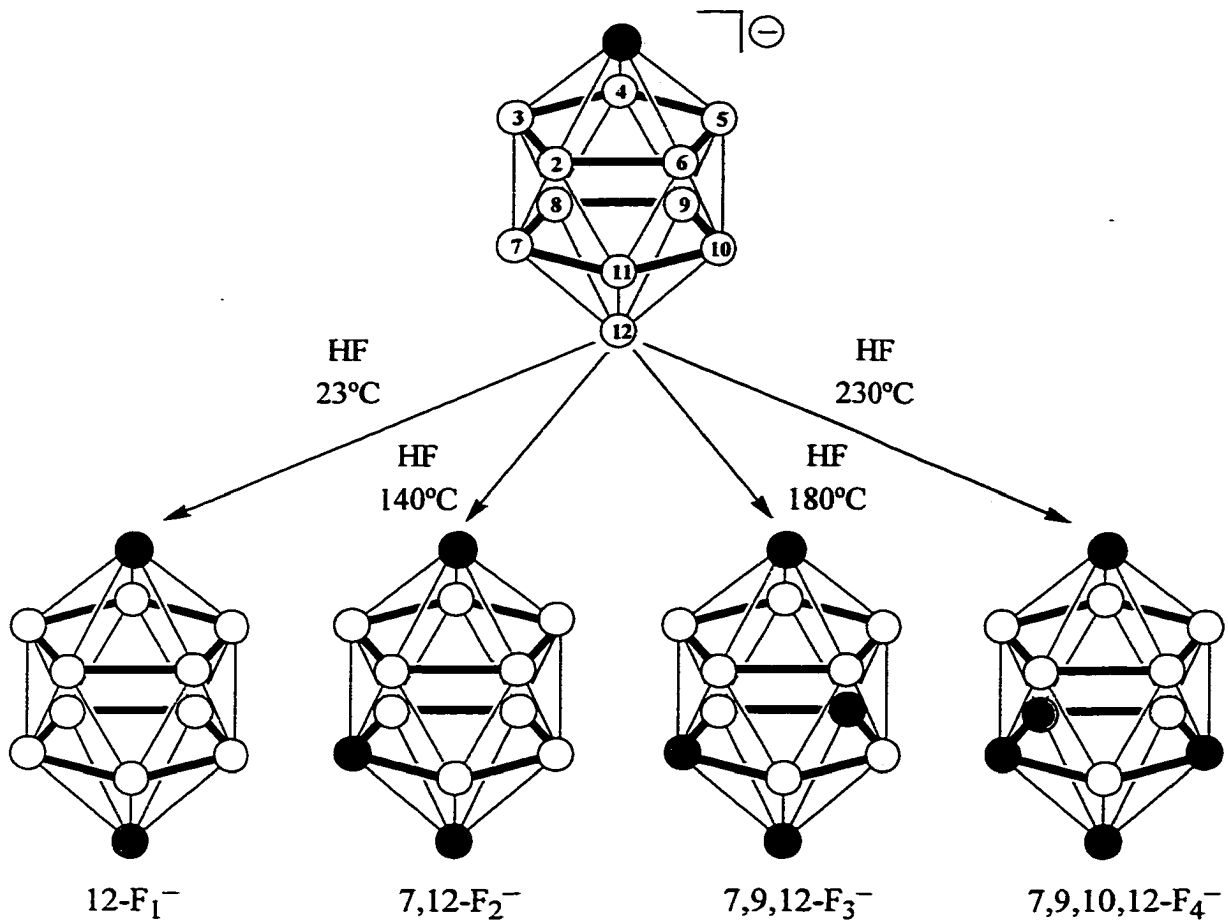

Figure I.2.6. Products of the reaction of $Cs(CB_{11}H_{12})$ with LAHF at various temperatures. Black circles represent C–H vertices; white circles represent B–H vertices; gray circles represent B–F vertices.

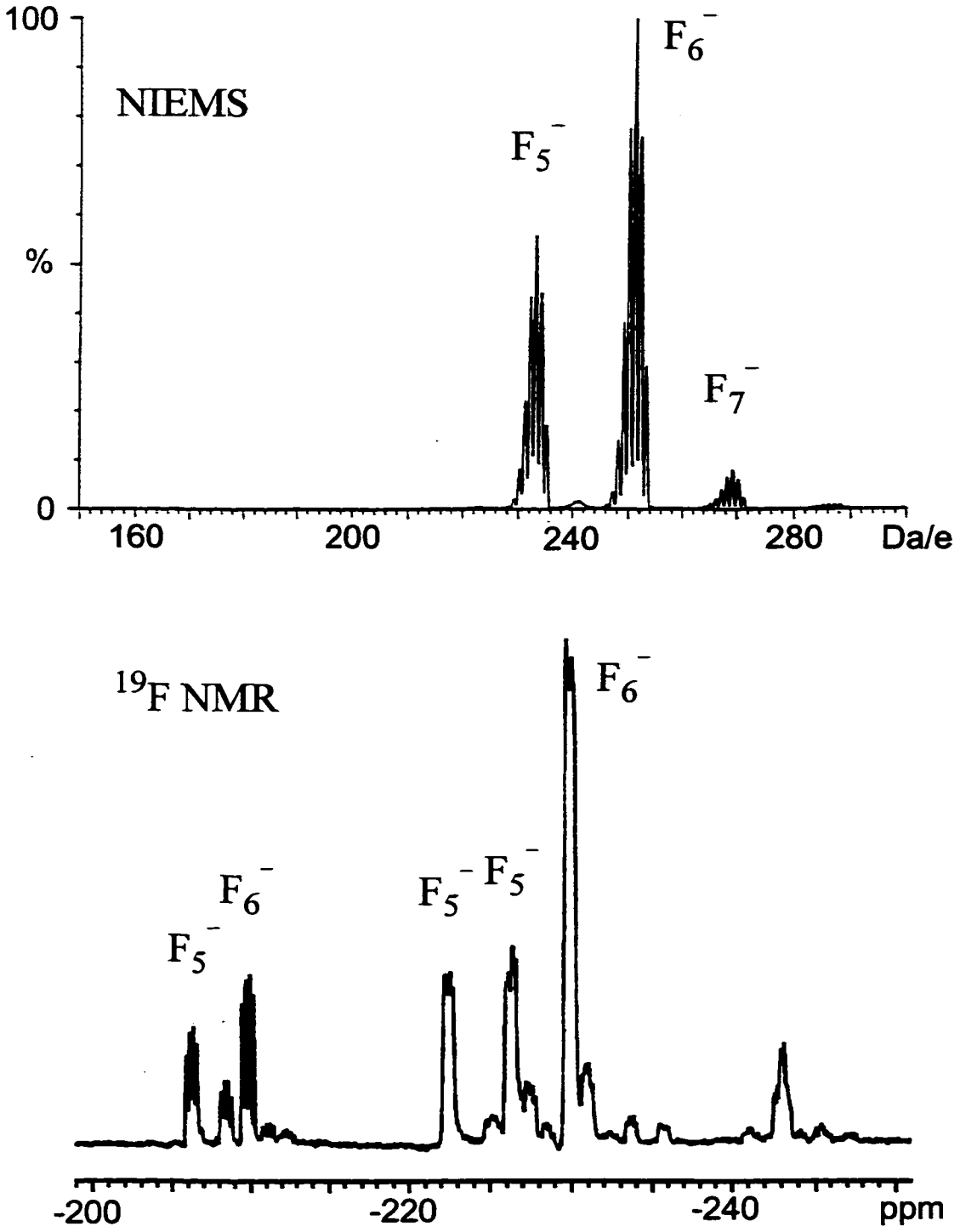

Figure I.2.7. NIEMS and ^{19}F NMR spectrum of the mixture resulting from the reaction of $Cs(CB_{11}H_{12})$ with LAHF at 390°C.

Initial attempts to fluorinate a *closo*-pnictaborane anion were performed by a B–F vertex insertion reaction analogous to those performed by Gaines et al. to produce 2-R-$CB_{11}H_{11}^-$ derivatives (R = F, OR, Ph, etc.).[48] Treatment of *nido*-$(Me_3NH)(AsB_{10}H_{12})$ with three equivalents of *n*-butyl lithium followed by the addition of one equivalent of $BF_3{\cdot}OEt_2$ produced 2-$AsB_{11}H_{10}F^-$ (Equations I.2.1 and I.2.2). The ^{11}B and ^{19}F NMR data are listed in Table I.2.2 and the spectra of the product are shown in Figure I.2.8. This reaction demonstrates a similarity in reaction chemistry of the carborane anion and the pnictaborane anions.

$$(Me_3NH)(AsB_{10}H_{12}) + 3\ \text{n-BuLi} \rightarrow Me_3N + Li_3AsB_{10}H_{10} + 3\ \text{BuH} \qquad \text{(I.2.1)}$$

$$Li_3AsB_{10}H_{10} + BF_3{\cdot}OEt_2 \rightarrow Li(2\text{-}AsB_{11}H_{10}F) + 2\ LiF + OEt_2 \qquad \text{(I.2.2)}$$

As in the case of *closo*-carborane, the above method of fluorination is limited. In order to polyfluorinate *closo*-pnictoborane anions, $EB_{11}H_{11}^-$ (E = As, Sb, Bi), fluorinations were attempted under conditions similar to those used to fluorinate $CB_{11}H_{12}^-$. Reaction of $Cs(AsB_{11}H_{11})$ with LAHF for 40 hours at 25°C produced a mixture of products. A NIEMS of the crude product showed a mixture of $AsB_{11}H_{11-n}F_n^-$ anions (Figure I.2.9). The major product was a monofluorinated derivative or derivatives (67%), but both starting material (26%) and a small amount of a difluorinated derivative (7%) were also present. Correlation of the NIEMS data with ^{11}B (1:5:5 intensity ratio) and ^{19}F NMR data indicate that 12-$AsB_{11}H_{10}F^-$ is the major product (Table I.2.2 and Figure I.2.10). In addition to the 12-AsF_1^- peak in the

Table I.2.2. NMR Spectral Data for Select $EB_{11}H_{11-n}F_n^-$ anions (E = As, Sb, Bi)

anion	atom #	$\delta(^{11}B)^{a,c}$	$^1J_{BH}{}^b$	$\delta(^{19}F)^{a,d}$	$^1J_{BF}{}^b$	$\delta(^1H)^a$
12-$AsB_{11}H_{10}F^-$	12	21.6		–158.9	62	
	7–11	–10.2				
	2–6	–12.3	162			
2-$AsB_{11}H_{10}F^-$	2	15.8		–192.7	78	
	12	4.6	134			
	7,11	–6.9				
	8,10	–8.7				
	3,6	–8.7				
	4,5	–11.3				
	9	–17.8	134			
7,9-$SbB_{11}H_9F_2^-$	7,9	13.1		–194.1	63	
	12	7.7				4.31
	8	–11.2				3.10
	10,11	–11.2				2.79
	3,4	–14.1				1.64
	6	–17.3				1.17
	2,5	–19.0				1.47
7,9-$BiB_{11}H_9F_2^-$	7,9	18.9		–190.8	57	
	12	12.3				
	8	–10.6				
	10,11	–10.6				
	3,4	–12.5				
	6	–15.9				
	2,5	–16.9	144			

[a] δ values are in ppm from TMS (^{13}C, ^1H), $BF_3{\cdot}OEt_2$ (^{11}B), and $CFCl_3$ (^{19}F). [b] ^1J units = Hz. [c] All ^{11}B signals for B–F boron atoms are broad singlets, all B–H signals are doublets. [d] ^{19}F signals are quartets due to ^{11}B splitting.

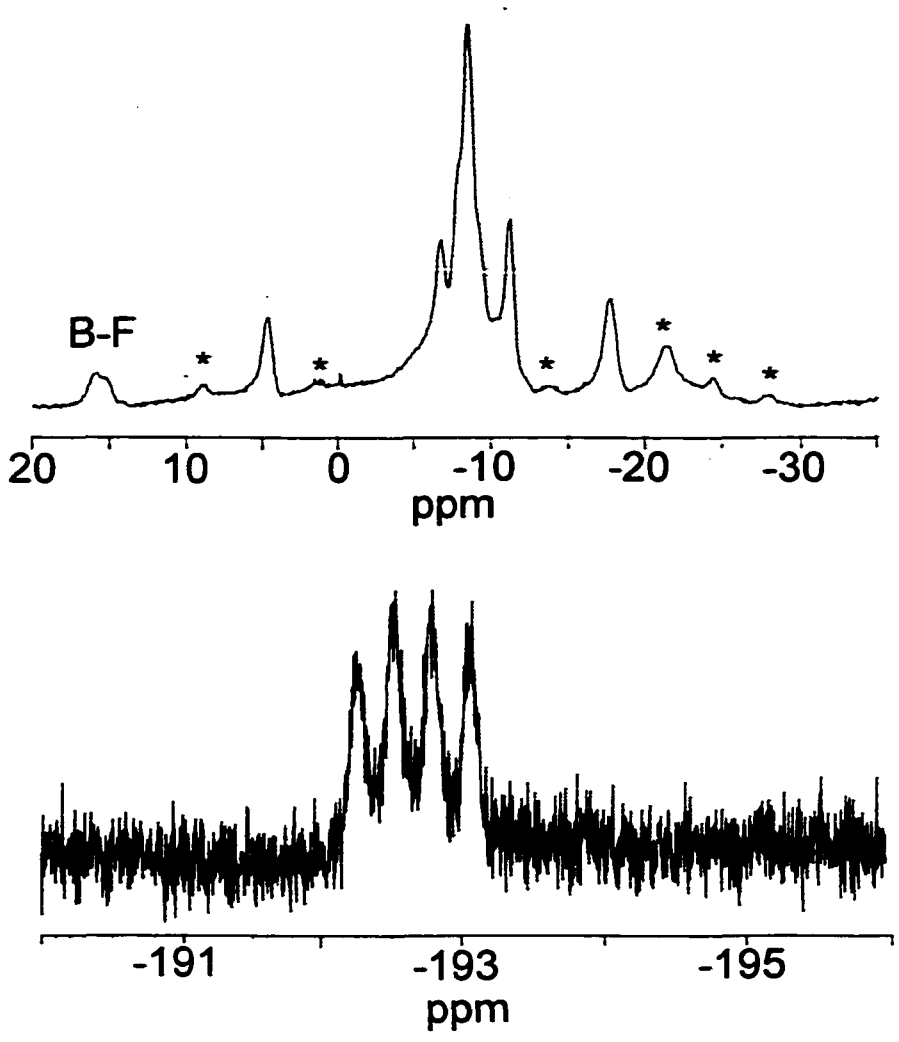

Figure I.2.8. $^{11}B\{^1H\}$ (top) and ^{19}F (bottom) NMR spectra of $(Me_3NH)(2\text{-}AsB_{11}H_{10}F)$ in acetone-d_6. Peaks due to impurities are marked with an astrick (*).

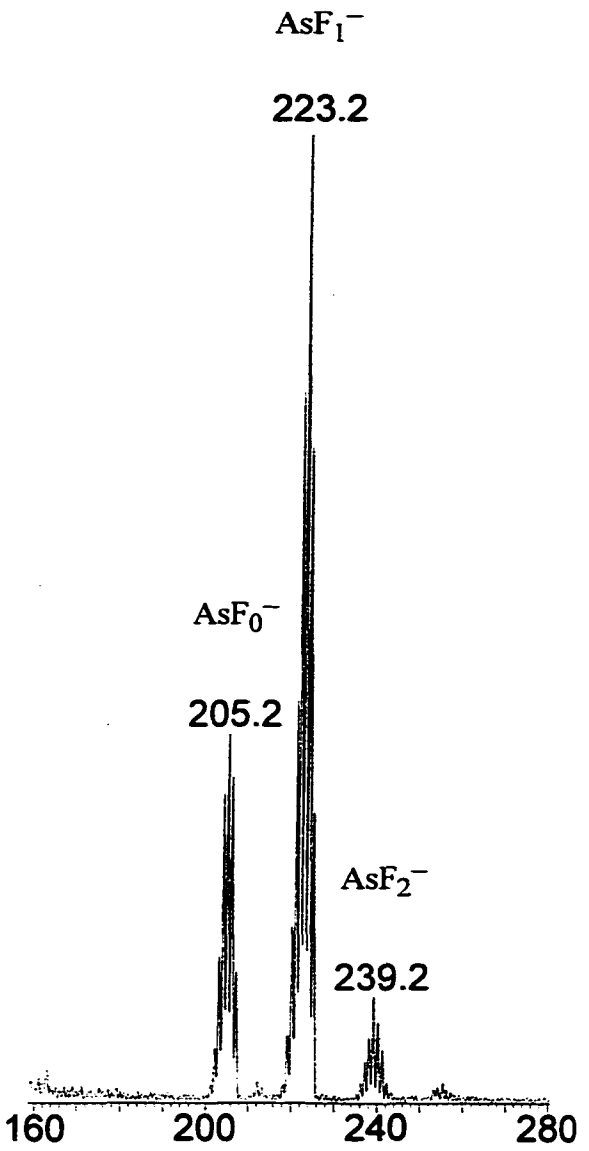

Figure I.2.9. NIEMS of the $AsB_{11}H_{11}^-$/LAHF (25°C, 40 hours) reaction mixture showing the parent cluster (*m/z* = 205.2) and mono- and difluorinated derivatives.

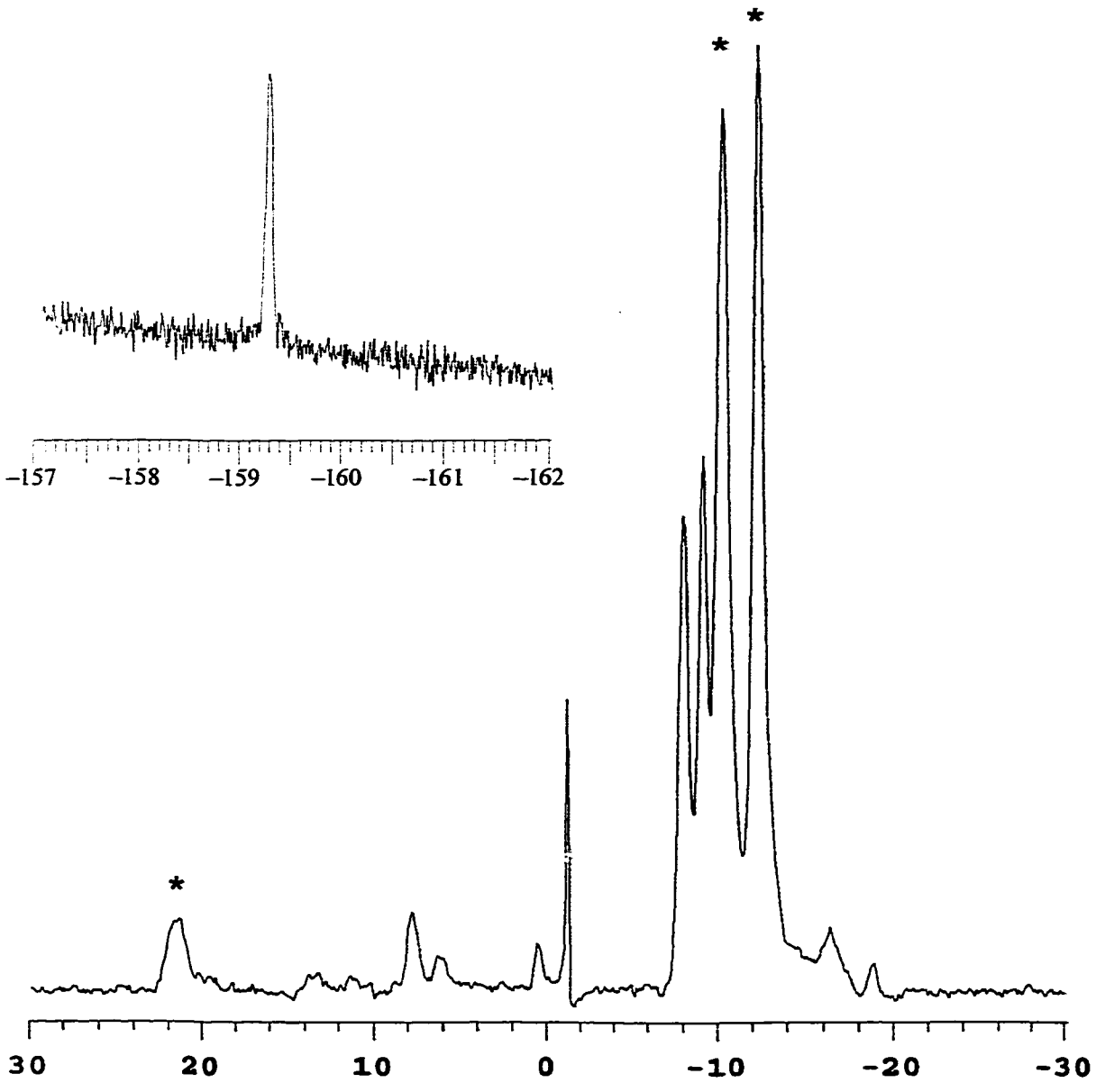

Figure I.2.10. $^{11}B\{^{1}H\}$ NMR spectrum of the reaction mixture from of $Cs(AsB_{11}H_{11})$ in LAHF at 25°C for 40 hours. Peaks due to the fluorinated arsaborane 12-$AsB_{11}H_{10}F^-$ are marked with an astrick (*). Inset: $^{19}F\{^{11}B\}$ NMR spectrum of the 12-$AsB_{11}H_{10}F^-$ anion. A small peak (~10% of the 12-AsF_1^- peak intensity) at –193.8 ppm is not shown.

^{19}F NMR spectrum, a second, smaller peak (~10% intensity) was present. The similarity in the intensity ratio of F_1^- and F_2^- products in both the NIEMS and ^{19}F NMR spectrum suggests that this peak is due to a difluoro derivative. The single difluoro peak in the ^{19}F NMR spectrum indicates that the fluorine substitution occurred at degenerate vertices in the cluster and rules out the 7,12-isomer. This strongly suggests that either the 7,8-, 7,9-, 2,3-, or 2,4-isomer was formed in the reaction.

Increasing the reaction time and temperature, to one week at 45°C, produced a similar mixture of anions but the percentage of unreacted material present was less. This mixture included 12-$AsB_{11}H_{10}F^-$ and other fluorinated derivatives tentatively assigned as 7-$AsB_{11}H_{10}F^-$, 7,12-$AsB_{11}H_9F_2^-$, and 7,9-$AsB_{11}H_9F_2^-$. Assignments of ^{19}F NMR spectral peaks (Figure I.2.11) were made based on intensity rations and by analogy with $CB_{11}H_{12-n}F_n^-$ derivatives. It is interesting to note that substitution appears to occurs at B(7) as well as at B(12). Further studies must be performed on this reaction to provide adequate data (^{11}B–^{11}B 2-D COSY, ^{19}F–^{11}B HMQC, ^{1}H–^{11}B HMQC) to support these assignments. Raising the reaction temperature to 200°C (64 hours) produced a mixture of starting material, $AsB_{11}H_7F_4^-$ (70%), and $AsB_{11}H_6F_5^-$ (20%) with $AsB_{11}H_7F_4^-$ derivatives as the major product.

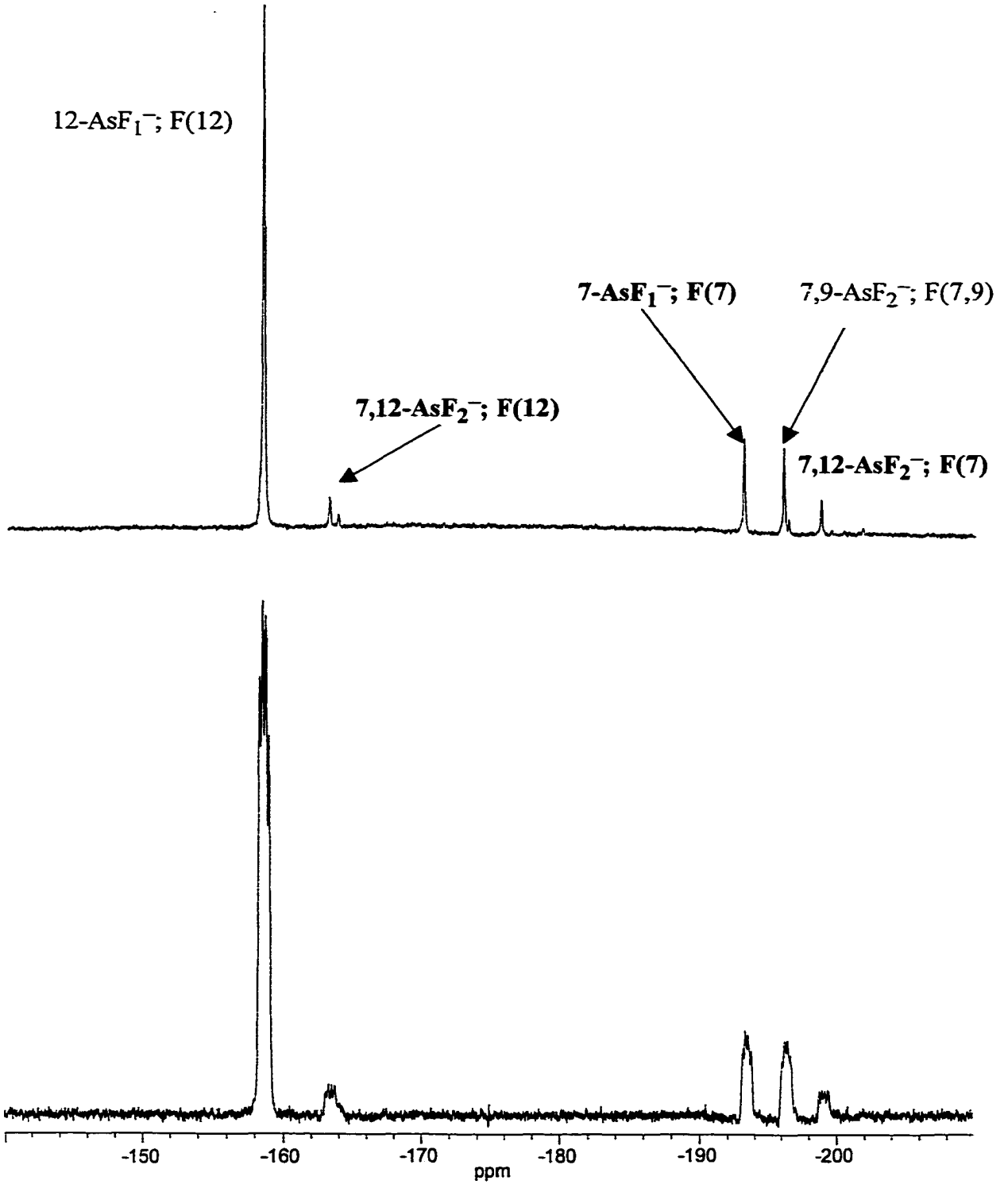

Figure I.2.11. $^{19}F\{^{11}B\}$(top) and ^{19}F (bottom) NMR spectra of the mixture resulting from the reaction of $Cs(AsB_{11}H_{11})$ with LAHF at 45°C for 7 days. Tentative assignments are in bold face type.

In the case of the antimony and bismuth derivatives, the fluorination reactions proceeded differently than the arsenic analogue. In both examples, only one isomerically pure derivative—the difluoro derivative—was formed as the major product. The reaction of *closo*-stibaborane with LAHF at 25°C for 44 hours produced, nearly exclusively, difluorinated derivatives (97+% by NIEMS) (Figure I.2.12). The presence of only one signal in the ^{19}F NMR spectrum suggests that only one major fluorinated derivative was formed. While the ^{19}F NMR spectrum indicates the presence of $SbB_{11}H_{10}F^-$, this derivative is <2% of the total products. The accidental degeneracy of the ^{11}B NMR peaks at –11.2 ppm (one 1B and one 2B peak equaling an intensity of 3B; Figure I.2.12) made the ^{11}B–^{11}B COSY spectrum assignment ambiguous (Figure I.2.13). In order to completely assign the ^{11}B peaks of the $SbB_{11}H_9F_2^-$ to a specific isomer, the ^{11}B NMR spectrum of 7,9,12-$CB_{11}H_9F_3^-$ was used as a model (Figure I.2.14). The 7,9,12-$CB_{11}H_9F_3^-$ anion is a good model for a 7,9-difluoro isomer of a twelve-vertex heteroborane; since fluorination of the B(12) vertex does not change the symmetry of the anion, the ordering of the peaks should be identical with the exception of the B(12) signal. The B(12) signal is shifted significantly to more positive δ values with respect to the parent anion when fluorinated and is shifted slightly to more negative δ values when a neighboring lower-belt vertex is fluorinated. The $SbB_{11}H_9F_2^-$ peaks were assigned analogously to 7,9,12-$CB_{11}H_9F_3^-$ with the unfluorinated peak at the highest δ value being assigned to B(12). With this assignment, the ^1H NMR peaks for $SbB_{11}H_9F_2^-$ were assigned using the 2D ^1H–^{11}B HMQC spectrum (Figure I.2.15). The intensities and the ordering of the peaks in the ^1H NMR spectrum are identical to the ^1H NMR peaks in the spectrum of 7,9,12-$CB_{11}H_9F_3^-$ (Appendix I.B; there is no H(12) signal since B(12) is fluorinated). Based on these similarities with 7,9,12-$CB_{11}H_9F_3^-$, the difluorinated stibaborane was assigned as the 7,9-$SbB_{11}H_9F_2^-$ isomer.

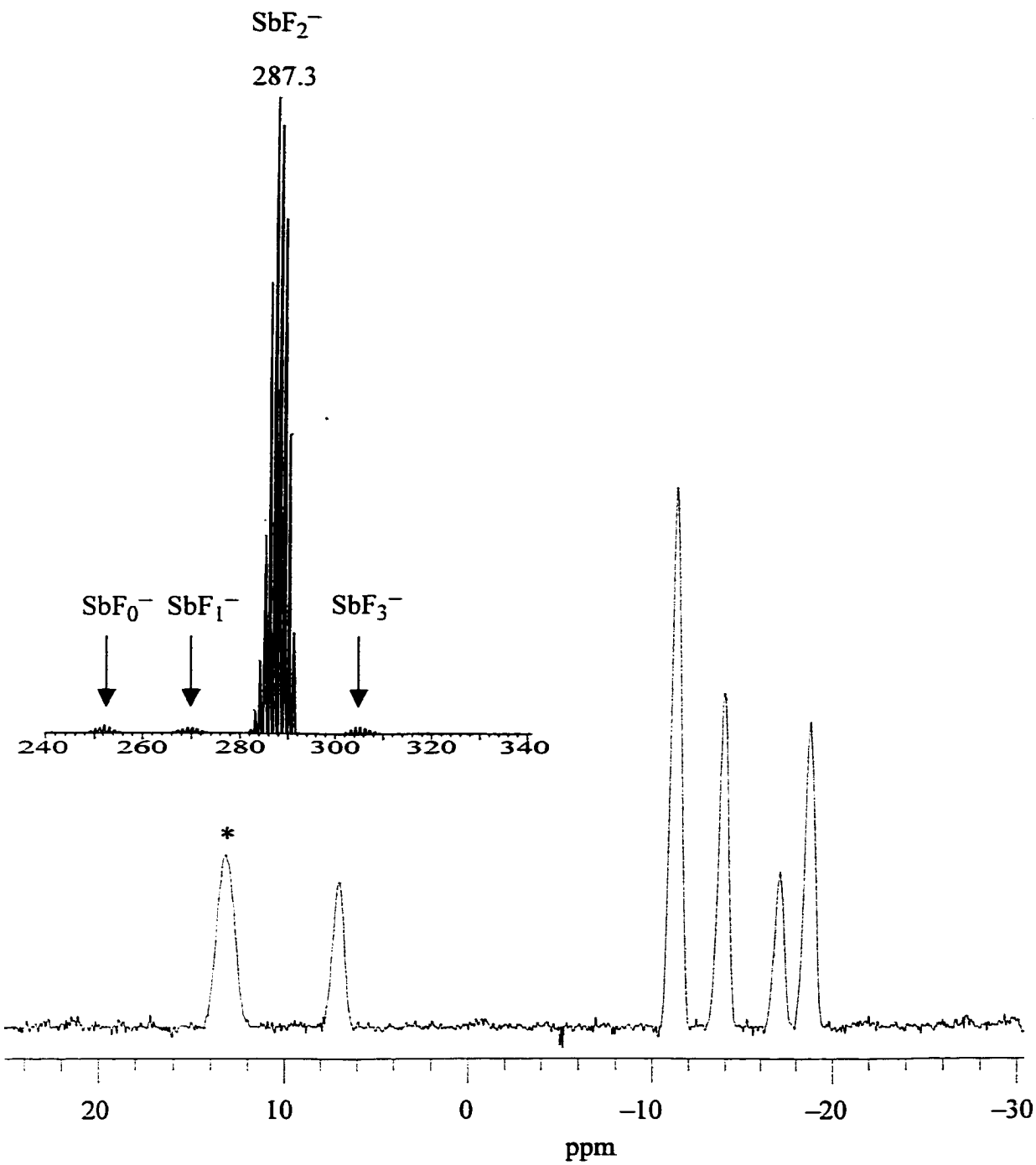

Figure I.2.12. $^{11}B\{^1H\}$ NMR spectrum (Me_3NH^+; acetonitrile-d_3) and NIEMS (inset) for the product of the reaction of $SbB_{11}H_{11}^-$ with LAHF at 40 °C for 44 hours. The peak labeled (*) is not coupled to a hydrogen atom in the ^{11}B NMR spectrum.

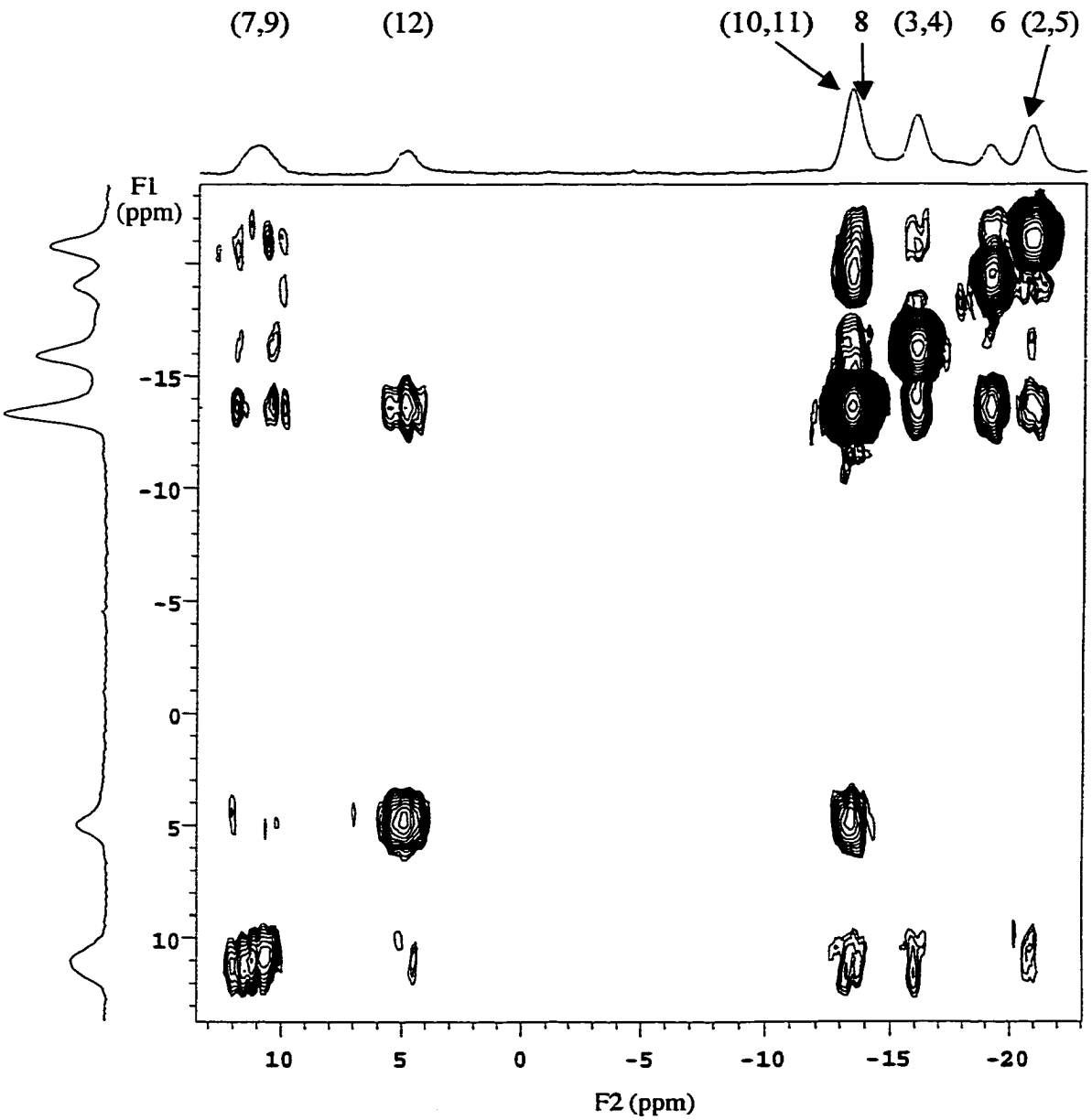

Figure I.2.13. Two-dimensional ^{11}B–^{11}B NMR spectrum for $(Me_3NH)(7,9\text{-}SbB_{11}H_9F_2)$ in acetonitrile-d_3. The peak assignments are above the peaks on the F2 axis. Expected Couplings (observed couplings in bold): B(12)→**B(8)**, **B(7,9)**, **B(10,11)**; B(8)→**B(12)**, **B(7,9)**, **B(3,4)**; B(7,9)→**B(12)**, **B(8)**, **B(10,11)**, **B(3,4)**, **B(2,5)**; B(10,11)→**B(12)**, **B(7,9)**, **B(2,5)**, **B(6)**; B(3,4)→**B(8)**, **B(7,9)**, **B(2,5)**; B(2,5)→**B(7,9)**, **B(10,11)**, **B(3,4)**, **B(6)**; B(6)→**B(10,11)**, **B(2,5)**.

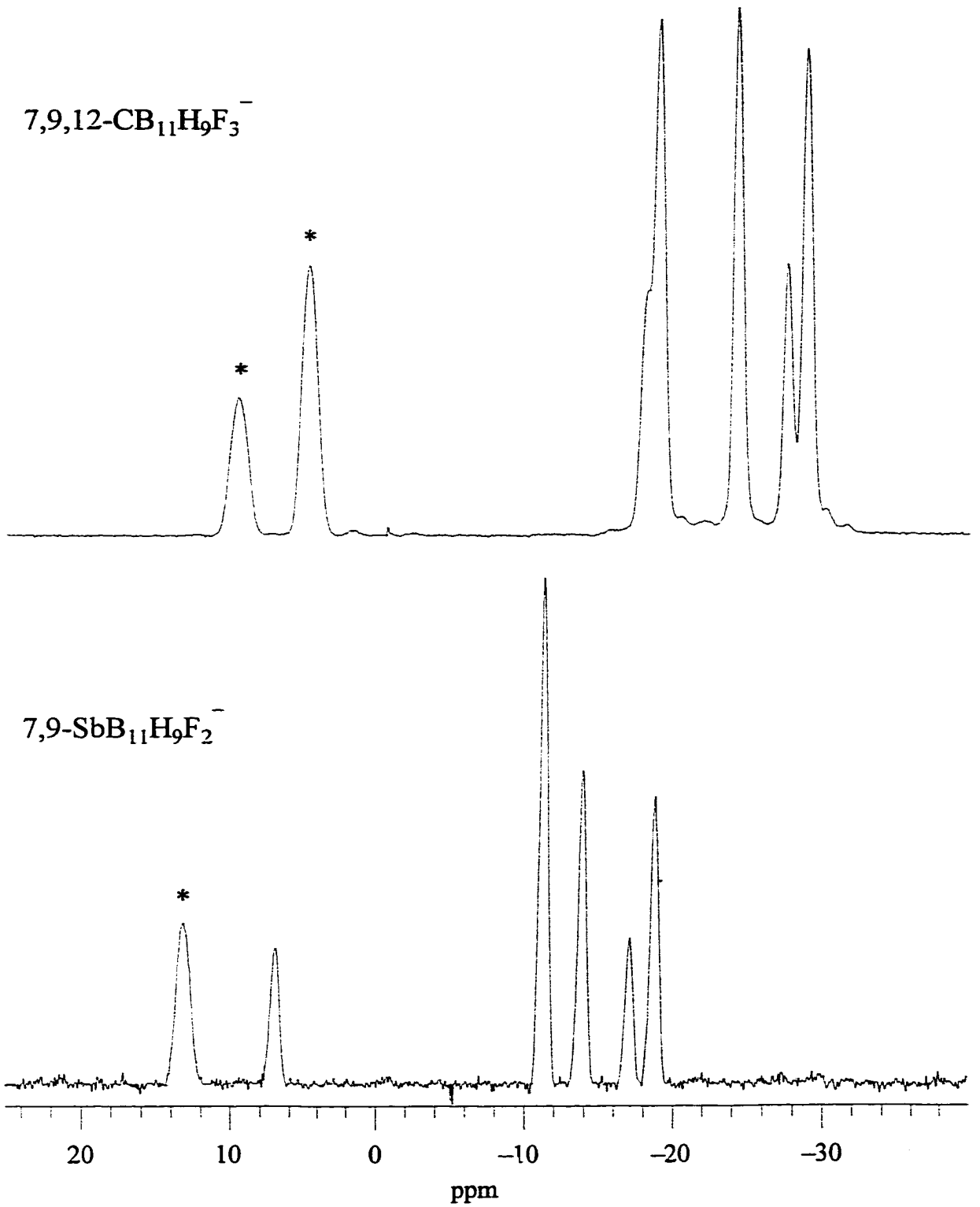

Figure I.2.14. $^{11}B\{^1H\}$ NMR spectra of 7,9,12-$CB_{11}H_9F_3^-$ (Cs^+; acetone-d_6; top) and 7,9-$SbB_{11}H_9F_2^-$ (Me_3NH^+; acetonitrile-d_3; bottom). The peaks labeled (*) are not coupled to a hydrogen atom in the ^{11}B NMR spectrum.

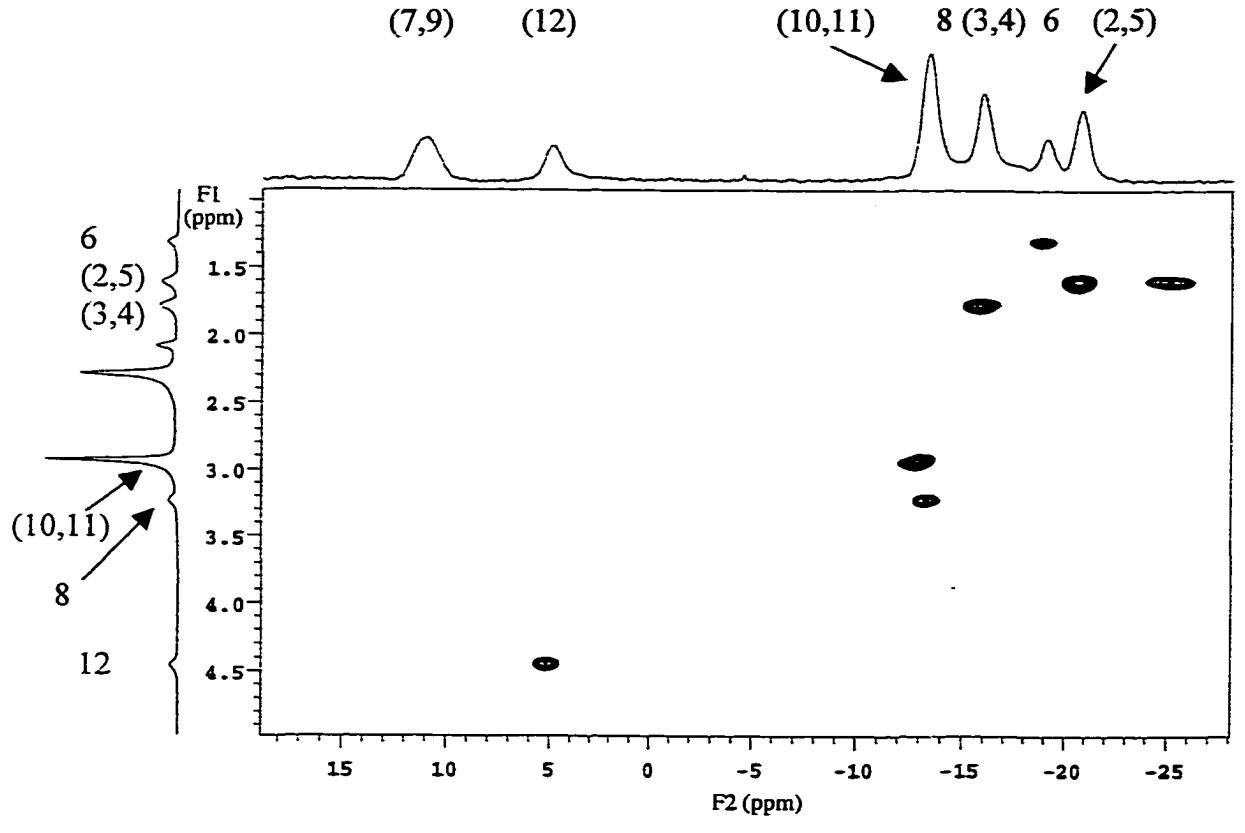

Figure I.2.15. Two-dimensional ^{11}H–^{11}B HMQC NMR spectrum for $(Me_3NH)(7,9\text{-}SbB_{11}H_9F_2)$ in acetonitrile-d_3. The peak assignments are above the peaks on the respective axis. The H(10,11) peak is accidentally degenerate with the nine methyl protons of Me_3NH^+.

When the *closo*-bismaborane, $BiB_{11}H_{11}^-$, was reacted with LAHF at the same reaction temperature as the arsenic and antimony derivatives (25°C for 44 hours), a mixture of $BiB_{11}H_{11-n}F_n^-$ derivatives was formed. The NIEMS spectrum, Figure I.2.16, shows that product anions with one to four fluorine atoms were formed (n = 1–4). This mixture was not separated, nor were specific isomers determined. To slow the substitution reactions, a second reaction was performed at 0°C for 40 hours. The ^{19}F NMR spectrum showed one major product whose chemical shift is similar to that of 7,9-$SbB_{11}H_9F_2^-$, and the NIEMS shows $BiB_{11}H_9F_2^-$ is the major fluorinated product (90+%) (Figure I.2.16). Based on this evidence, the difluoro isomer formed in the 0°C reaction was 7,9-$BiB_{11}H_9F_2^-$.

Fluorinations of $CB_{11}H_{12}^-$ using F-TEDA[81]

It has been demonstrated that the target fluorinated carboranes can be synthesized with high compositional and isomeric purity (at least for n = 1–4) using liquid anhydrous hydrogen fluoride. Unfortunately, the compounds containing a higher degree of fluorination (n = 5, 6), including the highly desired *B*-perfluorinated cluster $CB_{11}HF_{11}^-$, were formed only as mixtures of isomers with different degrees of fluorination or, in the later case, not at all. Also, the reactions using LAHF as a reagent involve expensive Monel reaction equipment and a dedicated metal vacuum line for the manipulation of LAHF. In addition, one must exercise extreme caution when using LAHF due to its corrosive nature; sealed reaction vessels containing supercritical LAHF reaction are potential explosion hazards.

For these reasons, milder reaction conditions were desired. To accomplish this goal, an organic *N*-fluoro reagent was chosen; this type of nitrogen based compound contain a reactive N–F bond that provides an easy-to-handle source of

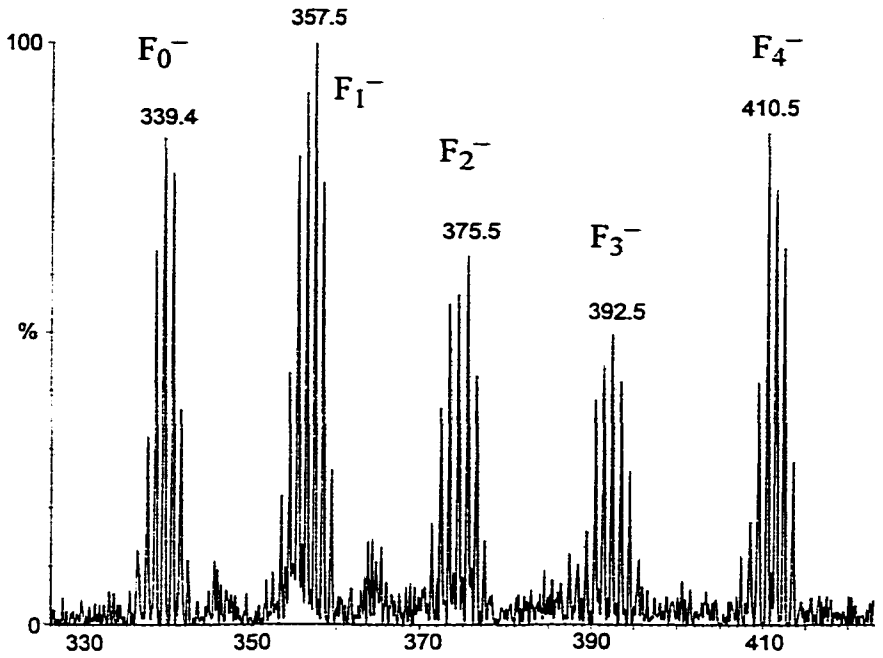

Figure I.2.16. NIEMS of the products from the reaction of $Cs(BiB_{11}H_{11})$ with LAHF at 25°C for 44 hours.

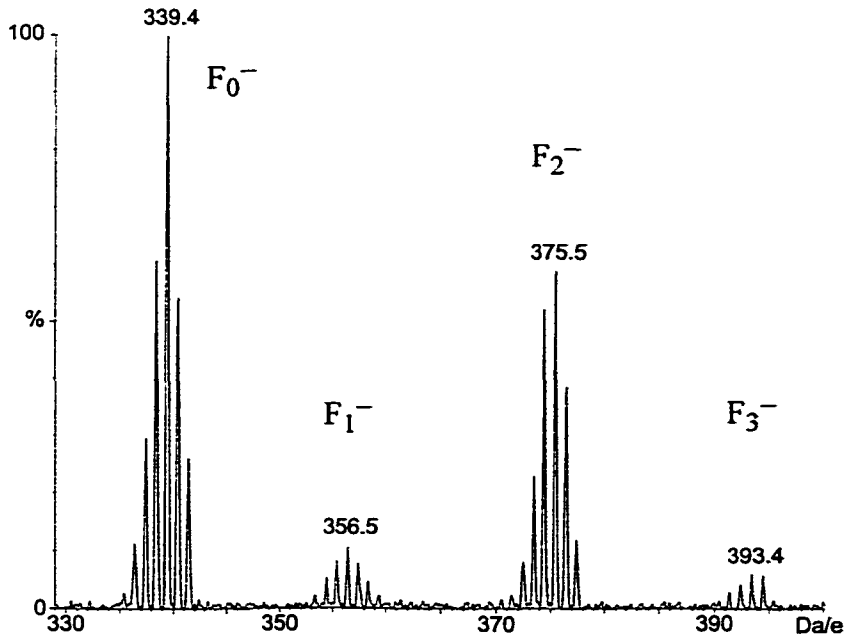

Figure I.2.17. NIEMS of the products from the reaction of $Cs(BiB_{11}H_{11})$ with LAHF at 0°C for 40 hours.

electrophilic fluorine (formally F^+).[77,82-84] Electrophilic fluorination has been used to incorporate fluorine into organic molecules.[85] *N*-fluoro compounds are relatively stable and have been shown to be highly selective in the fluorination of organic carbanions,[86] and *N*-fluoro reagents such as NF_4BF_4,[87] $(CF_3SO_2)_2NF$,[88] *N*-fluoropyridinium salts,[89] and F-TEDA-BF_4 (Selectfluor, Air Products and Chemical, Inc.)[90] have been shown to convert one or more aromatic C–H bonds to C–F bonds. Moreover, these transformations can be carried out using glass reaction vessels and common organic solvents. These results make organic *N*-fluoro reagents ideal choices for attempts to fluorinate *closo*-carborane anions. The *N*-fluoro reagent F-TEDA-BF_4 (hereafter referred to as F-TEDA) was chosen for studies with $CB_{11}H_{12}^-$ because of its relatively high reactivity compared to most N–F reagents[91] and because of its versatility in fluorinating organic compounds containing a variety of different organic substrates.[92]

The compound $Cs(CB_{11}H_{12})$ was dissolved in acetonitrile and treated with one or more equivalents of F-TEDA, at various temperatures. At selected time intervals, samples were withdrawn, and treated as follows. The acetonitrile was removed under vacuum and all carborane-containing salts were extracted from the solid residue with acetone. Acetone was removed under vacuum, the solid residues were dissolved in 5% aqueous KOH, and $(n\text{-}Bu)_4NCl$ was added to quantitatively precipitate all carborane anions as $(n\text{-}Bu)_4N^+$ salts. The salts were analyzed spectroscopically to determine (i) the composition, or relative amounts of anions with different numbers of fluorine atoms (negative ion electrospray mass spectrometry), (ii) the number of isomers present for a given degree of fluorine substitution (^{19}F NMR spectroscopy), and (iii) where possible, the geometric structure of the various isomers (1D and 2D ^{11}B NMR spectroscopy).

Treatment of $Cs(CB_{11}H_{12})$ with 10 equivalents of F-TEDA at 25°C, 40°C, and 100°C resulted in mixtures of fluorinated derivatives, $CB_{11}H_{12-n}F_n^-$, including the following anions prepared by treatment of $Cs(CB_{11}H_{12})$ with LAHF at various

temperatures and discussed in Part I, Chapter 2: 12-F_1, 7,12-F_2, 7,9,12-F_3, and 7,9,10,12-F_4.[79] Experimental and calculated NIEMS are displayed in Figure I.2.18. The observed isotope patterns are those expected for anions with eleven boron atoms having a natural abundance of 20% ^{10}B and 80% ^{11}B. The relative percentages of the products formed for the three reactions are tabulated in Table I.2.3. In each case, the percentages listed were estimated from the relative intensities of peaks in negative-ion electrospray mass spectra (NIEMS) of the reaction mixtures.

In favorable cases, the concentration ratio(s) of geometric isomers formed for a given value of *n* was determined from the relative intensities of peaks in ^{11}B and ^{19}F NMR spectra of the reaction mixtures (Figure I.2.19). Boron-11 and ^{19}F NMR spectra for the 40°C reaction mixture are displayed in Figure I.2.19. NMR data are listed in Table I.2.1. Peak assignments for the previously unknown monofluoro isomer 7-F_1 were made from a ^{11}B–^{11}B 2D COSY NMR spectrum of the 40°C reaction mixture, which is shown in Figure I.2.20. The 7-F_1 isomer is the third and final B–F isomer in the $CB_{11}H_{11}F^-$ system (in addition to 12-F_1 and 2-F_1). Some peaks in Figure I.2.19 have been tentatively assigned to the previously unknown difluoro isomers 7,8-F_2, and 7,9-F_2.

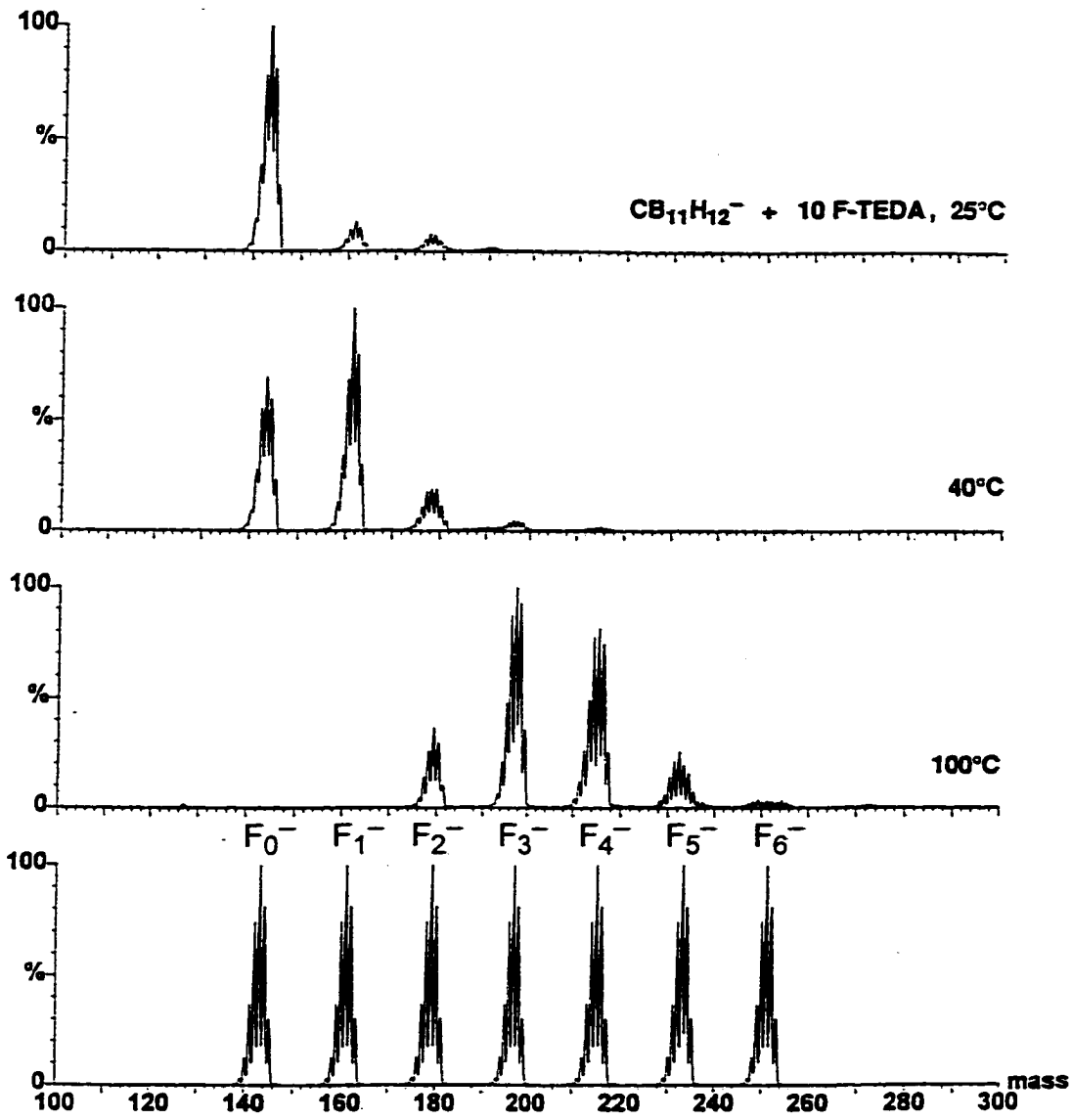

Figure I.2.18. The NIEMS of the products of the $Cs(CB_{11}H_{12})$/F-TEDA reactions at 25°C, 40°C, and 100°C in acetonitrile (top three spectra). Calculated spectra for $CB_{11}H_{12-n}F_n^-$ (n = 0–6) species (abbreviated F_n^-) are shown at the bottom. The mass scale is Daltons per electron.

Table I.2.3. Products of the Fluorination Reactions of $CB_{11}H_{12}^-$ with 10 equiv. of F-TEDA at Various Temperatures[a]

Conditions	Products (%)							Comments
	F_0^-	F_1^-	F_2^-	F_3^-	F_4^-	F_5^-	F_6^-	
25 °C, 90 h CH_3CN	82	11	7	tr				$[F_1^-]/[F_2^-] = 1.6$
40 °C, 90 h CH_3CN	35	52	10	3	tr			$[F_1^-]/[F_2^-] = 5.2$ $[12\text{-}F_1^-]/[7\text{-}F_1^-] = 1.3$; major F_2^- isomer = 7,12-F_2^-
100 °C, 90 h CH_3CN			15	40	34	10	1	major F_3^- isomer = 7,9,12-F_3^- major F_4^- isomer = 7,9,10,12-F_4^-

[a] tr = trace.

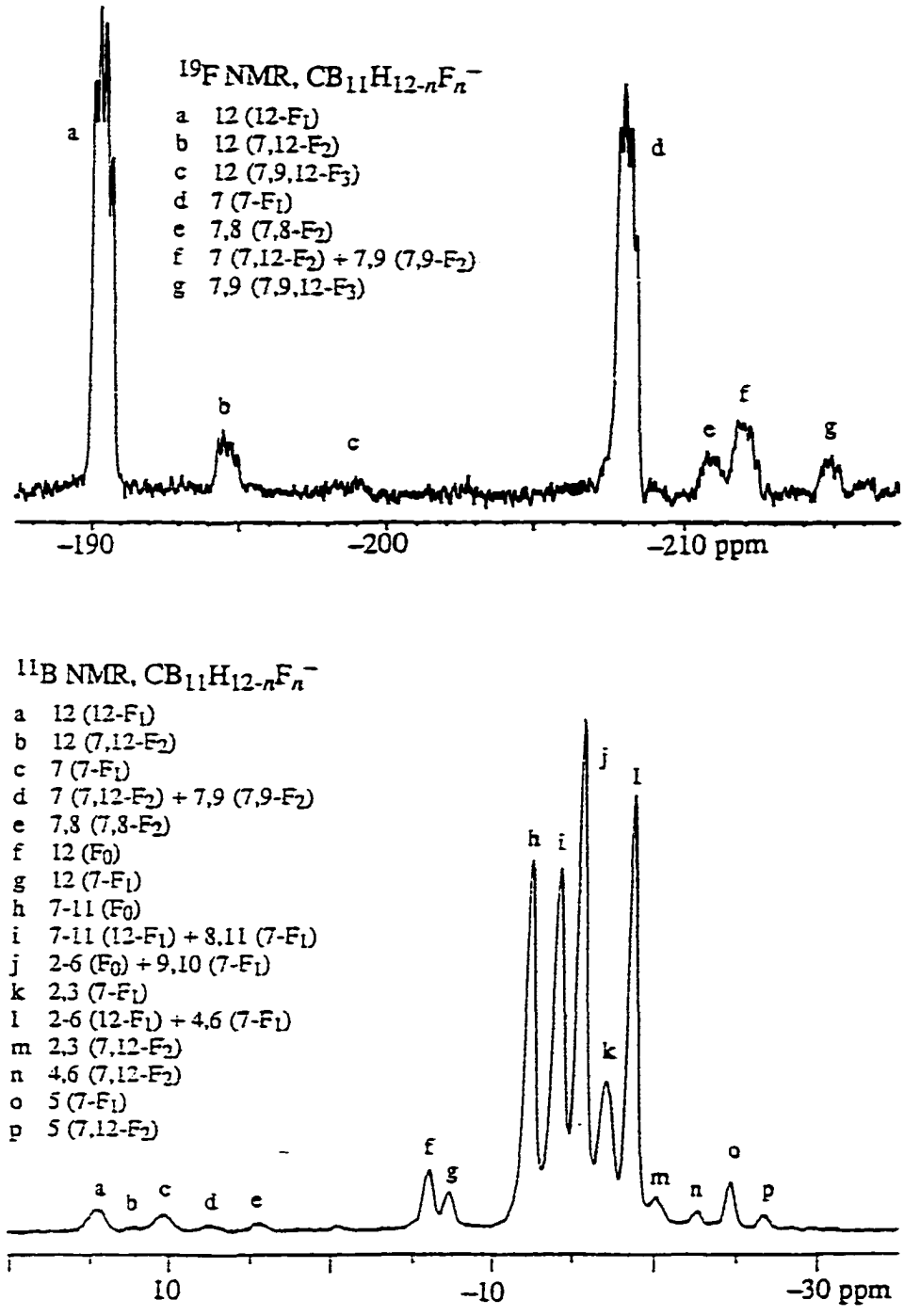

Figure I.2.19. The ^{19}F and ^{11}B{^{1}H} NMR spectra (acetone-d_6) for the mixture of products from the $Cs(CB_{11}H_{12})$/F-TEDA reaction mixture at 40 °C in acetonitrile.

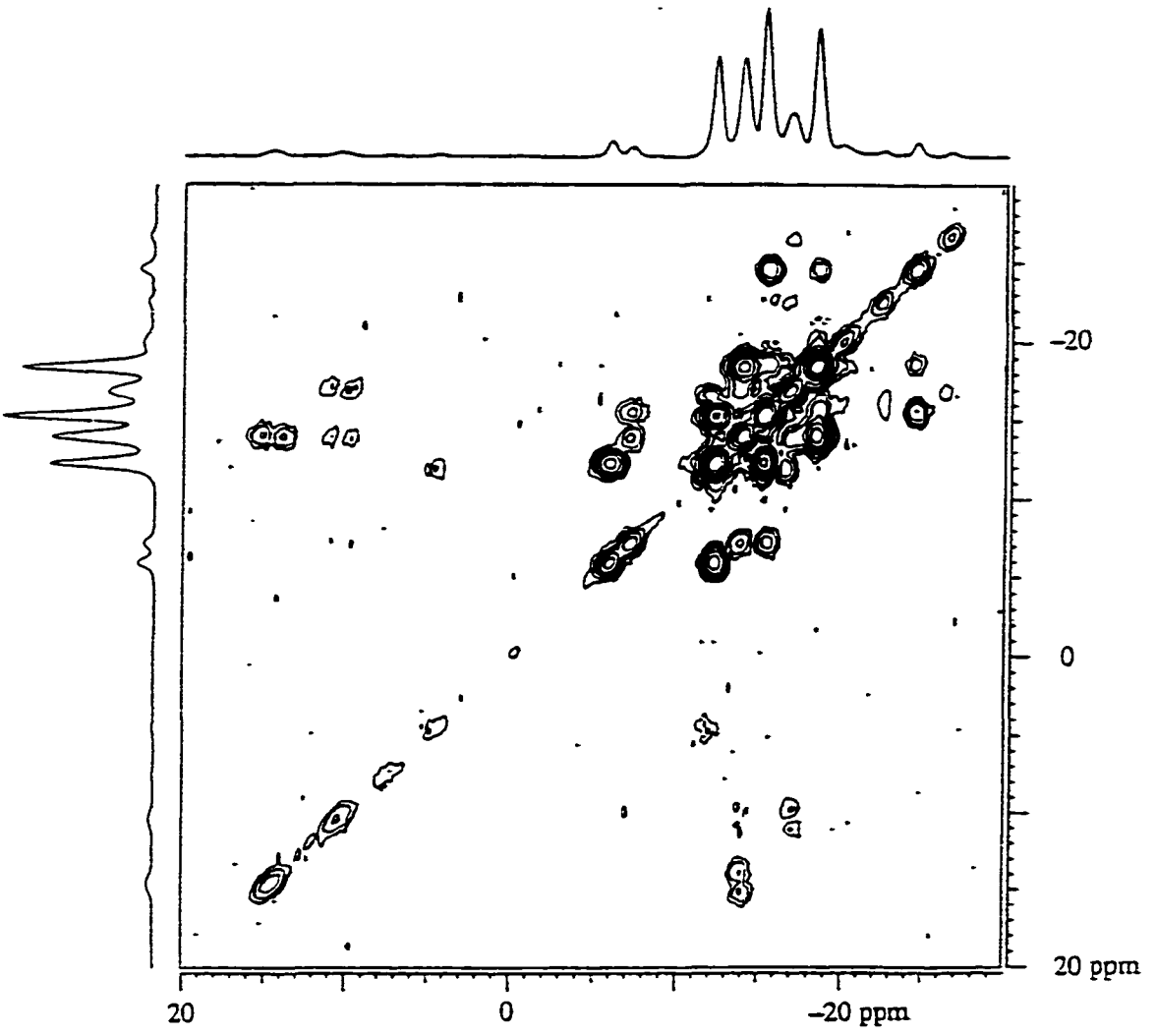

Figure I.2.20. The ^{11}B–^{11}B COSY NMR spectrum (acetone-d_6) of the mixture of products from the $Cs(CB_{11}H_{12})$/F-TEDA reaction at 40°C acetonitrile.

B–H → B–F conversion using *N*-fluoro reagents. Since then, Preetz et al. has used the method to synthesize $B_6H_5F^{2-}$ and $B_{12}H_{11}F^{2-}$.[80] The conversion consists of a series of sequential steps depicted generically for F-TEDA by the reaction below (Δ = a borane or carborane cluster minus one vertex, m = 1 or 2):

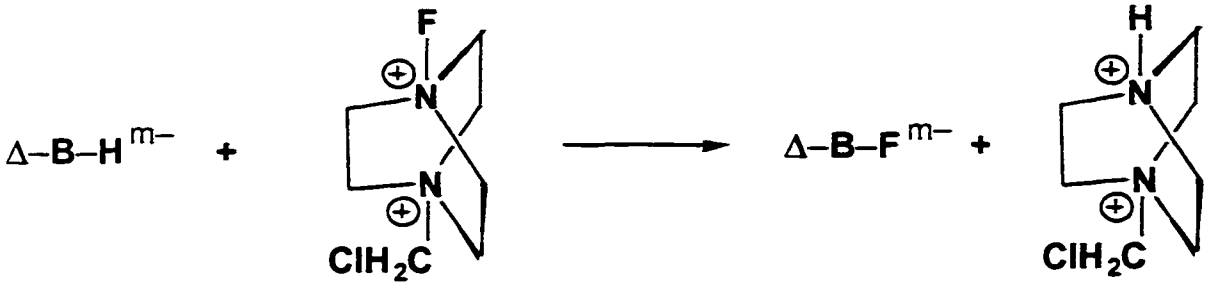

The compositional and isomeric purity of the $CB_{11}H_{11-n}F_n^-$ products formed using F-TEDA are quite different than those obtained when LAHF is used. For example, it was possible to obtain high yields of pure 12-F_1 and 7,12-F_2 using LAHF at 25°C and 140°C, respectively,[79] but it appears doubtful that this will be possible at any temperature using F-TEDA. However, F-TEDA would be the reagent of choice if isomerically pure salts of 7-F_1 were desired; this, of course, will require chromatographic, precipitation, extraction, or ion-exchange methodologies that are better developed than those at present. The results also clearly indicate that fluoro derivatives of $CB_{11}H_{12}^-$ with $n \geq 5$ can be prepared using glass apparatus and a common organic solvent. This represents an important advantage over the use of supercritical HF as a fluorinating agent. It was not possible to determine whether or not the C_{5v} isomer 7,8,9,10,11,12-$CB_{11}H_6F_6^-$ was present in the small amount of F_6^- that was formed at 100 °C. In on-going work, attempts will be made to increase the yield of F_6^- isomers and to improve ways to separate the products of the reactions.

Discussion

Theoretical studies by Mr. Douglas McLemore of the Strauss Research Group were conducted on the monofluorinated derivatives of *closo*-carborane, *x*-$CB_{11}H_{11}F^-$ (*x* = 2, 7, 12).[93] Using density functional theory, it was found that the 2-F_1^- isomer was marginally more stable than the 7-F_1^- isomer by 0.91 kcal/mol, while it was only 0.17 kcal/mol more stable than the 12-F_1^- isomer (at 0 K including zero-point energy corrections). Statistically, the 2-F_1^- isomer should be favored 5:1 over the 12-F_1^- (there are five upper-belt boron atoms and on antipodal boron atom); the theoretically predicted thermodynamic product ratio at 25°C is [2-F_1^-]/[12-F_1^-] = 6.6. In the fluorination reactions described above (both with LAHF and with F-TEDA), no derivates were formed with substitution in the B(2) position. From these results, it can be concluded that all of the $CB_{11}H_{11-n}F_n^-$ products produced were kinetic products; therefore, three questions need to be answered: (1) why did fluorination reactions of $CB_{11}H_{12}^-$ using LAHF produce different positional isomers than reactions of $EB_{11}H_{11}^-$ (E = As, Sb, Bi) under similar conditions? (2) why did fluorination reactions of $CB_{11}H_{12}^-$ using LAHF produce different positional isomers than fluorination reactions of $CB_{11}H_{12}^-$ using F-TEDA? (3) why did the fluorinations in the reactions of $CB_{11}H_{12}^-$ with LAHF occur where they did, i.e., why 7,9,12-F_3^- and not 7,8,12-F_3^- ?

The first two questions will be answered qualitatively in the following discussion. The third question will be addresses in Part I, Chapter 3 using ^{11}B, ^{13}C, ^{19}F, and ^1H NMR data for the $CB_{11}H_{11-n}F_n^-$ (*n* = 0–6) series of compounds to rationalize the observed substitution patterns.

Fluorination Reactions using LAHF

It has been proposed that substitution of boranes and heteroboranes first proceeds with the protonation of a B–H bond to form a three-center two-electron bond between the boron atom and the H–Y moiety (Figure I.2.21). This step is followed by B–HY bond breaking to leave a vacant p orbital on the boron atom and subsequent nucleophilic attack by Y^- (in the case of elemental halogens) or by Z^- (as in the case of LAHF) to form a B–Y or B–Z.[94,95] This mechanism is shown in detail in Figure I.2.21. It is thought that electrophilic attack occurs at the boron atom antipodal to the carbon atom because the carbon atom increases the electron density in the antipodal B–H bond (with respect to $B_{12}H_{12}^{2-}$), favoring attack by an electrophile at this vertex over the other possible vertices.[94,95]

When LAHF is used as a fluorinating agent, the fluorination of $CB_{11}H_{12}^-$ proceeds differently than the fluorination of $EB_{11}H_{11}^-$. In the former case, initial fluorination occurs exclusively at the boron atom antipodal to the carbon atom, B(12), whereas in the later case, a significant amount of lower belt mono and difluoro derivatives were formed. The effects of solvent dielectric and temperature, as discussed below for the reaction of $CB_{11}H_{12}^-$ with F-TEDA, can be ruled out since fluorination reactions were performed in LAHF at 25°C for all four anions and the reaction times were comparable. So, it is reasonable to conclude that the differences in substitution pattern and degree of substitution between $CB_{11}H_{12}^-$ and $EB_{11}H_{11}^-$ are a result of fundamental differences in the electronic distribution within the clusters.

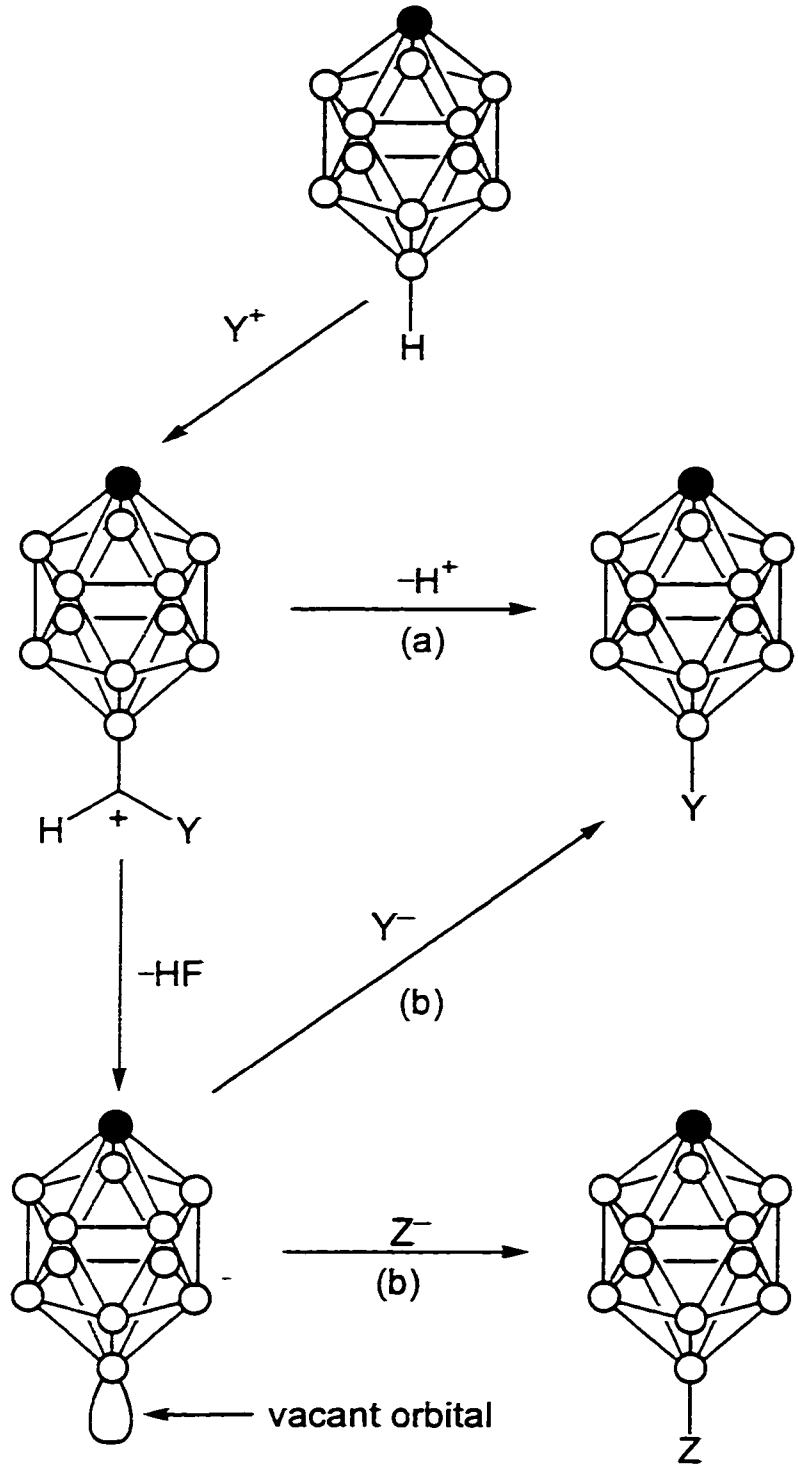

Figure I.2.21. Mechanism proposed by Heřmánek et al. for (a) electrophilic substitution and (b) nucleophilic substitution of $CB_{11}H_{12}^-$. The black circles represent C–H vertices and the open circles represent B–H vertices.[94,95]

The crystal structures of $BiB_{11}H_{11}^-$ is shown in Figure I.2.22, and Table I.2.4 is a comparison of the bond distances in $BiB_{11}H_{11}^-$ and $CB_{11}H_{12}^-$.[49] From this data it is clear that there are fundamental differences in the geometry of the two anions. In the former case, the bismuth atom is an average of 2.420(14) Å from the boron atoms of the top belt (B(2)–B(6)); in contrast, the carbon–boron bond lengths in $CB_{11}H_{12}^-$ are an average of 1.701 Å (The C–B bonds are actually shorter, at 3σ, than the corresponding antipodal bonds, B(7–11)–B(12).) Also, the distance between the boron atoms of the upper belt are longer in $BiB_{11}H_{11}^-$ (1.880 Å) than in $CB_{11}H_{12}^-$ (1.773 Å). The larger size and the presence of higher angular momentum orbitals of bismuth causes the overlap with the neighboring boron atoms to be poorer than orbital overlap between carbon and boron in $CB_{11}H_{12}^-$.

While the x-ray crystal structure data illustrate differences in the geometries of $CB_{11}H_{12}^-$ and $BiB_{11}H_{11}^-$, trends in ^1H and ^{11}B NMR chemical shifts can be used to probe the differences in electron distribution between the different clusters. As the heteroatom (i.e., E or position 1) becomes more positive relative to BH^{2-} in $B_{12}H_{12}^{2-}$, the chemical shifts for all of the hydrogen atom resonances become more positive relative to the hydrogen resonances in $CB_{11}H_{12}^-$ (Figure I.2.23). This suggests that as the heteroatom atom becomes more positive all of the hydrogen atoms become less shielded, or in other words, there is less electron density surrounding each hydrogen nucleus. This effect is felt most strongly by the antipodal hydrogen atom, H(12); remarkably, $\delta(^1H)$ for H(12) of $BiB_{11}H_{11}^-$, this hydrogen atom is 8.3 ppm *more positive* than the $\delta(^1H)$ for H(12) in $CB_{11}H_{12}^-$. Figure I.2.24 illustrates that the ^1H NMR chemical shift of the antipodal hydrogen atom becomes more negative (i.e., becomes more shielded) as the electronegativity of the heteroatom increases.

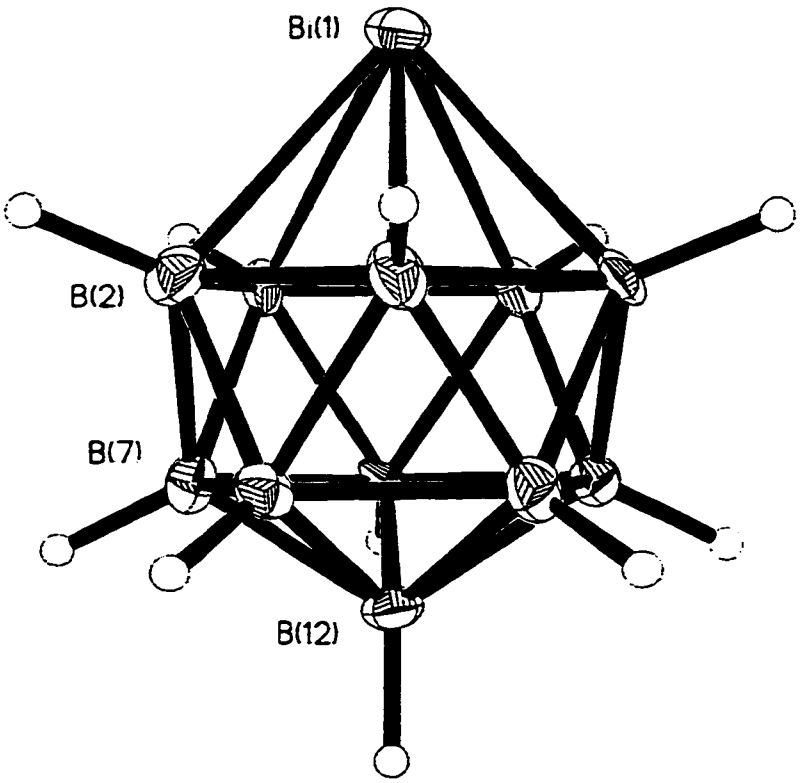

Figure I.2.22. Crystal structure of one of the unique $BiB_{11}H_{11}^{-}$ units in $Cs(BiB_{11}H_{11})\cdot 0.33(OC(CH_3)_2)$. For clarity, the Cs^{+} cation and acetone are not shown. Selected bond distances (Å) and angles (°): Bi(1)–B(2–6), 2.409–2.434; B(2–6)–B(2–6), 1.847–1.903; B(2–6)–B(7–11), 1.740–1.789; B(7–11)–B(7–11), 1.760-1.795; B(7–11)–B(12), 1.736-1.780.

Table I.2.4. Comparison of Bond Distance Data (Å) for $BiB_{11}H_{11}^-$ and $CB_{11}H_{12}^-$ (E = Bi or C)[a]

bond	$BiB_{11}H_{11}^-$		$CB_{11}H_{12}^-$	
	average	range	average	range
E(1)–top belt	2.420(14)	2.409-2.434	1.701(9)	1.686-1.716
top belt–top belt	1.880(14)	1.847-1.903	1.773(8)	1.745-1.788
top belt–bottom belt	1.768(14)	1.740-1.789	1.781(8)	1.766-1.796
bottom belt–bottom belt	1.778(14)	1.760-1.795	1.791(8)	1.767-1.804
top belt–B(12)	1.761(14)	1.736-1.780	1.776(8)	1.760-1.789

[a] Structural data comes from $Cs(BiB_{11}H_{11})\cdot 0.33(OC(CH_3)_2)$, this work, and $Ag(C_6H_6)(CB_{11}H_{12})$, reference [49].

Similar effects are seen in the ^{11}B NMR spectra of the $EB_{11}H_{11}$ heteroboranes (Figure I.2.23). As the heteroatom becomes more positive, the chemical shift of the B(12) boron atom resonance shifts to more positive δ values (i.e., becomes more deshielded). The heteroatom effect on B(7–11) is the same as for the antipodal atom, but here the effects are not as large; the upperbelt boron atoms (those next to the heteroatom, B(2–6)), however, do not follow any apparent trend. In the $CB_{11}H_{12}^-$ cluster, these atoms are shifted to more negative δ values relative to $B_{12}H_{12}^{2-}$, while for all other E atoms examined here $\delta(^{11}B)$ for B(2–6) are more positive than $\delta(^{11}B)$ for B(2–6) in $B_{12}H_{12}^{2-}$ and in $CB_{11}H_{12}^-$. Similar trends to those listed here are seen for the neutral *closo*-chalcoborane clusters $SB_{11}H_{11}$, $SeB_{11}H_{11}$, $TeB_{11}H_{11}$.[94,95] Correlations between the amount of electron density and ^{11}B NMR chemical shifts are more complex than those for ^1H NMR chemical shifts. The presence of 2p orbitals on the boron atoms

complicate the issue, but it has been shown that changes in electron density in the $2p_x$+$2p_y$ orbitals are proportional to changes in the ^{11}B NMR chemical shift: as the amount of electron density in the $2p_x$+$2p_y$ orbitals increases, $\delta(^{11}B)$ becomes more negative.[97] The opposite effect is seen as the $2p_z$ electron density increases, but the magnitude of these changes is smaller. These effects will be discussed in more detail in Part I, Chapter 3.

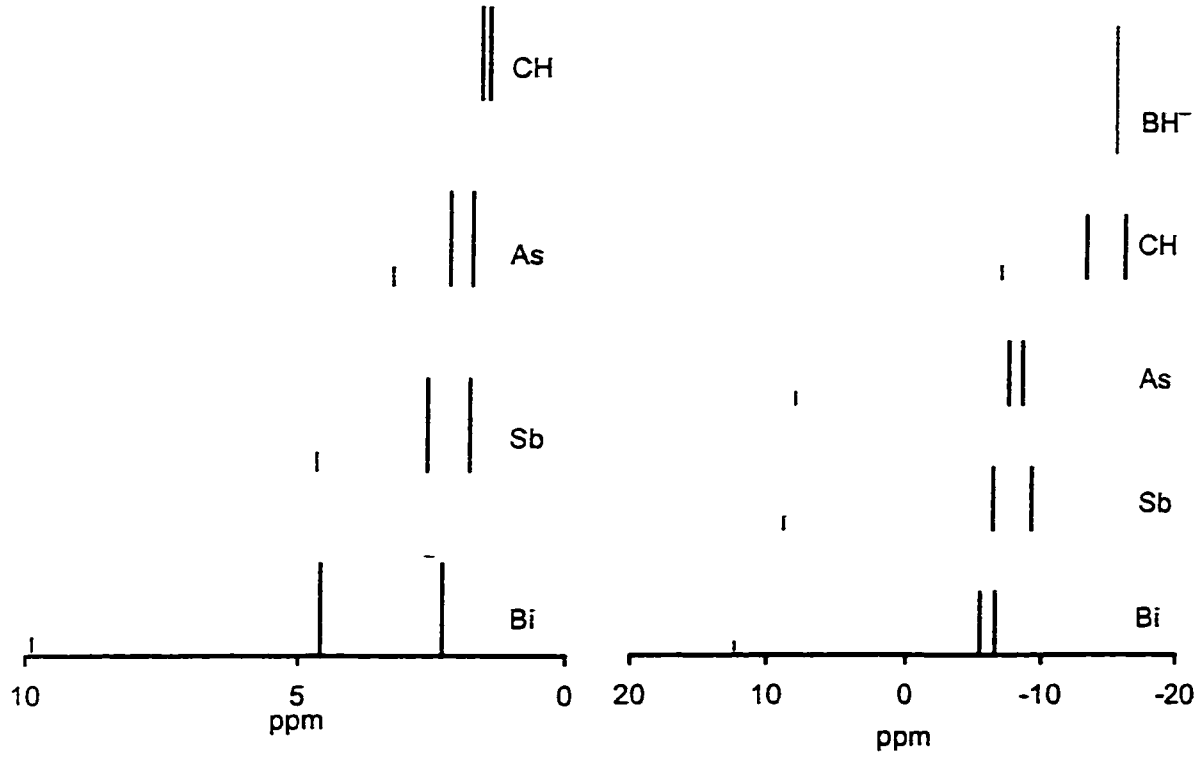

Figure I.2.23. Stick figure representations of the $^{1}H\{^{11}B\}$ NMR chemical shifts (left) and of the $^{11}B\{^{1}H\}$ NMR chemical shifts for the $EB_{11}H_{11}^{-}$ (E = BH^{-}, CH, As, Sb, Bi) anions. The single intensity lines represent the signal for the atom antipodal to the heteroatom (i.e., H(12) or B(12)).

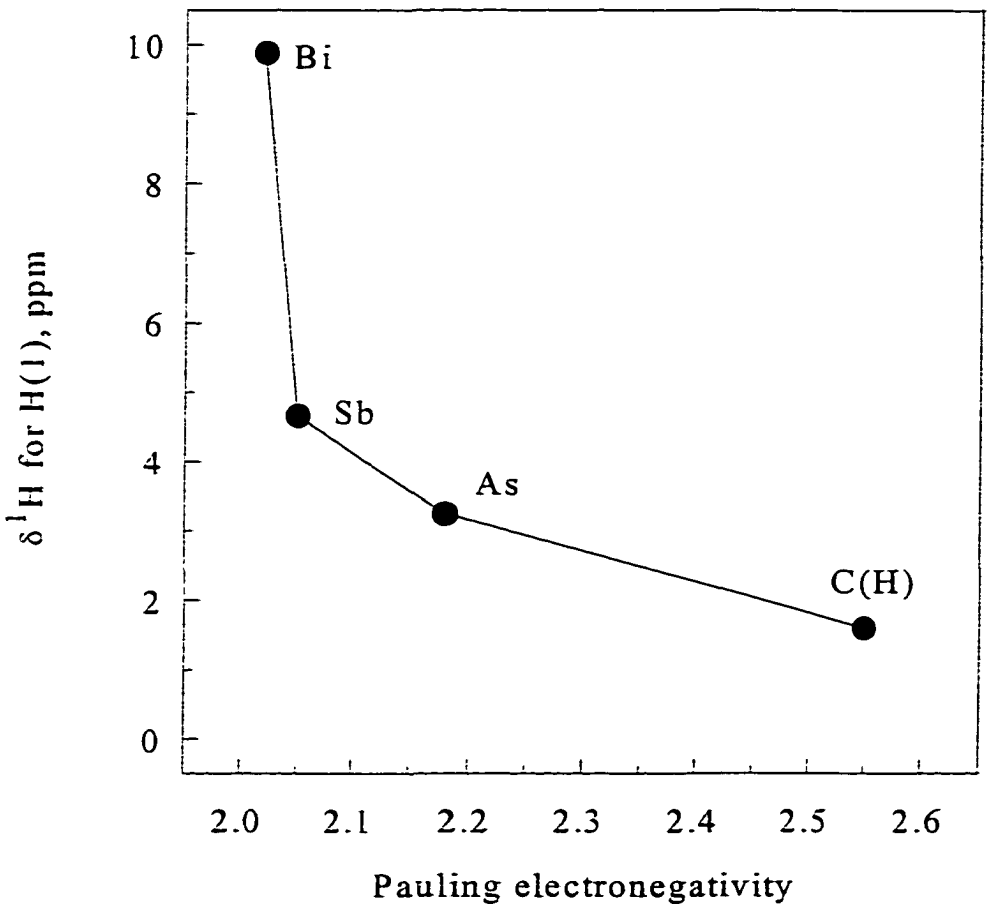

Figure I.2.24. Plot of the ^{1}H NMR chemical shift of H(12) versus the Pauling electronegativity of the heteroatom, E, in $EB_{11}H_{11}^{-}$ clusters (E = CH, As, Sb, Bi).

Initial halogenation of $CB_{11}H_{12}^-$ by nucleophiles (e.g., F^-, Cl^-, Br^-) occurs at B(12) under electrophilic conditions. The B(12) atom is the most deshielded boron atom in the cluster, indicating that it has the least $2p_x+2p_y$ electron density. The ^1H chemical shift of the hydrogen atom bonded to this boron atom, H(12), should be a good indication of the amount of $2p_z$ electron density at the boron atom. Examination of the ^1H NMR spectrum of $CB_{11}H_{12}^-$ shows that H(12) has a chemical shift between that of H(2–6) and H(7–11). Despite the fact that the hydrogen atom is neither the most deshielded nor the least deshielded, it is both deuterated first[46] and halogenated first by LAHF or by HOAc solutions of Cl_2 or Br_2 are used.[45,54]

As the heteroatom in $EB_{11}H_{11}$ is changed from CH^- to As^- to Sb^- to Bi^-, both the B(12) NMR signal and the H(12) NMR signal become more deshielded. It is reasonable to postulate that as the heteroatom becomes more positive, the dipole moment of the anion changes. (Dipole moments for anions are not measurable, but an analogy to the dipole moment of neutral species will be used here.) This redistribution of electron density, in part, causes the electron density in $2p_x+2p_y$ to decrease dramatically. In fact B(12) in $BiB_{11}H_{11}^-$ is approximately as deshielded as B(12) in 12-F_1^-. For all of the $EB_{11}H_{11}^-$ anions, the $\delta(^{11}B)$ signals from the B(7–11) vertices are at approximately the same chemical shift as B(12) in $CB_{11}H_{12}^-$. The combination of the deshielding of B(12) and the deshielding of H(12), relative to $CB_{11}H_{12}^-$, disfavors electrophilic assisted nucleophilic substitution at the B(12)–H(12) vertex and is the major cause of the difference in substitution patterns. This effect manifests itself as a continuum of substitution patterns. The $AsB_{11}H_{11}^-$ anion has B(12) and H(12) atoms that are more shielded than in the antimony and bismuth analogues but are more deshielded than in $CB_{11}H_{12}^-$. As result, a mixture of 12-F_1^- and 7-F_1^- substitution occurs for this anion. As the deshielding of B(12) and H(12) increases, as in $SbB_{11}H_{11}^-$ and $BiB_{11}H_{11}^-$, fluorination occurs almost exclusively at the lower belt positions.

Fluorination Reactions using F-TEDA

The *N*-fluoro reagent F-TEDA has been shown to be a useful reagent for the conversion of B–H bonds to B–F bonds in *closo*-$CB_{11}H_{12}^-$ (as well as the $CB_9H_{10}^-$ and $B_{12}H_{12}^{2-}$ clusters).[81] The degree of fluorination and the position of initial substitution are different for F-TEDA than for LAHF. F-TEDA is a source of electrophilic fluorine (formally F^+), whereas LAHF provides nucleophilic fluorine (F^-). For this reason, it is not unreasonable to think that the mechanism of initial substitution will be different for the two reagents causing differences in substitution patterns. One possible mechanism is shown in Figure I.2.25.

Coordination studies of $Fp(CB_{11}H_{12})$ ($Fp = CpFe(CO)_2^+$) in dichloromethane-d_2 have shown the presence of two linkage isomers, $Fp(12\text{-}CB_{11}H_{12})$ and $Fp(7\text{-}CB_{11}H_{12})$.[96] While detailed studies of this system have not been undertaken, the analogous $Fp(CB_9H_{10})$ system was studied in greater detail.[97] It was shown that coordination of $CB_9H_{10}^-$ to the electrophile Fp^+ occurs at all three possible sights on the cluster (i.e., the 2-, 6-, and 10-positions). The ratio of these linkage isomers was dependent on the solvent and on the temperature. In higher dielectric solvents, or at low temperatures, all three isomers were formed with 2-position < 6-position < 10-position. As the dielectric of the solvent was decreased, or as the temperature was increased, the 2-isomer disappeared completely and the 10-isomer increased in abundance. These effects were rationalized in the following way: (1) At higher temperatures, the dielectric of the solvent decreases; under these conditions, the 2- and 6-isomers are entropically favored because their symmetry (local C_s symmetry) is lower than that of the 10-isomer (local C_{4v}). (2) Lower dielectric solvents favor the 10-isomer over the other two isomers since this minimizes the Coulombic repulsion between the positive, C–H end of the cluster and the positive Fp^+ cation.

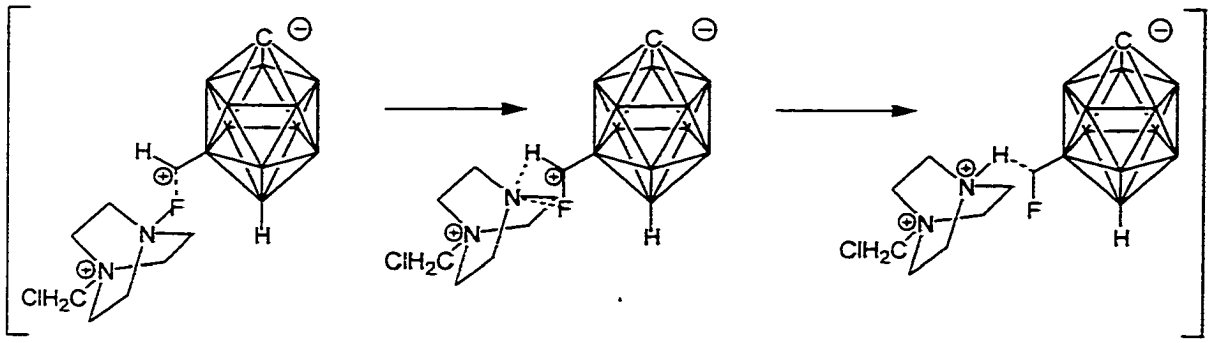

Figure I.2.25. Possible reaction mechanism for the fluorination of $Cs(CB_{11}H_{12})$ by F-TEDA-BF_4 in acetonitrile. Note, the overall charge for each of the three species is +1; the two BF_4^- anions and one Cs^+ cation are not shown.

It is possible that these effects were also at work in the reaction of F-TEDA with $CB_{11}H_{12}^-$. These reactions were performed in CH_3CN, which has a dielectric constant of 37.5. In this reasonably high dielectric solvent, the molecular dipole of the intermediate $[F\text{-}TEDA\text{-}CB_{11}H_{12}]^+$ will be lessened, and the formation of a 7-isomer complex should be favorable (as compared to a low dielectric solvent). As the temperature increases, the ratio of the 7-isomer to the 12-isomer is expected to increase due to the entropy increase caused by coordination of F-TEDA to B(7). Since the J_{BH} of $CB_{11}H_{12}^-$ are roughly equal, 136 Hz for B(7)–H(7) through B(11)–H(11) versus 134 Hz for B(12)–H(12), and since H(7–11) are more shielded than H(12), electrophilic attack seems most likely at these sites over the upper belt positions (J_{BH} = 155 Hz).

Separation of $CB_{11}H_{12}^-$ Anions

The hexafluorinated derivative of $CB_{11}H_{12}^-$ was a target molecule when this project began. It was shown above that $CB_{11}H_6F_6^-$ can be formed using both LAHF and F-TEDA as fluorinating agents, but the result was a mixture of anions containing both

anions with different degrees of fluorination and with different isomers for each derivative. Therefore, attempts were made to separate and purify the mixtures of anions so that the higher-order derivative could be studied. Initial thin-layer chromatographic experiments indicated that a mixture of $(n\text{-Bu})_4N^+$ salts of 12-$CB_{11}H_{11}F^-$ ($R_f = 0.50$), 7,12-$CB_{11}H_{10}F_2^-$ ($R_f = 0.47$), and 7,9,12-$CB_{11}H_9F_3^-$ ($R_f = 0.44$) could be separated on silica using 90:10 (v/v) chloroform:acetonitrile.

Because of the complexity of the mixtures with higher order substitution, two different size-exclusion resins were used for the separation of the more highly substituted mixtures—Sephadex G-25 (20–80 μm particle size) and Bio-Gel P-2 (45–90 μm particle size). Monitoring of the effluent at 205 nm using UV-visible spectroscopy allowed for detection of the products in the eluent. Dr. Svetlana M. Ivanova of the Strauss Research Group performed the separations discussed below.[98]

Using a pH = 7.5 phosphate buffer as the mobile phase and a flow rate ranging from 0.1–0.5 ml/min, complex mixtures of F_4^-, F_5^-, F_6^-, and F_7^- were separated. It was found that each resin performed differently. For example, the order of separation when Bio-Gel P-2 was used was

$$\text{isomers of } CB_{11}H_5F_7^- < \text{7–12-}CB_{11}H_6F_6^- \approx \text{2,7–10,12-}CB_{11}H_6F_6^- <$$
$$\text{7–10,12-}CB_{11}H_5F_5^- \approx \text{2,7,9,10,12-}CB_{11}H_5F_5^- < \text{7,9,10,12-}CB_{11}H_8F_4^-$$

In this case, the anions were eluted based strictly on the degree of substitution, and it was not possible to separate positional isomers of anions with the same value of *n*. Figure I.2.26 shows a NIEMS of a mixture of $CB_{11}H_8F_4^-$ and $CB_{11}H_7F_5^-$ isomers before separation using the Bio Gel P-2 resin (top) and after separation using the Bio Gel P-2 resin (bottom). These results clearly illustrate that a reaction mixture that was 1:1 F_4^- isomers to F_5^- isomers before the separation was 7:3 F_4^- isomers to F_5^- isomers after

the separation. The use of Sephadex allowed for the separation of positional isomers but did not efficiently separate anions with different values of degrees of fluorination:

$$7\text{–}12\text{-}CB_{11}H_6F_6^- \approx \text{isomers of } CB_{11}H_5F_7^- < 7\text{–}10,12\text{-}CB_{11}H_5F_5^- \approx 2,7\text{–}10,12\text{-}CB_{11}H_6F_6^- < 7\text{–}10,12\text{-}CB_{11}H_5F_5^- < 7,9,10,12\text{-}CB_{11}H_8F_4^- \approx 2,7,9,10,12\text{-}CB_{11}H_5F_5^-$$

To separate anions with both different degrees of substitution, *n*, and different positional isomers, the two resins were used in parallel. Separation of these complex mixtures required fractions from one separation to be rerun multiple times with each resin. This process was time consuming and the overall yield of each derivative decreased dramatically during the process. While this method was not practical for producing large quantities of a particular isomer, it produced quantities large enough for characterization of the higher order derivatives in the $CB_{11}H_{12-n}F_n^-$ series. For example, separations using these commercially available resins allowed for the isolation and x-ray crystallographic characterization of the target anion $(Me_3NH)(7\text{–}12\text{-}CB_{11}H_6F_6)$. The crystal structure of the anion is shown in Figure I.2.27.[99]

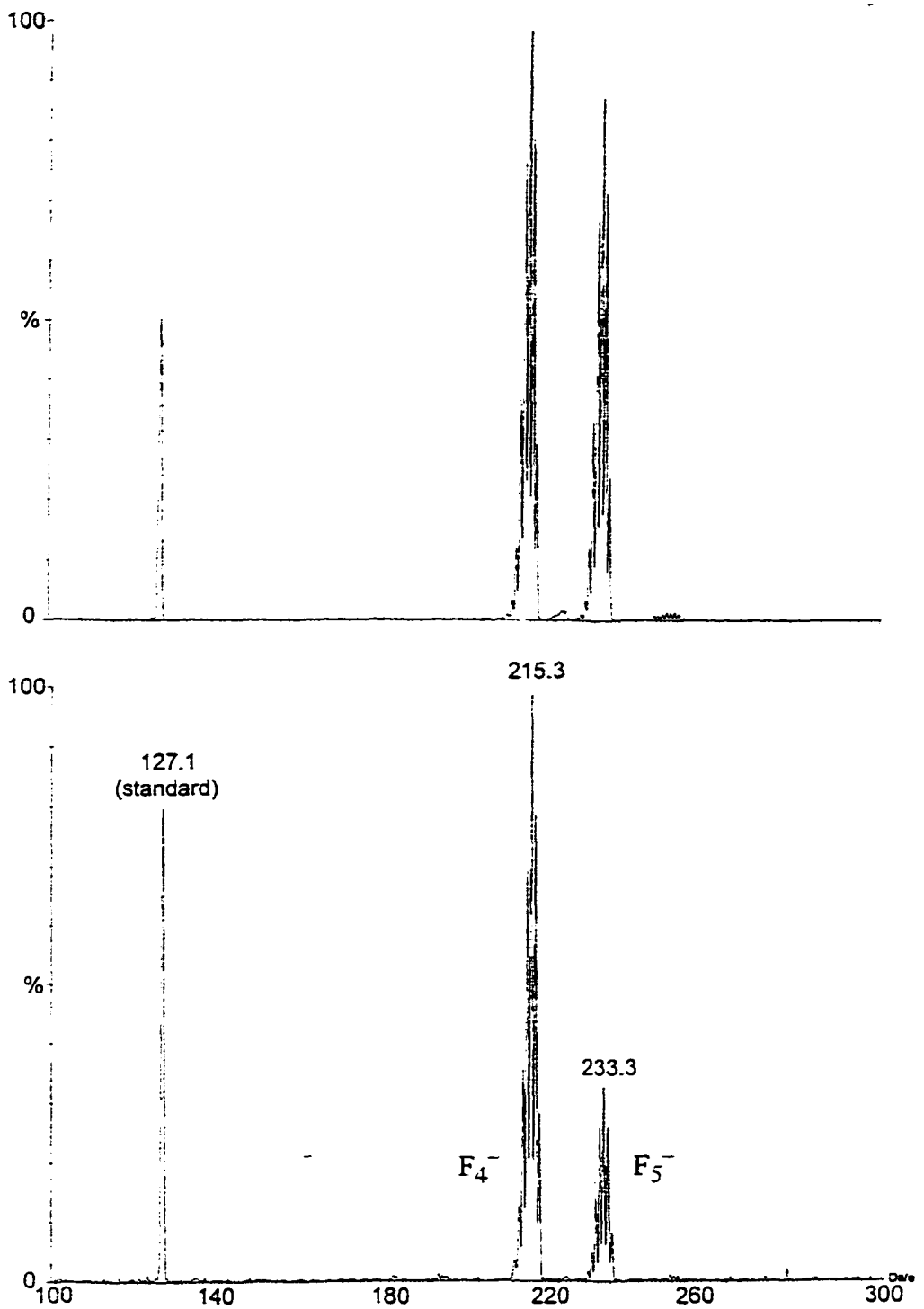

Figure I.2.26. NIEMS of a mixture of $CB_{11}H_8F_4^-$ (F_4^-) and $CB_{11}H_7F_5^-$ (F_5^-) isomers. The top spectrum is before separation; the bottom spectrum is after separation using Bio Gel P-2 resin.

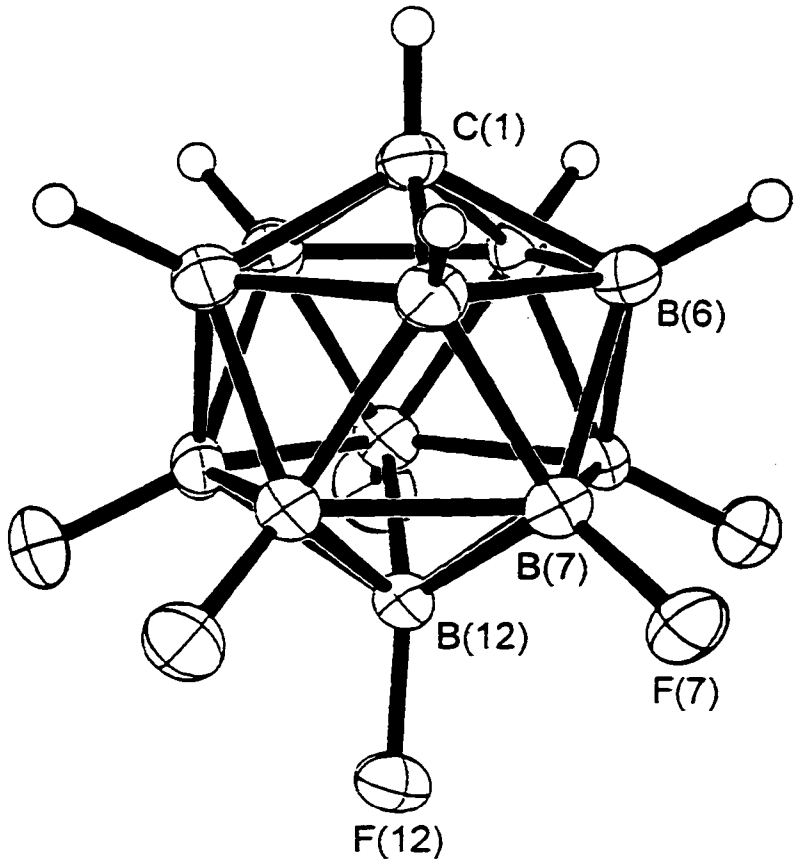

Figure I.2.27. Crystal structure of the $CB_{11}H_6F_6^-$ anion. The $(CH_3)_3NH^+$ cation has been omitted for clarity. Boron-fluorine bond distances range from 1.367(7)–1.388(7) Å.

Weakly Coordinating Ability of $CB_{11}H_{11-n}F_n^-$ Anions

It was demonstrated above that fluoroheteroborane anions can be synthesized by two different techniques. Once this new class of anions can be routinely synthesized, it was appropriate to determine if they are indeed more weakly coordinating than their predecessors. A variety of techniques have been proposed for determining the weakly coordinating ability of an anion.[50,51,60,61] Two techniques will be examined here—one qualitative test and one more quantitative test. The first is the direct examination of the coordination of the 12-$CB_{11}H_{11}F^-$ anion to a silver(I) cation in the solid state; the second is the measurement of lithium ion conductivity.

Cation exchange reactions have allowed the Ag^+ salt of 12-$CB_{11}H_{11}F^-$ to be isolated in good yield. For example, extraction of an aqueous solution of Cs(12-$CB_{11}H_{11}F$) and $AgNO_3$ with benzene, followed by cooling of the benzene solution, yielded crystals of $Ag(C_6H_6)_2$(12-$CB_{11}H_{11}F$). The structure (Figure I.2.28a) consists of a silver(I) cation coordinated to two benzene ligands in an asymmetric η^2 fashion and to two terminal B–H hydrogen atoms of two *pseudo*icosahedral *closo*-12-$CB_{11}H_{11}F^-$ anions. The Ag–C distances are 2.46(1) and 2.73(1) Å for the "top" benzene ligand and 2.53(1) and 2.59(1) Å for the other. The Ag–H7 and Ag–H8' distances are 2.18 and 2.28 Å, respectively, and the H7–Ag–H8' angle is 135°. Significantly, there is no interaction between the silver ion and the fluorine atom: the closest Ag···F interaction is >4.6 Å, more than 1.4 Å longer than the sum of van der Waals radii. In the structure of $Ag(C_6H_6)$(12-$CB_{11}H_{11}Br$),[8] the two Ag–C distances are 2.485(9) and 2.616(10) Å and the Ag–Br, Ag–H7', Ag–H8" distances are 2.642(1), 2.27(9), and 2.20(8) Å, respectively. In harmony with hard and soft acid/base principles, the silver(I)-halogen interaction is lost on changing from the 12-bromo to the 12-fluoro carborane anion: the Ag–Br bond in $Ag(C_6H_6)$(12-$CB_{11}H_{11}Br$) is replaced by an additional arene ligand in $Ag(C_6H_6)_2$(12-$CB_{11}H_{11}F$). This suggests that $CB_{11}H_{12-n}F_n^-$ anions may be more

weakly coordinating than $CB_{11}H_{12-n}Br_n^-$ anions for a given value of n, at least for applications in which soft metal centers are involved.

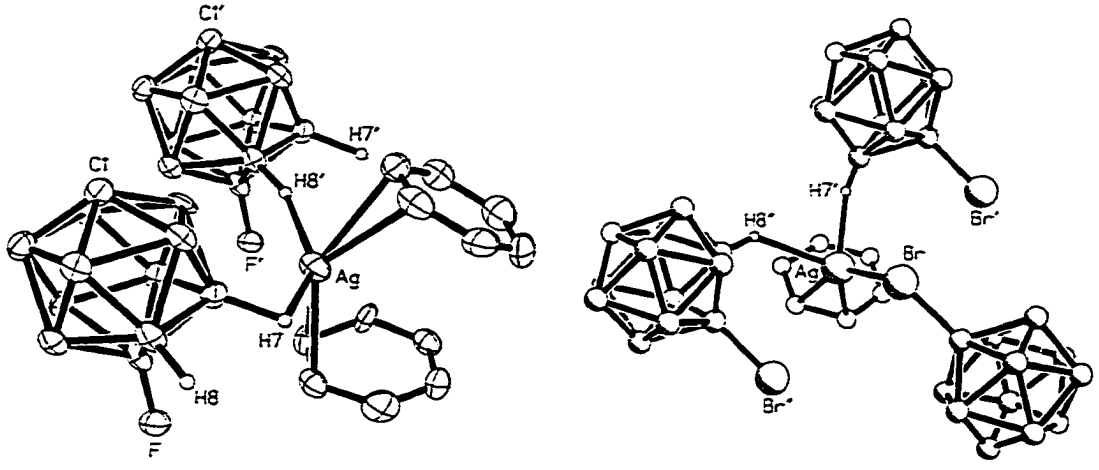

(a) (b)

Figure I.2.28. (a) X-ray crystal structure of $Ag(C_6H_6)_2(12\text{-}CB_{11}H_{11}F)$. Two anions but only one and cation are shown. Selected distances (Å) and angles (°): Ag–C, 2.46(1)–2.73(1); Ag–H7, 2.18; Ag–H8', 2.28; H7–Ag–H8', 135. The closest Ag···F interaction is >4.6 Å. (b) X-ray crystal structure of $Ag(C_6H_6)(12\text{-}CB_{11}H_{11}Br)$. Three anions and one cation are shown.

One quantitative test of weakly coordinating ability is the lithium ion conductivity of Li^+A^- salts, where A^- is any anion. This test is valuable since it correlates directly with the use of our anions in a industrial application, lithium electrolyte batteries. Table I.2.5 shows the lithium ion conductivities for the fluorcarborane anions F_0^- and $12\text{-}F_1^-$, described above, and $1\text{-}CH_3\text{-}CB_{11}F_{11}^-$, synthesized in the Strauss Research Group by Dr. Sergei V. Ivanov.[100] Mr. Benjamin Nolan of the Strauss Research Group

performed the conductivity measurements.[39] $LiSO_3CF_3$ and $CB_{11}H_6Br_6^-$ are included for comparison.

Table I.2.5. Conductivities of Selected Anions (0.01 M in THF)[39]

compound	conductivity ($mS\ cm^{-1}$)	equivalent conductivity ($S\ cm^2\ mol^{-1}$)
$LiSO_3CF_3$	0.0015	0.15
$Li(CB_{11}H_{12})$	0.059	5.9
$Li(12\text{-}CB_{11}H_{11}F)$	0.085	8.5
$Li(CB_{11}H_6Br_6)$	0.15	15
$Li(1\text{-}CH_3\text{-}CB_{11}F_{11})$	0.17	17

From this data, a general idea about the coordinating ability of the fluorocarboranes can be ascertained. First, at a concentration of 0.01 M in THF, all of the carborane anions studied outperform the industry standard, $LiSO_3CF_3$, by at least one order of magnitude; the highly halogenated derivatives $1\text{-}CH_3\text{-}CB_{11}F_{11}^-$ and $CB_{11}H_6Br_6^-$ conduct two orders of magnitude better than $LiSO_3CF_3$. As fluorination of the parent cluster increases, so does the conductivity of the solution. This indicates that the cluster becomes more weakly coordinating as more fluorine atoms are added. Figure I.2.29 is a graphical representation of the data in Table I.2.5. From the graph, it appears that the $CB_{11}H_6Br_6^-$ anion has approximately the same conductance as that predicted for $CB_{11}H_6F_6^-$. Although no direct comparisons of halogenated carborane anions have been made, it would be interesting to compare the conductivities of the easily accessible $12\text{-}CB_{11}H_{11}X^-$ and $7,12\text{-}CB_{11}H_{10}X_2^-$ (X = F, Cl,

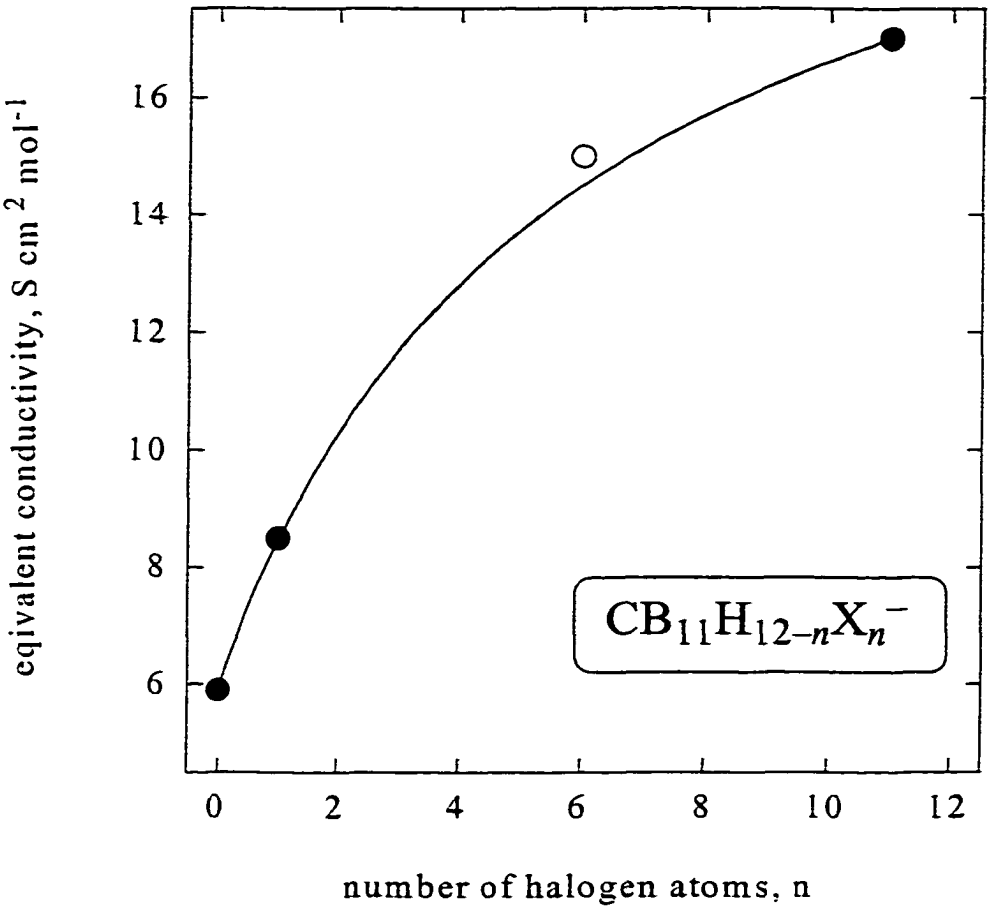

Figure I.2.29. Plot of equivalent conductivity versus number of fluorine atoms, *n*. The solid circles represent $CB_{11}H_{12-n}F_n^-$ anions and the open circle represents, $CB_{11}H_6Br_6^-$. Note, the solid line is for visual purposes only.

Br, I) anions and of the hexahalo derivatives, including F_6^- once pure samples in adequate quantities can be prepared. It would be expected, based solely on hard and soft acid/base principles (Li^+ is hard), that the order of conductivities would be I > Br > Cl > F. It remains to be seen if this trend would hold or if more complex factors are at work within the system.

Conclusions

The data presented in this chapter illustrate that both $EB_{11}H_{11}^-$ (E = CH, As, Sb, Bi) clusters can be polyfluorinated using liquid anhydrous hydrogen fluoride. Fluorination of the $CB_{11}H_{12}^-$ anion has also been achieved using an organic fluorinating agent, F-TEDA, in glass reaction vessels with organic solvents. The fluorination of $CB_{11}H_{12}^-$ and 2-$CB_{11}H_{11}F^-$ proceeded by stepwise, regioselective attack of HF on the anion. Fluorination reactions of the $EB_{11}H_{11}^-$ anions using LAHF produced mixtures of isomers and varying degrees of substitution under conditions similar to those used for the fluorination of $CB_{11}H_{12}^-$ in LAHF: for $AsB_{11}H_{11}^-$ a mixture of isomeric products result, while for $SbB_{11}H_{11}^-$ and $BiB_{11}H_{11}^-$ greater regioselectivity is observed. The differences in substitution patterns between the $CB_{11}H_{12}^-$ anion and the $EB_{11}H_{11}^-$ anions provides the experimentalist with yet another degree of freedom in the designing of new superweak anions tailored for a specific application.

The first members of the $CB_{11}H_{12-n}F_n^-$ (n =1–4) class of anions are robust, stable in aqueous acid (1 M H_2SO_4) and base (1 M NaOH), and promise to be extremely weakly coordinating. Equally important, as far as their use as *SWAs* is concerned, is the fact that they can be prepared with high compositional and excellent isomeric purity. If separation techniques can be improved and large batches of relatively pure salts of 7–12-$CB_{11}H_6F_6^-$ can be prepared, its stability and coordinating ability can be compared with

the hexachloro, -bromo, and -iodo analogues, which have been the focus of an important series of studies by Reed and co-workers.[60,61]

In addition to the work presented here, the *closo*-carborane cluster 1-H-$CB_{11}F_{11}^-$ has been synthesized, isolated, and fully characterized.[100] This highly fluorinated derivative of $CB_{11}H_{12}^-$ exhibits increased stability and increased weakly coordinating ability compared to the $CB_{11}H_{12-n}F_n^-$ anions described above, reinforcing the idea that highly-fluorinated derivatives of $CB_{11}H_{12}^-$ show promise as new superweak anions.

CHAPTER 3

NMR Spectroscopy of the *closo*-Fluorocarboranes

Introduction

In this chapter, the NMR spectra of a complete series of $CB_{11}H_{12-n}F_n^-$ anions (n = 1–6) will be examined in detail. Wherever appropriate, additional information from the literature, namely spectra for the recently completed series of anions $B_{12}H_{12-n}F_n^-$ (n = 1–12),[71] will be provided to support the observations and conclusions being made. The fluorocarborane anions provide a wealth of NMR data. In these clusters, every atom type has one or more isotopes that is NMR active: ^{11}B, ^{1}H, ^{13}C, and ^{19}F. This provides a unique opportunity to compare the trends and predictions of $CB_{11}H_{12-n}F_n^-$ NMR data with the currently accepted theories about the ^{11}B and ^{13}C chemical shift trends. In addition, the information present in the boron cluster literature about the effect of cage heteroatoms and *exo* substituents on the chemical shift of *exo* atoms (i.e., the effect of B–F bonds on B–H and C–H ^{1}H and ^{19}F chemical shifts with increasing fluoride substitution and with substitution of *E*) is limited, and in no case has there been a study that has included a series of similar $EB_{11}H_{11}^-$ anions with varying degrees of fluorine atom substitution for comparison.

General Factors Affecting NMR Chemical Shifts

For NMR active nuclei such as ^{13}C, ^{19}F, ^{31}P, etc. a number of well established effects correlate with the chemical shift of the nucleus. These effects include the atom's connectivity (i.e., coordination number), hybridization of the vertex in question, electron density at the nucleus of interest, anisotropy effect of heavy atoms next to the nucleus of interest, and special effects such as the presence of a ring current.[51] Decades of data have shown that these simple correlations do not hold for ^{11}B NMR spectroscopy. In an extensive study of the literature, Heřmánek concluded that the shielding of the ^{11}B nucleus is influenced by the B–H vertex connectivity, the presence of an opposite hydrogen bridge, the asymmetry of the electron density distribution around the nucleus of interest, and the presence of a heteroatom or an *exo*-substituent antipodal to the nucleus in question.[94,95] In the cluster anions of interest in the study, only the last two points are of concern since there are no μ-H bridges in the clusters and since the connectivity of the cage atoms remains constant (i.e., six).

The effects governing the chemical shift a cluster boron atom can be described in terms of the nuclear shielding equation given below in Equation I.3.1:[101-104]

$$\sigma = \sigma_d^L + \sigma_p^L + \sigma_p^N + \sigma_d^N + \sigma_s \qquad \text{(I.3.1)}$$

In the above equation, L represents local shielding parameters and N represents neighboring shielding parameters while the subscripts d and p stand for diamagnetic and paramagnetic. The fifth term, σ_s, incorporates solvent contributions to the nuclear shielding. For heavy nuclei (i.e., those other than ^1H), the local paramagnetic term, σ_p^L, is the dominant factor affecting the chemical shift of a nucleus (Equation I.3.2).

$$\sigma_p^L(A) = -\frac{\mu_0 e^2 h^2}{6\pi m^2 \Delta E}\left\langle r^{-3}\right\rangle_{2p} P_u \qquad \text{(I.3.2)}$$

Three factors in the above equation determine the chemical shift of a heavy nucleus—ΔE, $<r^{-3}>_{2p}$, and P_u.[105] The ΔE term is the average energy of the electronic excited states in the species of interest. In practice, this term is approximated by using any electronic transition in the species of interest that is close to the average of all possible transitions from the ground state to excited states. For atoms within the same molecule, this value will be the same and, therefore, does not affect the chemical shift values when describing the ordering of the signals in a specific fluorocarborane isomer. Related molecules in this study are not expected to have the same electronic structures, but it will be assumed that this term will not significantly affect the shielding parameter for the anions of interest. The remaining factors play more dominant roles in determining the chemical shifts for the cage nuclei to be examined here. The $<r^{-3}>_{2p}$ term is the size of the 2p orbitals and is proportional to the electron density in these orbitals on the nucleus of interest. It has been shown in a computational study by Heřmánek and co-workers that the ^{11}B NMR shift of a boron atom antipodal to a heteroatom in a *closo*-heteroborane, $EB_{11}H_{11}$ anions (E = $AlMe^{2-}$, BH^{2-}, CH^-, NH and S), correlates with the electron density in the boron p orbitals.[106] There is an inverse linear correlation between the electron density in the p orbitals perpendicular to the B–H bond, the degenerate $2p_x$ and $2p_y$ orbitals, and $\delta(^{11}B)$ (i.e., as electron density *increases*, $\delta(^{11}B)$ *decreases*); in contrast, as the electron density in the p_z orbital *increases*, $\delta(^{11}B)$ *increases*. For this reason, the $2p_x$+$2p_y$ orbitals have been termed NMR-active orbitals. The P_u term is related to the above term; it is the orbital expansion term and describes the population imbalance in the 2p orbitals. This term manifests itself by causing a deshielding of the nucleus as the asymmetry of the electron density around the nucleus in question increases.

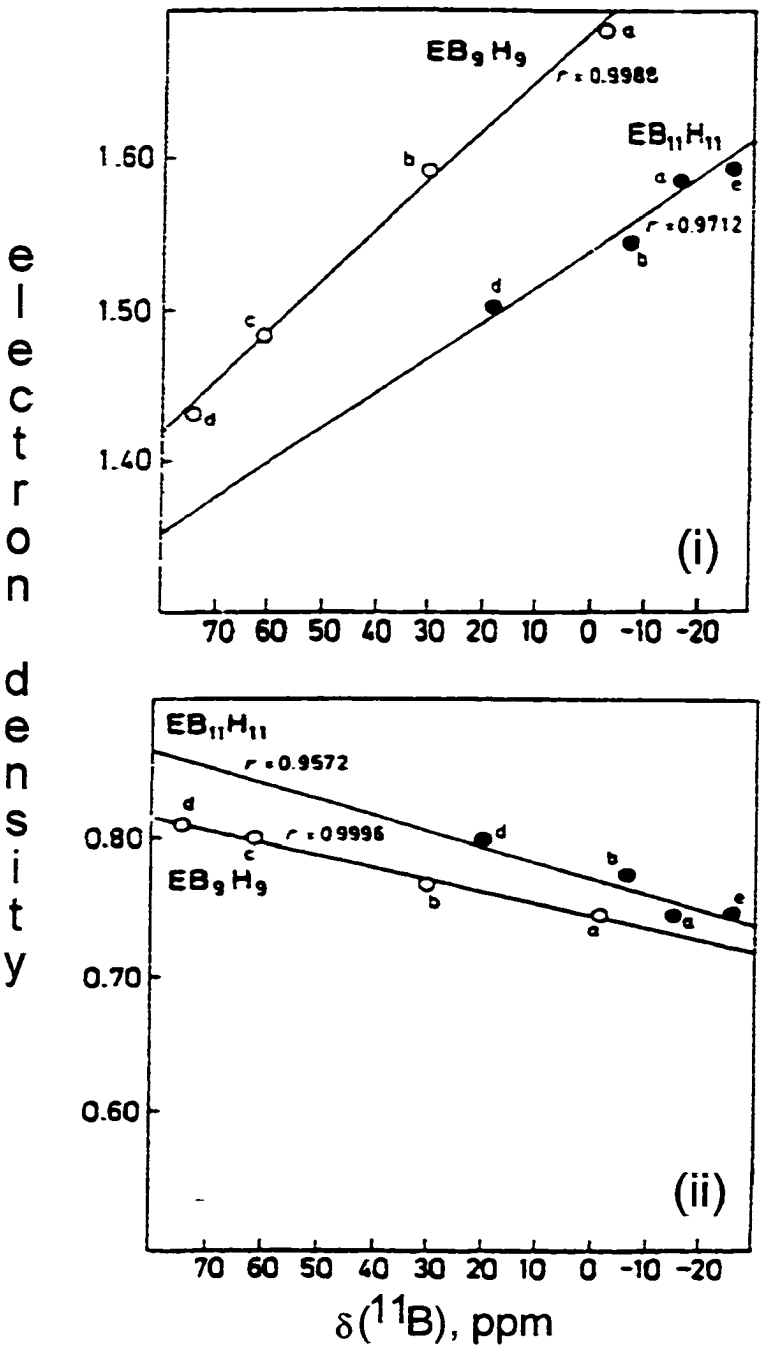

Figure I.2.30. Correlation between $\delta(^{11}B)$ and (i) boron $2p_x+2p_y$ and (ii) boron $2p_z$ electron density for 1-$EB_9H_9^-$ and 1-$EB_{11}H_{11}^-$ clusters (E = (a) BH^{2-}; (b) CH^-; (c) NH; (d) S; (e) $AlMe^{2-}$). Electron densities were calculated using the CNDO method.[106]

Heteroatom Influences on ^{11}B Chemical Shifts[94,95,106-112]

In the twelve-vertex *closo* clusters to be examined in this study, there are three interactions that a cage heteroatom, E, or an *exo*-substituent, X, can have on the other atoms: the antipodal effect (AE, A-effect, or *para* effect); the rhombahedral effect (RE, *meta* effect, or γ effect), and the neighbor effect (NE, ortho effect, or β effect). These effects will be discussed individually below and examples of each effect will be given using $CB_{11}H_{12}^-$ and $B_{12}H_{11}F^{2-}$ as examples.

Antipodal effect

The antipodal effect caused by cage heteroatoms, E, or *exo*-substituents, X, represents a specific mutual influence of two opposite vertices in a polyhedral cluster. In order for this effect to manifest itself, it is necessary to have a plane of symmetry that contains the two atoms, a condition that holds for all of the clusters to be examined here. This effect is the dominant influence in a boron cluster and causes the largest $\delta(^{11}B)$ shift of the three possible effects. A cage heteroatom, E, shifts the signal of the antipodal vertex to larger δ values; the boron atom, B(12), antipodal to the carbon atom in $CB_{11}H_{12}^-$ has a chemical shift of –7.0 ppm, which is 8.3 ppm more positive than the degenerate boron signal in $B_{12}H_{12}^{2-}$. In contrast, a substituent X that has lone-pair electrons (*M*+) shifts the signal of the antipodal vertex to more positive (i.e., less negative) δ values; the ^{11}B NMR signal of boron atom antipodal to the B–F bond in 1-$B_{12}H_{11}F^{2-}$ is 11.0 ppm more negative than the chemical shift of the degenerate boron atom signal in the unsubstituted cluster. For those X without lone pair electrons (*M*–) the effects are negligible.

A possible explanation for the ^{11}B NMR chemical shift effects of an antipodal heteroatom is shown in Figure I.3.1.[94,95,106] As the electron attracting power of a

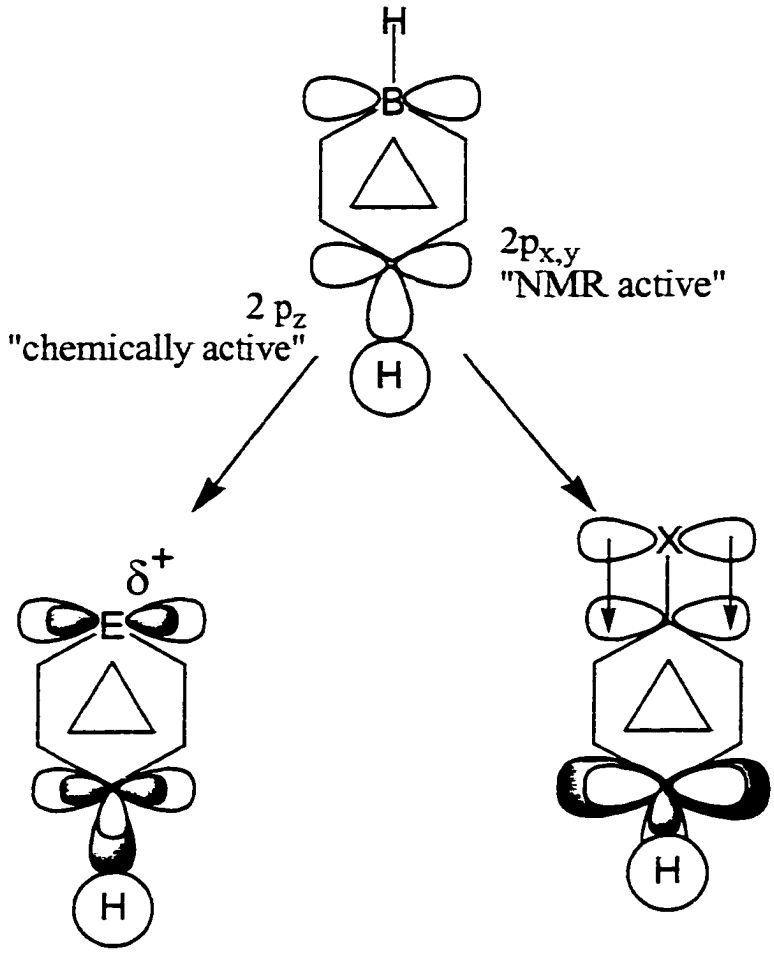

Figure I.3.1. Mechanism for the antipodal effect, according to Heřmánek, evoked by an electron attracting heteroatom (left) and an electron donating (*M*+) *exo*-substituent such as fluorine (right). The white orbitals represent the original size (or amount of electron density) and the gray orbitals represent the size of the orbitals after addition of the heteroatom to the cluster.

cage heteroatom, E, increases (i.e., as the heteroatom becomes more "positive") its $2p_x+2p_y$ orbitals become smaller. This decrease in electron density causes a corresponding decrease in the electron density in the antipodal boron atom $2p_x+2p_y$ orbitals and thus a downfield $\delta(^{11}B)$ shift. Note that this is a π effect not an inductive effect through the σ orbitals. If the cluster is substituted with a π donating substituent, such as a fluorine atom, electron density in the $2p_x+2p_y$ orbitals on the substituted boron atom increases. This in turn causes an increase in the amount of electron density in the antipodal boron $2p_x+2p_y$ orbitals on the boron atom antipodal to the B–X vertex. Based on the electron density/$\delta(^{11}B)$ correlation discussed above, the electron density in the $2p_x+2p_y$ orbitals is linked to the electron density in the $2p_z$ orbital: the amount of electron density in the $2p_z$ orbital of the boron atom antipodal to a heteroatom, E, decreases as the electron density in the $2p_x+2p_y$ orbitals increases; conversely, the amount of electron density in the $2p_z$ orbital of the boron atom antipodal to a B–X bond decreases as the electron density in the $2p_x+2p_y$ orbitals increases.

The γ Effect

The effect of a heteroatom on the cage boron atoms two vertices away (i.e., γ or *meta* effect) is small. Inductive effects through the σ bonds of the cluster drop off rapidly with increasing distance from the heteroatom and are not expected to influence the *meta* vertices significantly; therefore, any changes in the vertices γ to E or to a B–X bond will provide an idea of the overall effect of π donation on the total electron density of the cluster. As an example, the fluorination of $B_{12}H_{12}^{2-}$ to form 1-$B_{12}H_{11}F^{2-}$ causes the δ value of the γ vertices to become more negative by 3.0 ppm, indicating an increase in electron density around these boron atoms. The *meta* effect of a CH^- vertex on the cluster atoms causes the γ resonance for B(7)–B(11) to a more

positive δ value relative to the boron signals in $B_{12}H_{12}^{2-}$. This indicates that the *meta* boron atoms become more deshielded upon introduction of a heteroatom into the cluster that is more positive than BH^{2-}.

The β Effect

Substitution of a boron vertex in a cluster with a heteroatom that has more electron density than a BH^{2-} vertex causes the δ values of the neighboring atoms to become more negative, while for heteroatoms that are more positive the opposite is true. This is caused by an inductive effect (Figure I.3.2). For example, the $\delta(^{11}B)$ value for the boron atoms in $B_{12}H_{12}^{2-}$ is –15.3. When a BH^{2-} vertex is replaced with an Al–Me^{2-} vertex, the chemical shift of the neighboring boron atoms is shifted to more negative δ values by 3.5 ppm. For the CH^- vertex, the *ortho* boron atom signals remain mostly unchanged ($\delta(^{11}B) = -15.4$). If the vertex is replaced with a vertex with a more positive vertex (such as As^-, Sb^-, or Bi^-) the neighboring boron atoms shift to more positive δ values to $\delta(^{11}B) = -8.6$, –9.3, and –5.6, respectively.[95]

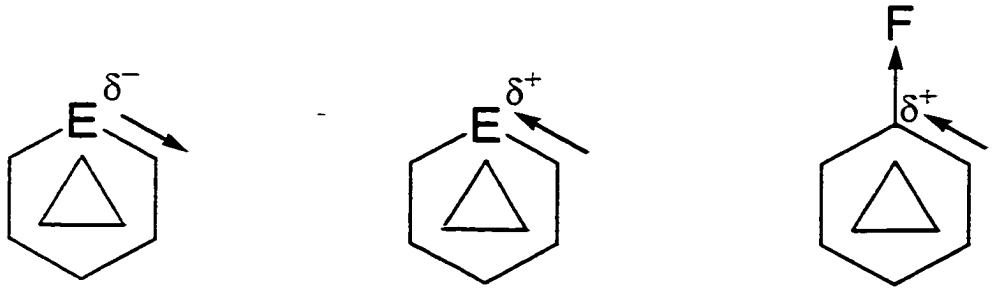

Figure I.3.2. Donating (left) or withdrawing (middle, right) inductive effects (I+) caused by a cage heteroatom, E, or an *exo*-substituent, X. The arrows represent the flow of electron density caused by the heteroatom.

A similar effect is seen for heteroatoms *exo* to the cluster (Figure I.3.2). The effect of an *M*+ substituent, such as F^-, causes donation of π-electron density to the vertex to which it is attached (α vertex), but unlike the effect of *M*+ in aromatic organic compounds this effect is not transmitted to β vertices, rather, the amount of electron density on the β vertex is dominant by inductive effects through σ bonds. For the series of 1-X-$B_{12}H_{11}^{2-}$ anions, the ordering of the X substituent based on the magnitude of the effect each has on the β boron atom is F (–1.4) < OH (–1.2) < H (0.0) < Cl (0.5) < Br (1.0) < I < (1.6) < SH (2.1), where the change in $\delta(^{11}B)$ relative to $B_{12}H_{12}^{2-}$ is in parenthesis.[95] Note however that this effect is, in general, much smaller than that seen with heteroatoms incorporated into the cage. Notice that it would be expected that an F^- substituent would decrease the amount of electron density on the neighboring vertex relative to the parent cluster due to its high electronegativity, but instead the chemical shift decreases. These results are consistent with (1) a decrease in electron density at the boron atom caused by removal of σ electron density by the β fluorine atom and (2) an increase in electron density at the β boron atom caused by the π donation of the fluorine atom to the entire cluster (–3.0 ppm for $B_{12}H_{11}F^{2-}$). Therefore, if the two effects are deconvoluted, the inductive effect causes the δ value of the boron atom β to a fluorine atom to increase by 1.6 ppm.

Results and Discussion

There are two competing effects at work in the $CB_{11}H_{12-n}F_n^-$ anions which determine the order of fluorination: (1) the directing effect of the skeletal heteroatom, carbon, and (2) the directing effect of any *exo*-fluorine atom(s). These two effects work in opposite directions, as described above. For the first time, a complete set of compounds now exists that incorporates both of these effects into one

system. In the $CB_{11}H_{12-n}F_n^-$ anions, the cluster has a carbon heteroatom within the framework and fluorine atoms *exo* to the cluster. The series of anions with n = 0–6 allows for the examination of these competing effects and of how they work to determine, in a systematic way, the ordering of the signals in the ^{11}B, ^{13}C, ^{1}H, and ^{19}F NMR spectra, as well as how these effects serve to direct the position of the $(n + 1)^{th}$ fluorine atom.

^{11}B NMR Spectra

The ^{11}B NMR chemical shifts for $CB_{11}H_{12-n}F_n^-$ (n = 0–6) are represented in Figure I.3.3 as stick figures. It is immediately clear that there are three separate regions in the spectra: (1) fluorinated boron signals; (2) lower belt boron signals; and (3) upper belt boron signals. Chemical shifts for fluorinated boron atoms occur at the most positive δ values. The lower belt boron atoms are *meta* to the C–H bond and have the most positive (e.g., least negative) δ values of the unfluorinated boron atom signals. These resonances form the second "cluster" of signals. The upper belt boron atoms are next to the carbon atom and have the most negative δ values of the three groups.

Fluorination of the boron vertex antipodal to the carbon atom shifts $\delta(^{11}B)$ for this boron atom to a more positive value with respect to $CB_{11}H_{12}^-$, while the resonances of the boron atoms in the two belts are shifted to more negative δ values. With each additional fluorination (i.e, as n increases), the average $\delta(^{11}B)_{BF}$ value becomes less positive, as do all of the non-fluorinated ^{11}B signals. Other trends can be seen for the individual signals within the major groupings. In 7,12-F_2^-, there are two fluorine atoms capable of directing the chemical shifts of the B–H boron atoms. The C_{5v} degeneracy of the F_0^- and 12-F_1^- anions is broken, leaving an anion of C_s symmetry

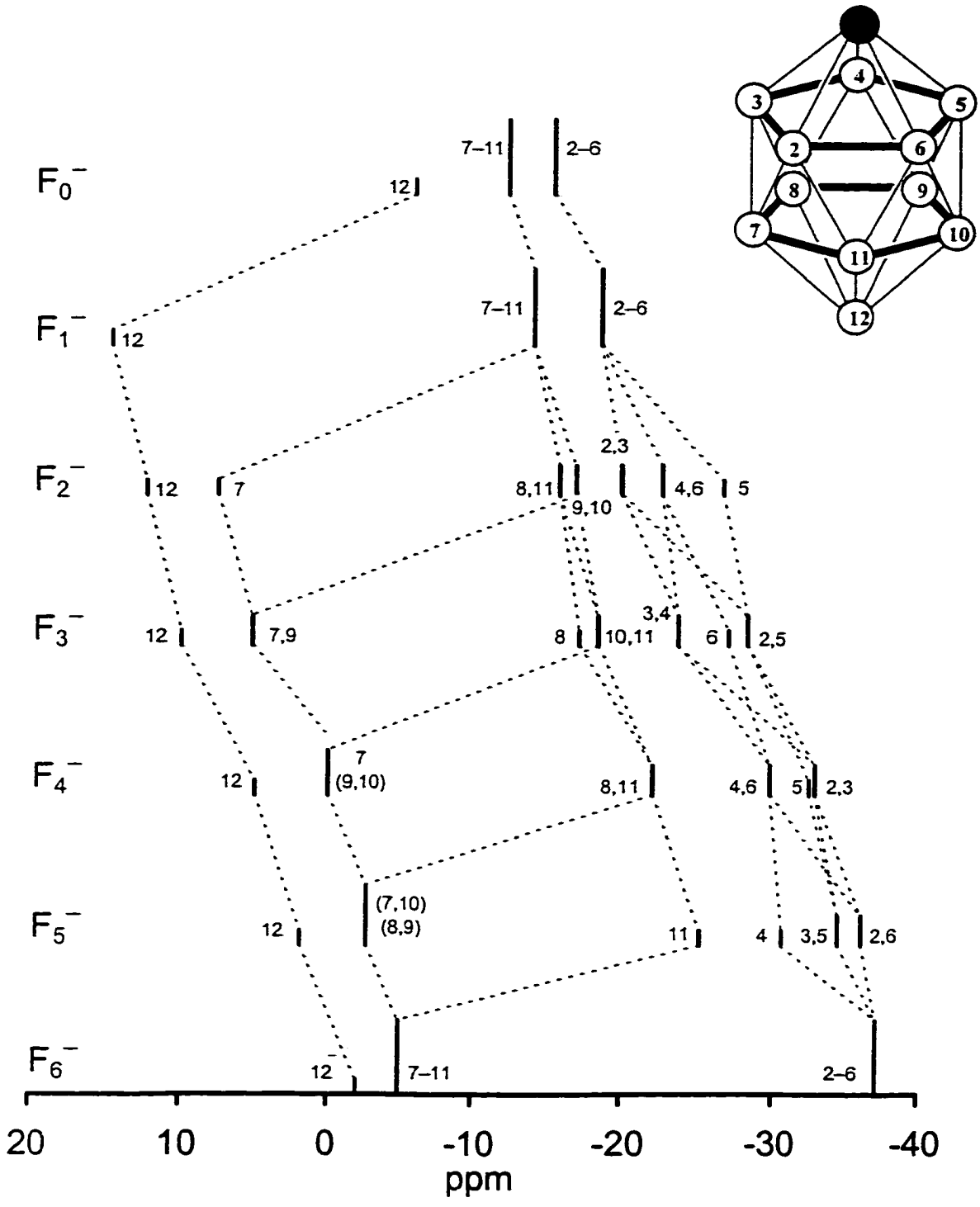

Figure I.3.3. Stick figure representation of the $^{11}B\{^1H\}$ NMR spectra for the $CB_{11}H_{12-n}F_n^-$ anions (n = 0–6; Cs^+ salts; acetone-d_6). The carborane numbering scheme is shown in the upper right corner (black circle represents carbon, position 1).

(the C_s symmetry persists for $n = 3–5$). As a result, there are only singly and double degenerate boron signals. This complicates the spectra significantly. Using 2-D $^{11}B–^{11}B$ COSY NMR spectroscopy, all of the ^{11}B resonances for each of the anions in this study were assigned (see Part I, Chapter 2 and Appendix I.B for individual 2-D spectra). These assignments revealed an elegant logic to the ordering of the ^{11}B resonance patterns. The two groupings of B–H signals in 12-F_1^- are split by the fluorine atom bonded to B(7). Within either group, the δ values for the *ortho* B–H signals (B(8,11) for the lower belt and B(2,3) for the upper belt) are more positive than those of any other signal within the group. The boron atom antipodal to B(7) (i.e., B(5)) resonates the most negative δ value of any signal. As the number of B–F bonds increases these trends persist (with respect to B–F bonds): $\delta(^{11}B)_{ortho} > \delta(^{11}B)_{meta} > \delta(^{11}B)_{para}$. In the cases where a vertex is both antipodal to and *ortho* to a B–F bond, the effects are additive and the signal resonates at a more positive δ value than the vertex/vertices that are only antipodal (*para*) to a B–F vertex. In addition, there is a relationship between the resonances in different groupings: the more positive the δ value of a resonance in one group is, the more negative the resonance of the antipodal boron atom is. For example, in 7,9,12-F_3^-, the δ values of the lower belt boron atoms are 5.2 ppm for B(7,9) > –17.2 ppm for B(8) > –18.4 ppm for B(10,11); the ordering of the δ values of the antipodal boron atoms (upper belt) are reversed: –23.7 ppm for B(3,4) {10,11}> –27.0 ppm for B(6)_{8} > –28.2 ppm for B(2,5) {7,9} (antipodal atoms are listed in {} brackets).

These trends also hold for the two series of isomers: the monofluoro series 2-, 7-, and 12-F_1^- and the difluoro series 2,12- and 7,12-F_2^- (Figure I.3.4). For example, the upper belt B–H boron signals are at more negative δ values than the lower belt signals, and the boron signal antipodal to the B–F bond resonates at the negative δ value. In all cases, fluorination of a B–H bond causes the remaining B–H signals to shift to lower frequencies; this is consistent with the data presented above. The ordering of the

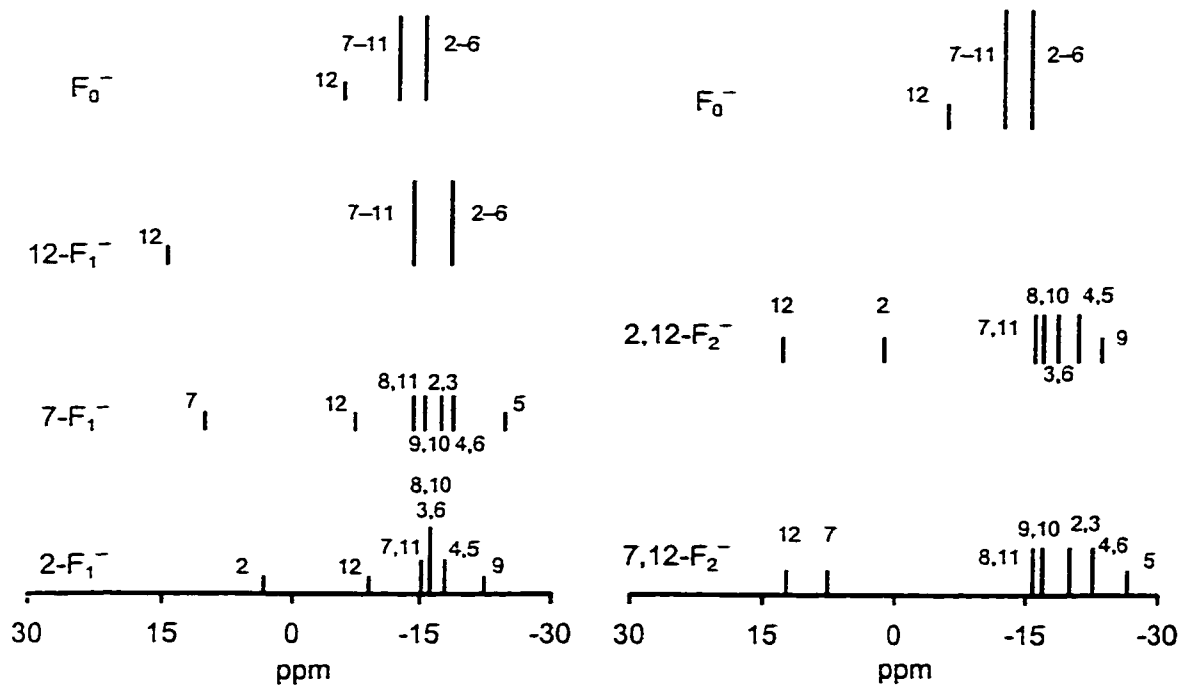

Figure I.3.4. Stick figure representations of the $^{11}B\{^1H\}$ NMR spectra (Cs^+ salts; acetone-d_6) for the three x-$CB_{11}H_{11}F^-$ isomers (left) and for the two $x,12$-$CB_{11}H_{10}F_2^-$ isomers (right).

unfluorinated boron signals in the 2-F_1^- and 2,12-F_2^- are the same as are those in the set 7-F_1^- and 7,12-F_2^-. This demonstrates that once the general trends for a group of compounds are known, this information can then be utilized to assign peaks in related compounds.

Examination of one of the ^{11}B boron signals, the one for the boron atom antipodal to the carbon atom (B(12)), can provide insight into the α-, β-, and γ-effects of an *exo*-fluorine substituent on a cage atom (Figure I.3.5). There are three separate regions in the graph of $\delta(^{11}B)$ for B(12) versus *n*. The first region occurs between F_0^- and F_1^-. In this region, the chemical shift of the boron atom *increases* dramatically as the B–H bond is converted into a B–F bond (i.e., 12-F_1^-). There is an expected *increase* in the electron density in the $2p_x+2p_y$ orbitals of B(12) from the donation of fluorine π electron density; at the same time, the fluorine atom is much more electronegative than the boron atom, causing a polarization of the B–F bond toward the fluorine atom. This effect is expected to deshield the boron nucleus. In addition, the asymmetry of the bonding electrons around the ^{11}B nucleus should increase; this increases the paramagnetic shielding, P_u, and shifts the boron signal to more positive δ values. This effect appears to dominate the chemical shift of B(12).

If either the 2-position (*meta* to B(12)) or the 7-position (*ortho* to B(12)) is fluorinated first instead of B(12), the chemical shift of B(12) becomes more negative. A fluorine atom *meta* to B(12) causes $\delta(^{11}B)_{B(12)}$ to become more negative than a fluorine atom *ortho* to B(12), by 1 ppm. This shifting of the δ value to more negative values suggests an increase in the $2p_x+2p_y$ electron density on B(12) relative to $CB_{11}H_{12}^-$. For the 2-F_1^- isomer, the chemical shift of B(12) is 2.3 ppm more negative than in the unfluorinated cluster; this shift in δ value is nearly identical to the shift caused by a single fluorine atom on the resonance of a boron atom *meta* to the B–F bond in 1-$B_{11}H_{11}F^-$. These results suggest that the π electron density donated by a fluorine atom to the cluster causes the chemical shift for all of

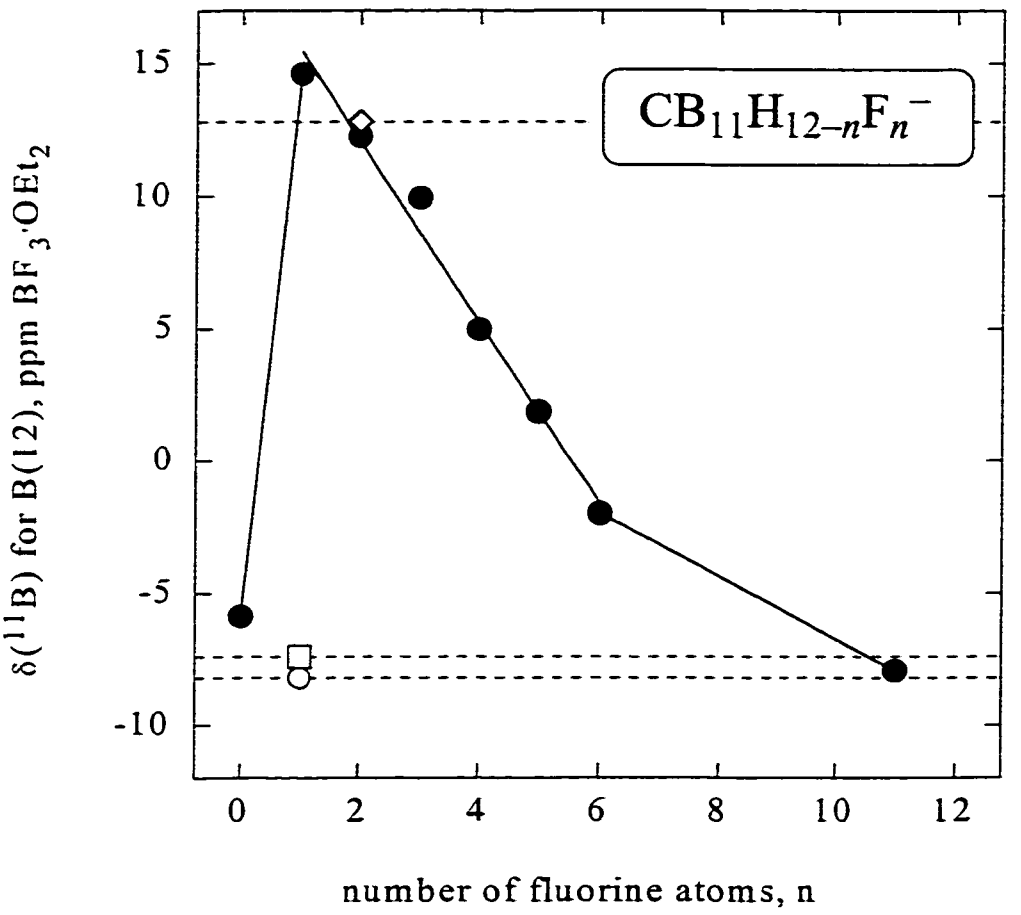

Figure I.3.5. Plot of $\delta(^{11}B)$ for B(12) versus the degree of fluorine substitution, *n*, in acetone-d_6. Data were collected using Cs^+ salts (7-F_1^- was the n-Bu_4N^+ salt). The solid circles represent the normal isomers of $CB_{11}H_{12-n}F_n^-$ (i.e., 12-F_1^-, 7,12-F_2^-, 7,9,12-F_3^-, etc.) The open circle represents 2-F_1^-; the open square represents 7-F_1^-; the open diamond represents 2,12-F_2^-. The solid and dotted lines are for visual reference.

the cage atoms in the cluster (boron *and* carbon) to become more negative by approximately 2–3 ppm. The *ortho* fluorine atom in 7-F_1^- shifts the B(12) resonance to more negative δ values than the *meta* fluorine atom of 2-F_1^- does. For 7-F_1^- the B(12) resonance should be shifted to more negative δ values by 2.3 ppm because of the fluorine atom π donation to the cage. The small chemical shift difference from the 2-F_1^- isomer can be explained by consideration of the inductive effect caused by the neighboring fluorine atom. The B(12) vertex will experience a removal of electron density through the σ bonding network which will, in turn, cause a removal of $2p_x$+$2p_y$ electron density from B(12) and cause an increase in the chemical shift value (by +0.8 ppm in this case). The π donation effect is the dominant effect and therefore the $\delta(^{11}B)_{B(12)}$ for 7-F_1^- is more negative than in $CB_{11}H_{12}^-$.

The next five B–H bond substitutions occur at the 7–11 positions—positions *ortho* to the B(12) boron vertex; this forms the second region of the graph. The chemical shift of B(12) becomes more negative when the first *ortho* B–H bond is substituted. The rational for this is the same for 7-F_1^-. The addition of a second fluorine atom in the 2-position instead of in the 7-position to form 2,12-$CB_{11}H_{10}F_2^-$ causes the δ value of B(12) to become more positive than in $CB_{11}H_{12}^-$ and is 0.5 ppm more positive than B(12) in 7,12-F_2^-. Increased anisotropy (P_u) effects in the 7,12-isomer most likely account for the reversal in chemical shift ordering compared to the monofluorinated derivatives: the *ortho* fluorine atom would be expected to induce a greater asymmetry change in the bonding electrons of B(12) than the B–F bond in 2-F_1^- that is two vertices removed. The decrease in chemical shift caused by the addition of one B–F bond *ortho* to B(12) continues in a linear fashion with each additional *ortho* B–F vertex (until n =6; 5 *ortho* vertices).

The final trend present in the graph occurs from n = 6–11 (upper belt substitution). Although only two points are present in this region, a general trend can be extrapolated. The upper belt fluorine atoms (*meta* fluorine atoms) continue to shield

B(12) by donating π electron density but to a much lesser degree than the *ortho* fluorine atoms. This trend is consistent with that seen in 2-F_1^- and 2,12-F_2^-, the other isomers with fluorine atoms *meta* to B(12). However, the shielding effect of one fluorine atom *meta* to B(12) (2-F_1^-) is slightly greater than in F_{11}^-, where there are six fluorine atoms *meta* to B(12). It can be concluded that the decrease in the slope arises from the competition of effects caused by the upper and lower belt fluorine atoms. The *meta* fluorine atoms donate electron density to the cluster and shield B(12) while the inductive effect of six *ortho* fluorine atoms deshields B(12).

^{13}C NMR Spectra

The ^{13}C NMR data for $CB_{11}H_{12-n}F_n^-$ (n = 0–6) are represented graphically in Figure I.3.6. Like the ^{11}B NMR chemical shift data, the ^{13}C NMR data allows for the examination of the effects of *exo*-fluorine substituents on a cage heteroatom vertex. As with the B(12) ^{11}B NMR spectra, there are three distinct regions in the ^{13}C chemical shift graph. Boron nuclei antipodal to a B–F bond are shielded (Figure I.3.3) relative to the other boron vertices. The carbon nucleus in 12-F_1^- is also shielded compared with the carbon vertex in $CB_{11}H_{12}^-$. This demonstrates that the effects described above for boron vertices are generic to all vertices (carbon and boron). The effects of a B–F vertex *meta* to the carbon atom are the same as for the boron vertices: as the number of *meta* B–F bonds increases, the amount of electron density provided to the cage increase, shifting $\delta(^{13}C)$ to more negative δ values (the carbon atom becomes more shielded).

The *ortho* effect on the carbon vertex is different than for the boron vertices; the carbon atom in 1-H-$CB_{11}F_{11}^-$ is deshielded relative to $CB_{11}H_6F_6^-$ (i.e., it has a more positive chemical shift). A number of possible explanations exist for this difference. Donation of π electron density to the cluster would be expected to continue to shield the carbon atom, thus decreasing $\delta(^{13}C)$, while the inductive effect of the *ortho*

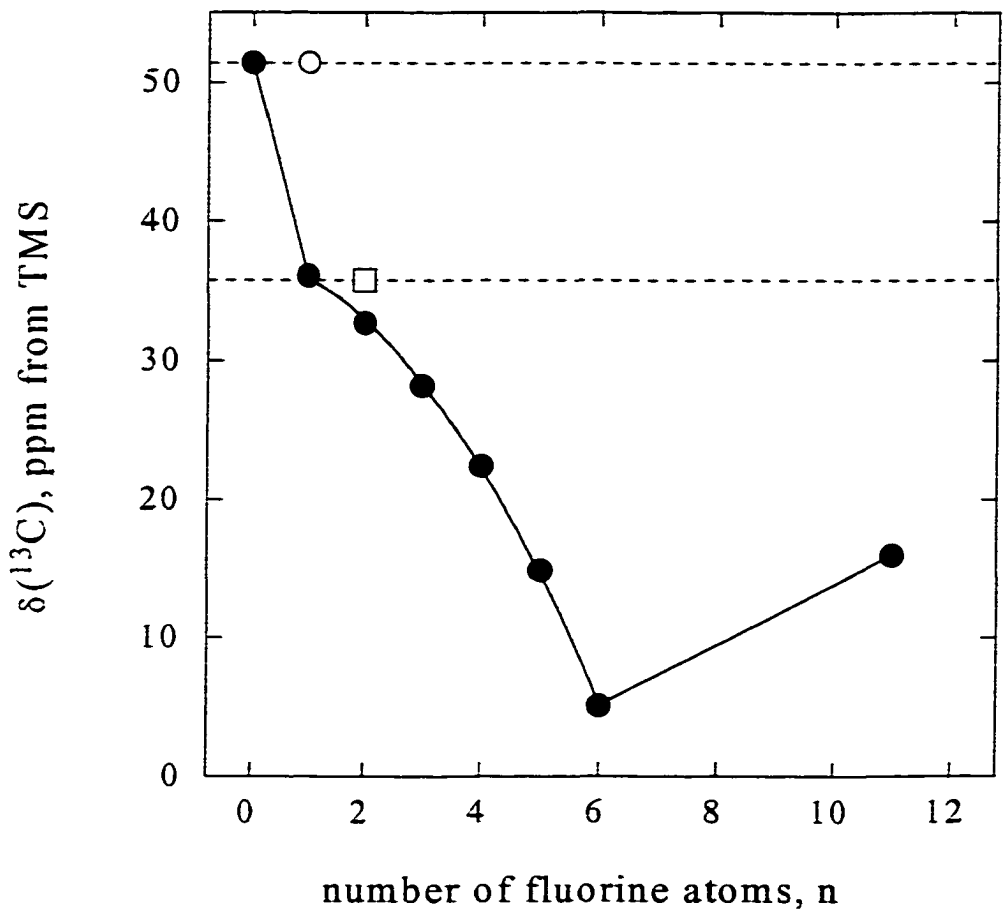

Figure I.3.6. Plot of $\delta(^{13}C)$ versus the degree of fluorine substitution, n (Cs^+ salts, acetone-d_6). The solid circles represent the normal isomers of $CB_{11}H_{12-n}F_n^-$ (i.e., 12-F_1^-, 7,12-F_2^-, 7,9,12-F_3^-, etc.) The open circle represents 2-F_1^-; the open square represents 2.12-F_2^-. The solid and dotted lines are for visual reference.

fluorine atoms should remove σ electron density and deshield the carbon, thus increasing $\delta(^{13}C)$. Inductive effects seem to dominate the chemical shift of the carbon atom. The C–H bond is polarized toward the carbon atom (since carbon is more electronegative than hydrogen), so the carbon vertex is more negative than a boron vertex (Figure I.3.7). This would create a larger asymmetry in the electron density around the carbon vertex than in the electron density around a boron vertex; the paramagnetic factor will play a more dominant role in determining the chemical shift of the carbon atom. This effect would be exaggerated in a donor solvent like acetone where the C–H bond would be further polarized toward the carbon atom because of coordination of the basic oxygen to the proton. The same effect is seen in the 2-F_1^- isomer and the 2,12-F_2^- isomers; the carbon atom in both of these isomers is deshielded relative to the lower-belt analogues 12-F_1^- and 7,12-F_2^-.

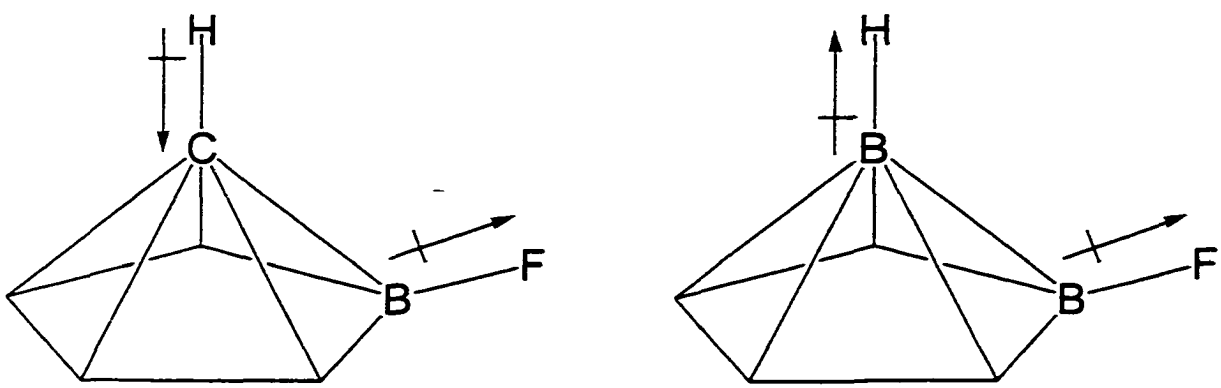

Figure I.3.7. The difference in polarization effects for a B–F bond *ortho* to a carbon vertex (left) and a boron vertex (right). For clarity only a portion of the cluster is shown.

^{1}H NMR Spectra

The ^{1}H NMR chemical shifts for Cs^+ salts of the $CB_{11}H_{12-n}F_n^-$ (n = 0–6) anions are represented as stick figures in Figure I.3.8. Unlike the ^{11}B NMR spectra, there is not an immediately obvious trend in the signals; the correlation of ^{1}H NMR spectra with substitution patterns of the fluorocarborane anions appears to be more complex. A number of features are worth noting for the B–H hydrogen atom signals. First, the position of the (B)H signal that is next to be fluorinated, fluctuates with number of fluorine atoms, n; $\delta(^1H)$ increases from n = 1–4 and decreases from n = 4–6. The presence of a fluorine atom *ortho* to a B–H bond shifts the signal to more positive δ value (i.e., deshields the hydrogen atom). This effect is additive; the more B–F bonds a (B)H atom is next to, the more positive the $\delta(^1H)$ value of the hydrogen atom. For example, in 7,8,9,10,12-F_5^-, the H(3,5) resonance (these hydrogen atoms are *ortho* to all four of the lower belt B–F bonds) is +0.34 ppm more positive than the H(2,6) resonance (these hydrogen atoms are *ortho* to only two of the four B–F bonds). There is also a correlation between the B–F bonds and the hydrogen atoms antipodal to these bonds: the hydrogen atoms antipodal to a B–F bond(s) have the most negative chemical shift values. The one exception to this observation occurs in the ^{1}H NMR spectrum of 7,9,12-F_3^-. In this cluster, the δ value for the H(6) atom is more negative than the δ value for the H(2,5) atoms; note that the H(2,5) atoms are antipodal to the B(7,9)–F(7,9) bonds. While H(6) is not antipodal to a B–F bond, it is antipodal to the B(8)–H(8) vertex which is *ortho* to the two B–F bonds. It appears that the effect of the two B–F bonds causes the electron density at the B(8) vertex to be like that around a single B(F) vertex.

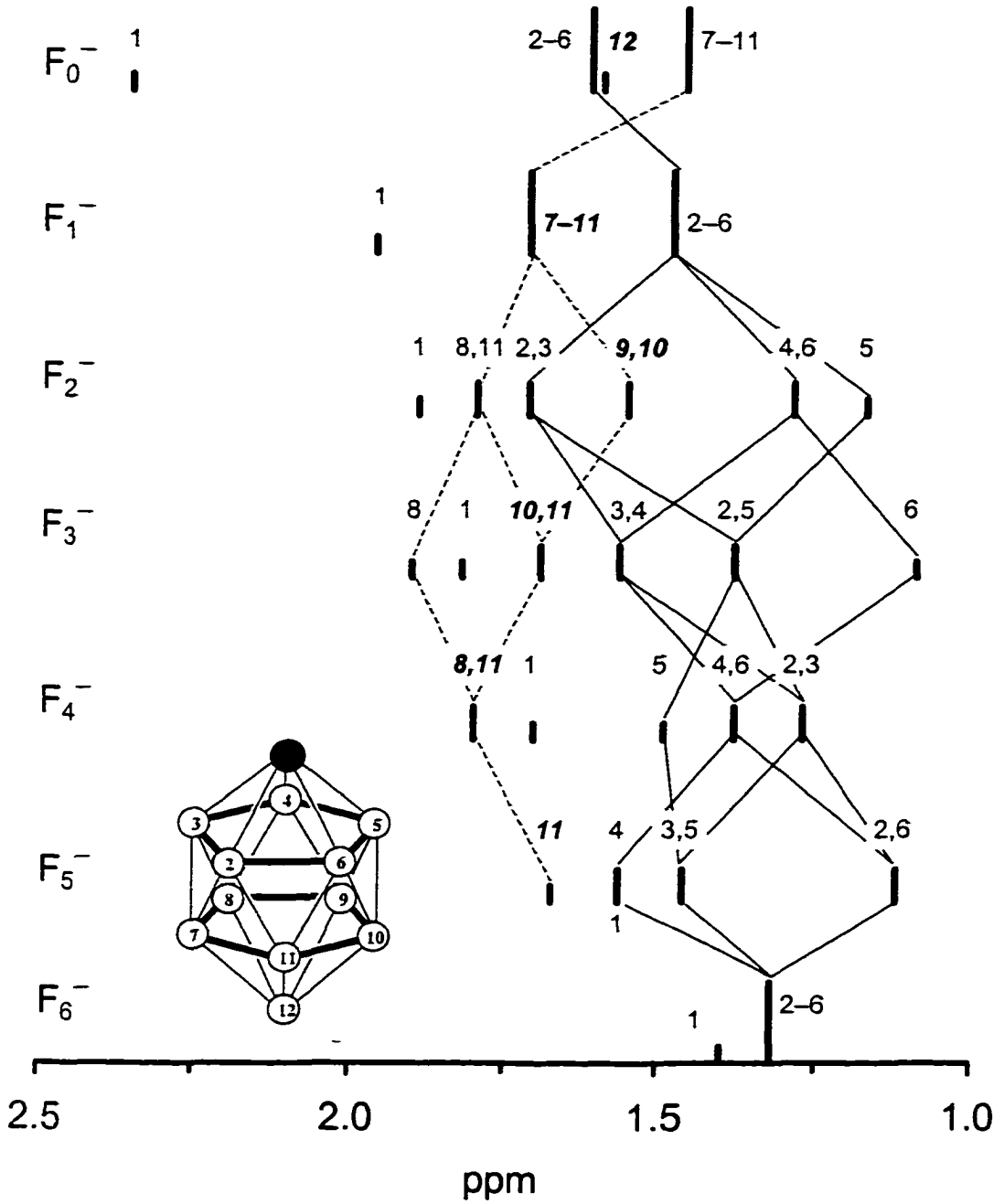

Figure I.3.8. Stick figure representation of the $^{1}H\{^{11}B\}$ NMR spectra for the $CB_{11}H_{12-n}F_n^-$ anions (n = 0–6; Cs^+ salts; acetone-d_6). The bold italicized numbers indicate the hydrogen atoms that are next to be substituted. The carborane numbering scheme is located in the bottom left corner (the black circle represents carbon, position 1).

The final observation centers around the ^1H resonance of the hydrogen atom attached to the carbon atom. The δ value of C–H hydrogen atom resonance is the most positive resonance in the ^1H NMR spectrum of $CB_{11}H_{12}^-$. Initial fluorination of the cluster causes the $\delta(^1H)$ for H(1) to become more negative (i.e., more shielded). This trend is shown graphically in Figure I.3.9. Again there are three distinct regions: F_0^- to F_1^-; F_1^- through F_6^-; upper belt substitution. In the first region, the $\delta(^1H)$ of the C–H proton becomes significantly more negative (i.e., more shielded) as the B–H bond antipodal to it is fluorinated. This is consistent with the effect of a fluorine atom on the antipodal cage atom—the electron density in the p_z orbital of the antipodal atom, in this case carbon, decreases, causing the proton to become more hydridic. Note that this trend is also seen for the (B)H resonances; the δ value of the hydrogen atom attached to B(5) (the vertex antipodal to the B(7)–F(7) bond) is the most negative of the ^1H resonances. The next five fluorine substitutions occurs at the 7–11 positions—position *meta* to the carbon atom; this provides insight into the effect of an *exo*-fluorine atom on a *meta exo*-hydrogen atom. With each *meta*-fluorine atom, the chemical shift of H(1) becomes more negative. This effect is additive, decreasing the δ value of H(1) by a roughly equal amount with each additional *meta*-fluorine atom. So, a fluorine atom *meta* to the C–H bond causes the (C)H atom to become more shielded (i.e., more negative δ value), but to a lesser degree than an antipodal fluorine atom does.

Additional data is also available for F_8^-, F_{10}^- and F_{11}^-. When B–F bonds are located in positions *ortho* to the C–H bond (2, 4, and 5 fluorine atoms, respectively), the $\delta(^1H)$ trend reverses, compared to the trend for F_0^- through F_6^-, and $\delta(^1H)$ becomes more positive. This change signifies a decrease in the hydridic nature of the C–H bond; the C–H bond in 1-H-$CB_{11}F_{11}^-$ is mildly acidic with a $pK_a = 13$.[96] This effect can be isolated by examination of the 2-F_1^- isomer. Fluorination of $CB_{11}H_{12}^-$ in the 2-positon causes the $\delta(^1H)_{CH}$ value to increase by +0.4 ppm, recall

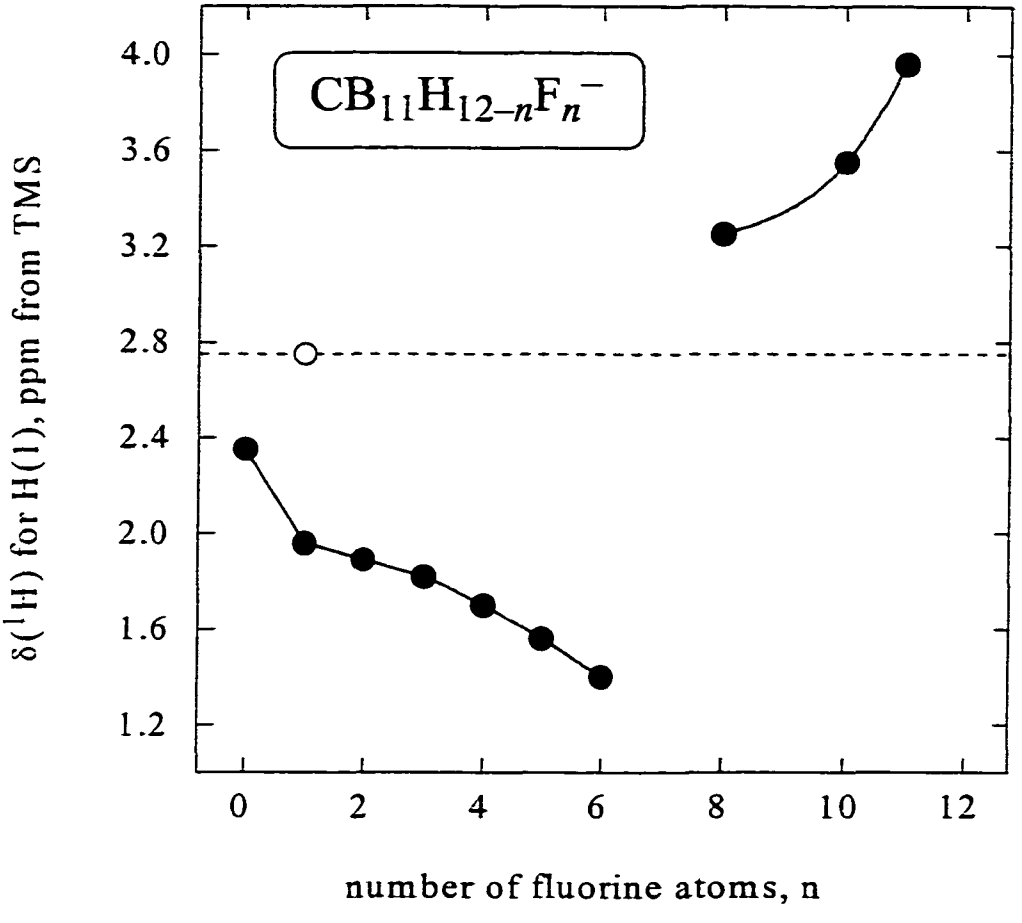

Figure I.3.9. Plot of $\delta(^1H)$ for H(1) in acetone-d_6 (Cs^+ salts) versus the degree of fluorine substitution, n. The solid circles represent the normal isomers of $CB_{11}H_{12-n}F_n^-$ (i.e., 12-F_1^-, 7,12-F_2^-, 7,9,12-F_3^-, etc.). The open circle represents 2-F_1^-. The solid and dotted lines are for visual reference.

that the 12-F_1 isomer has $\Delta\delta(^1H)_{CH} = -0.4$. These conclusions could be supported by reacting 2-$CB_{11}H_{10}F^-$ and 12-$CB_{11}H_{11}F^-$ with n-BuLi in the following reaction:

$$2\text{-}CB_{11}H_{10}F^- + 12\text{-}CB_{11}H_{11}F^- + \text{n-BuLi} \rightarrow$$
$$1\text{-Li-}2\text{-}CB_{11}H_{10}F^- + 12\text{-}CB_{11}H_{11}F^- + \text{BuH}$$

If the reaction proceeds as written, it could be concluded that the 2-F_1^- anion has a more acidic C–H bond than the 12-F_1^- anion. A similar set of reactions could be conducted using $CB_{11}H_{12}^-$/2-$CB_{11}H_{11}F^-$ and $CB_{11}H_{12}^-$/12-$CB_{11}H_{11}F^-$. In the first case, the 2-F_1^- anion should be lithiated, while in the second case; the $CB_{11}H_{12}^-$ anion should be lithiated.

In order to probe the effect of solvent on the chemical shift of the C–H proton, the ^1H NMR spectra of a sampling of compounds were recorded in dichloromethane-d_2. Dichloromethane-d_2 was chosen because of its low dielectric constant ($\varepsilon = 9.1$; acetone, $\varepsilon = 20.7$); it was also assumed that the interactions with the C–H proton would be lessened compared with acetone. A plot of $\delta(^1H)$ in CD_2Cl_2 versus the number of fluorine atoms, *n*, is shown in Figure I.3.10. The general behavior of the C–H proton is the same in CD_2Cl_2 as in acetone-d_6. The main difference between the two solvents is the magnitude of the chemical shift change; in CD_2Cl_2 the chemical shift range is 1.64 ppm (1.09–2.73 ppm), while in acetone-d_6 it is larger—2.56 ppm (1.40–3.96 ppm). Also, the $\delta(^1H)$ trend in CD_2Cl_2 seems to be linear between F_0^- and F_6^- and from F_6^- and F_{11}^-. Figure I.3.10 shows the relationship between $\delta(^1H)$ in acetone-d_6 and $\delta(^1H)$ in CD_2Cl_2. It is immediately obvious that there is not a simple correlation between the chemical shifts in the two solvents. It is however evident that if the chemical

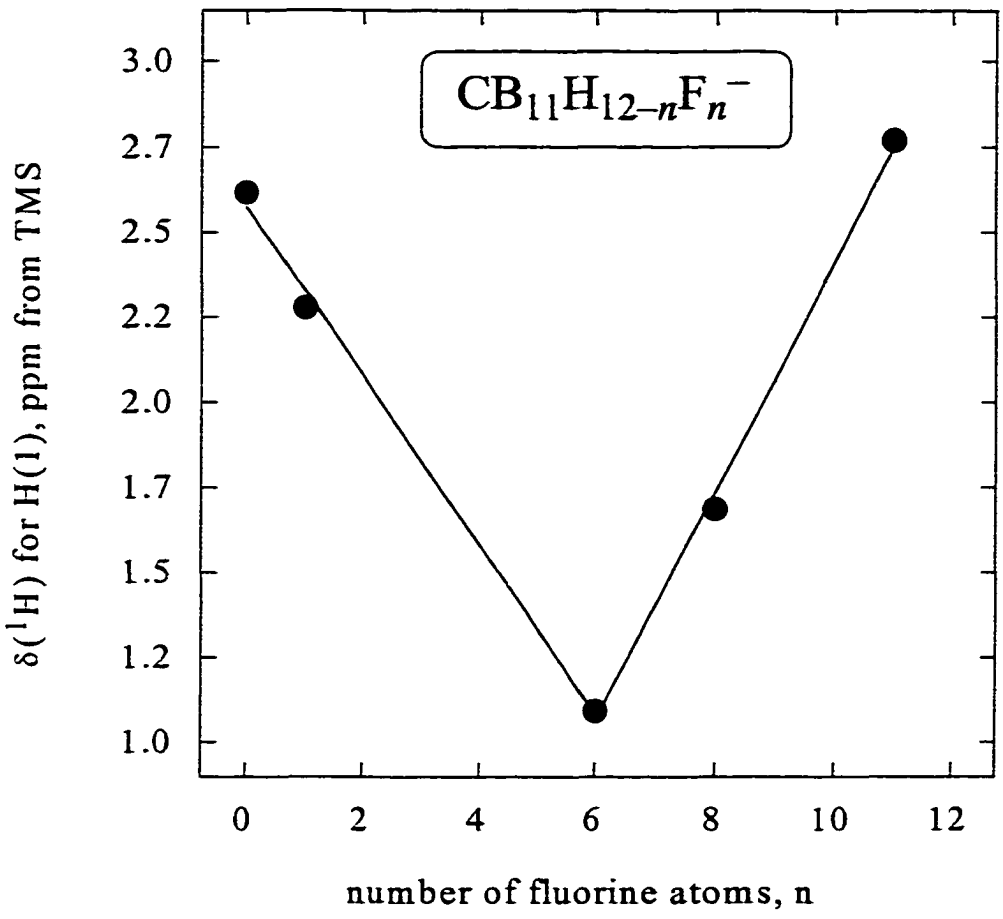

Figure I.3.10. Plot of $\delta(^1H)$ for H(1) in CD_2Cl_2 (Ph_4P^+ salts) versus the degree of fluorine substitution, *n*. The solid lines are for visual reference.

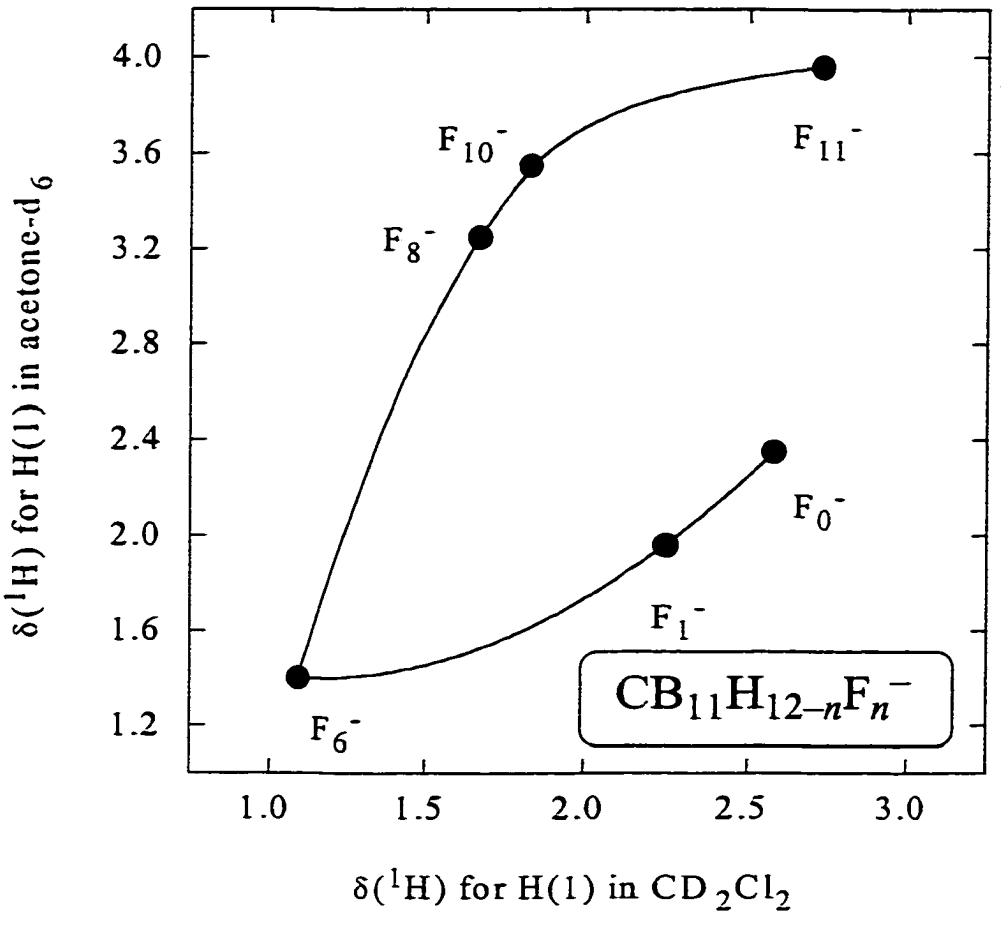

Figure I.3.11. Plot of $\delta(^1H)$ for H(1) acetone-d_6 (Cs^+ salts) versus $\delta(^1H)$ for H(1) in CD_2Cl_2 (Ph_4P^+ salts) for $CB_{11}H_{11-n}F_n^-$ anions (n = 0–11). The solid lines are for visual reference.

shift decreases in one solvent it also decreases in the other; the converse is also true. In other words, the effect of solvent on $\delta(^1H)$ can be taken as a constant value. So, it can be concluded that the ideas developed above are valid when either acetone-d_6 or CD_2Cl_2 is used as a solvent.

^{19}F NMR Spectra

A stick figure representation of the $^{19}F\{^{11}B\}$ spectra for $CB_{11}H_{11-n}F_n^-$ anions is shown in Figure I.3.12. These spectra are much simpler than either the ^{11}B of ^1H NMR spectra. Initial fluorination of the $CB_{11}H_{12}^-$ anion with LAHF occurs at the boron atom antipodal to the carbon atom. The ^{19}F chemical shifts of the 7-F_1^- and 2-F_1^- isomers occur at more negative δ values. This indicates that the closer a B–F bond is to the carbon atom, the more shielded it becomes. These trends mirror the ^{11}B chemical shifts where the boron atoms closest to the carbon atom have the most negative δ values. As the cluster continues to be fluorinated, all $\delta(^{19}F)$ values become more negative. A comparison of the chemical shift for the fluorine atom antipodal to the carbon, F(12), as a function of the total number of fluorine atoms, *n*, (Figure I.3.13) provides a picture of the effect of *ortho* and *meta* fluorine atoms on an *exo*-fluorine atom. There are two regions in this plot. The first region corresponds to the effect of *ortho* fluorine atoms on F(12). This portion of the plot is linear and suggests that each *ortho* fluorine atom contributes and equal amount of electron density to F(12). In the second region, the δ value for F(12) continues to shift to more negative values. At first, the effect is small; the slope of the line between F_6^- and F_8^- is less negative than that between F_0^- and F_6^-. From F_9^- to F_{11}^-, the change in $\delta(^{19}F)$ is very rapid, ending at a δ value approximately 150 ppm more negative than the $\delta(^{19}F)$ of F(12) in the monofluorinated derivative.

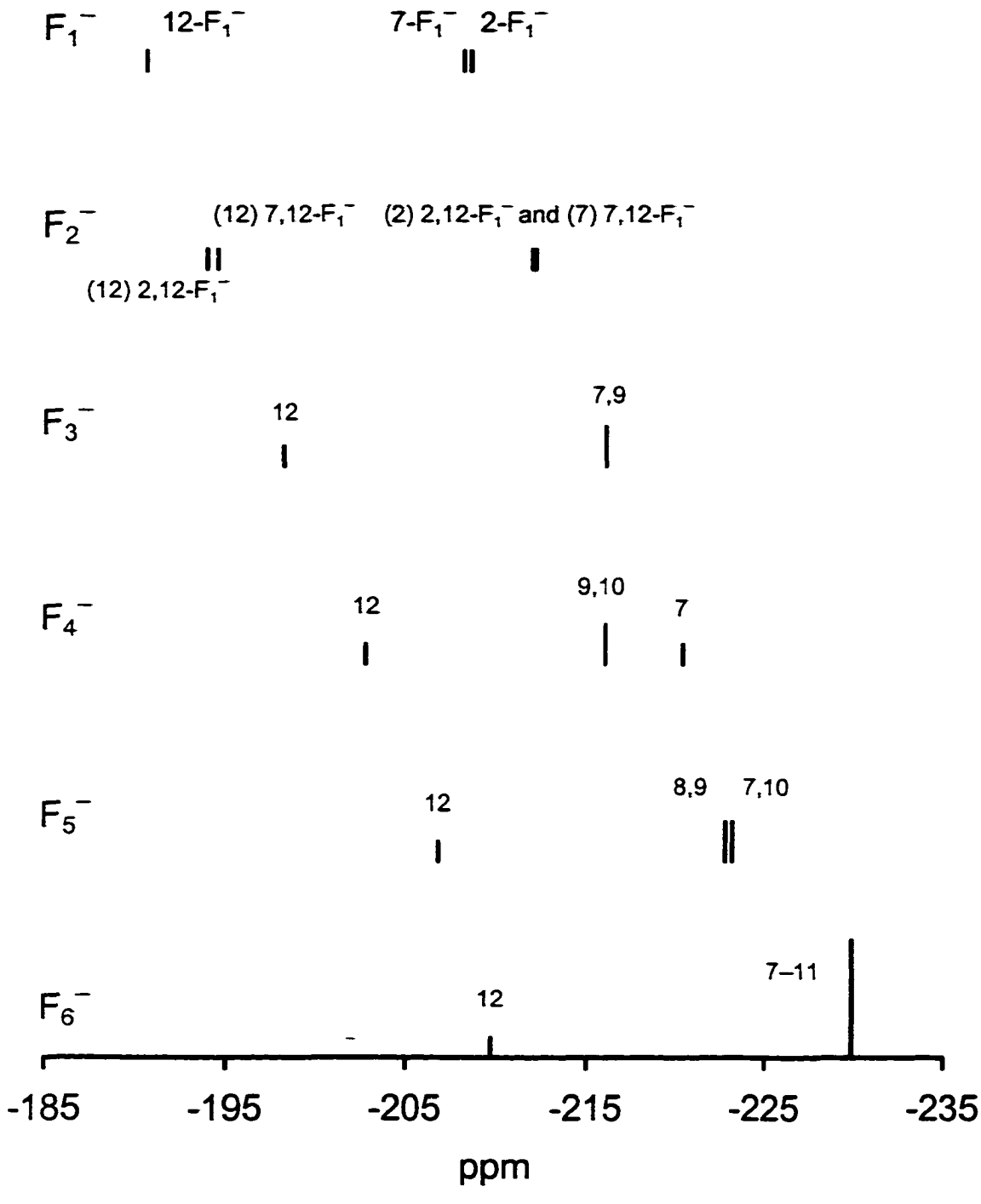

Figure I.3.12. Stick figure representation of the $^{19}F\{^{11}B\}$ NMR spectra for the $CB_{11}H_{12-n}F_n^-$ anions (n = 0–6; Cs+ salts; acetone-d_6).

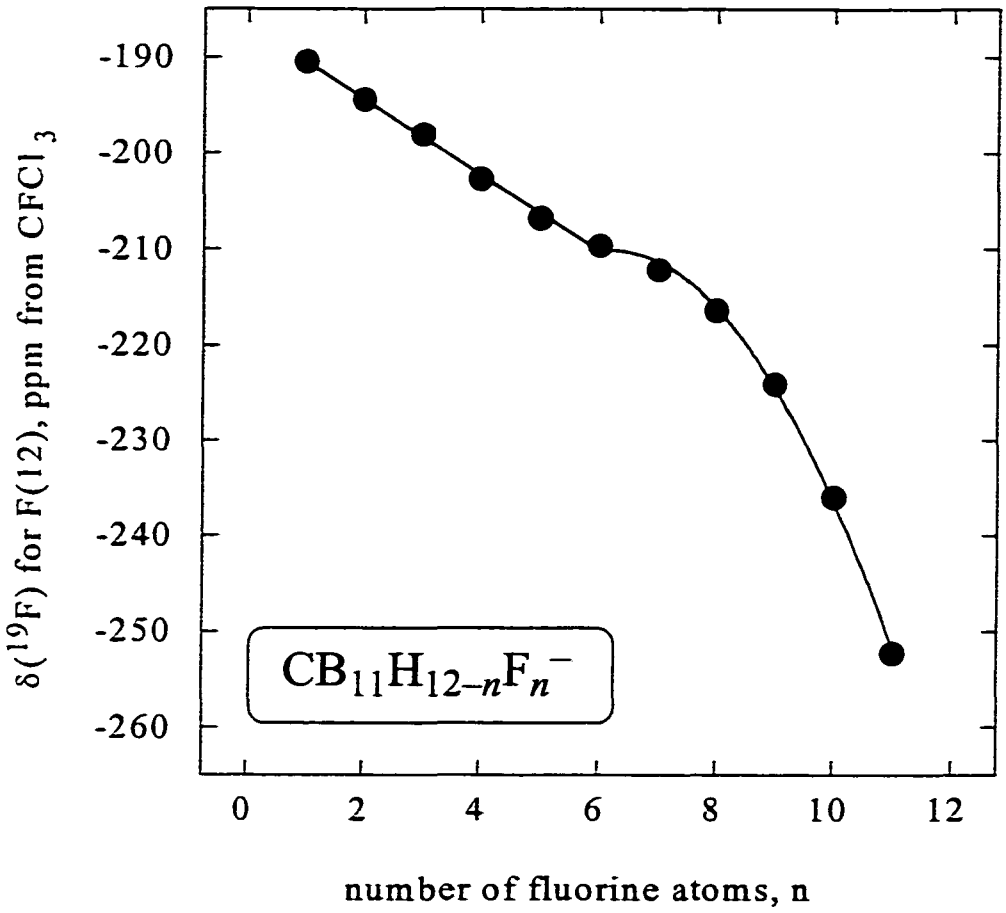

Figure I.3.13. Plot of $\delta(^{19}F)$ for F(12) in acetone-d_6 (Cs^+ salts) versus the degree of fluorine substitution, n. The solid circles represent the normal isomers of $CB_{11}H_{12-n}F_n^-$ (i.e., 12-F_1^-, 7,12-F_2^-, 7,9,12-F_3^-, etc.).

Correlation of NMR Shifts with Fluorination Order

As mentioned in Part I, Chapter 2, the $CB_{11}H_{12}^-$ cluster was sequentially fluorinated under electrophilic conditions (i.e., in LAHF). Based on the mechanism proposed by Heřmánek et al., this reaction occurs first by protonation of the B–H bond and second by attack of the boron vertex by a nucleophile (F^- in this case).[94,95] In reality, the reaction is most likely a concerted reaction in which the electrophilic hydrogen end of an HF molecule (or H_2F^+ cation) is attacked by the B–H bond. This is followed by nucleophilic attack by the fluoride end of the molecule on the boron atom. This idea is illustrated in Figure I.3.14. The NMR trends discussed above will be used to rationalize the substitution order for the reaction of $CB_{11}H_{12}^-$ with LAHF based on this mechanism.

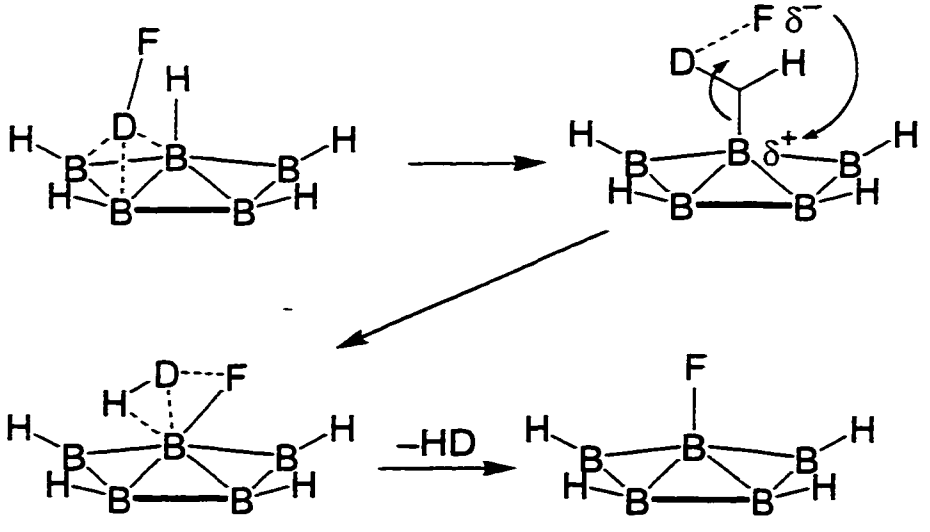

Figure I.3.14. Possible mechanism for the fluorination of $CB_{11}H_{12}^-$ in LAHF.

Before proceeding, a few assumptions must be clarified. First, it is assumed that the idea of NMR active orbitals developed by Heřmánek et al. is valid.[106] Once again, this idea states that as the electron density in the $2p_x+2p_y$ orbitals on a boron atom decreases, $\delta(^{11}B)$ of that boron atom becomes more positive. Correspondingly, as the $2p_x+2p_y$ electron density decreases the $2p_z$ electron density (the electron density in the B–H bond) increases but to a much lesser extent. These ideas are supported by theoretical calculations on a series of $EB_{11}H_{11}$ compounds.[106] Also, it will be assumed that as the chemical shift of a hydrogen atom becomes more negative, the atom becomes more shielded and, therefore, has more electron density surrounding it; this should be a valid assumption given that the hydrogen atom has only a 1s orbital available for bonding with a boron atom and that paramagnetic contributions to the ^1H chemical shift should be negligible. Finally, the mechanism described in Figure I.3.14 is assumed to be correct: (1) the attack of the B–H bond by H^+ occurs at a hydrogen atom or at a B–H bond; a measure of the electron density at the B–H bond or the B $2p_z$ orbital is given by the ^1H NMR chemical shift; (2) the fluoride attack occurs at the boron atom and is, therefore, influenced by the electron density in the boron $2p_x+2p_y$ orbitals.

In the $CB_{11}H_{12}^-$ anion, the boron atom farthest from the carbon vertex is fluorinated first when LAHF is used as a fluorinating agent. Based on NMR spectra, there are two explanations why fluorination should not (and does not) occur at the top belt boron atoms. First, the upper belt hydrogen atoms are the most positive. Since these hydrogen atoms have the most electron density (except for the carbon hydrogen), attack at these positions by an electrophile, like H^+, should be unfavorable. Examination of the electron density on the top belt boron atoms reveals a second reason why fluorination of the upper belt boron atoms is unfavorable. The upper belt boron atoms resonate at the most negative $\delta(^{11}B)$. These boron atoms should therefore have the highest $2p_x+2p_y$ electron density and should be disfavored for attack of a nucleophile, like F^-. For these reasons, the upper belt vertices will not be considered in the discussion below.

The second fluorination ($n = 2$) occurs at the lower belt boron atoms and not the top belt boron atoms (for the reasons described above). There are three possibilities for the third fluorination—*para* to the second B–F bond (i.e, B(5) next to the carbon atom), *ortho* to the second B–F bond, or *meta* to the second B–F bond. Experimentally, the trifluorinated derivative is exclusively 7,9,12-F_3^- isomer, i.e., the derivative with the third fluorine atom *meta* to the second B–F bond. In the absence of a directing heteroatom, as in the $B_{12}H_{12-n}F_n^{2-}$ system, the same trend is seen. The difluoro derivative is exclusively 1,7-$B_{12}H_{10}F_2^{2-}$ instead of the 1,2- or 1,12-isomer.[71] The positions *meta* to the most B–F bonds continue to be fluorinated until no other possibilities remain. This *meta* directing effect dominates the substitution chemistry of the cluster.

The *meta* directing effect caused by the B–F bonds can be explained using the electronic information provided by the ^{11}B and ^{1}H NMR spectra. The 7,12-F_2^- anion will be used as the prototypical example. Examination of the NMR spectra for the vertex antipodal (*para*) to the second B–F bond, the B(5)–H(5) bond, reveals that the this boron has the most negative $\delta(^{11}B)$ value and has, therefore, the most electron density of any boron atom in the cluster. The ^{1}H resonance for H(5) also has the most negative $\delta(^{11}B)$ value and, likewise, has the most electron density. The upper belt vertices meta to B(7)–H(7) have the problems described above. The lower belt B–H vertices *meta* to B(7)–F(7), the degenerate vertices (9,10), have $\delta(^{11}B)$ and $\delta(^{1}H)$ values that are between those of the antipodal vertex, which has a more positive δ value, and the lower belt B–H vertices *ortho* to B(7)–F(7), the degenerate vertices (8,11), have more negative δ values. These properties are tabulated in Table I.3.1.

From these observations, it is immediately obvious that the third fluorine substitution of $CB_{11}H_{12}^-$ in LAHF should occur at the vertex with boron and hydrogen electron densities between the most shielded antipodal vertex and the least shielded *ortho* vertices. The shielded hydrogen atom of the antipodal vertex B(5)–H(5) should favor

attack by a proton, but the shielded boron atom is expected to disfavor nucleophilic attack by F^-. The unfavorable fluoride attack is a problem with all of the upper belt boron atoms. The lower belt *ortho* vertices B(8,11)–H(8,11) have the opposite problem: the deshielded hydrogen atom should be the least likely to undergo electrophilic attack by H^+ but should be the most suitable for nucleophilic attack. It can be concluded that the combination of effects—a hydrogen atom (B–H bond) that is not too hydridic and a boron vertex that is not too deshielded—provides the right environment for nucleophilic substitution of $CB_{11}H_{12}^-$ (and $B_{12}H_{12}^{2-}$) by F^- under the electrophilic conditions present in LAHF. A similar analysis can explain all subsequent fluorinations of $CB_{11}H_{11-n}F_n^-$ ($n = 0$–6).

Table I.3.1. Effect of the Fluorinated Vertex B(7)–F(7) on Other Lower Belt Vertices

position relative to B(7)	^{1}H NMR signals	^{11}B NMR signals
antipodal; B(5)–H	most negative δ	most negative δ
meta; B(9,10)–H	δ(^{1}H) > δ(^{1}H) for B(5) δ(^{1}H) < δ(^{1}H) for B(8,11)	δ(^{11}B) > δ(^{11}B) for B(5) δ(^{11}B) < δ(^{11}B) for B(8,11)
ortho; B(8,11)–H	most positive δ	most positive δ B–H signal

These results are at odds with the qualitative explanation for the preferential deuteration and halogenation of the carborane cluster at the antipodal position and for the *meta* directing effect in the haloborane anions given by Heřmánek.[94,95,106] Based on the heteroatom effect on an antipodal B–H vertex described in Figure I.3.1, a rational for the substitution patterns was given. For $CB_{11}H_{12}^-$ (or any $EB_{11}H_{11}^-$ with a δ^+ E), the increase in the electron density in the antipodal boron $2p_z$ orbital was used to explain the preferential deuteration of the B(12) vertex. It was then postulated that, in the presence of a nucleophile, the protonated B–H bond dissociates to form H_2 and a vacant boron orbital. The nucleophile then attacks the vacant orbital on the boron atom. Although this mechanism provides an explanation for electrophilic attack at the most deshielded boron vertex, it is qualitative and neglects the nucleophile; it is unrealistic to think that there would be a vacant orbital on the boron atom in solution. Also, this mechanism is also based solely on ^{11}B NMR data. Inclusion of the ^1H NMR data indicates that the H(12) is not the most hydridic hydrogen atom in $CB_{11}H_{12}^-$ (since it is not the most shielded). The mechanism proposed for the preferential *meta* substitution in 1-$B_{11}H_{11}F^{2-}$ is the counter of that given for $EB_{11}H_{11}$ systems (E more positive than BH^{2-}): since the antipodal B–H bond is decreased in electron density relative to the unsubstituted cluster, electrophilic attack must be unfavorable at this position. Although this may be a reasonable qualitative explanation for electrophilic substitution, it is inconsistent with ^1H NMR data which suggest that the hydrogen atom antipodal to a B–F bond is the *most shielded* hydrogen atom and should therefore be *most likely* to undergo electrophilic attack. In addition, the mechanism neither explains the lack of 1,2-substitution nor does it explain completely the preferential nucleophilic substitution of 1-$B_{12}H_{11}F^{2-}$ at the 7-position.

Conclusions

In this chapter, the NMR spectra of a complete series of $CB_{11}H_{12-n}F_n^-$ anions (n = 1–6) were examined in detail. The wealth of NMR spectroscopic data available for the $CB_{11}H_{11-n}F_n^-$ anions (^{11}B, ^1H, ^{13}C and ^{19}F) has allowed for a detailed understanding of the electronic distribution within these clusters that has never before been possible. These new insights have called into question the existing mechanism for nucleophilic substitution under electrophilic conditions, which is qualitatively reasonable based on the experimental results, but in light of the new, more complete data presented above, can be concluded to be incomplete. Many of the ideas described in this chapter, as well as those presented elsewhere,[94,95,106-112] are difficult, if not impossible, to confirm based on NMR data alone. Only through the combination of thorough kinetic studies and detailed theoretical examination of the electron density distributions/kinetics can these important questions begin to be answered in a convincing manner.

It is hoped that this new understanding can then be used to *aid* experimental chemists in their rationalization of the substitution pattern of a cluster under a specified set of conditions. It is even possible that the substitution patterns of new systems will be able to be predicted in the future, allowing for the tailoring of an anion to a particular application. Despite the fact that the first boron based cluster compounds to be isolated were hydrides, a very limited set of ^1H NMR data is presented in the literature. With the advent of more advanced decoupling and heteronuclear two-dimensional techniques in recent years, this type of data collection has become routine. It is expected as the value of these techniques becomes apparent, an increased number of experimentalists will utilize these techniques to probe all of the nuclei present in the system of concern. When a more complete set of data becomes available for other heteroborane and borane systems, NMR analyses, such as those presented in this dissertation, can provide a *new*

understanding of the reaction chemistry of long established systems as well as systems currently being developed.

References for Part I

1. Reed, C. A. *Acc. Chem. Res.* **1998**, *31*, 133-139.

2. Seppelt, K. *Angew. Chem., Int. Ed.* **1993**, *32*, 1025.

3. Strauss, S. H. *Chem. Rev.* **1993**, *93*, 927-42.

4. Bochmann, M. *Angew. Chem., Int. Ed.* **1992**, *31*, 1181.

5. Drews, T.; Seppelt, K. *Angew. Chem., Int. Ed.* **1997**, *36*, 273.

6. Reed, C. A.; Fackler, N. L. P.; Kim, K.-C.; Stasko, D.; Evans, D. *J. Am. Chem. Soc.* **1999**, *121*, 6314-6315.

7. Guram, A. S.; Jordan, R. F. *Comprehensive Organometallic Chemistry*; 2nd ed.; Lappert, M. F., Ed.; Pergamon: Oxford, 1995; Vol. 4.

8. Marks, T. J. *Acc. Chem. Res.* **1992**, *25*, 57.

9. Barbarich, T. J.; Handy, S. T.; Miller, S. M.; Anderson, O. P.; Grieco, P. A.; Strauss, S. H. *Organometallics* **1996**, *15*, 3776-3778.

10. Lupinetti, A. J.; Strauss, S. H. *Chemtracts–Inorg. Chem.* **1998**, *11*, 565-595.

11. DesMarteau, D. D. *Bis(perfluoroalkyl)sulfonylimides as weakly coordinating anions, abstract (INOR 050)*, 215th ACS National Meeting, Dallas, TX, March/April 1998.

12. Strauss, S. H. *Chemtracts–Inorg. Chem.* **1994**, *6*, 1.

13. Turner, H. W. European Patent Appl. 277,004 (assigned to Exxon), 1988.

14. Ichikawa, J.; Kobayashi, H.; Sonoda, T. *Yuki Gosei Kagaku Kyokaishi* **1988**, *46*, 943.

15. Hauptman, E.; Brookhart, M.; Fagan, P. J.; Calabrese, J. C. *Organometallics* **1994**, *13*, 774.

16. Tjaden, E. B.; Swenson, D. C.; Jordan, R. F.; Peterson, J. L. *Organometallics* **1995**, *14*, 371.

17. Nishida, H.; Takada, N.; Yoshimura, M.; Sonoda, T.; Kobayashi, H. *Bull. Chem. Soc. Jpn.* **1984**, *57*, 2600.

18. Colsman, M. R.; Newbound, T. D.; Marshall, L. J.; Noirot, M. D.; Miller, M. M.; Wulfsberg, G. P.; Frye, J. S.; Anderson, O. P.; Strauss, S. H. *J. Am. Chem. Soc.* **1990,** *112,* 2349-62.

19. Hurlburt, P. K.; Anderson, O. P.; Strauss, S. H. *J. Am. Chem. Soc.* **1991,** *113,* 6277-8.

20. Hurlburt, P. K.; Rack, J. J.; Dec, S. F.; Anderson, O. P.; Strauss, S. H. *Inorg. Chem.* **1993,** *32,* 373-4.

21. Rockwell, J. J.; Kloster, G. M.; DuBay, W. J.; Grieco, P. A.; Shriver, D. F.; Strauss, S. H. *Inorg. Chim. Acta* **1997,** *263,* 195-200.

22. Newman, G. H.; Francis, R. W.; Gaines, L. H.; Rao, B. M. L. *J. Electrochem. Soc.* **1980,** *127,* 2025.

23. Rhodes, M. R.; Mann, K. R. *Inorg. Chem.* **1984,** *23,* 2053.

24. Appel, M.; Schloter, K.; Heidrich, J.; Beck, W. *J. Organomet. Chem.* **1987,** *322,* 77.

25. Bond, A. M.; Ellis, S. R.; Hollenkamp, A. F. *J. Am. Chem. Soc.* **1988,** *110,* 5293.

26. Hill, M. G.; Lammana, W. M.; Mann, K. R. *Inorg. Chem.* **1991,** *30,* 4687.

27. Ehlert, T. C.; Hsia, M. M. *J. Chem. Eng. Data* **1972,** *17,* 18.

28. Lawless, E. W.; Wiegand, C. J. W.; Mizumoto, Y.; Weis, C. *Inorg. Chem.* **1971,** *10,* 1084.

29. Plankhotnik, V. N.; Tul'chinskii, V. B.; Steba, V. K. *Russ. J. Inorg. Chem.* **1976,** *21,* 451.

30. Geske, D. H. *J. Phys. Chem.* **1959,** *63,* 1062.

31. Geske, D. H. *J. Phys. Chem.* **1962,** *66,* 1743.

32. Turner, W. R.; Elving, P. *Anal. Chem.* **1965,** *207.*

33. Bancroft, E. E.; Blount, H. N.; Janzen, E. G. *J. Am. Chem. Soc.* **1979,** *101,* 3692.

34. Albano, P.; Aresta, M.; Manassero, M. *Inorg. Chem.* **1980,** *19,* 1069.

35. Hlatky, G. G.; Turner, H. W.; Eckman, R. R. *J. Am. Chem. Soc.* **1989,** *111,* 2728.

36. One example is Horton, A. D.; Frijns, J. H. G. *Angew. Chem., Int. Ed.* **1991,** *30,* 1152.

37. Mann, K. R., *personal communication to S. H. Strauss*, 1992.

38. Yang, X.; Stern, C. L.; Marks, T. J. *Organometallics* **1991**, *10*, 840.

39. Nolan, B. J., *unpublished results*.

40. Barbarich, T. J., *unpublished results*.

41. Knoth, W. H. *J. Am. Chem. Soc.* **1967**, *89*, 1274-1275.

42. Knoth, W. H. *Inorg. Chem.* **1971**, *10*, 598-605.

43. Plešek, J.; Jelínek, T.; Štíbr, B. *Polyhedron* **1984**, *3*, 1351-5.

44. Plešek, J.; Jelínek, T.; Drdakova, E.; Heřmánek, S.; Štíbr, B. *Collect. Czech. Chem. Commun.* **1984**, *49*, 1559-62.

45. Jelínek, T.; Plešek, J.; Heřmánek, S.; Štíbr, B. *Collect. Czech. Chem. Commun.* **1986**, *51*, 819-29.

46. Jelínek, T.; Plešek, J.; Mares, F.; Heřmánek, S.; Štíbr, B. *Polyhedron* **1987**, *6*, 1981.

47. Khan, S. A.; Morris, J. H.; Siddiqui, S. *J. Chem. Soc., Dalton Trans.* **1990**, 2053.

48. Mair, F. S.; Morris, J. H.; Gaines, D. F.; Powell, D. *J. Chem. Soc. Dalton Trans.* **1993**, 123-141.

49. Shelly, K.; Finster, D. C.; Lee, Y. J.; Scheidt, W. R.; Reed, C. A. *J. Am. Chem. Soc.* **1985**, *107*, 5955-9.

50. Shelly, K.; Reed, C. A.; Lee, Y. J.; Scheidt, W. R. *J. Am. Chem. Soc.* **1986**, *108*, 3117-18.

51. Liston, D. J.; Reed, C. A.; Eigenbrot, C. W.; Scheidt, W. R. *Inorg. Chem.* **1987**, *26*, 2739-40.

52. Liston, D. J.; Lee, Y. J.; Scheidt, W. R.; Reed, C. A. *J. Am. Chem. Soc.* **1989**, *111*, 6643-8.

53. Jelínek, T.; Baldwin, P.; Scheidt, W. R.; Reed, C. A. *Inorg. Chem.* **1993**, *32*, 1982-90.

54. Reed, R. W.; Xie, Z.; Manning, J.; Mathur, R.; Bau, R.; Reed, C. A. *Phosphorus, Sulfur Silicon Relat. Elem.* **1994**, *93-94*, 485.

55. Srivastava, R. R.; Hamlin, D. K.; Wilber, D. S. *J. Org. Chem.* **1996**, *61*, 9041-9044.

56. Xie, Z.; Tsang, C.-W.; Xue, T.; Mak, T. C. W. *Inorg. Chem.* **1997**, *36*, 2246-2247.

57. Xie, Z.; Tsang, C.-W.; Sze, E. T.-P.; Tang, Q.; Chan, D. T. W.; Mak, T. C. W. *Inorg. Chem.* **1998**, *37*, 6444-6451.

58. King, B. T.; Janousek, Z.; Gruener, B.; Trammell, M.; Noll, B. C.; Michl, J. *J. Am. Chem. Soc.* **1996**, *118*, 3313-14.

59. King, B. T.; Zharov, I.; Moss, S.; Clayton, J.; Ceremuga, J. T.; Pospisil, L.; Michl, J. *Alkylated and fluoroalkylated carba-closo-dodecaborates(-)*, 215th ACS National Meeting, Dallas, TX, March/April 1998.

60. Reed, C. A.; Xie, Z.; Bau, R.; Benesi, A. *Science* **1993**, *262*, 402-4.

61. Xie, Z.; Manning, J.; Reed, R. W.; Mathur, R.; Boyd, P. D. W.; Benesi, A.; Reed, C. A. *J. Am. Chem. Soc.* **1996**, *118*, 2922-8.

62. Plešek, J.; Jelínek, T.; Drdáková, E.; Hermánek, S.; Stîbr, B. *Coll. Czech. Chem. Commun.* **1984**, *49*, 1559-1562.

63. Little, J. L.; Pao, S. S.; Sugathan, K. K. *Inorg. Chem.* **1974**, *13*, 1752-6.

64. Hanusa, T. P.; Roig de Parisi, N.; Kester, J. G.; Arafat, A.; Todd, L. J. *Inorg. Chem.* **1987**, *26*, 4100-2.

65. Ouassas, A.; R'Kha, C.; Mongeot, H.; Frange, B. *Inorg. Chim. Acta* **1991**, *180*, 257.

66. Little, J. L. *Inorg. Chem.* **1979**, *18*, 1598-600.

67. Little, J. L.; Whitesell, M. A.; Kester, J. G.; Folting, K.; Todd, L. J. *Inorg. Chem.* **1990**, *29*, 804-8.

68. Knoth, W. H.; Miller, H. C.; Sauer, J. C.; Balthis, J. H.; Chia, Y. T.; Muetterties, E. L. *Inorg. Chem.* **1964**, *3*, 159-167.

69. Miller, H. C.; Muetterties, E. L. United States Patent 3,555,120 (assigned to DuPont), 1970.

70. Solntsev, K. A.; Mebel, A. M.; Votinova, N. A.; Kuznetsov, N. T.; Charkin, O. P. *Koord. Khimiya* **1992**, *18*, 340-364.

71. Solntsev, K. A.; Ivanov, S. V.; Sakharov, S. G.; Kaster, S. B.; Chernyavskii, A. S.; Votinova, N. A.; Klyuchishche, E. A.; Kuznetsov, N. T. *Russ. J. Coord. Chem.* **1997**, *23*, 369-376.

72. Lupinetti, A. J., *unpublished results.*

73. Mueller, J.; Runsink, J.; Paetzold, P. *Angew. Chem.* **1991**, *103*, 201 (See also *Angew. Chem., Int. Ed.* **1991**, *30*, 175-6.

74. Getman, T. D.; Deng, H. B.; Hsu, L. Y.; Shore, S. G. *Inorg. Chem.* **1989**, *28*, 3612.

75. Shriver, D. F.; Drezdzom, M. A. *The Manipulation of Air-Sensitive Compounds*; 2nd ed.; Wiley-Interscience: New York, 1986.

76. F-TEDA-BF4 = 1-(chloromethyl)-4-fluoro-1,4-diazabicyclo[2.2.2]octane bis(tetra fluoroborate).

77. Banks, R. E. United States Patent 5,086,178, 1992.

78. Hop, C. E. C. A.; Saulys, D. A.; Gaines, D. F. *Inorg. Chem.* **1995**, *34*, 1977.

79. Ivanov, S. V.; Lupinetti, A. J.; Miller, S. M.; Anderson, O. P.; Solntsev, K. A.; Strauss, S. H. *Inorg. Chem.* **1995**, *34*, 6419-20.

80. Thomsen, H.; Haeckel, O.; Krause, U.; Preetz, W. *Z. anorg. allg. Chem.* **1996**, *622*, 2061-2064.

81. Ivanov, S. V.; Lupinetti, A. J.; Solntsev, K. A.; Strauss, S. H. *J. Fluorine Chem.* **1998**, *89*, 65-72.

82. Murtagh, V. *Perform. Chem.* **1991**, *6*, 36.

83. Banks, R. E.; Murtagh, V.; Tsiliopoulous, E. *J. Fluorine Chem.* **1991**, *52*, 389.

84. Resnati, G.; DesMarteau, D. D. *J. Org. Chem.* **1991**, *56*, 4925.

85. German, L.; Zemskov, S. *New Fluorinating Agents in Organic Synthesis*; Springer-Verlag: Berlin, Heidelberg, 1989.

86. Lal, G. S.; Pez, G. P.; Syvret, R. G. *Chem. Rev.* **1996**, *96*, 1737-1755.

87. Schack, C. J.; Christe, K. O. *J. Fluorine Chem.* **1981**, *18*, 363.

88. Singh, S.; DesMarteau, D. D.; Zuberi, S. S.; Witz, M.; Huang, H.-N. *J. Am. Chem. Soc.* **1987**, *109*, 7194.

89. Umemoto, T.; Fukami, S.; Tomizawa, G.; Harasawa, K.; Kawada, K.; Tomita, K. *J. Am. Chem. Soc.* **1990**, *112*, 8563.

90. Lal, G. S. *J. Org. Chem.* **1993**, *58*, 2791.

91. Gilicinski, A. G.; Pez, G. P.; Syvret, R. G.; Lal, G. S. *J. Fluorine Chem.* **1992**, *59*, 157.

92. Banks, R. E.; Mohialdin-Khaffaf, S. N.; Lal, G. S.; Sharif, I.; Syvret, R. G. *J. Chem. Soc., Chem. Commun.* **1992**, 595.

93. McLemore, D. K.; Dixon, D. A.; Strauss, S. H., *submitted 1999*.

94. Heřmánek, S. *Chem. Rev.* **1992**, *92*, 325-62.

95. Heřmánek, S. *Inorg. Chim. Acta* **1999**, *289*, 20-44.

96. Ivanov, S. V., *unpublished results*.

97. Rockwell, J. J. Ph.D. Thesis, Colorado State University, 1998.

98. Ivanova, S. M., *unpublished results*.

99. Ivanov, S. V.; Ivanova, S. M., *unpublished results*.

100. Ivanov, S. V.; Rockwell, J. J.; Polyakov, O. G.; Gaudinski, C. M.; Anderson, O. P.; Solntsev, K. A.; Strauss, S. H. *J. Am. Chem. Soc.* **1998**, *120*, 4224-4225.

101. Ramsey, N. F. *Phys. Rev.* **1950**, *78*, 689.

102. Ramsey, N. F. *Pure Appl. Chem.* **1972**, *29*, 627.

103. Ramsey, N. F. *Pure. Appl. Chem.* **1976**, *45*, 219.

104. Pople, J. A. *Mol. Phys.* **1964**, *7*, 301.

105. Webb, G. A.; Harris, K. R. and Mann, B. E., Ed.; Academic Press: London, New York, San Francisco, 1978, pp 60.

106. Heřmánek, S.; Hnyk, D.; Havlas, Z. *J. Chem. Soc., Chem. Commun.* **1989**, 1859-61.

107. Siedle, A. R.; Bodner, G. M.; Garber, A. R.; Beer, D. C.; Todd, L. J. *Inorg. Chem.* **1974**, *13*, 2321-4.

108. Heřmánek, S.; Gregor, V.; Štíbr, B.; Plešek, J.; Janousek, Z.; Antonovich, V. V. *Collect. Czech. Chem. Commun.* **1976**, *41*, 1492-9.

109. Smith, W. L.; Menghelli, B. J.; Thompson, D. A.; Klymko, P.; McClure, N.; Bower, M.; Rudolph, R. W. *Inorg. Chem.* **1977**, *16*, 3008-3012.

110. Teixidor, F.; Vinas, C.; Rudolph, R. W. *Inorg. Chem.* **1986**, *25*, 3339-3345.

111. Fehlner, T. P.; Czech, P. T.; Fenske, R. F. *Inorg. Chem.* **1990**, *29*, 3103-3109.

112. Buehl, M.; Schleyer, P. v. R.; Havlas, Z.; Hnyk, D.; Heřmánek, S. *Inorg. Chem.* **1991**, *30*, 3107-11.

APPENDIX I.A

MSDS Sheets: Hydrofluoric Acid and Decaborane(14)

HYDROFLUORIC ACID

MSDS Number: H3994 — Effective Date: 09/16/97

1. Product Identification

Synonyms: Fluorohydric acid; fluoric acid; Hydrogen fluoride solution
CAS No.: 7664-39-3
Molecular Weight: 20.01
Chemical Formula: HF in Aqueous Solution.
Product Codes:
J.T. Baker: 5368, 5659, 5818, 5824, 5840, 6904, 9559, 9560, 9563, 9564, 9567, 9572, 9573, 9574, 9575 Mallinckrodt: 2640, 2648, V580

2. Composition/Information on Ingredients

Ingredient	CAS No	Percent	Hazardous
Water	7732-18-5	48 - 52%	No
Hydrogen Fluoride	7664-39-3	48 - 52%	Yes

3. Hazards Identification

Emergency Overview

POISON! DANGER! CORROSIVE. EXTREMELY HAZARDOUS LIQUID AND VAPOR. CAUSES SEVERE BURNS WHICH MAY NOT BE IMMEDIATELY PAINFUL OR VISIBLE. MAY BE FATAL IF SWALLOWED OR INHALED. LIQUID AND VAPOR CAN BURN SKIN, EYES AND RESPIRATORY TRACT. CAUSES BONE DAMAGE. REACTION WITH CERTAIN METALS GENERATES FLAMMABLE AND POTENTIALLY EXPLOSIVE HYDROGEN GAS.

J.T. Baker SAF-T-DATA(tm) Ratings (Provided here for your convenience)

Health Rating:	4 - Extreme (Poison)
Flammability Rating:	0 - None
Reactivity Rating:	2 - Moderate
Contact Rating:	4 - Extreme (Corrosive)
Lab Protective Equip:	GOGGLES & SHIELD; LAB COAT & APRON; VENT HOOD; PROPER GLOVES
Storage Color Code:	White (Corrosive)

Potential Health Effects

Exposure to hydrofluoric acid can produce harmful health effects that may not be immediately apparent.

Inhalation:
Severely corrosive to the respiratory tract. May cause sore throat, coughing, labored breathing and lung congestion/inflammation.

Ingestion:
Corrosive. May cause sore throat, abdominal pain, diarrhea, vomiting, severe burns of the digestive tract, and kidney dysfunction.

Skin Contact:
Corrosive to the skin. Skin contact causes serious skin burns which may not be immediately apparent or painful. Symptoms may be delayed 8 hours or longer. The fluoride ion readily penetrates the skin causing destruction of deep tissue layers and even bone.

Eye Contact:
Corrosive to the eyes. Symptoms of redness, pain, blurred vision, and permanent eye damage may occur.

Chronic Exposure:
Intake of more than 6 mg of fluorine per day may result in fluorosis, bone and joint damage. Hypocalcemia and hypomagnesemia can occur from absorption of fluoride ion into blood stream.

Aggravation of Pre-existing Conditions:
Persons with pre-existing skin disorders, eye problems, or impaired kidney or respiratory function may be more susceptible to the effects of this substance.

---

4. First Aid Measures

For any route of contact: Detailed First Aid procedure should be planned before beginning work with HF.

Inhalation:

Get medical help immediately. If patient is unconscious, give artificial respiration or use inhalator. Keep patient warm and resting, and send to hospital after first aid is complete.

Ingestion:

If swallowed, DO NOT INDUCE VOMITING. Give large quantities of water. Never give anything by mouth to an unconscious person. Get medical attention immediately.

Skin Contact:

FOR ACID BURNS TO THE BODY: 1) Remove the victim from the contaminated area and immediately place him under a safety shower or wash him with a water hose, whichever is available. 2) Remove all contaminated clothing. 3) Keep washing with large amounts of water for a minimum of 15 to 20 minutes. 4) Have someone make arrangements for medical attention while you continue flushing the affected area with water. 5) a) If available, after thorough washing, the burned area should be immersed in a solution of 0.2% iced aqueous Hyamine 1622 or 0.13% iced aqueous Zephiran Chloride. If immersion is not practical, towels should be soaked with one of the above solutions and used as compresses for the burn area. Ideally compresses should be changed every 2 minutes. 5) b) An alternative treatment to 5a is for the physician to inject sterile 10% aqueous calcium gluconate solution subcutaneously beneath, around, and in the burned area. Initially use no more than 0.5 cc per square centimeter and do not distort appearance of skin. If pain is not completely relieved, additional treatment is indicated. 6) Seek medical attention as soon as possible for all burns regardless of how minor they may appear initially. Hyamine 1622 is a trade name for Tetracaine Benzethonium Chloride, Merck Index Monograph 1078, a quaternary ammonium compound sold

by Rohm & Haas, Philadelphia. Zephiran Chloride is a trade name for Benzalkonium Chloride, Merck Index Monograph 1059, also a quaternary ammonium compound, sold by SANOFI Winthrop Pharmaceutical, New York, NY.

Eye Contact:

FOR ACID IN THE EYES: 1) Irrigate eyes for at least 30 minutes with copious quantities of water, keeping the eyelids apart and away from eyeballs during irrigation. 2) Get competent medical attention immediately, preferably an eye specialist. 3) If a physician is not immediately available, apply one or two drops of 0.5% Pontocaine Hydrochloride solution. 4) Do not use oily drops or ointment. Place ice pack on eyes until reaching emergency room.

Note to Physician:

For burns of large skin areas, (greater than 25 square inches), for ingestion and for significant inhalation exposure, severe systemic effects may occur. Monitor and correct for hypocalcemia, cardiac arrhythmias, hypomagnesemia and hyperkalemia. In some cases renal dialysis may be indicated. For certain burns, especially of the digits, use of intra-arterial calcium glucaonate may be indicated. Treat as chemical pneumonia. Monitor for hypocalcemia, 2.5% calcium gluconate in normal saline by nebulizer or by IPPB with 100% oxygen may decrease pulmonary damage. Bronchodilators may also be administered. Medical Surveillance: Provide phycical examinations of exposed personnel every six months including fluoride determinations in urine, studies of liver and kidney function: chest X-ray, annually. Protect from exposure those individuals with diseases of kidneys, liver, and lung. (ITII. Toxic and Hazardous Industrial Chemicals Safety Manual). AN ALTERNATIVE FIRST AID PROCEDURE: Hydrofluoric Acid (HF) is a highly corrosive and toxic acid, even in a dilute form. It can severely damage the skin and eyes causing severe burns which are extremely painful. Additionally, the vapor from anhydrous HF or its concentrated solutions can cause damage to skin, eyes and the respiratory system. HF differs from other strong acids in that it not only causes surface burns but rapidly penetrates the skin, even in dilute solution, and causes destruction of underlying tissue and even bone by the extraction of Calcium. For this reason, washing the burn with water is not sufficient. A neutralizing agent which will also penetrate the skin is required. The effect of HF, i.e. onset of pain, particularly in dilute solutions, may not be felt for up to 24 hours. It is important, therefore, that

persons using HF have immediate access to an effective antidote even when they are away from their work place in order that first aid treatment can be commenced immediately while the patient seeks medical advice. HOW TO TREAT HYDROFLUORIC ACID BURNS: It has been conclusively shown (references 1,2,3 and 4 below) that flushing the affected area with water for one minute and then massageing HF Antidote Gel into the wound until there is a cessation of pain is the most effective first aid treatment available. HF Antidote Gel contains Calcium Gluconate which combines with HF to form insoluble Calcium Fluoride, thus preventing the extraction of Calcium from the body tissue and bones. HF Antidote Gel is available in 25g tubes, and since the effects of the dilute acid may nto be apparent for some hours, we recommend that any person in contact with HF should carry, or have access to a tube of HF Antidote Gel at all times; ideally with one tube at the work place, one on the person and one at home. Fore safety's sake, we believe that HF Antidote Gel should be issued to all employees who may come into contact with HF. EYE INJURIES: Irrigate the affected part immediately with copious amounts of cold water. Urgent medical advice must be sought. HF Antidote Gel is NOT for use in the eye. It is imperative that any person who has been contaminated by HF should seek medical advice even when the treatment by HF Antidote Gel has been applied. REFERENCES: 1. Browno, T.D. Treatment of Hydrofluoric Acid Burns 2. Sprout, W.L. et al Treatment of Severe Hydrofluoric Acid Exposures (Journal of American Occupational Medicine 25:12, 1993) 3. Bracken, W.M. et al Comparative Effectiveness of Topical Treatments for Hydrofluoric Acid Burns, University of Kansas (Journal of Occupational Medicine 27:10:1985) 4. Burke, W.J. , et al Systemic Fluoride Poisoning Resulting from A Flouride Skin Burn (Journal of Occupational Medicine (5,39:1973) Distributed by PHARMASCIENCE INC., Montreal, Canada.

---

5. Fire Fighting Measures

Fire:

Not considered to be a fire hazard. Fire may produce poisonous or irritating gases.

Explosion:

Violent exothermic reaction occurs with water. Sufficient heat may be produced to ignite combustible materials. Reacts with metals forming flammable Hydrogen gas.

Fire Extinguishing Media:

Keep upwind of fire. Use water or carbon dioxide on fires in which Hydrofluoric Acid is involved. Halon or foam may also be used. In case of fire, the sealed containers can be kept cool by spraying with water.

Special Information:

In the event of a fire, wear full protective clothing and NIOSH-approved self-contained breathing apparatus with full facepiece operated in the pressure demand or other positive pressure mode. Avoid getting water in tanks or drums; water can cause generation of heat and spattering. In contact with air, the acid gives off corrosive fumes which are heavier than air.

---

6. Accidental Release Measures

Notify safety personnel, provide adequate ventilation, and remove ignition sources since hydrogen may be generated by reactions with metals. Wear appropriate personal protective equipment as specified in Section 8. Do not flush to sewers or waterways. Spills: Evacuate the danger area. Apply magnesium sulfate (dry) to the spill area. Follow up with inert absorbent (acid spill tamer) and add soda ash or magnesium oxide and slaked lime. Collect in appropriate plastic containers and save for disposal. Wash spill site with soda ash solution. NOTE: Porous materials (concrete, wood, plastic, etc.) will absorb HF and become a hazard for an indefinite time. Such spills should be cleaned and neutralized immediately. US Regulations (CERCLA) require reporting spills and releases to soil, water and air in excess of reportable quantities. The toll free number for the US Coast Guard National Response Center is (800) 424-8802.

J. T. Baker TEAM(tm) 'Low Na+' acid neutralizer is recommended for spills of this product.

---

7. Handling and Storage

Keep in tightly closed polyethylene containers. Store in a cool, dry place with adequate ventilation separated from other chemicals. Protect from

physical damage. Storage facilities should be constructed for containment and neutralization of spills. Handling and storage of HF requires special materials and technology for containers, pipes, valves, etc., which is available from suppliers. Containers of this material may be hazardous when empty since they retain product residues (vapors, liquid); observe all warnings and precautions listed for the product.

---

8. Exposure Controls/Personal Protection

Airborne Exposure Limits:

Hydrogen fluoride:
OSHA Permissible Exposure Limit (PEL): 3 ppm (TWA)
ACGIH Threshold Limit Value (TLV): 3 ppm Ceiling as F

Ventilation System:

A system of local and/or general exhaust is recommended to keep employee exposures as low as possible. Local exhaust ventilation is generally preferred because it can control the emissions of the contaminant at its source, preventing dispersion of it into the general work area. Please refer to the ACGIH document, *Industrial Ventilation, A Manual of Recommended Practices*, most recent edition, for details.

Personal Respirators (NIOSH Approved):

If the exposure limit is exceeded, a full facepiece respirator with an acid gas cartridge may be worn up to 50 times the exposure limit or the maximum use concentration specified by the appropriate regulatory agency or respirator supplier, whichever is lowest. For emergencies or instances where the exposure levels are not known, use a full-facepiece positive-pressure, air-supplied respirator. WARNING: Air purifying respirators do not protect workers in oxygen-deficient atmospheres. Since the IDLH is low (30 ppm), the above cartridge system is not specifically approved for HF. (3M Respirator Selection Guide)

Skin Protection:

Wear protective clothing, including boots or safety shoes with polyvinyl chloride (PVC) or neoprene. Use chemical goggles and/or a full face

shield. Wear coveralls with long sleeves, gauntlets and gloves of PVC or neoprene. A high degree of protection is obtained with an air-inflated suit with mask and safety belt. Use protection suitable for conditions.

Eye Protection:

Use chemical safety goggles and/or full face shield where splashing is possible. Maintain eye wash fountain and quick drench facilities in work area.

---

9. Physical and Chemical Properties

Appearance:
Colorless, fuming liquid.
Odor:
Acrid odor. Do not breathe fumes.
Solubility:
Infinitely soluble.
Specific Gravity:
1.15 -1.18
pH:
1.0 (0.1M solution)
% Volatiles by volume @ 21C (70F):
100 (as water and acid)
Boiling Point:
108C (226F)
Melting Point:
< -36C (< -33F)
Vapor Density (Air=1):
1.97
Vapor Pressure (mm Hg):
25 @ 20C (68F)
Evaporation Rate (BuAc=1):
No information found.

---

10. Stability and Reactivity

Stability:

Stable at room temperature (68°F) when stored and used under proper conditions.

Hazardous Decomposition Products:

On contact with metals, liberates hydrogen gas. On heating to decomposition, could yield toxic fumes of fluorides. Attacks glass and other silicon containing compounds. Reacts with silica to produce silicon tetrafluoride, a hazardous colorless gas.

Hazardous Polymerization:

Will not occur.

Incompatibilities:

Hydrofluoric acid is incompatible with arsenic trioxide, phosphorus pentoxide, ammonia, calcium oxide, sodium hydroxide, sulfuric acid, vinyl acetate, ethylenediamine, acetic anhydride, alkalis, organic materials, most common metals, rubber, leather, water, strong bases, carbonates, sulfides, cyanides, oxides of silicon, especially glass, concrete, silica, fluorine. Will also react with steam or water to produce toxic fumes.

Conditions to Avoid:

Moisture and incompatibles.

---

11. Toxicological Information

Hydrofluoric acid: Inhalation rat LC50: 1276 ppm/1H; Investigated as a mutagen, reproductive effector.

--------\Cancer Lists\----------

	NTP Carcinogen		
Ingredient	Known	Anticipated	IARC Category
Hydrogen Fluoride (7664-39-3)	No	No	None
Water (7732-18-5)	No	No	None

12. Ecological Information

Environmental Fate:

If the pH is > 6.5, soil can bind fluorides tightly. High calcium content will immobilize fluorides, which can be damaging to plants when present in acid soils.

Environmental Toxicity:

This material is expected to be slightly toxic to aquatic life. 60 ppm/*/Fish/Lethal/Fresh Water *=time period not specified. > 300ppm/48hr./Shrimp/LC50/Aerated Saltwater

13. Disposal Considerations

Whatever cannot be saved for recovery or recycling should be handled as hazardous waste and sent to a RCRA approved incinerator or disposed in a RCRA approved waste facility. Processing, use or contamination of this product may change the waste management options. State and local disposal regulations may differ from federal disposal regulations. Dispose of container and unused contents in accordance with federal, state and local requirements.

14. Transport Information

Domestic (Land, D.O.T.)

Proper Shipping Name: RQ, HYDROFLUORIC ACID (WITH NOT MORE THAN 60% STRENGTH)

Hazard Class: 8, 6.1

UN/NA: UN1790 Packing Group: II

Information reported for product/size: 250LB

International (Water, I.M.O.)

Proper Shipping Name: HYDROFLUORIC ACID (WITH NOT MORE THAN 60% STRENGTH)

Hazard Class: 8, 6.1

UN/NA: UN1790 Packing Group: II

Information reported for product/size: 250LB

---

15. Regulatory Information

--------\Chemical Inventory Status - Part 1\--------------------------

Ingredient	TSCA	EC	Japan	Australia
Hydrogen Fluoride (7664-39-3)	Yes	Yes	Yes	Yes
Water (7732-18-5)	Yes	Yes	Yes	Yes

--------\Chemical Inventory Status - Part 2\--------------------------

		--Canada--		
Ingredient	Korea	DSL	NDSL	Phil.
Hydrogen Fluoride (7664-39-3)	Yes	Yes	No	Yes
Water (7732-18-5)	Yes	Yes	No	Yes

--------\Federal, State & International Regulations - Part 1\----------

	-SARA 302-		-------SARA 313-------	
Ingredient	RQ	TPQ	List	Chemical Catg.
Hydrogen Fluoride (7664-39-3)	100	100	Yes	No
Water (7732-18-5)	No	No	No	No

--------\Federal, State & International Regulations - Part 2\----------

		-RCRA-	-TSCA-
Ingredient	CERCLA	261.33	8(d)
Hydrogen Fluoride (7664-39-3)	100	U134	No
Water (7732-18-5)	No	No	No

Chemical Weapons Convention: Yes TSCA 12(b): No CDTA: No
SARA 311/312: Acute: Yes Chronic: Yes Fire: No Pressure: No
Reactivity: Yes (Mixture / Liquid)

Australian Hazchem Code: 2R

Poison Schedule: S7

WHMIS:
This MSDS has been prepared according to the hazard criteria of the Controlled Products Regulations (CPR) and the MSDS contains all of the information required by the CPR.

---

16. Other Information

NFPA Ratings: Health: **4** Flammability: **0** Reactivity: **1**

Label Hazard Warning:

POISON! DANGER! CORROSIVE. EXTREMELY HAZARDOUS LIQUID AND VAPOR. CAUSES SEVERE BURNS WHICH MAY NOT BE IMMEDIATELY PAINFUL OR VISIBLE. MAY BE FATAL IF SWALLOWED OR INHALED. LIQUID AND VAPOR CAN BURN SKIN, EYES AND RESPIRATORY TRACT. CAUSES BONE DAMAGE. REACTION WITH CERTAIN METALS GENERATES FLAMMABLE AND POTENTIALLY EXPLOSIVE HYDROGEN GAS.

Label Precautions:

Do not get in eyes, on skin, or on clothing. Do not breathe vapor. Cool before opening. Use only with adequate ventilation. Wash thoroughly after handling. Store in a tightly closed container.

Label First Aid:

IN ALL CASES, CALL PHYSICIAN IMMEDIATELY. First Aid procedures should be pre-planned for HF emergencies. A supply of 50:50 water/magnesium sulfate paste or 2 1/2% Calcium Gluconate paste should be available where first aid medications are administered. If ingested, DO

NOT INDUCE VOMITING. If patient is conscious, give large quantities of milk or water and send to hospital. If inhaled and patient is unconscious, give artificial respiration or use inhalator and send to hospital. In case of eye contact, wash open eyes with large but gentle stream of water for 15 minutes. Place ice pack on eyes until reaching emergency room. In case of skin contact, remove contaminated clothing and wash burn area with plenty of water to remove acid. Cover burn area with a poultice of 50:50 water/magnesium sulfate paste or 2 1/2% calcium gluconate paste. Leave in place until medical help arrives or patient is transferred to hospital.

Product Use:

Laboratory Reagent.

Revision Information:

Disclaimer:

****

Mallinckrodt Baker, Inc. provides the information contained herein in good faith but makes no representation as to its comprehensiveness or accuracy. This document is intended only as a guide to the appropriate precautionary handling of the material by a properly trained person using this product. Individuals receiving the information must exercise their independent judgment in determining its appropriateness for a particular purpose. MALLINCKRODT BAKER, INC. MAKES NO REPRESENTATIONS OR WARRANTIES, EITHER EXPRESS OR IMPLIED, INCLUDING WITHOUT LIMITATION ANY WARRANTIES OF MERCHANTABILITY, FITNESS FOR A PARTICULAR PURPOSE WITH RESPECT TO THE INFORMATION SET FORTH HEREIN OR THE PRODUCT TO WHICH THE INFORMATION REFERS. ACCORDINGLY, MALLINCKRODT BAKER, INC. WILL NOT BE RESPONSIBLE FOR DAMAGES RESULTING FROM USE OF OR RELIANCE UPON THIS INFORMATION.

****

Prepared by: Strategic Services Division Phone Number: (314) 539-1600 (U.S.A.)

Decaborane(14)*

ICN BIOMEDICALS -- DECABORANE, 150784
MATERIAL SAFETY DATA SHEET
NSN: 681000N055287
Manufacturer's CAGE: 30060
Part No. Indicator: A
Part Number/Trade Name: DECABORANE, 150784

==========

General Information

==========

Company's Name: ICN BIOMEDICALS
Company's Street: 1263 S. CHILLICOTHE RD
Company's City: AURORA
Company's State: OH
Company's Country: US
Company's Zip Code: 44202
Company's Emerg Ph #: 800-424-9300 (CHEMTREC)
Company's Info Ph #: 216-562-1500
Record No. For Safety Entry: 001
Tot Safety Entries This Stk#: 001
Status: SMJ
Date MSDS Prepared: 07JAN94
Safety Data Review Date: 14NOV94
MSDS Preparer's Name: RL
Preparer's Company: SAME
MSDS Serial Number: BVZZM
Hazard Characteristic Code: NK

==========

Ingredients/Identity Information

==========

Proprietary: NO
Ingredient: DECABORANE(14); (DECABORANE) (DECABORONTETRADECAHYDRIDE)(SARA III)
Ingredient Sequence Number: 01
NIOSH (RTECS) Number: HD1400000
CAS Number: 17702-41-9
OSHA PEL: S, 0.05PPM
ACGIH TLV: S, 0.05PPM

==========

Physical/Chemical Characteristics

==========

Appearance And Odor: COLORLESS CRYSTALLINE
Melting Point: 210°F,99°C
Vapor Pressure (MM Hg/70°F): 19MM@100°C
Specific Gravity: (SUPP DATA)
Solubility In Water: INSOLUBLE

Fire and Explosion Hazard Data

Flash Point:	NOT AVAILABLE
Lower Explosive Limit:	N/A
Upper Explosive Limit:	N/A
Extinguishing Media:	CO_2, DRY CHEMICAL, FOAM.
Special Fire Fighting Proc:	WEAR NIOSH/MSHA APPROVED SCBA & FULL PROTECTIVE EQUIPMENT (FP N).
Unusual Fire And Expl Hazrds:	MIXTURE IN AIR EXPOSED TO HEAT OR FLAMES.

Reactivity Data

Stability:	YES
Cond To Avoid (Stability):	NONE SPECIFIED BY MANUFACTURER.
Materials To Avoid:	IGNITES IN O*2 @ 100C. FORMS IMPACT INTENSIVE EXPLO MIX W/ETHERS (EG. DIOXANE) & HALOCARBONS (EG. CARBON (SUPP DATA)
Hazardous Decomp Products:	TOXIC FUMES OF BO*X.
Hazardous Poly Occur:	NO
Conditions To Avoid (Poly):	NOT RELEVANT

Health Hazard Data

LD50-LC50 Mixture: LD50(ORAL,RAT):64 MG/KG.

Route Of Entry - Inhalation:	YES
Route Of Entry - Skin:	YES
Route Of Entry - Ingestion:	YES

Health Haz Acute And Chronic: POISON BY INHALATION, INGESTION, SKIN CONTACT AND INTRAPERITONEAL ROUTES. MODERATE TO SEVERE ERYTHEMA (REDNESS)AND MODERATE EDEMA (RAISED SKIN).

REMARKS:	POISON.
Carcinogenicity - NTP:	NO
Carcinogenicity - IARC:	NO
Carcinogenicity - OSHA:	NO
Explanation Carcinogenicity:	NOT RELEVANT
Signs/Symptoms Of Overexp:	SEE HEALTH HAZARDS.
Med Cond Aggravated By Exp:	NONE SPECIFIED BY MANUFACTURER.

Emergency/First Aid Proc: SKIN:REMOVE CONTAM CLTHG, RINSE LIBERALLY WITH SOAP AND WATER FOR A CONSIDERABLE PERIOD. CALL MD. INGEST:RINSE MOUTH SEVERAL TIMES WITH WATER, DO NOT SWALLOW. CALL MD OR TAKE PATIENT TO A HOSPITAL. EYES:RINSE LIBERALLY WITH WATER FOR AT LEAST 15 MINUTES. CALL MD OR TAKE PATIENT TO A HOSPITAL. INHAL:TAKE PATIENT INTO FRESH AIR & ALLOW TO REST. CALL MD OR TAKE PATIENT TO A HOSPITAL.

Precautions for Safe Handling and Use

Steps If Matl Released/Spill: ABSORB THE LIQUID IN DRY SAND, DIATONITE, VERMICULITE, ETC., SHOVEL THE MIXTURE INTO PLASTIC BAGS AND REMOVE TO THE CENTRAL DEPOT FOR CHEMICAL WASTE.

Neutralizing Agent: NONE SPECIFIED BY MANUFACTURER.

Waste Disposal Method: INCINERATE OR LANDFILL AS COMPLIES WITH FEDERAL, STATE & LOCAL REGULATIONS.

Precautions-Handling/Storing: ALWAYS WEAR GLOVES, MASK, GOGGLES AND USE A HOOD. STORE AT ROOM TEMPERATURE.
Other Precautions: SWEEP INTO SUITABLE CONTAINER FOR DISPOSAL.

Control Measures

Respiratory Protection: USE NIOSH/MSHA APPROVED RESPIRATOR APPROPRIATE FOR EXPOSURE OF CONCERN (FP N).
Ventilation: LOCAL EXHAUST REQUIRED.
Protective Gloves: IMPERVIOUS GLOVES (FP N).
Eye Protection: ANSI APPROVED CHEM WORKERS GOGGS (FP N).
Other Protective Equipment: NONE SPECIFIED BY MANUFACTURER.
Work Hygienic Practices: WASH WITH SOAP AND WATER.
Suppl. Safety & Health Data: SPEC GRAV:0.94 @ SOLID/0.78 @ LIQ. MATLS TO AVOID:TETRACHLORIDE) DMSO.

Transportation Data

Disposal Data

Label Data

Label Required: YES
Technical Review Date: 15NOV94
Label Status: G
Common Name: DECABORANE, 150784
Chronic Hazard: NO
Signal Word: DANGER!
Acute Health Hazard-Moderate: X
Contact Hazard-Slight: X
Fire Hazard-Severe: X
Reactivity Hazard-None: X
Special Hazard Precautions: FLAMMABLE. ACUTE:POISON BY INHALATION, INGESTION, SKIN CONTACT AND INTRAPERITONEAL ROUTES. MODERATE TO SEVERE ERYTHEMA (REDNESS) AND MODERATE EDEMA (RAISED SKIN). CHRONIC:NONE SPECIFIED BY MANUFACTURER.
Protect Eye: Y
Protect Skin: Y
Protect Respiratory: Y
Label Name: ICN BIOMEDICALS
Label Street: 1263 S. CHILLICOTHE RD
Label City: AURORA
Label State: OH
Label Zip Code: 44202
Label Country: US
Label Emergency Number: 800-424-9300 (CHEMTREC)

* MSDS prepared by ICN BIOMEDICALS. MSDS sheet obtained from

APPENDIX I.B

NMR Spectra of Selected Carborane Anions

Table of Contents

Carboranes

Note: **Bold values** in the 2-D ^{11}B–^{11}B NMR assignments signify B–F boron vertices. For spectra of mixtures, impurities are labeled (*).

1. Cs(12–$CB_{11}H_{11}F$) in acetone-d_6: $^{11}B\{^1H\}$ and ^{11}B NMR spectra

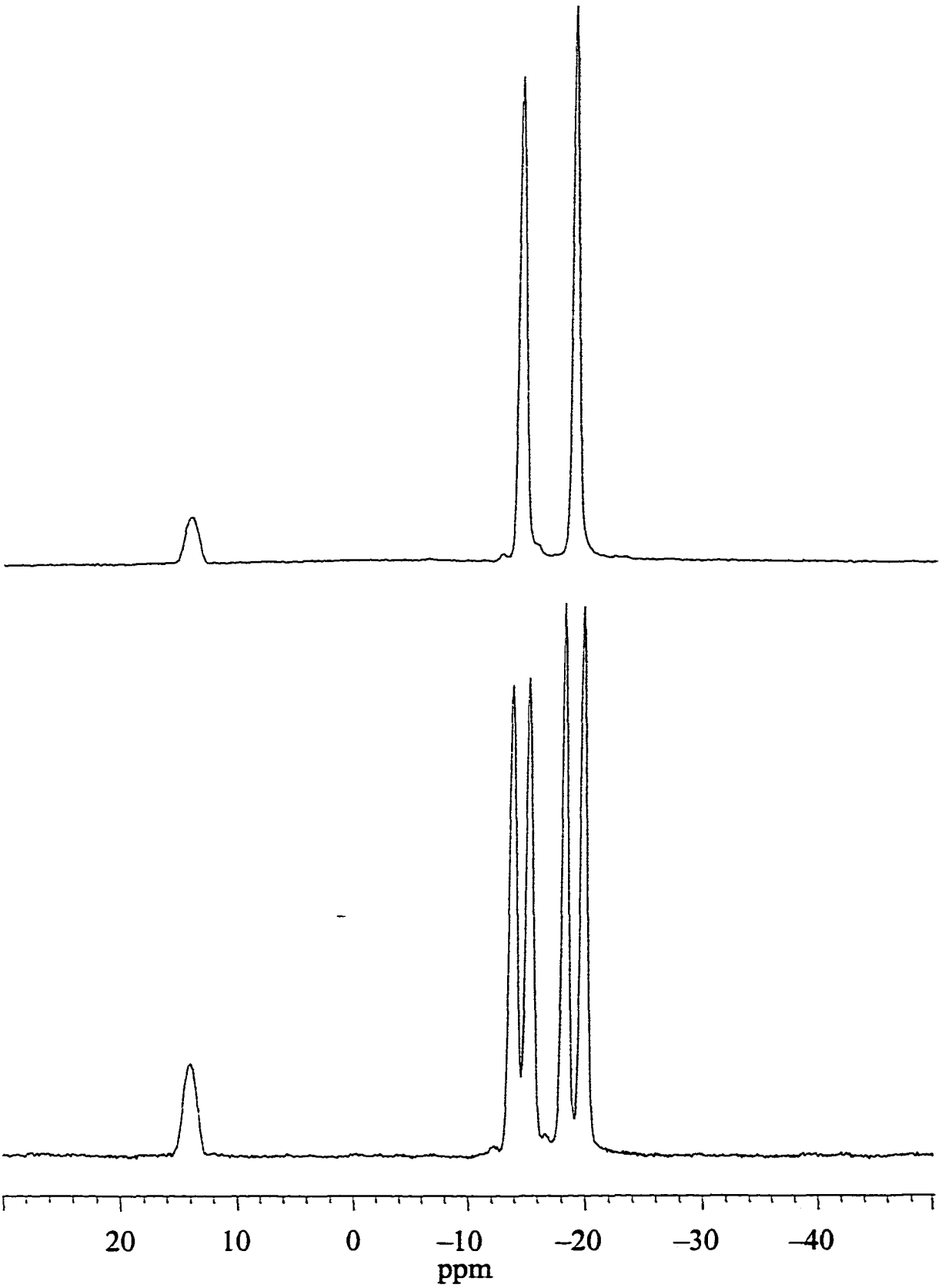

1. Cs(12–$CB_{11}H_{11}F$) in acetone-d_6: $^{19}F\{^{11}B\}$ and ^{19}F NMR spectra

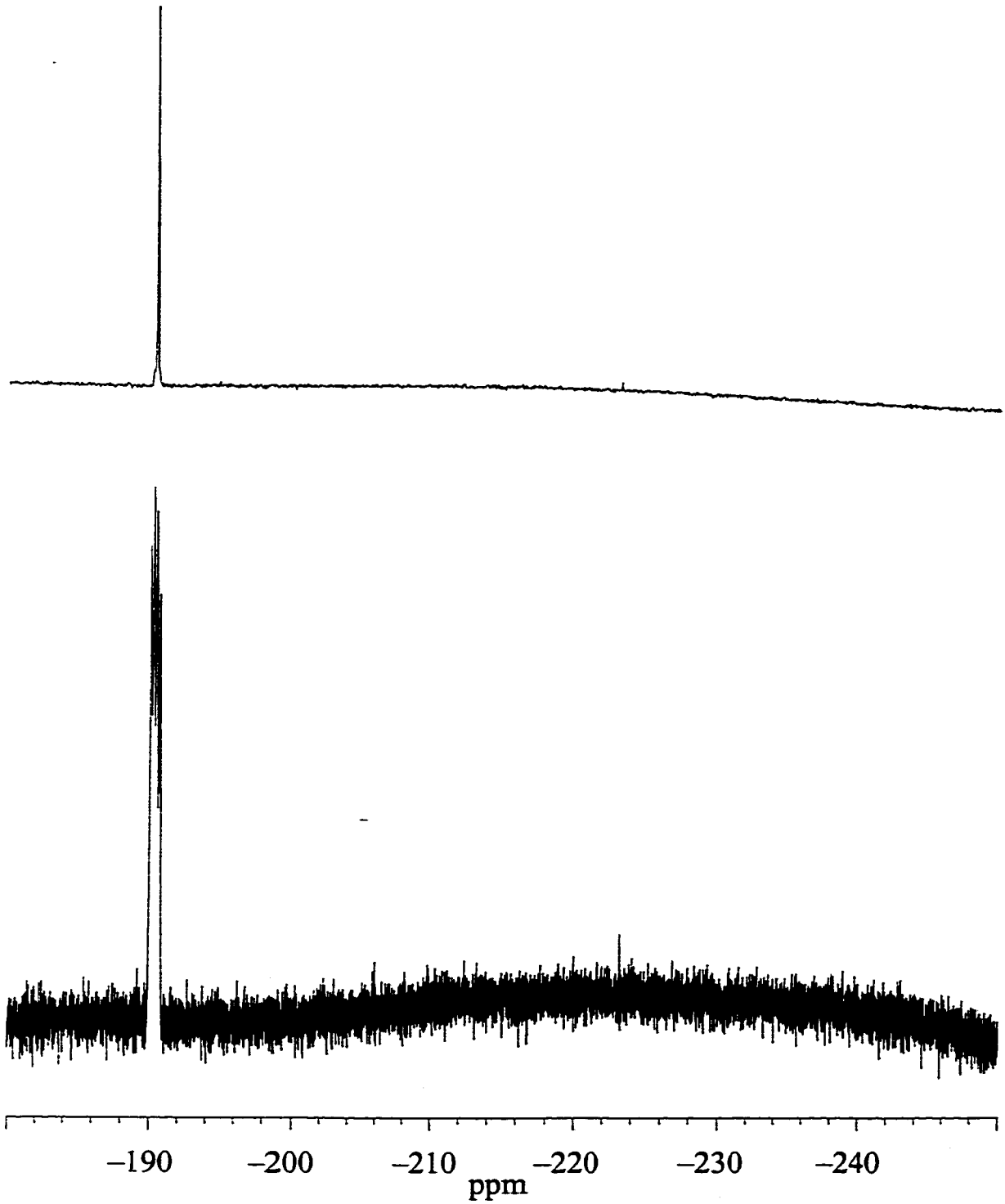

1. Cs(12-$CB_{11}H_{11}F$) in acetone-d_6: $^{11}B\{^1H\}$–$^{11}B\{^1H\}$ COSY spectrum

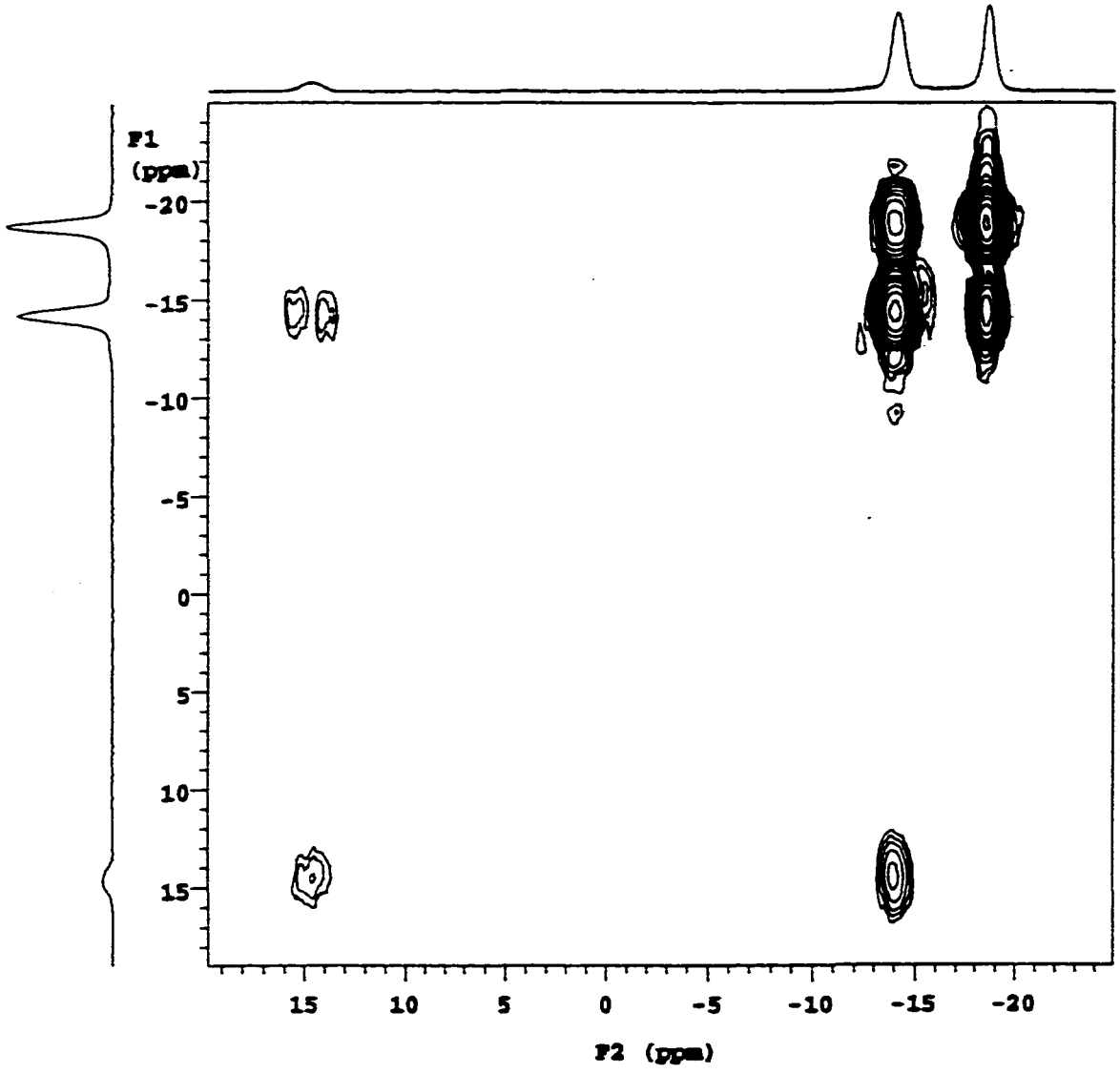

Expected Couplings:

B(12)	→	B(7–11)
B(7–11)	→	**B(12)**; B(2-6)
B(2–6)	→	B(7–11)

2. $Cs(7,12\text{-}CB_{11}H_{10}F_2)$ in acetone-d_6: $^{11}B\{^1H\}$ and ^{11}B NMR spectra

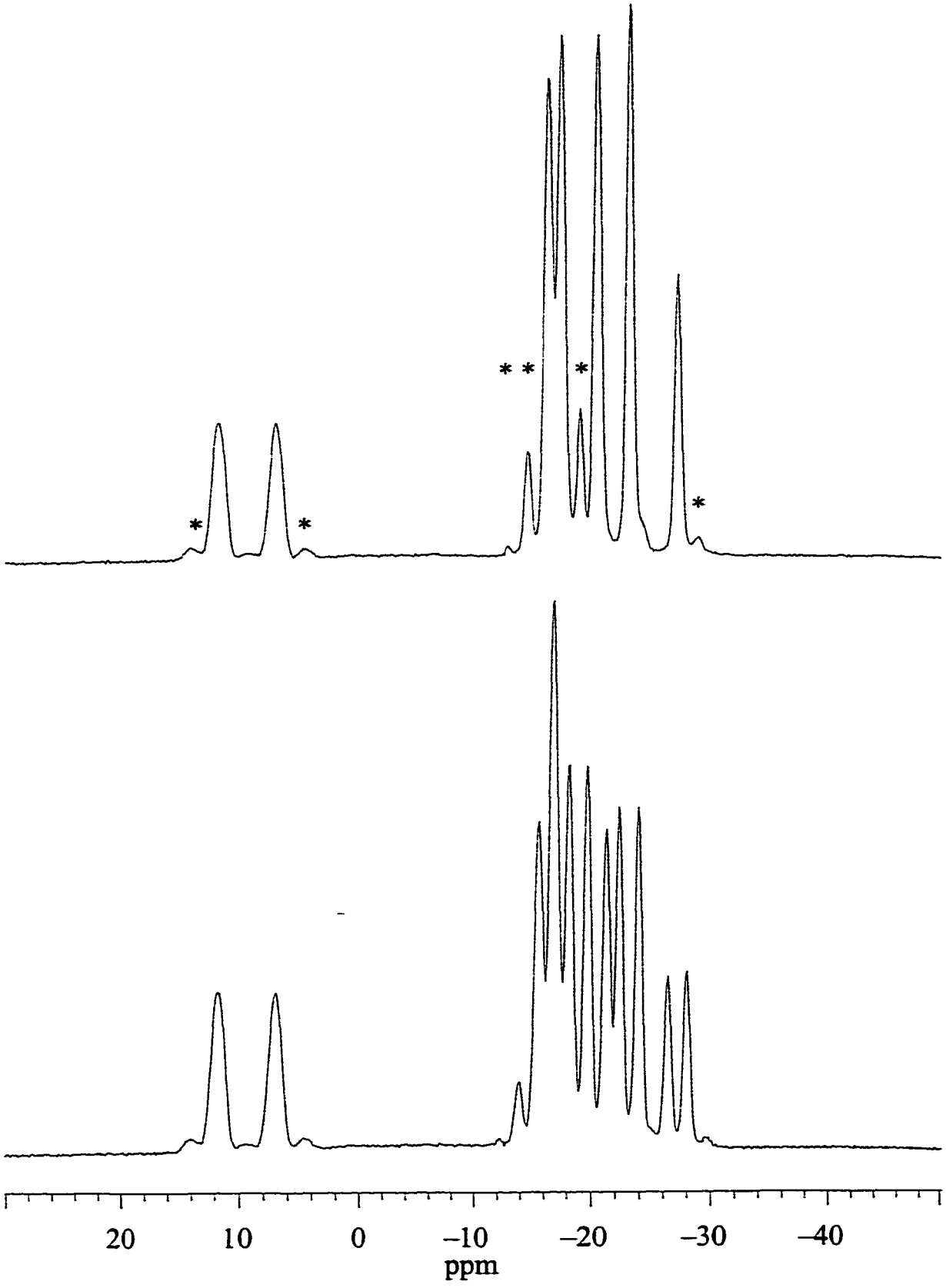

2. $Cs(7,12\text{-}CB_{11}H_{10}F_2)$ in acetone-d_6: $^{19}F\{^{11}B\}$ and ^{19}F NMR spectra

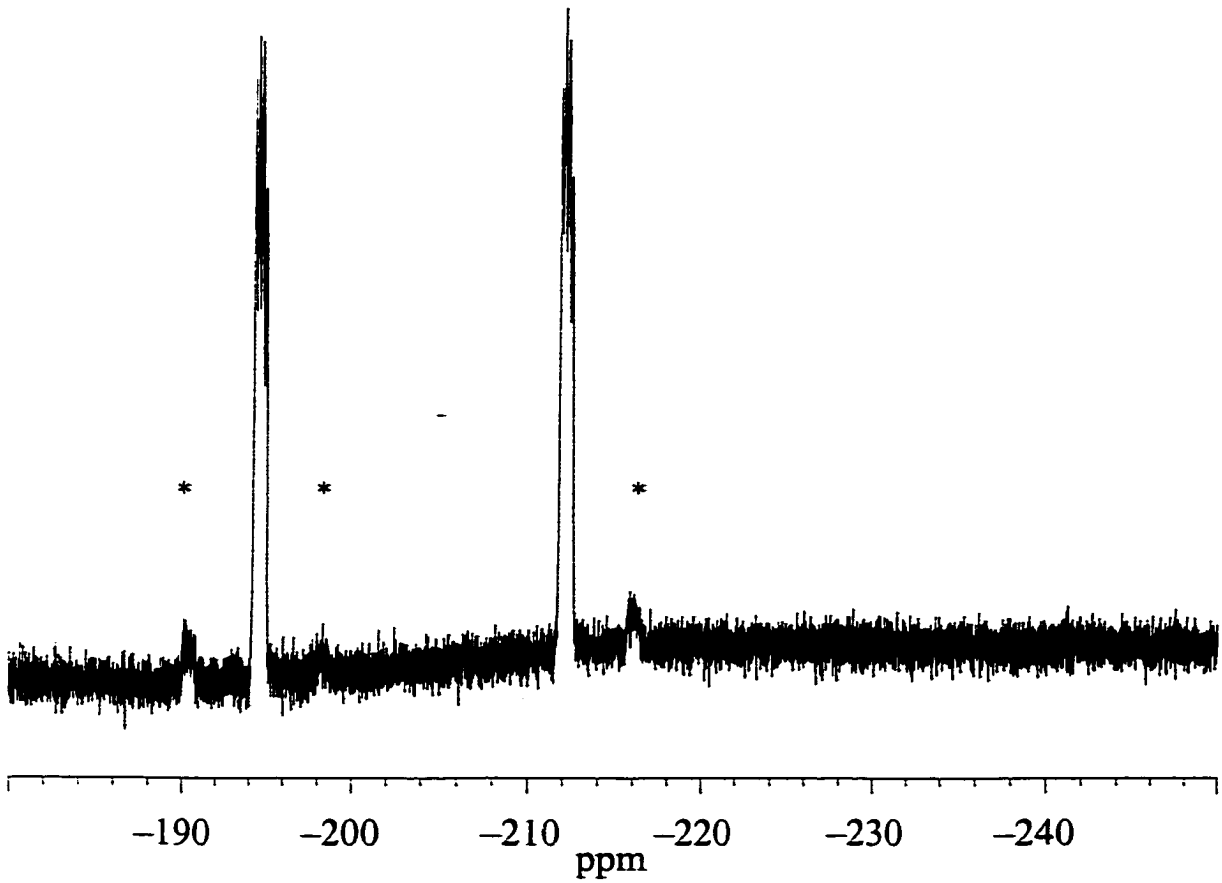

2. Cs(7,12-$CB_{11}H_{10}F_2$) in acetone-d_6: $^{11}B\{^1H\}$–$^{11}B\{^1H\}$ COSY spectrum

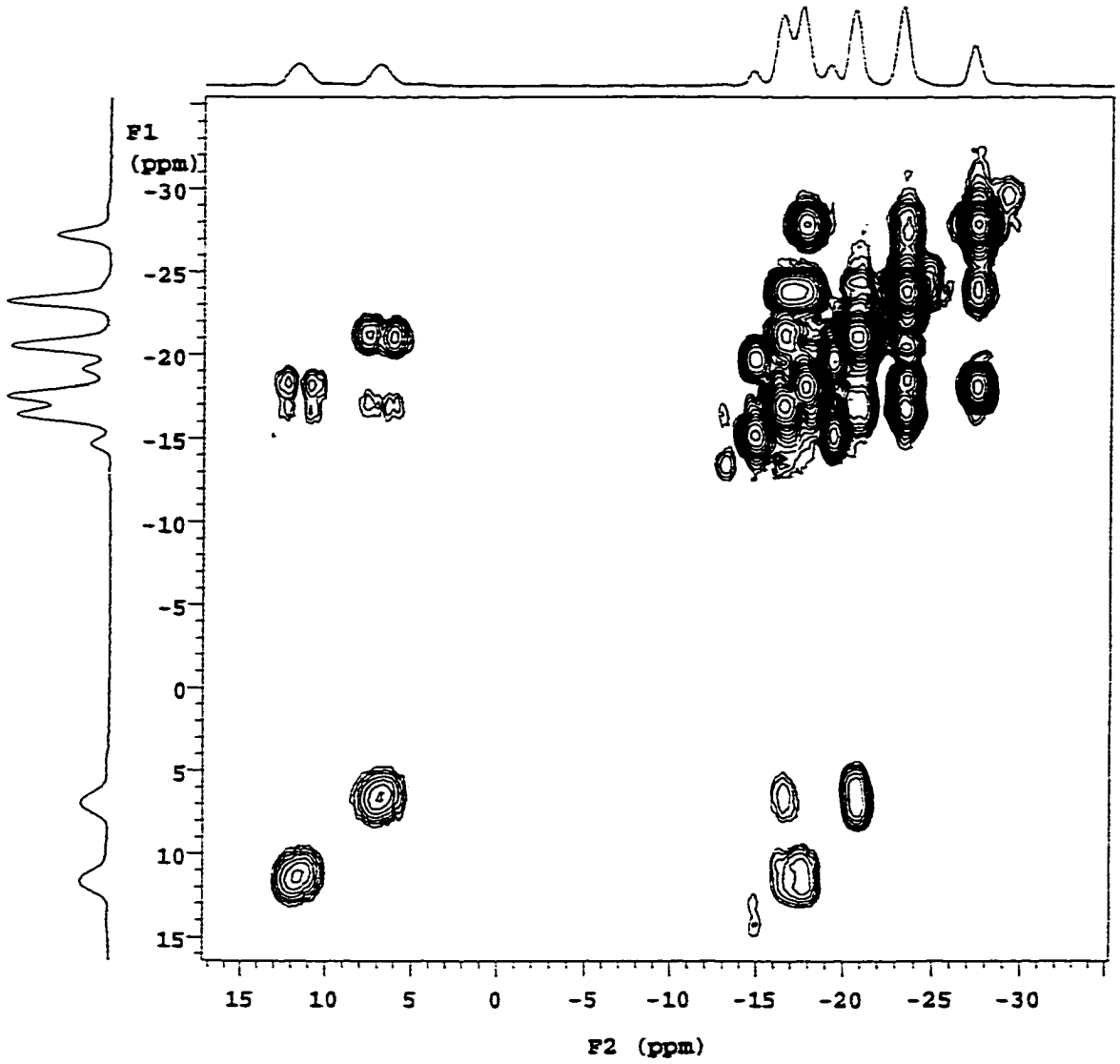

Expected Couplings:

B(12)	→	**B(7)**; B(8,11); B(9,10)
B(7)	→	**B(12)**; B(8,11); B(2,3)
B(8,11)	→	**B(12)**; B(9,10); B(2,3); B(4,6)
B(9,10)	→	**B(12)**; B(8,11); B(4,6); B(5)
B(2,3)	→	**B(7)**; B(8,11); B(4,6)
B(4,6)	→	B(5); B(2,3); B(8,11); B(9,10)
B(5)	→	B(4,6); B(9,10); B(4,6)

2. Cs(7,12-$CB_{11}H_{10}F_2$) in acetone-d_6: $^1H\{^{11}B\}$–^{11}B HMQC spectrum

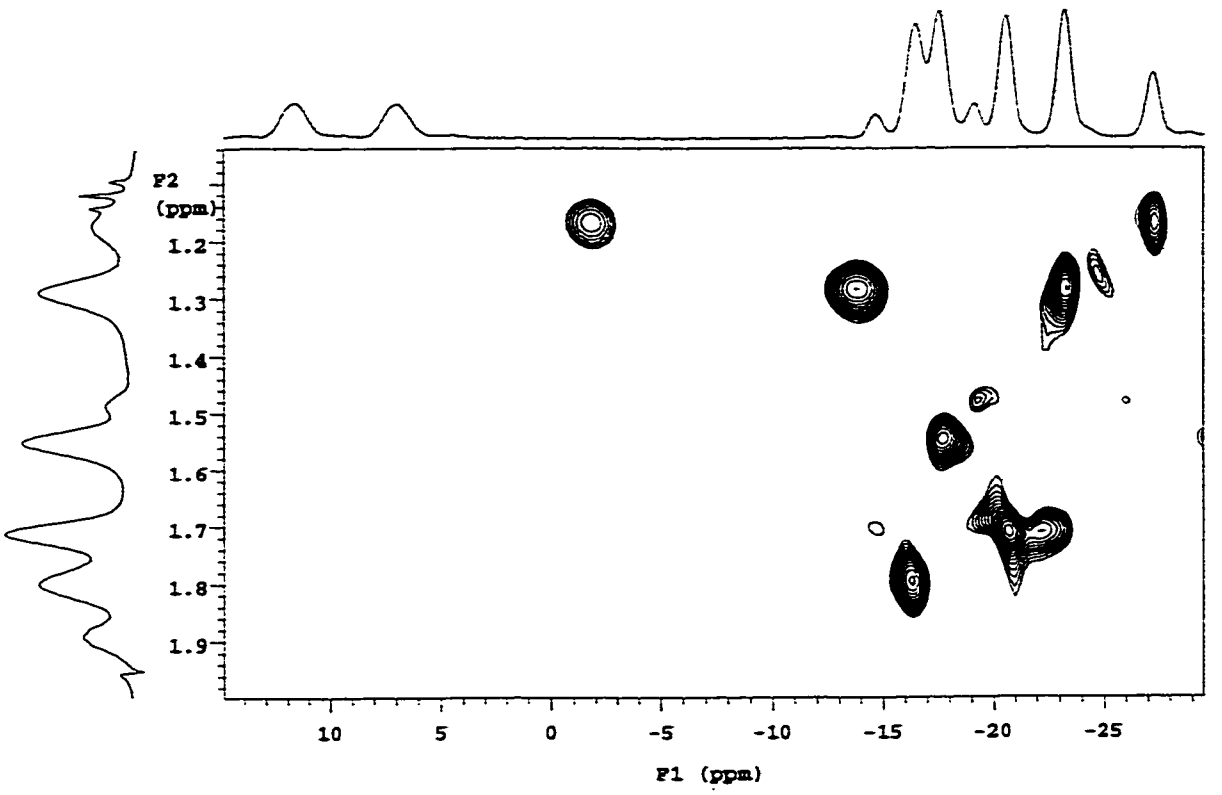

3. Cs(7,9,12-$CB_{11}H_9F_3$) in acetone-d_6: $^{11}B\{^1H\}$ and ^{11}B NMR spectra

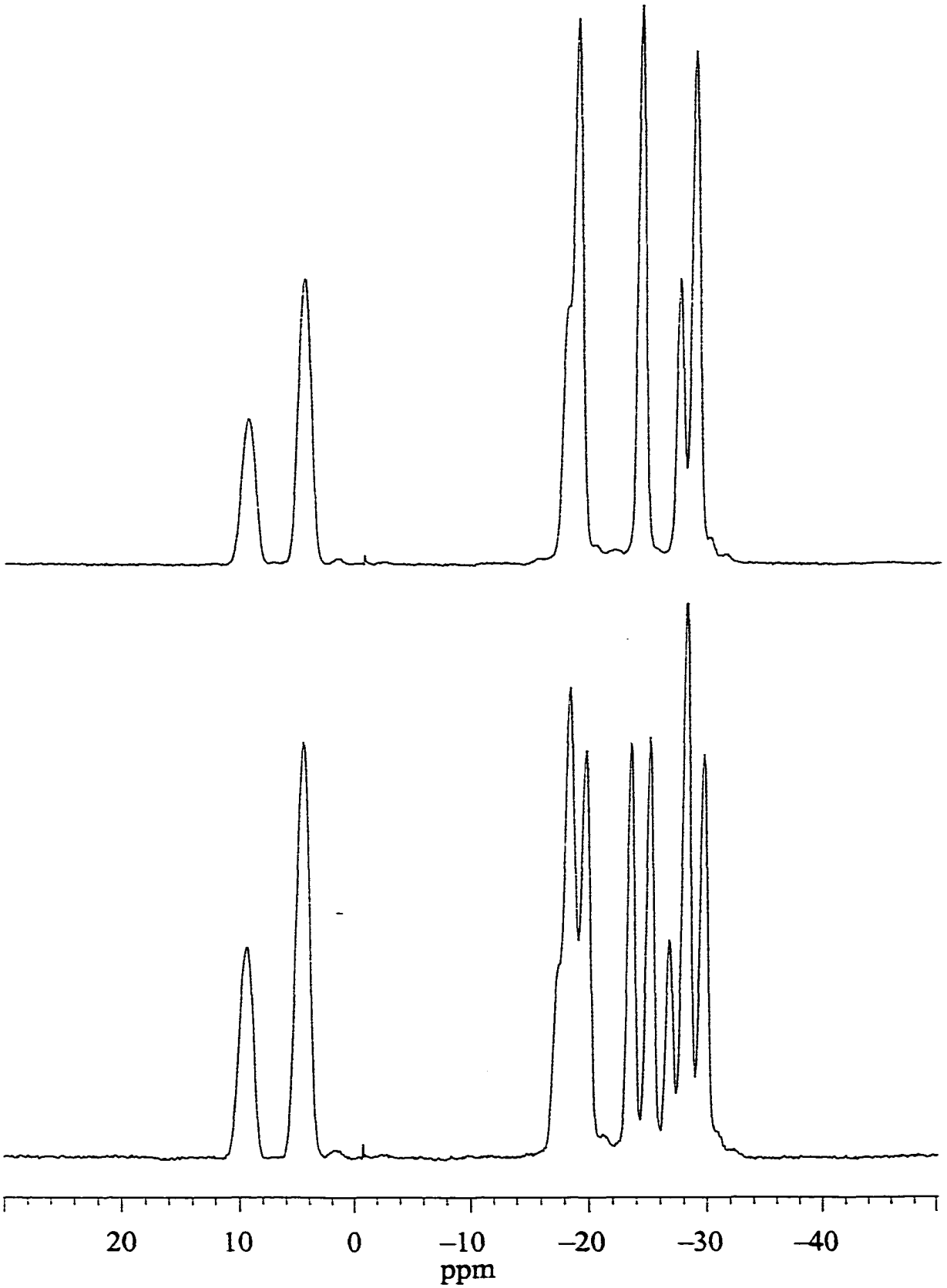

3. $Cs(7,9,12\text{-}CB_{11}H_9F_3)$ in acetone-d_6: $^{19}F\{^{11}B\}$ and ^{19}F NMR spectra

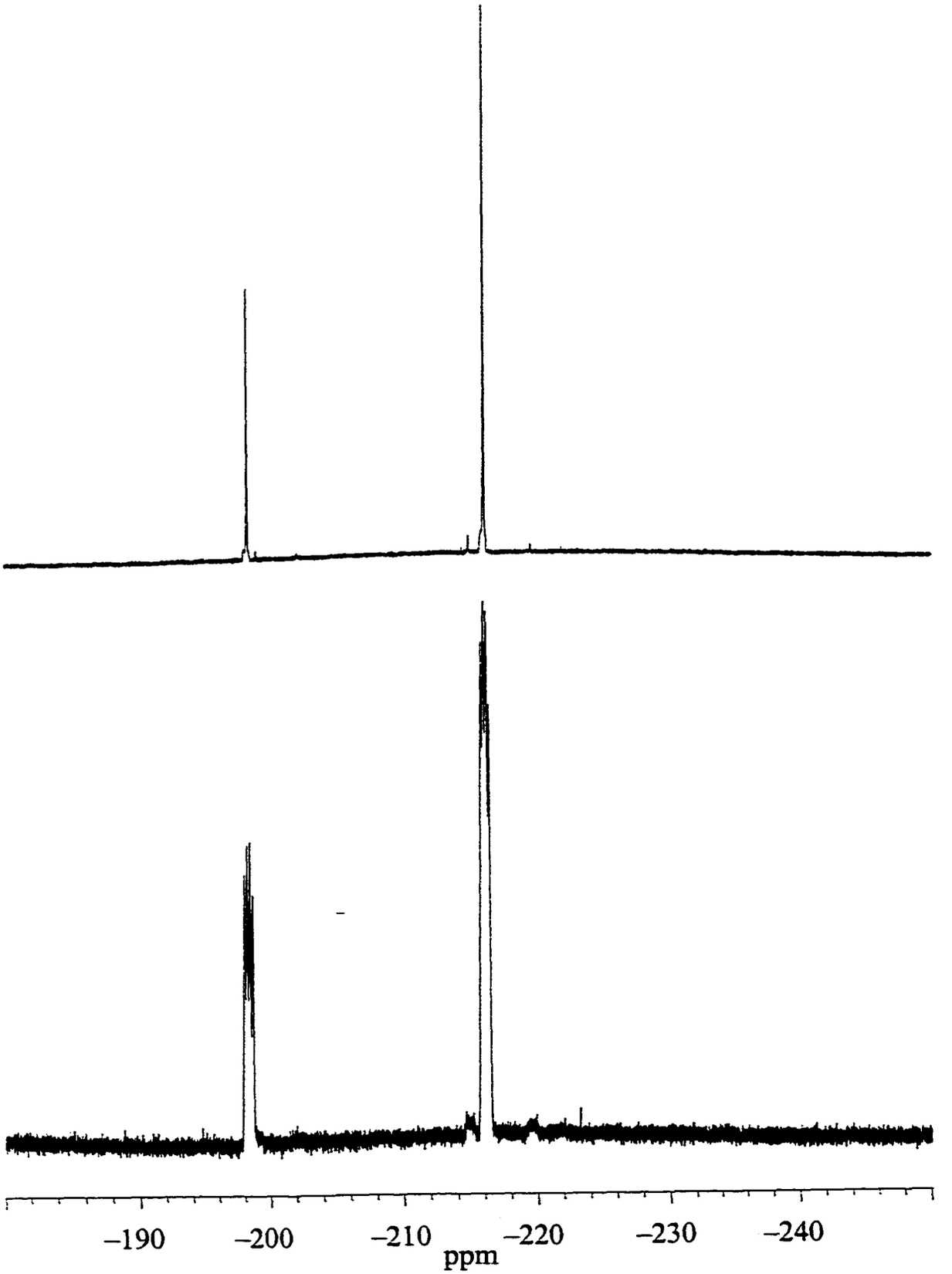

3. Cs(7,9,12-$CB_{11}H_9F_3$) in acetone-d_6: $^{11}B\{^1H\}$–$^{11}B\{^1H\}$ COSY NMR spectrum

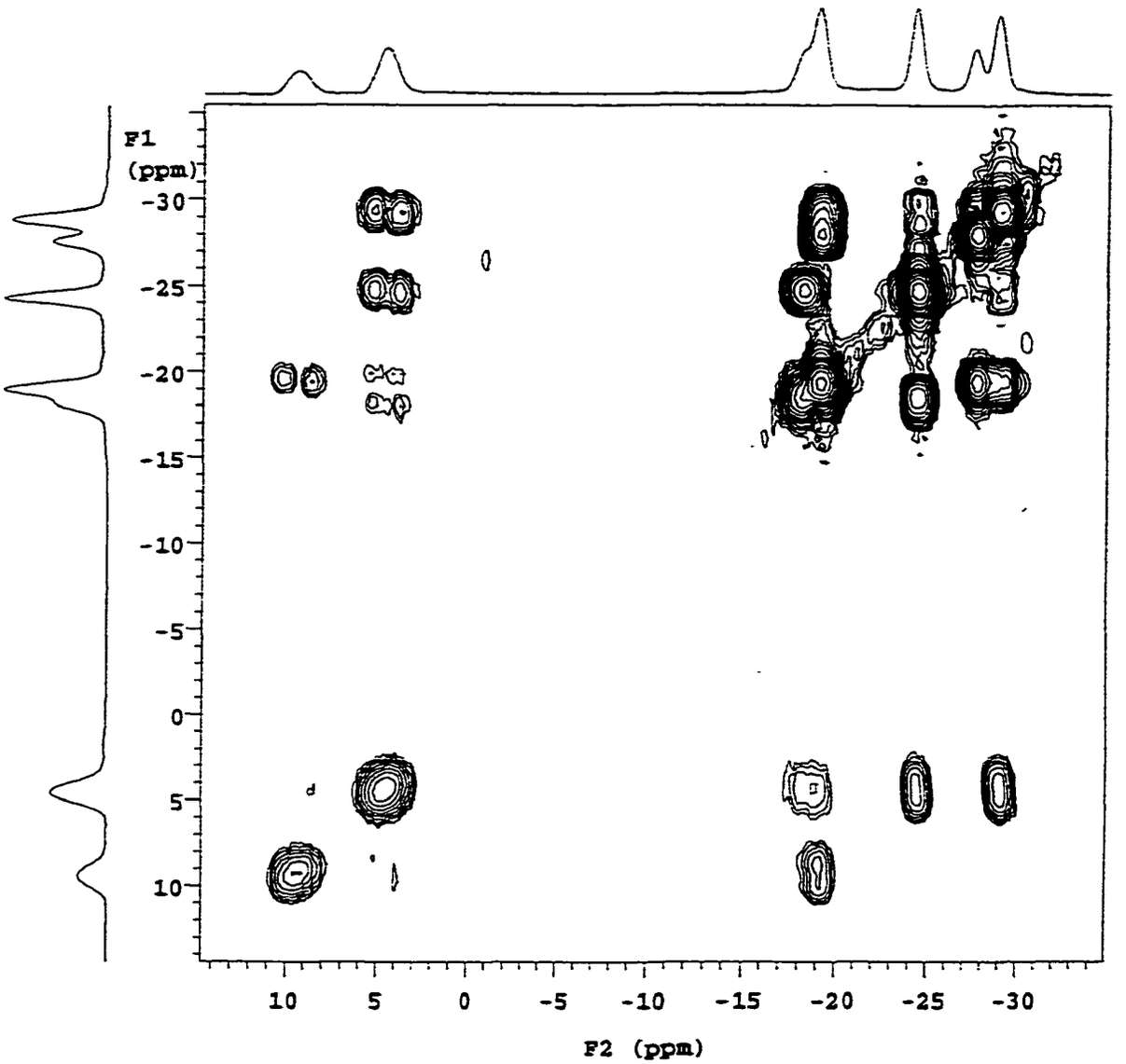

Expected Couplings:

B(12)	→	**B(7,9)**; B(8); B(10,11)
B(7,9)	→	**B(12)**; B(8); B(10,11); B(2,5); B(3,4)
B(8)	→	**B(12)**; **B(7,9)**; B(3,4)
B(10,11)	→	**B(12)**; **B(7,9)**; B(6); B(2,5)
B(2,5)	→	**B(7,9)**; B(10,11); B(3,4); B(6)
B(3,4)	→	**B(7,9)**; B(8); B(2,5)
B(6)	→	B(10,11); B(2,5)

3. $Cs(7,9,12\text{-}CB_{11}H_9F_3)$ in acetone-d_6: $^1H\{^{11}B\}$–^{11}B HMQC NMR spectrum

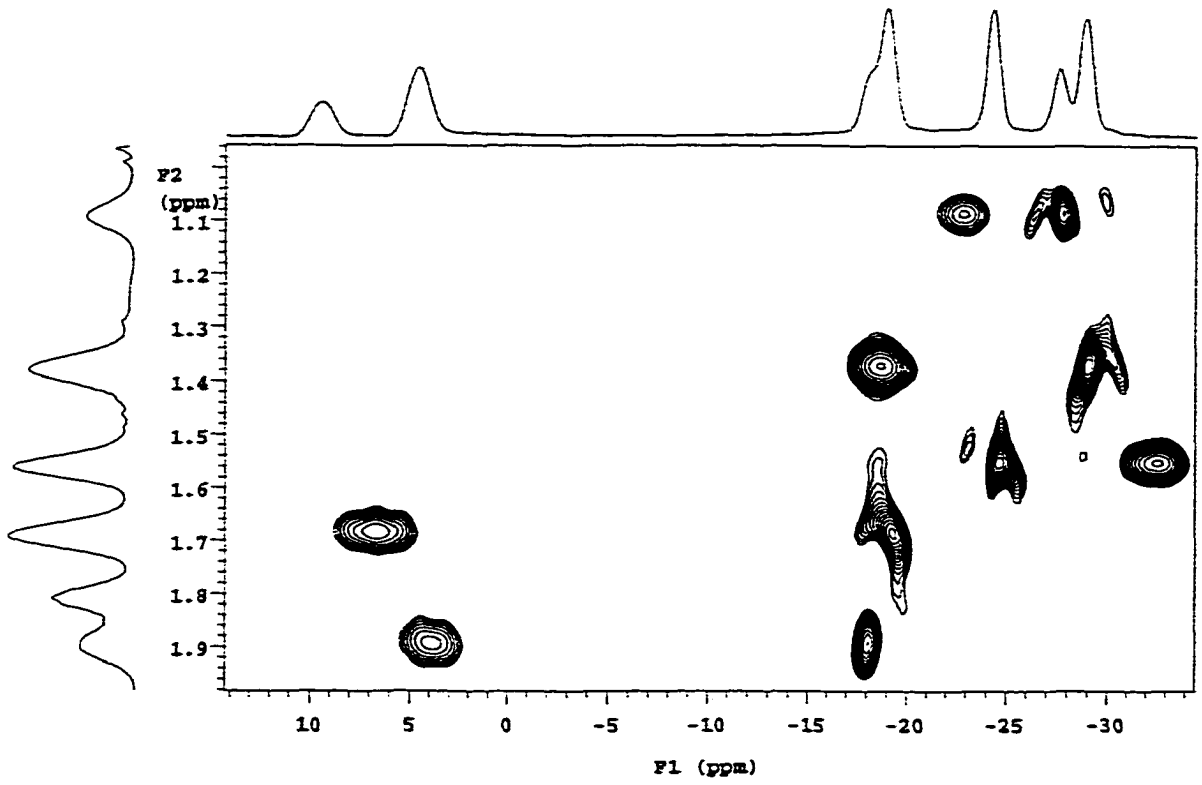

4. Cs(7,9,10,12-$CB_{11}H_8F_4$) in acetone-d_6: $^{11}B\{^1H\}$–$^{11}B\{^1H\}$ COSY spectrum

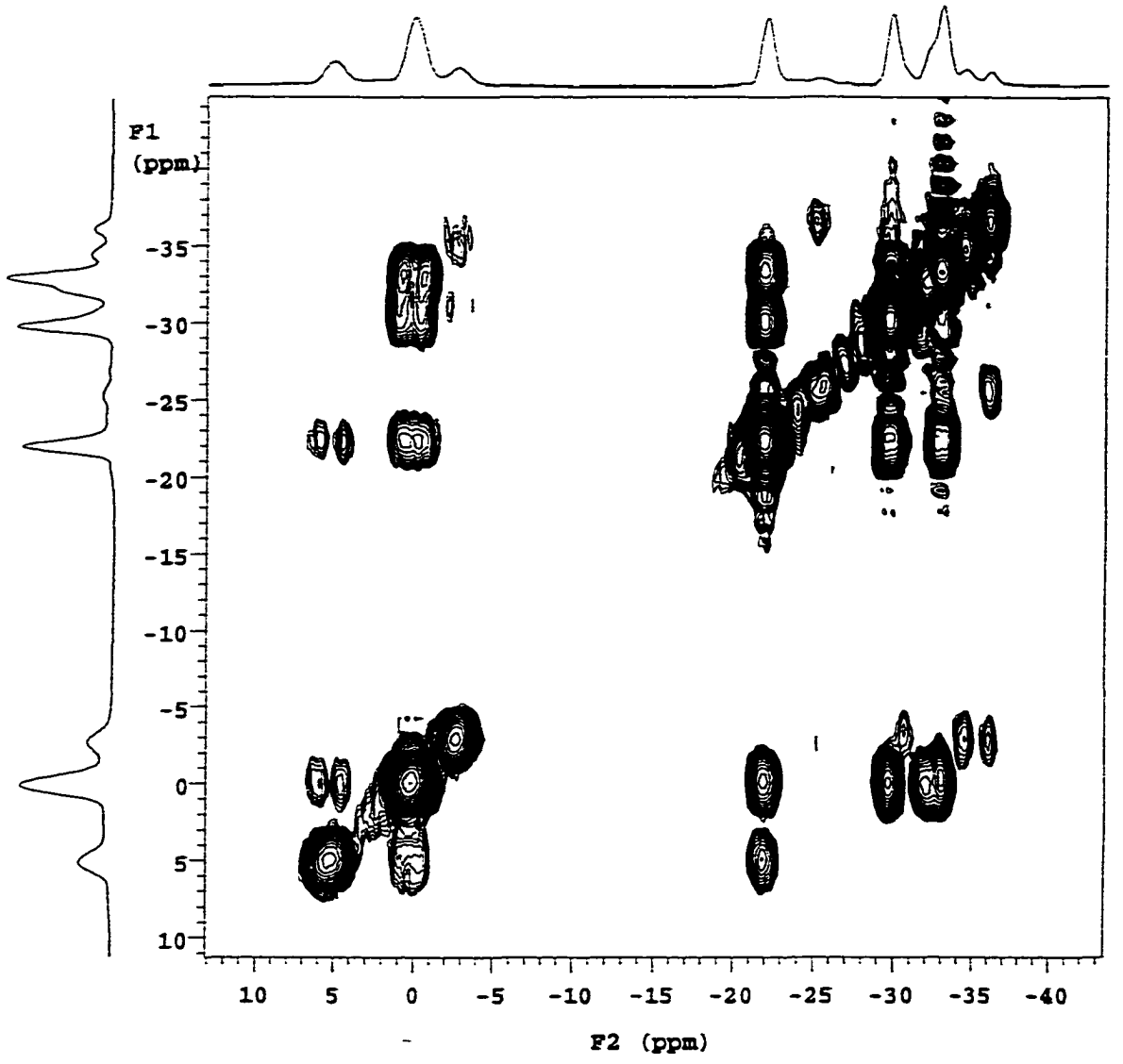

Expected Couplings:

B(12)	→	**B(7)**; **B(9,10)**; B(8,11)
B(7)	→	**B(12)**; B(8,11); B(2,3)
B(9,10)	→	**B(12)**; B(8,11); B(4,6); B(5)
B(8,11)	→	**B(12)**; **B(7)**; **B(9,10)**; B(4,6); B(2,3)
B(4,6)	→	**B(9,10)**; B(8,11); B(5); B(2,3);
B(5)	→	**B(9,10)**; B(4); B(4,6)
B(2,3)	→	**B(7,10)**; B(8,11); B(4,6)

5. Cs(7,8,9,10,12-$CB_{11}H_7F_5$) in acetone-d_6: $^{11}B\{^1H\}$–$^{11}B\{^1H\}$ COSY NMR

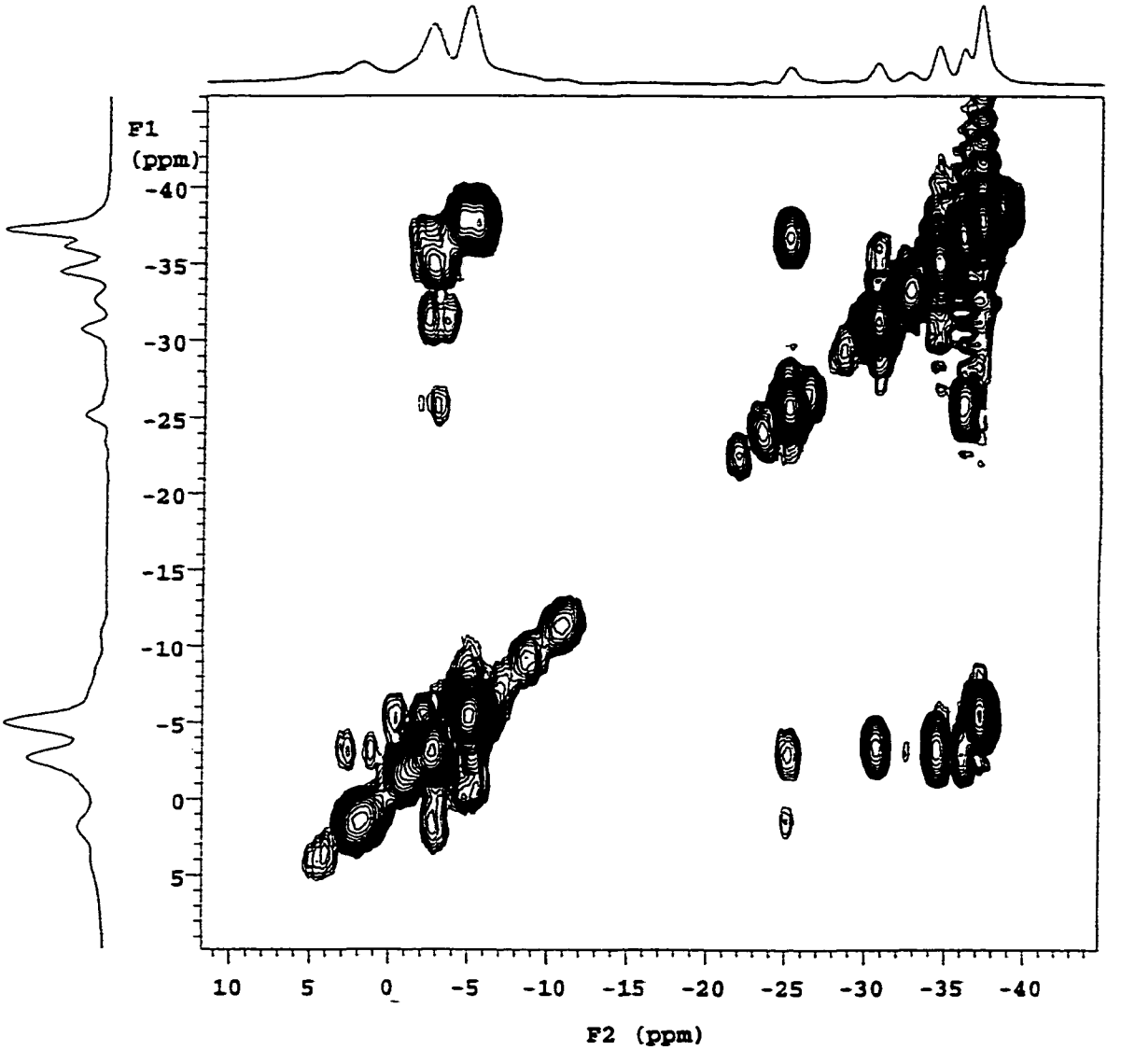

Expected Couplings:

B(12)	→	**B(7,10)**; **B(8,9)**; B(11)
B(7,10)	→	**B(12)**; **B(8,9)**; B(11); B(3,5); B(2,6)
B(8,9)	→	**B(12)**; **B(7,10)**; B(4); B(3,5)
B(11)	→	**B(12)**; **B(7,10)**; B(2,6)
B(4)	→	**B(8,9)**; B(3,5)
B(3,5)	→	**B(7,10)**; B(8,9); B(4); B(2,6)
B(2,6)	→	**B(7,10)**; B(11); B(3,5)

5. Cs(7,8,9,10,12-$CB_{11}H_7F_5$) in acetone-d_6: $^1H\{^{11}B\}$–^{11}B HMQC spectrum

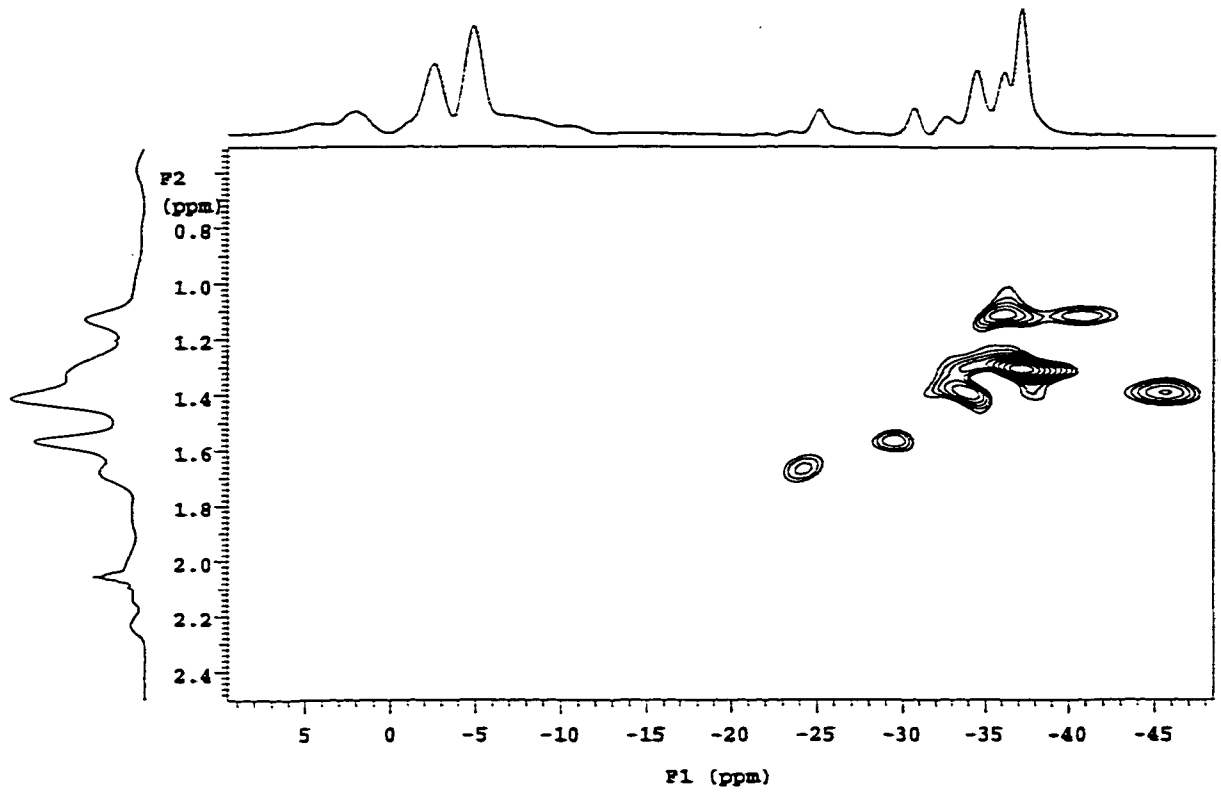

6. $Cs(7\text{–}12\text{-}CB_{11}H_6F_6)$ in acetone-d_6: $^{11}B\{^1H\}$ and ^{11}B NMR spectra

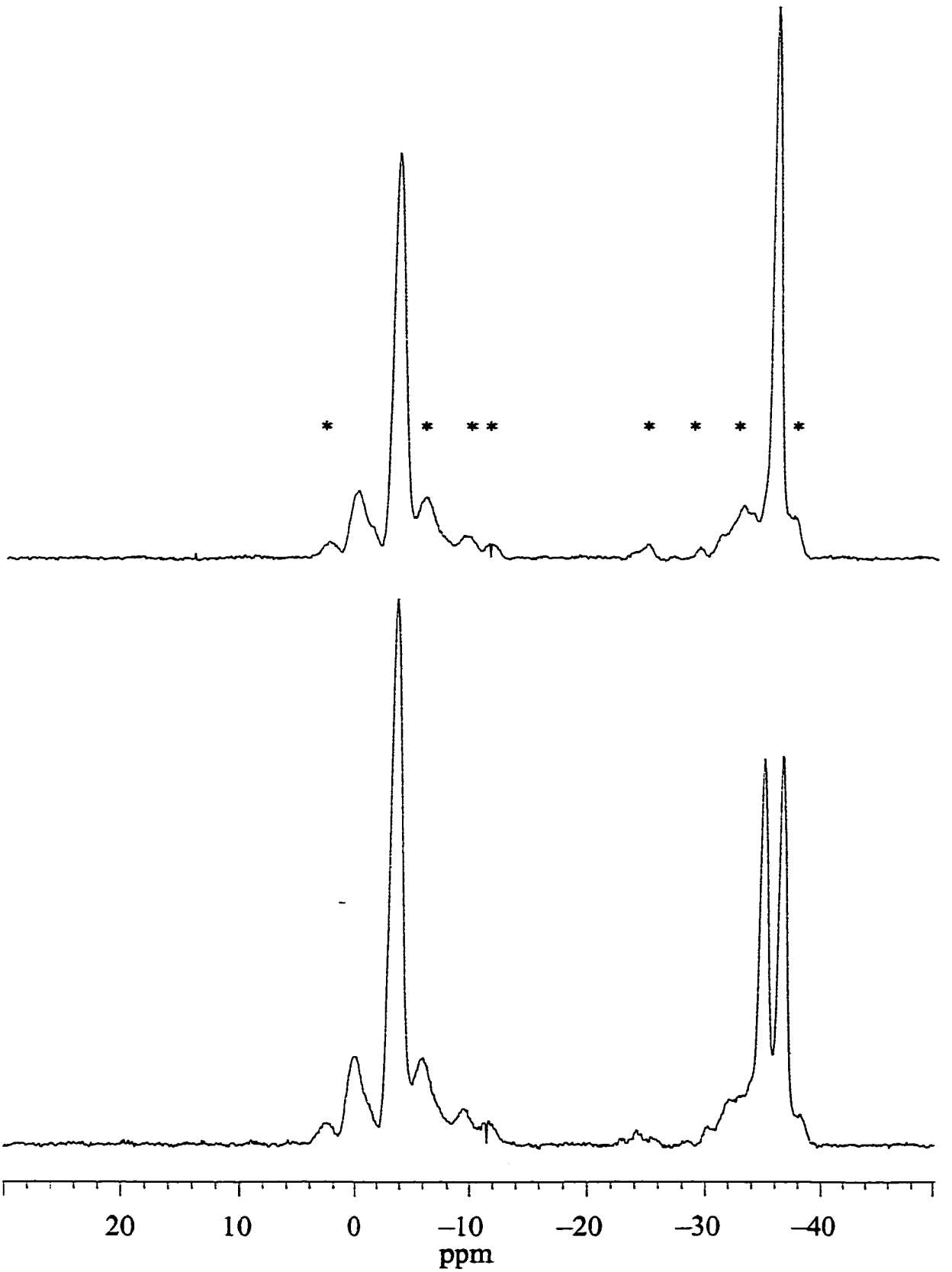

6. Cs(7–12-$CB_{11}H_6F_6$) in acetone-d_6: $^{19}F\{^{11}B\}$ and ^{19}F NMR spectra

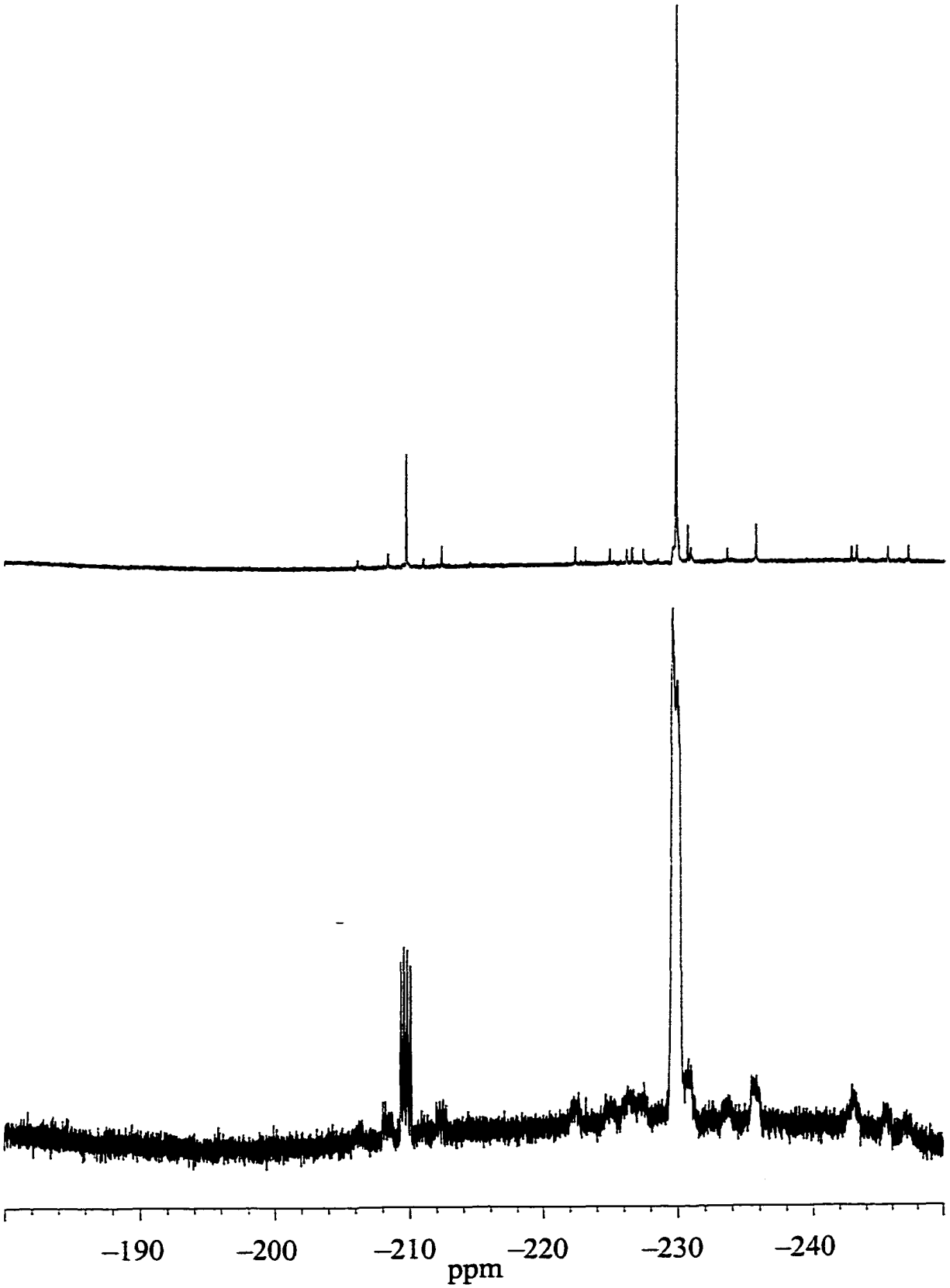

6. Cs(7–12-$CB_{11}H_6F_6$) in acetone-d_6: $^1H\{^{11}B\}$–^{11}B HMQC spectrum

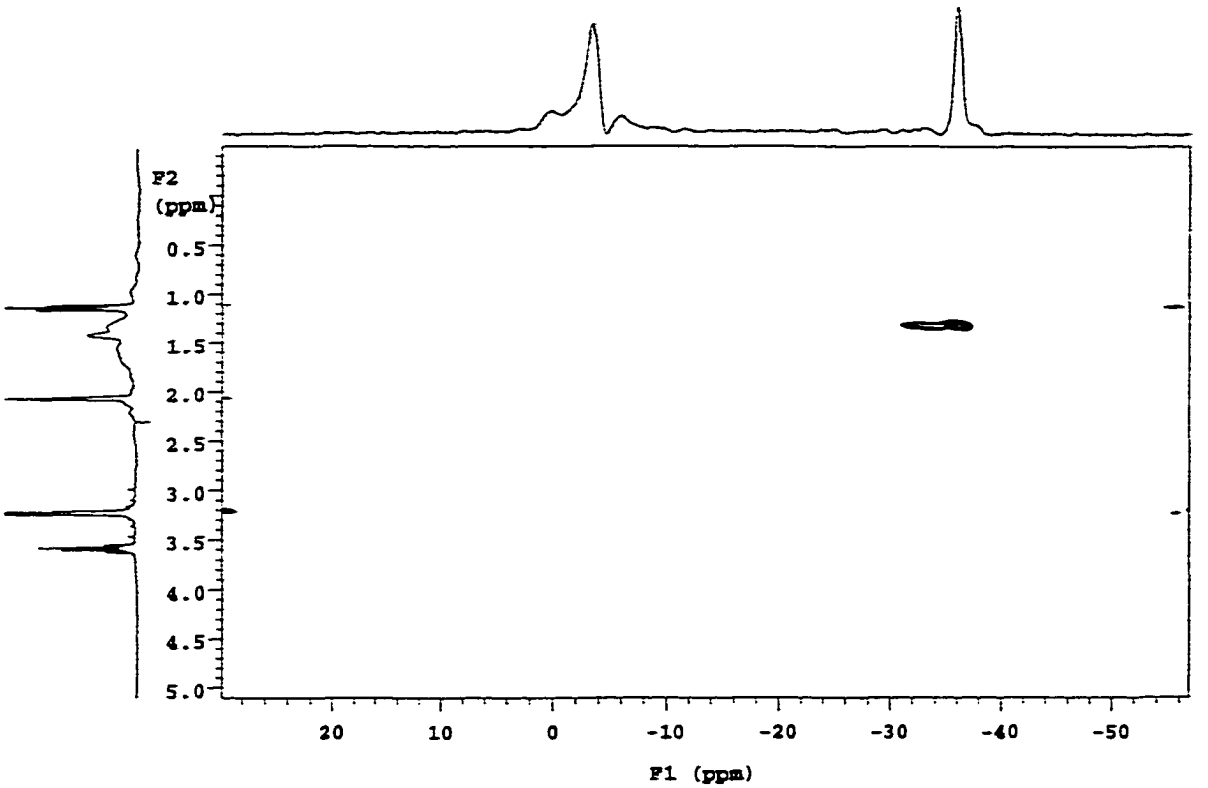

APPENDIX I.C

Antipodal Atom Pairs in Heteroborane Anions

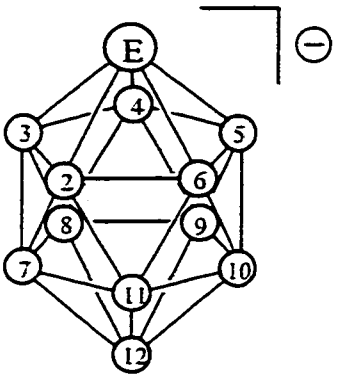

$$EB_{11}H_{11}^{-}$$

(E = CH, As, Sb, Bi)

In a twelve-vertex cluster, antipodal atom pairs are atoms at opposite vertices. In order for this effect to manifest itself, it is necessary to have a plane of symmetry between the two atoms, a condition that holds for all of the clusters examined in this work.

Antipodal Atom Pairs

1↔12

2↔ 9

3↔10

4↔11

5↔ 7

6↔ 8

APPENDIX I.D

Selected Crystallographic Information from the

$Cs(BiB_{11}H_{11})\cdot 0.33(OC(CH_3)_2)$ and $Ag(C_6H_6)_2(12\text{-}CB_{11}H_{11}F)$ Structures

(Part I, Chapter 2)

$Cs(BiB_{11}H_{11})\cdot 0.33(OC(CH_3)_2)$

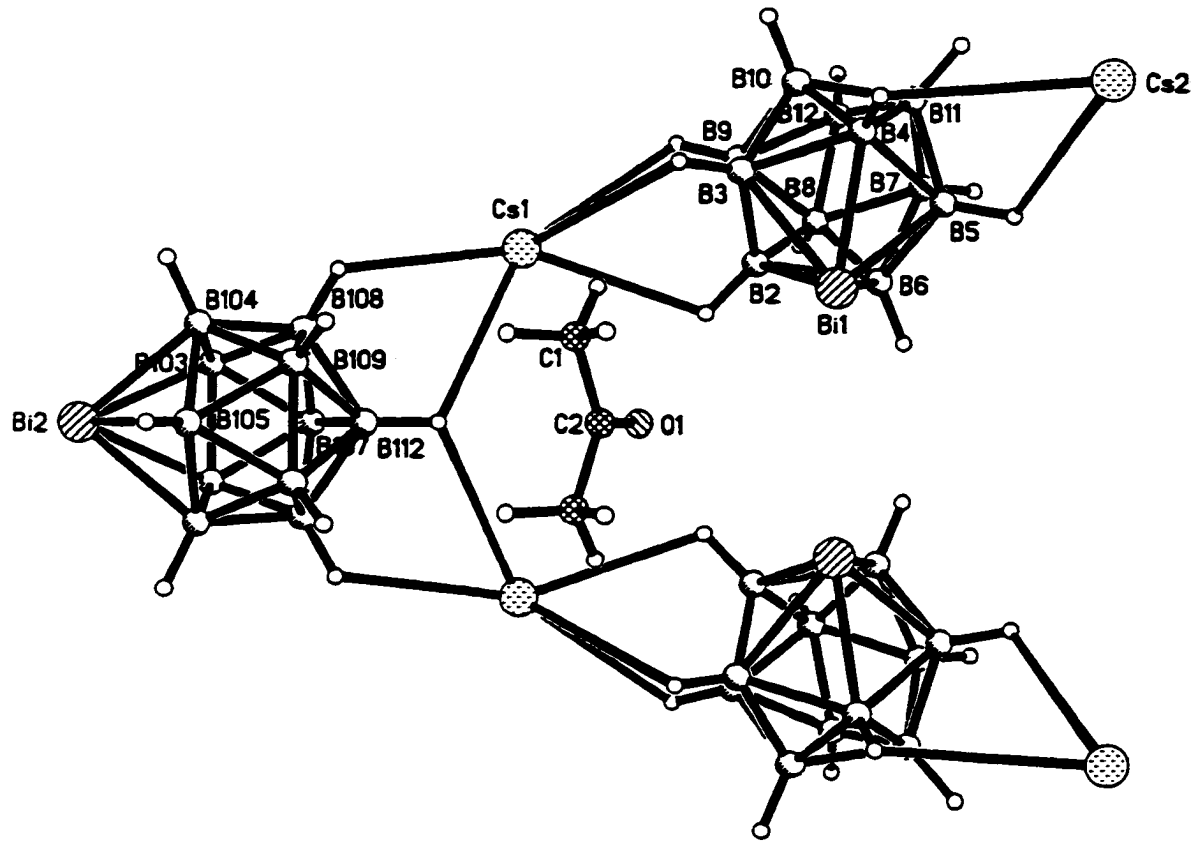

Figure AI.A.1. Crystal structure of $Cs(BiB_{11}H_{11})\cdot 0.33(OC(CH_3)_2)$ showing the numbering scheme and the unique portions of the molecule.

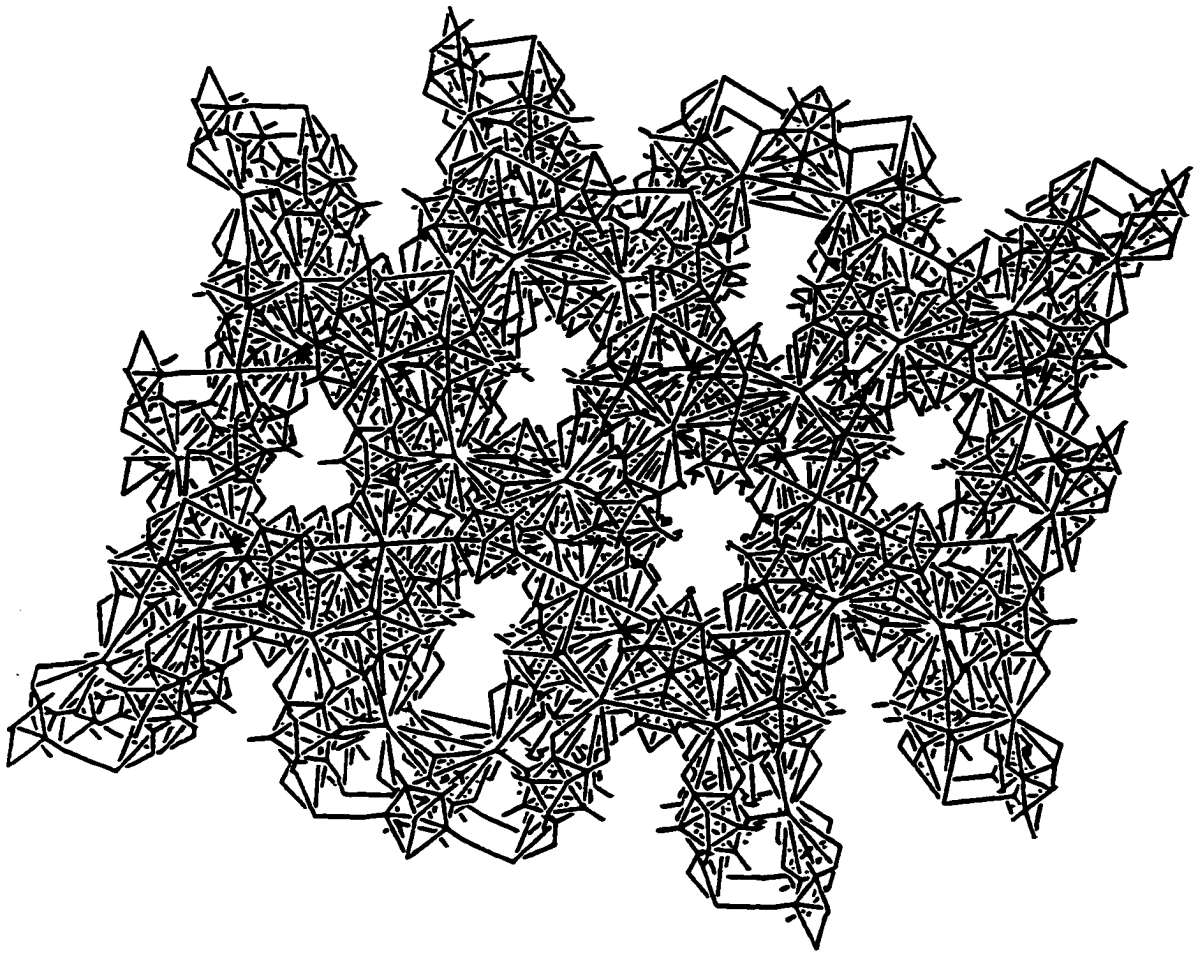

Figure AI.A.2. Crystal packing view of $Cs(BiB_{11}H_{11})\cdot 0.33(OC(CH_3)_2)$. Note the channels running through the cell.

Table 1. Crystal data and structure refinement for Bismorane.

Identification code	dkm-bismorane
Empirical formula	$CH_{13}B_{11}BiCsO_{0.33}$
Formula weight	491.25
Temperature	163(2) K
Wavelength	0.71073 Å
Crystal system	Orthorhombic
Space group	Pnma
Unit cell dimensions	a = 13.1848(2) Å alpha = 90° b = 19.9104(2) Å beta = 90° c = 14.2706(2) Å gamma = 90°
Volume, Z	3746.24(9) $Å^3$, 12
Density (calculated)	2.613 Mg/m^3
Absorption coefficient	16.940 mm^{-1}
F(000)	2576
Crystal size	0.08 x 0.22 x 0.28 mm
θ range for data collection	1.76 to 28.39°
Limiting indices	$-11 \le h \le 17$, $-26 \le k \le 26$, $-16 \le l \le 18$
Reflections collected	25881
Independent reflections	4705 (R_{int} = 0.0943)
Absorption correction	SADABS
Refinement method	Full-matrix least-squares on F^2
Data / restraints / parameters	4705 / 0 / 260
Goodness-of-fit on F^2	1.057
Final R indices [I>2σ(I)]	R1 = 0.0427, wR2 = 0.0790
R indices (all data)	R1 = 0.0721, wR2 = 0.0891
Extinction coefficient	0.00114(5)
Largest diff. peak and hole	1.928 and -2.067 $eÅ^{-3}$

Table 2. Atomic coordinates [x 10^4] and equivalent isotropic displacement parameters [$Å^2$ x 10^3] for 1. U(eq) is defined as one third of the trace of the orthogonalized U_{ij} tensor.

	x	y	z	U(eq)
O(1)	10234(11)	2500	304(13)	113(6)
C(1)	11693(10)	1873(5)	-16(8)	52(3)
C(2)	11153(10)	2500	115(9)	33(4)
Bi(1)	9548(1)	1472(1)	2198(1)	21(1)
Bi(2)	11200(1)	2500	-5563(1)	18(1)
Cs(1)	8888(1)	1104(1)	-1330(1)	23(1)
Cs(2)	10000	0	5000	29(1)
B(2)	8169(8)	1212(5)	1140(7)	18(2)
B(3)	9190(8)	537(5)	1161(7)	19(2)
B(4)	9358(7)	279(5)	2416(7)	17(2)
B(5)	8428(8)	782(5)	3155(7)	20(2)
B(6)	7736(8)	1360(4)	2368(7)	20(2)
B(7)	7214(7)	584(5)	2772(6)	16(2)
B(8)	7054(8)	834(5)	1572(7)	20(2)
B(9)	7900(7)	360(5)	882(6)	15(2)
B(10)	8609(7)	-182(5)	1616(7)	17(2)
B(11)	8178(8)	-48(5)	2781(7)	19(2)
B(12)	7312(8)	-10(4)	1843(7)	18(2)
B(103)	9882(8)	2026(5)	-4585(7)	23(2)
B(104)	11184(8)	1740(4)	-4243(6)	17(2)
B(105)	11985(10)	2500	-4038(10)	17(3)
B(108)	10186(8)	1772(5)	-3435(7)	24(2)
B(109)	11422(8)	2049(4)	-3099(7)	19(2)
B(112)	10322(12)	2500	-2701(9)	23(3)
B(107)	9406(10)	2500	-3604(11)	24(3)

Table 3. Bond lengths [Å] and angles [°] for 1.

O(1)-C(2)	1.24(2)	C(1)-C(2)	1.449(12)
C(2)-C(1)#1	1.449(12)	Bi(1)-B(4)	2.409(9)
Bi(1)-B(6)	2.412(11)	Bi(1)-B(2)	2.420(10)
Bi(1)-B(3)	2.424(10)	Bi(1)-B(5)	2.435(10)
Bi(2)-B(105)	2.411(14)	Bi(2)-B(104)#1	2.416(9)
Bi(2)-B(104)	2.416(9)	Bi(2)-B(103)	2.421(10)
Bi(2)-B(103)#1	2.421(10)	Cs(1)-B(2)	3.656(10)
Cs(1)-B(11)#2	3.667(10)	Cs(1)-B(108)	3.704(10)
Cs(1)-B(9)	3.723(9)	Cs(1)-B(12)#2	3.747(9)
Cs(1)-B(3)	3.751(10)	Cs(1)-B(105)#3	3.781(9)
Cs(1)-B(10)#4	3.798(9)	Cs(1)-B(109)#3	3.844(10)
Cs(1)-B(104)#3	3.872(10)	Cs(1)-B(7)#2	3.879(9)
Cs(1)-B(112)	3.889(10)	Cs(2)-B(5)	3.695(10)
Cs(2)-B(5)#5	3.695(10)	Cs(2)-B(4)	3.824(10)
Cs(2)-B(4)#5	3.824(10)	Cs(2)-B(8)#6	3.889(10)
Cs(2)-B(8)#7	3.889(10)	Cs(2)-B(104)#4	3.951(9)
Cs(2)-B(104)#8	3.951(9)	B(2)-B(8)	1.763(14)
B(2)-B(9)	1.772(13)	B(2)-B(6)	1.867(14)
B(2)-B(3)	1.901(13)	B(3)-B(10)	1.749(14)
B(3)-B(9)	1.781(13)	B(3)-B(4)	1.877(13)
B(4)-B(11)	1.765(14)	B(4)-B(10)	1.767(13)
B(4)-B(5)	1.903(14)	B(4)-Cs(1)#4	3.915(9)
B(5)-B(7)	1.737(14)	B(5)-B(11)	1.769(14)
B(5)-B(6)	1.849(14)	B(6)-B(7)	1.788(13)
B(6)-B(8)	1.788(14)	B(7)-B(12)	1.780(13)
B(7)-B(11)	1.790(13)	B(7)-B(8)	1.795(13)
B(7)-Cs(1)#6	3.879(9)	B(8)-B(12)	1.757(13)
B(8)-B(9)	1.762(13)	B(8)-Cs(2)#2	3.889(10)
B(9)-B(12)	1.739(13)	B(9)-B(10)	1.770(13)
B(10)-B(12)	1.774(14)	B(10)-B(11)	1.777(14)
B(10)-Cs(1)#4	3.798(9)	B(11)-B(12)	1.762(14)
B(11)-Cs(1)#6	3.667(10)	B(12)-Cs(1)#6	3.747(9)
B(103)-B(108)	1.762(14)	B(103)-B(107)	1.80(2)
B(103)-B(104)	1.87(2)	B(103)-B(103)#1	1.89(2)
B(104)-B(108)	1.750(14)	B(104)-B(109)	1.773(13)
B(104)-B(105)	1.868(12)	B(104)-Cs(1)#9	3.872(10)
B(104)-Cs(2)#10	3.951(9)	B(105)-B(109)	1.78(2)
B(105)-B(109)#1	1.78(2)	B(105)-B(104)#1	1.868(12)
B(105)-Cs(1)#9	3.781(9)	B(105)-Cs(1)#11	3.781(9)
B(108)-B(109)	1.786(14)	B(108)-B(107)	1.794(13)
B(108)-B(112)	1.798(13)	B(109)-B(109)#1	1.80(2)
B(109)-B(112)	1.80(2)	B(109)-Cs(1)#9	3.844(10)
B(112)-B(107)	1.77(2)	B(112)-B(108)#1	1.798(13)
B(112)-B(109)#1	1.80(2)	B(112)-Cs(1)#1	3.890(10)
B(107)-B(108)#1	1.794(13)	B(107)-B(103)#1	1.80(2)

O(1)-C(2)-C(1)	120.5(6)	O(1)-C(2)-C(1)#1	120.5(6)
C(1)-C(2)-C(1)#1	119.0(13)	B(4)-Bi(1)-B(6)	78.1(3)
B(4)-Bi(1)-B(2)	78.0(3)	B(6)-Bi(1)-B(2)	45.5(3)
B(4)-Bi(1)-B(3)	45.7(3)	B(6)-Bi(1)-B(3)	78.3(3)
B(2)-Bi(1)-B(3)	46.2(3)	B(4)-Bi(1)-B(5)	46.2(3)
B(6)-Bi(1)-B(5)	44.8(3)	B(2)-Bi(1)-B(5)	76.9(3)
B(3)-Bi(1)-B(5)	77.9(3)	B(105)-Bi(2)-B(104)#1	45.5(3)
B(105)-Bi(2)-B(104)	45.5(3)	B(104)#1-Bi(2)-B(104)	77.5(4)

B(105)-Bi(2)-B(103)	77.7(4)	B(104)#1-Bi(2)-B(103)	77.8(3)
B(104)-Bi(2)-B(103)	45.5(3)	B(105)-Bi(2)-B(103)#1	77.7(4)
B(104)#1-Bi(2)-B(103)#1	45.5(3)	B(104)-Bi(2)-B(103)#1	77.8(3)
B(103)-Bi(2)-B(103)#1	45.9(5)	B(2)-Cs(1)-B(11)#2	100.0(2)
B(2)-Cs(1)-B(108)	151.7(2)	B(11)#2-Cs(1)-B(108)	105.6(2)
B(2)-Cs(1)-B(9)	27.8(2)	B(11)#2-Cs(1)-B(9)	78.8(2)
B(108)-Cs(1)-B(9)	172.9(2)	B(2)-Cs(1)-B(12)#2	126.5(2)
B(11)#2-Cs(1)-B(12)#2	27.5(2)	B(108)-Cs(1)-B(12)#2	80.8(2)
B(9)-Cs(1)-B(12)#2	102.2(2)	B(2)-Cs(1)-B(3)	29.7(2)
B(11)#2-Cs(1)-B(3)	103.5(2)	B(108)-Cs(1)-B(3)	145.9(2)
B(9)-Cs(1)-B(3)	27.6(2)	B(12)#2-Cs(1)-B(3)	122.0(2)
B(2)-Cs(1)-B(105)#3	69.6(2)	B(11)#2-Cs(1)-B(105)#3	88.6(2)
B(108)-Cs(1)-B(105)#3	98.9(2)	B(9)-Cs(1)-B(105)#3	86.7(2)
B(12)#2-Cs(1)-B(105)#3	104.1(2)	B(3)-Cs(1)-B(105)#3	99.2(3)
B(2)-Cs(1)-B(10)#4	110.9(2)	B(11)#2-Cs(1)-B(10)#4	109.4(2)
B(108)-Cs(1)-B(10)#4	71.6(2)	B(9)-Cs(1)-B(10)#4	101.7(2)
B(12)#2-Cs(1)-B(10)#4	90.6(2)	B(3)-Cs(1)-B(10)#4	82.2(2)
B(105)#3-Cs(1)-B(10)#4	161.2(2)	B(2)-Cs(1)-B(109)#3	87.5(2)
B(11)#2-Cs(1)-B(109)#3	65.1(2)	B(108)-Cs(1)-B(109)#3	92.5(2)
B(9)-Cs(1)-B(109)#3	94.5(2)	B(12)#2-Cs(1)-B(109)#3	77.3(2)
B(3)-Cs(1)-B(109)#3	116.0(2)	B(105)#3-Cs(1)-B(109)#3	26.9(2)
B(10)#4-Cs(1)-B(109)#3	161.6(2)	B(2)-Cs(1)-B(104)#3	62.5(2)
B(11)#2-Cs(1)-B(104)#3	64.9(2)	B(108)-Cs(1)-B(104)#3	118.6(2)
B(9)-Cs(1)-B(104)#3	68.2(2)	B(12)#2-Cs(1)-B(104)#3	87.0(2)
B(3)-Cs(1)-B(104)#3	89.8(2)	B(105)#3-Cs(1)-B(104)#3	28.2(2)
B(10)#4-Cs(1)-B(104)#3	168.8(2)	B(109)#3-Cs(1)-B(104)#3	26.6(2)
B(2)-Cs(1)-B(7)#2	105.8(2)	B(11)#2-Cs(1)-B(7)#2	27.3(2)
B(108)-Cs(1)-B(7)#2	102.5(2)	B(9)-Cs(1)-B(7)#2	78.7(2)
B(12)#2-Cs(1)-B(7)#2	26.9(2)	B(3)-Cs(1)-B(7)#2	95.3(2)
B(105)#3-Cs(1)-B(7)#2	115.7(2)	B(10)#4-Cs(1)-B(7)#2	82.6(2)
B(109)#3-Cs(1)-B(7)#2	92.1(2)	B(104)#3-Cs(1)-B(7)#2	90.5(2)
B(2)-Cs(1)-B(112)	124.7(2)	B(11)#2-Cs(1)-B(112)	126.6(3)
B(108)-Cs(1)-B(112)	27.3(2)	B(9)-Cs(1)-B(112)	151.8(2)
B(12)#2-Cs(1)-B(112)	105.7(2)	B(3)-Cs(1)-B(112)	129.8(3)
B(105)#3-Cs(1)-B(112)	82.4(2)	B(10)#4-Cs(1)-B(112)	82.5(2)
B(109)#3-Cs(1)-B(112)	87.4(3)	B(104)#3-Cs(1)-B(112)	108.7(2)
B(7)#2-Cs(1)-B(112)	129.4(2)	B(5)-Cs(2)-B(5)#5	180.0
B(5)-Cs(2)-B(4)	29.3(2)	B(5)#5-Cs(2)-B(4)	150.7(2)
B(5)-Cs(2)-B(4)#5	150.7(2)	B(5)#5-Cs(2)-B(4)#5	29.3(2)
B(4)-Cs(2)-B(4)#5	180.0	B(5)-Cs(2)-B(8)#6	101.6(2)
B(5)#5-Cs(2)-B(8)#6	78.4(2)	B(4)-Cs(2)-B(8)#6	117.7(2)
B(4)#5-Cs(2)-B(8)#6	62.3(2)	B(5)-Cs(2)-B(8)#7	78.4(2)
B(5)#5-Cs(2)-B(8)#7	101.6(2)	B(4)-Cs(2)-B(8)#7	62.3(2)
B(4)#5-Cs(2)-B(8)#7	117.7(2)	B(8)#6-Cs(2)-B(8)#7	180.0
B(5)-Cs(2)-B(104)#4	87.3(2)	B(5)#5-Cs(2)-B(104)#4	92.7(2)
B(4)-Cs(2)-B(104)#4	77.1(2)	B(4)#5-Cs(2)-B(104)#4	102.9(2)
B(8)#6-Cs(2)-B(104)#4	60.5(2)	B(8)#7-Cs(2)-B(104)#4	119.5(2)
B(5)-Cs(2)-B(104)#8	92.7(2)	B(5)#5-Cs(2)-B(104)#8	87.3(2)
B(4)-Cs(2)-B(104)#8	102.9(2)	B(4)#5-Cs(2)-B(104)#8	77.1(2)
B(8)#6-Cs(2)-B(104)#8	119.5(2)	B(8)#7-Cs(2)-B(104)#8	60.5(2)
B(104)#4-Cs(2)-B(104)#8	180.0	B(8)-B(2)-B(9)	59.8(5)
B(8)-B(2)-B(6)	58.9(5)	B(9)-B(2)-B(6)	106.6(6)
B(8)-B(2)-B(3)	106.4(6)	B(9)-B(2)-B(3)	57.9(5)
B(6)-B(2)-B(3)	108.2(6)	B(8)-B(2)-Bi(1)	120.0(6)
B(9)-B(2)-Bi(1)	119.0(5)	B(6)-B(2)-Bi(1)	67.0(4)
B(3)-B(2)-Bi(1)	67.0(4)	B(8)-B(2)-Cs(1)	121.9(5)
B(9)-B(2)-Cs(1)	78.2(4)	B(6)-B(2)-Cs(1)	173.5(5)
B(3)-B(2)-Cs(1)	77.9(4)	Bi(1)-B(2)-Cs(1)	114.8(3)

B(10)-B(3)-B(9)	60.2(5)	B(10)-B(3)-B(4)	58.2(5)
B(9)-B(3)-B(4)	105.8(7)	B(10)-B(3)-B(2)	105.9(7)
B(9)-B(3)-B(2)	57.4(5)	B(4)-B(3)-B(2)	107.0(6)
B(10)-B(3)-Bi(1)	119.2(6)	B(9)-B(3)-Bi(1)	118.4(6)
B(4)-B(3)-Bi(1)	66.7(4)	B(2)-B(3)-Bi(1)	66.8(4)
B(10)-B(3)-Cs(1)	123.5(5)	B(9)-B(3)-Cs(1)	75.3(4)
B(4)-B(3)-Cs(1)	178.3(5)	B(2)-B(3)-Cs(1)	72.4(4)
Bi(1)-B(3)-Cs(1)	111.6(3)	B(11)-B(4)-B(10)	60.4(5)
B(11)-B(4)-B(3)	106.2(6)	B(10)-B(4)-B(3)	57.3(5)
B(11)-B(4)-B(5)	57.5(5)	B(10)-B(4)-B(5)	105.7(6)
B(3)-B(4)-B(5)	107.9(6)	B(11)-B(4)-Bi(1)	119.6(5)
B(10)-B(4)-Bi(1)	119.1(6)	B(3)-B(4)-Bi(1)	67.6(4)
B(5)-B(4)-Bi(1)	67.6(4)	B(11)-B(4)-Cs(2)	81.8(5)
B(10)-B(4)-Cs(2)	132.2(5)	B(3)-B(4)-Cs(2)	170.5(5)
B(5)-B(4)-Cs(2)	71.6(4)	Bi(1)-B(4)-Cs(2)	104.2(3)
B(11)-B(4)-Cs(1)#4	112.2(5)	B(10)-B(4)-Cs(1)#4	73.1(4)
B(3)-B(4)-Cs(1)#4	83.4(4)	B(5)-B(4)-Cs(1)#4	166.0(5)
Bi(1)-B(4)-Cs(1)#4	125.5(3)	Cs(2)-B(4)-Cs(1)#4	98.6(2)
B(7)-B(5)-B(11)	61.4(6)	B(7)-B(5)-B(6)	59.7(5)
B(11)-B(5)-B(6)	107.9(7)	B(7)-B(5)-B(4)	107.4(7)
B(11)-B(5)-B(4)	57.3(5)	B(6)-B(5)-B(4)	108.0(7)
B(7)-B(5)-Bi(1)	120.7(6)	B(11)-B(5)-Bi(1)	118.1(6)
B(6)-B(5)-Bi(1)	66.9(5)	B(4)-B(5)-Bi(1)	66.1(4)
B(7)-B(5)-Cs(2)	130.2(5)	B(11)-B(5)-Cs(2)	85.7(5)
B(6)-B(5)-Cs(2)	166.4(5)	B(4)-B(5)-Cs(2)	79.1(4)
Bi(1)-B(5)-Cs(2)	107.3(3)	B(7)-B(6)-B(8)	60.3(5)
B(7)-B(6)-B(5)	57.0(5)	B(8)-B(6)-B(5)	105.6(6)
B(7)-B(6)-B(2)	106.5(6)	B(8)-B(6)-B(2)	57.6(5)
B(5)-B(6)-B(2)	108.7(6)	B(7)-B(6)-Bi(1)	119.6(6)
B(8)-B(6)-Bi(1)	119.2(6)	B(5)-B(6)-Bi(1)	68.2(5)
B(2)-B(6)-Bi(1)	67.5(4)	B(5)-B(7)-B(12)	108.6(7)
B(5)-B(7)-B(6)	63.3(6)	B(12)-B(7)-B(6)	107.8(6)
B(5)-B(7)-B(11)	60.2(6)	B(12)-B(7)-B(11)	59.1(5)
B(6)-B(7)-B(11)	109.7(7)	B(5)-B(7)-B(8)	110.2(7)
B(12)-B(7)-B(8)	58.8(5)	B(6)-B(7)-B(8)	59.9(5)
B(11)-B(7)-B(8)	106.6(7)	B(5)-B(7)-Cs(1)#6	116.0(5)
B(12)-B(7)-Cs(1)#6	72.4(4)	B(6)-B(7)-Cs(1)#6	179.2(5)
B(11)-B(7)-Cs(1)#6	69.8(4)	B(8)-B(7)-Cs(1)#6	120.8(5)
B(12)-B(8)-B(9)	59.2(5)	B(12)-B(8)-B(2)	108.9(7)
B(9)-B(8)-B(2)	60.4(5)	B(12)-B(8)-B(6)	108.9(7)
B(9)-B(8)-B(6)	110.6(7)	B(2)-B(8)-B(6)	63.5(6)
B(12)-B(8)-B(7)	60.2(5)	B(9)-B(8)-B(7)	108.1(7)
B(2)-B(8)-B(7)	110.8(7)	B(6)-B(8)-B(7)	59.9(5)
B(12)-B(8)-Cs(2)#2	81.6(5)	B(9)-B(8)-Cs(2)#2	83.7(4)
B(2)-B(8)-Cs(2)#2	124.1(5)	B(6)-B(8)-Cs(2)#2	165.2(6)
B(7)-B(8)-Cs(2)#2	120.9(5)	B(12)-B(9)-B(8)	60.2(5)
B(12)-B(9)-B(10)	60.7(5)	B(8)-B(9)-B(10)	109.2(7)
B(12)-B(9)-B(2)	109.3(7)	B(8)-B(9)-B(2)	59.8(6)
B(10)-B(9)-B(2)	110.8(6)	B(12)-B(9)-B(3)	109.5(7)
B(8)-B(9)-B(3)	111.9(7)	B(10)-B(9)-B(3)	59.0(5)
B(2)-B(9)-B(3)	64.7(5)	B(12)-B(9)-Cs(1)	173.4(5)
B(8)-B(9)-Cs(1)	118.8(5)	B(10)-B(9)-Cs(1)	124.1(5)
B(2)-B(9)-Cs(1)	74.0(4)	B(3)-B(9)-Cs(1)	77.1(4)
B(3)-B(10)-B(4)	64.5(5)	B(3)-B(10)-B(9)	60.8(5)
B(4)-B(10)-B(9)	111.2(7)	B(3)-B(10)-B(12)	109.4(6)
B(4)-B(10)-B(12)	108.7(7)	B(9)-B(10)-B(12)	58.8(5)
B(3)-B(10)-B(11)	111.4(7)	B(4)-B(10)-B(11)	59.7(5)
B(9)-B(10)-B(11)	107.1(7)	B(12)-B(10)-B(11)	59.5(5)

B(3)-B(10)-Cs(1)#4	88.6(5)	B(4)-B(10)-Cs(1)#4	80.5(4)
B(9)-B(10)-Cs(1)#4	133.6(5)	B(12)-B(10)-Cs(1)#4	161.9(5)
B(11)-B(10)-Cs(1)#4	116.8(5)	B(12)-B(11)-B(4)	109.3(7)
B(12)-B(11)-B(5)	108.0(7)	B(4)-B(11)-B(5)	65.1(6)
B(12)-B(11)-B(10)	60.2(5)	B(4)-B(11)-B(10)	59.9(5)
B(5)-B(11)-B(10)	111.3(7)	B(12)-B(11)-B(7)	60.2(5)
B(4)-B(11)-B(7)	111.4(7)	B(5)-B(11)-B(7)	58.4(5)
B(10)-B(11)-B(7)	109.0(6)	B(12)-B(11)-Cs(1)#6	78.8(5)
B(4)-B(11)-Cs(1)#6	165.6(5)	B(5)-B(11)-Cs(1)#6	124.8(6)
B(10)-B(11)-Cs(1)#6	118.4(5)	B(7)-B(11)-Cs(1)#6	83.0(5)
B(9)-B(12)-B(8)	60.5(5)	B(9)-B(12)-B(11)	109.2(7)
B(8)-B(12)-B(11)	109.5(7)	B(9)-B(12)-B(10)	60.5(5)
B(8)-B(12)-B(10)	109.3(7)	B(11)-B(12)-B(10)	60.3(6)
B(9)-B(12)-B(7)	109.8(6)	B(8)-B(12)-B(7)	61.0(5)
B(11)-B(12)-B(7)	60.7(5)	B(10)-B(12)-B(7)	109.5(7)
B(9)-B(12)-Cs(1)#6	169.4(5)	B(8)-B(12)-Cs(1)#6	128.9(5)
B(11)-B(12)-Cs(1)#6	73.7(4)	B(10)-B(12)-Cs(1)#6	114.9(5)
B(7)-B(12)-Cs(1)#6	80.7(4)	B(108)-B(103)-B(107)	60.4(6)
B(108)-B(103)-B(104)	57.5(5)	B(107)-B(103)-B(104)	106.0(7)
B(108)-B(103)-B(103)#1	106.7(5)	B(107)-B(103)-B(103)#1	58.4(4)
B(104)-B(103)-B(103)#1	107.7(4)	B(108)-B(103)-Bi(2)	119.1(6)
B(107)-B(103)-Bi(2)	119.6(6)	B(104)-B(103)-Bi(2)	67.1(4)
B(103)#1-B(103)-Bi(2)	67.0(3)	B(108)-B(104)-B(109)	61.0(5)
B(108)-B(104)-B(105)	107.0(7)	B(109)-B(104)-B(105)	58.3(6)
B(108)-B(104)-B(103)	58.1(6)	B(109)-B(104)-B(103)	107.3(6)
B(105)-B(104)-B(103)	108.3(6)	B(108)-B(104)-Bi(2)	119.9(6)
B(109)-B(104)-Bi(2)	120.0(5)	B(105)-B(104)-Bi(2)	67.1(5)
B(103)-B(104)-Bi(2)	67.4(4)	B(108)-B(104)-Cs(1)#9	124.4(5)
B(109)-B(104)-Cs(1)#9	75.8(5)	B(105)-B(104)-Cs(1)#9	73.2(5)
B(103)-B(104)-Cs(1)#9	176.9(5)	Bi(2)-B(104)-Cs(1)#9	111.2(3)
B(108)-B(104)-Cs(2)#10	85.1(5)	B(109)-B(104)-Cs(2)#10	128.7(5)
B(105)-B(104)-Cs(2)#10	167.5(6)	B(103)-B(104)-Cs(2)#10	80.4(4)
Bi(2)-B(104)-Cs(2)#10	109.8(3)	Cs(1)#9-B(104)-Cs(2)#10	97.7(2)
B(109)-B(105)-B(109)#1	60.8(7)	B(109)-B(105)-B(104)#1	106.9(8)
B(109)#1-B(105)-B(104)#1	58.1(5)	B(109)-B(105)-B(104)	58.1(5)
B(109)#1-B(105)-B(104)	106.9(8)	B(104)#1-B(105)-B(104)	108.1(9)
B(109)-B(105)-Bi(2)	120.1(7)	B(109)#1-B(105)-Bi(2)	120.1(7)
B(104)#1-B(105)-Bi(2)	67.4(5)	B(104)-B(105)-Bi(2)	67.4(5)
B(109)-B(105)-Cs(1)#9	78.5(4)	B(109)#1-B(105)-Cs(1)#9	123.0(6)
B(104)#1-B(105)-Cs(1)#9	172.9(6)	B(104)-B(105)-Cs(1)#9	78.6(4)
Bi(2)-B(105)-Cs(1)#9	114.2(3)	B(109)-B(105)-Cs(1)#11	123.0(6)
B(109)#1-B(105)-Cs(1)#11	78.5(4)	B(104)#1-B(105)-Cs(1)#11	78.6(4)
B(104)-B(105)-Cs(1)#11	172.9(6)	Bi(2)-B(105)-Cs(1)#11	114.2(3)
Cs(1)#9-B(105)-Cs(1)#11	94.6(3)	B(104)-B(108)-B(103)	64.4(6)
B(104)-B(108)-B(109)	60.2(6)	B(103)-B(108)-B(109)	111.7(7)
B(104)-B(108)-B(107)	111.8(8)	B(103)-B(108)-B(107)	60.9(7)
B(109)-B(108)-B(107)	108.0(7)	B(104)-B(108)-B(112)	109.7(8)
B(103)-B(108)-B(112)	109.5(7)	B(109)-B(108)-B(112)	60.2(7)
B(107)-B(108)-B(112)	58.9(7)	B(104)-B(108)-Cs(1)	150.3(6)
B(103)-B(108)-Cs(1)	138.8(6)	B(109)-B(108)-Cs(1)	108.3(5)
B(107)-B(108)-Cs(1)	97.7(6)	B(112)-B(108)-Cs(1)	82.1(5)
B(104)-B(109)-B(105)	63.5(6)	B(104)-B(109)-B(108)	58.9(5)
B(105)-B(109)-B(108)	109.6(8)	B(104)-B(109)-B(109)#1	110.3(4)
B(105)-B(109)-B(109)#1	59.6(4)	B(108)-B(109)-B(109)#1	108.0(4)
B(104)-B(109)-B(112)	108.7(8)	B(105)-B(109)-B(112)	108.8(7)
B(108)-B(109)-B(112)	60.2(6)	B(109)#1-B(109)-B(112)	60.0(4)
B(104)-B(109)-Cs(1)#9	77.6(5)	B(105)-B(109)-Cs(1)#9	74.6(5)
B(108)-B(109)-Cs(1)#9	124.3(5)	B(109)#1-B(109)-Cs(1)#9	119.31(13)

B(112)-B(109)-Cs(1)#9	173.6(6)	B(107)-B(112)-B(108)	60.4(6)
B(107)-B(112)-B(108)#1	60.4(6)	B(108)-B(112)-B(108)#1	107.5(9)
B(107)-B(112)-B(109)	108.8(8)	B(108)-B(112)-B(109)	59.6(5)
B(108)#1-B(112)-B(109)	107.4(8)	B(107)-B(112)-B(109)#1	108.8(8)
B(108)-B(112)-B(109)#1	107.4(8)	B(108)#1-B(112)-B(109)#1	59.6(5)
B(109)-B(112)-B(109)#1	59.9(7)	B(107)-B(112)-Cs(1)	92.0(6)
B(108)-B(112)-Cs(1)	70.6(4)	B(108)#1-B(112)-Cs(1)	145.2(8)
B(109)-B(112)-Cs(1)	101.2(3)	B(109)#1-B(112)-Cs(1)	155.2(7)
B(107)-B(112)-Cs(1)#1	92.0(6)	B(108)-B(112)-Cs(1)#1	145.2(8)
B(108)#1-B(112)-Cs(1)#1	70.6(4)	B(109)-B(112)-Cs(1)#1	155.2(7)
B(109)#1-B(112)-Cs(1)#1	101.2(3)	Cs(1)-B(112)-Cs(1)#1	91.2(3)
B(112)-B(107)-B(108)	60.7(6)	B(112)-B(107)-B(108)#1	60.7(6)
B(108)-B(107)-B(108)#1	107.9(10)	B(112)-B(107)-B(103)	109.2(8)
B(108)-B(107)-B(103)	58.7(5)	B(108)#1-B(107)-B(103)	109.1(9)
B(112)-B(107)-B(103)#1	109.2(8)	B(108)-B(107)-B(103)#1	109.1(9)
B(108)#1-B(107)-B(103)#1	58.7(5)	B(103)-B(107)-B(103)#1	63.2(8)

Symmetry transformations used to generate equivalent atoms:

#1 x,-y+1/2,z #2 -x+3/2,-y,z-1/2 #3 x-1/2,y,-z-1/2

#4 -x+2,-y,-z #5 -x+2,-y,-z+1 #6 -x+3/2,-y,z+1/2

#7 x+1/2,y,-z+1/2 #8 x,y,z+1 #9 x+1/2,y,-z-1/2

#10 x,y,z-1 #11 x+1/2,-y+1/2,-z-1/2

Table 4. Anisotropic displacement parameters [$Å^2$ x 10^3] for 1.
The anisotropic displacement factor exponent takes the form:
$-2\pi^2$ [$(ha^*)^2U_{11}$ + ... + 2hka*b*U_{12}]

	U11	U22	U33	U23	U13	U12
O(1)	55(10)	130(15)	154(16)	0	51(11)	0
C(1)	59(8)	42(6)	55(7)	0(6)	5(7)	-6(6)
C(2)	14(7)	74(11)	12(6)	0	12(6)	0
Bi(1)	17(1)	18(1)	28(1)	2(1)	-5(1)	-5(1)
Bi(2)	25(1)	17(1)	11(1)	0	2(1)	0
Cs(1)	19(1)	31(1)	20(1)	2(1)	5(1)	1(1)
Cs(2)	26(1)	34(1)	25(1)	11(1)	-5(1)	-2(1)
B(2)	15(5)	16(4)	24(5)	4(4)	-3(4)	5(4)
B(3)	14(5)	23(5)	20(5)	-2(4)	-2(4)	6(4)
B(4)	8(5)	21(4)	22(5)	-3(4)	-7(4)	4(4)
B(5)	17(5)	23(5)	21(5)	1(4)	-5(4)	3(4)
B(6)	24(6)	16(4)	21(5)	-5(4)	-5(4)	2(4)
B(7)	14(5)	19(4)	15(4)	4(4)	-4(4)	-1(4)
B(8)	20(6)	16(4)	24(5)	-3(4)	1(4)	5(4)
B(9)	6(4)	24(4)	16(4)	5(4)	-3(4)	-5(4)
B(10)	14(5)	16(4)	22(5)	-2(4)	-5(4)	2(4)
B(11)	16(5)	22(5)	20(5)	2(4)	-4(4)	3(4)
B(12)	18(5)	14(4)	21(5)	-1(4)	-2(4)	-4(4)
B(103)	17(5)	29(5)	23(5)	1(4)	-8(4)	-4(4)
B(104)	24(5)	14(4)	12(4)	1(4)	9(4)	-1(4)
B(105)	10(7)	19(6)	23(7)	0	7(6)	0
B(108)	28(6)	21(5)	24(5)	2(4)	8(5)	-3(5)
B(109)	19(5)	11(4)	26(5)	7(4)	-4(4)	-4(4)
B(112)	33(9)	27(7)	9(7)	0	4(6)	0
B(107)	6(7)	39(8)	29(8)	0	0(6)	0

Table 5. Hydrogen coordinates (x 10^4) and isotropic displacement parameters ($Å^2$ x 10^3) for 1.

	x	y	z	U(eq)
H(1A)	11231(10)	1496(5)	96(8)	78
H(1B)	12260(10)	1849(5)	427(8)	78
H(1C)	11953(10)	1849(5)	-658(8)	78
H(2)	8127(63)	1609(39)	585(53)	22
H(3)	9804(66)	496(40)	622(57)	23
H(4)	10087(67)	72(39)	2699(54)	20
H(5)	8551(66)	900(41)	3914(57)	24
H(6)	7421(67)	1854(42)	2608(53)	25
H(7)	6570(65)	584(39)	3284(55)	19
H(8)	6299(67)	1000(41)	1297(55)	24
H(9)	7698(61)	213(39)	147(55)	18
H(10)	8879(62)	-685(41)	1370(54)	21
H(11)	8169(65)	-468(40)	3304(56)	23
H(12)	6718(64)	-406(40)	1747(55)	21
H(103)	9357(66)	1721(44)	-5031(61)	28
H(104)	11506(65)	1246(40)	-4469(52)	20
H(105)	12829(91)	2500(1728959)	-4133(77)	21
H(108)	9863(71)	1289(44)	-3166(63)	29
H(109)	11909(65)	1755(42)	-2604(53)	22
H(112)	10086(97)	2500(1432582)	-1947(84)	28
H(107)	8576(99)	2500(1176936)	-3435(84)	29

$Ag(C_6H_6)_2(12\text{-}CB_{11}H_{11}F)$

Table 2. Crystal data and structure refinement for 1.

Identification code	shs71
Empirical formula	$C_{13}H_{23}AgB_{11}F$
Formula weight	425.09
Temperature	173(2) K
Wavelength	0.71073 Å
Crystal system	Orthorhombic P
Space group	$Pca2_1$
Unit cell dimensions	a = 16.323(3) Å alpha = 90° b = 6.7550(10) Å beta = 90° c = 17.095(3) Å gamma = 90°
Volume, Z	1884.9(6) $Å^3$, 4
Density (calculated)	1.498 Mg/m^3
Absorption coefficient	1.071 mm^{-1}
F(000)	848
Crystal size	0.45 x 0.28 x 0.04 mm
θ range for data collection	2.38 to 27.50°
Limiting indices	$-1 \le h \le 21$, $-1 \le k \le 8$, $-22 \le l \le 1$
Reflections collected	2949
Independent reflections	2375 (R_{int} = 0.0677)
Refinement method	Full-matrix least-squares on F^2
Data / restraints / parameters	2375 / 1 / 235
Goodness-of-fit on F^2 -	0.982
Final R indices [$I>2\sigma(I)$]	R1 = 0.0602, wR2 = 0.1342
R indices (all data)	R1 = 0.0763, wR2 = 0.1394
Absolute structure parameter	0.14(7)
Extinction coefficient	0.0091(12)
Largest diff. peak and hole	2.092 and -1.104 $eÅ^{-3}$

Table 3. Atomic coordinates [x 10^4] and equivalent isotropic displacement parameters [$Å^2$ x 10^3] for 1. U(eq) is defined as one third of the trace of the orthogonalized U_{ij} tensor.

	x	y	z	U(eq)
Ag	1818(1)	-9612(1)	0(1)	33(1)
F	2653(3)	-5072(7)	1476(3)	30(1)
C	-149(6)	-5855(12)	1502(5)	25(2)
B(2)	282(6)	-5024(14)	651(6)	27(2)
B(3)	221(6)	-3514(13)	1503(6)	24(2)
B(4)	294(7)	-5081(15)	2336(6)	26(2)
B(5)	428(3)	-7546(8)	1995(3)	26(2)
B(6)	402(3)	-7526(7)	962(3)	24(2)
B(7)	1268(3)	-6108(6)	646(3)	24(2)
B(8)	1138(3)	-3642(8)	978(3)	25(2)
B(9)	1151(3)	-3662(8)	2012(3)	23(2)
B(10)	1295(6)	-6159(15)	2324(6)	23(2)
B(11)	1359(6)	-7688(14)	1479(6)	24(2)
B(12)	1818(6)	-5282(14)	1484(5)	22(2)
C(21)	815(6)	-10797(17)	-963(6)	37(2)
C(22)	899(6)	-8943(16)	-1303(6)	39(2)
C(23)	1415(7)	-8696(21)	-1912(7)	46(3)
C(24)	1891(6)	-10184(21)	-2197(6)	48(3)
C(25)	1798(7)	-12075(19)	-1882(6)	42(3)
C(26)	1279(6)	-12377(16)	-1252(6)	37(2)
C(31)	3325(6)	-9119(18)	253(6)	32(2)
C(32)	3195(6)	-11024(15)	483(5)	31(2)
C(33)	3318(5)	-12595(14)	-65(8)	31(2)
C(34)	3597(6)	-12161(15)	-793(5)	31(2)
C(35)	3709(6)	-10254(14)	-1024(6)	33(2)
C(36)	3566(7)	-8684(18)	-501(7)	41(3)

Table 4. Selected bond lengths [Å] for 1.

Ag-H7	2.180(5)
Ag-H8a	2.282(8)

Symmetry transformations used to generate equivalent atoms:

X, Y+1, Z

Table 5. Bond lengths [Å] and angles [°] for 1.

Ag-C(21)	2.455(10)	Ag-C(31)	2.520(10)
Ag-C(32)	2.578(9)	F-B(12)	1.371(11)
C-B(4)	1.682(13)	C-B(3)	1.693(12)
C-B(5)	1.704(10)	C-B(2)	1.710(13)
C-B(6)	1.714(9)	B(2)-B(7)	1.769(11)
B(2)-B(8)	1.772(11)	B(2)-B(3)	1.781(13)
B(2)-B(6)	1.782(10)	B(3)-B(8)	1.748(11)
B(3)-B(9)	1.753(11)	B(3)-B(4)	1.778(14)
B(4)-B(5)	1.777(11)	B(4)-B(9)	1.784(12)
B(4)-B(10)	1.79(2)	B(5)-B(11)	1.760(11)
B(5)-B(6)	1.767(4)	B(5)-B(10)	1.787(11)
B(6)-B(7)	1.791(4)	B(6)-B(11)	1.798(12)
B(7)-B(8)	1.772(4)	B(7)-B(12)	1.780(10)
B(7)-B(11)	1.786(11)	B(8)-B(9)	1.769(4)
B(8)-B(12)	1.791(10)	B(9)-B(10)	1.784(12)
B(9)-B(12)	1.788(11)	B(10)-B(12)	1.773(13)
B(10)-B(11)	1.779(14)	B(11)-B(12)	1.790(13)
C(21)-C(22)	1.39(2)	C(21)-C(26)	1.40(2)
C(22)-C(23)	1.35(2)	C(23)-C(24)	1.36(2)
C(24)-C(25)	1.39(2)	C(25)-C(26)	1.39(2)
C(31)-C(32)	1.36(2)	C(31)-C(36)	1.38(2)
C(32)-C(33)	1.431(14)	C(33)-C(34)	1.36(2)
C(34)-C(35)	1.359(13)	C(35)-C(36)	1.41(2)

C(21)-Ag-C(31)	144.0(3)	C(21)-Ag-C(32)	132.5(3)
C(31)-Ag-C(32)	31.0(4)	B(4)-C-B(3)	63.6(5)
B(4)-C-B(5)	63.3(5)	B(3)-C-B(5)	115.3(6)
B(4)-C-B(2)	116.3(7)	B(3)-C-B(2)	63.1(5)
B(5)-C-B(2)	114.4(6)	B(4)-C-B(6)	115.8(7)
B(3)-C-B(6)	115.4(6)	B(5)-C-B(6)	62.3(3)
B(2)-C-B(6)	62.7(5)	C-B(2)-B(7)	104.0(6)
C-B(2)-B(8)	103.3(6)	B(7)-B(2)-B(8)	60.1(4)
C-B(2)-B(3)	58.0(5)	B(7)-B(2)-B(3)	106.9(6)
B(8)-B(2)-B(3)	58.9(4)	C-B(2)-B(6)	58.8(5)
B(7)-B(2)-B(6)	60.6(3)	B(8)-B(2)-B(6)	108.6(6)
B(3)-B(2)-B(6)	107.8(6)	C-B(3)-B(8)	105.0(6)
C-B(3)-B(9)	104.9(6)	B(8)-B(3)-B(9)	60.7(4)
C-B(3)-B(4)	57.9(5)	B(8)-B(3)-B(4)	109.0(7)
B(9)-B(3)-B(4)	60.7(5)	C-B(3)-B(2)	58.9(5)
B(8)-B(3)-B(2)	60.3(5)	B(9)-B(3)-B(2)	109.0(6)
B(4)-B(3)-B(2)	108.1(6)	C-B(4)-B(5)	59.0(5)
C-B(4)-B(3)	58.5(5)	B(5)-B(4)-B(3)	107.7(6)
C-B(4)-B(9)	104.0(6)	B(5)-B(4)-B(9)	107.7(6)
B(3)-B(4)-B(9)	59.0(5)	C-B(4)-B(10)	104.9(7)
B(5)-B(4)-B(10)	60.1(5)	B(3)-B(4)-B(10)	107.1(7)
B(9)-B(4)-B(10)	59.9(5)	C-B(5)-B(11)	105.5(6)
C-B(5)-B(6)	59.2(3)	B(11)-B(5)-B(6)	61.3(4)
C-B(5)-B(4)	57.7(5)	B(11)-B(5)-B(4)	108.8(6)
B(6)-B(5)-B(4)	108.5(4)	C-B(5)-B(10)	104.0(5)
B(11)-B(5)-B(10)	60.2(5)	B(6)-B(5)-B(10)	109.3(4)
B(4)-B(5)-B(10)	60.2(5)	C-B(6)-B(5)	58.6(3)
C-B(6)-B(2)	58.5(5)	B(5)-B(6)-B(2)	107.9(4)
C-B(6)-B(7)	103.0(3)	B(5)-B(6)-B(7)	106.6
B(2)-B(6)-B(7)	59.3(4)	C-B(6)-B(11)	103.4(5)
B(5)-B(6)-B(11)	59.1(4)	B(2)-B(6)-B(11)	107.5(5)

B(7)-B(6)-B(11)	59.7(3)	B(2)-B(7)-B(8)	60.0(3)
B(2)-B(7)-B(12)	109.0(5)	B(8)-B(7)-B(12)	60.6(3)
B(2)-B(7)-B(11)	108.6(5)	B(8)-B(7)-B(11)	108.5(4)
B(12)-B(7)-B(11)	60.3(5)	B(2)-B(7)-B(6)	60.1(3)

B(8)-B(7)-B(6)	108.2	B(12)-B(7)-B(6)	108.9(4)
B(11)-B(7)-B(6)	60.4(4)	B(3)-B(8)-B(9)	59.8(4)
B(3)-B(8)-B(2)	60.8(5)	B(9)-B(8)-B(2)	108.7(4)
B(3)-B(8)-B(7)	108.3(3)	B(9)-B(8)-B(7)	108.1
B(2)-B(8)-B(7)	59.9(3)	B(3)-B(8)-B(12)	108.2(5)
B(9)-B(8)-B(12)	60.3(3)	B(2)-B(8)-B(12)	108.4(5)
B(7)-B(8)-B(12)	59.9(3)	B(3)-B(9)-B(8)	59.5(4)
B(3)-B(9)-B(10)	108.4(5)	B(8)-B(9)-B(10)	107.9(4)
B(3)-B(9)-B(4)	60.3(5)	B(8)-B(9)-B(4)	107.7(4)
B(10)-B(9)-B(4)	60.2(5)	B(3)-B(9)-B(12)	108.1(5)
B(8)-B(9)-B(12)	60.5(3)	B(10)-B(9)-B(12)	59.5(5)
B(4)-B(9)-B(12)	107.8(5)	B(12)-B(10)-B(11)	60.5(5)
B(12)-B(10)-B(9)	60.3(5)	B(11)-B(10)-B(9)	108.3(6)
B(12)-B(10)-B(5)	107.5(6)	B(11)-B(10)-B(5)	59.1(5)
B(9)-B(10)-B(5)	107.3(6)	B(12)-B(10)-B(4)	108.2(7)
B(11)-B(10)-B(4)	107.4(7)	B(9)-B(10)-B(4)	59.9(5)
B(5)-B(10)-B(4)	59.6(5)	B(5)-B(11)-B(10)	60.6(5)
B(5)-B(11)-B(7)	107.2(6)	B(10)-B(11)-B(7)	107.2(6)
B(5)-B(11)-B(12)	108.0(6)	B(10)-B(11)-B(12)	59.6(5)
B(7)-B(11)-B(12)	59.7(4)	B(5)-B(11)-B(6)	59.6(4)
B(10)-B(11)-B(6)	108.2(6)	B(7)-B(11)-B(6)	59.9(4)
B(12)-B(11)-B(6)	108.1(6)	F-B(12)-B(10)	121.4(7)
F-B(12)-B(7)	121.7(7)	B(10)-B(12)-B(7)	107.7(6)
F-B(12)-B(9)	123.2(7)	B(10)-B(12)-B(9)	60.1(5)
B(7)-B(12)-B(9)	106.9(6)	F-B(12)-B(11)	120.6(7)
B(10)-B(12)-B(11)	59.9(5)	B(7)-B(12)-B(11)	60.0(5)
B(9)-B(12)-B(11)	107.7(6)	F-B(12)-B(8)	123.2(7)
B(10)-B(12)-B(8)	107.4(6)	B(7)-B(12)-B(8)	59.5(3)
B(9)-B(12)-B(8)	59.2(3)	B(11)-B(12)-B(8)	107.5(6)
C(22)-C(21)-C(26)	119.1(9)	C(22)-C(21)-Ag	85.5(6)
C(26)-C(21)-Ag	97.2(6)	C(23)-C(22)-C(21)	119.8(11)
C(22)-C(23)-C(24)	122.8(12)	C(23)-C(24)-C(25)	118.4(10)
C(26)-C(25)-C(24)	120.1(10)	C(25)-C(26)-C(21)	119.6(10)
C(32)-C(31)-C(36)	121.1(10)	C(32)-C(31)-Ag	76.8(6)
C(36)-C(31)-Ag	98.4(6)	C(31)-C(32)-C(33)	119.3(9)
C(31)-C(32)-Ag	72.2(5)	C(33)-C(32)-Ag	100.8(6)
C(34)-C(33)-C(32)	119.2(9)	C(33)-C(34)-C(35)	121.1(9)
C(34)-C(35)-C(36)	120.5(9)	C(31)-C(36)-C(35)	118.7(10)

Symmetry transformations used to generate equivalent atoms:

Table 6. Anisotropic displacement parameters [$Å^2 \times 10^3$] for 1.
The anisotropic displacement factor exponent takes the form:
$-2\pi^2 [(ha^*)^2 U_{11} + ... + 2hka^*b^* U_{12}]$

	U11	U22	U33	U23	U13	U12
Ag	30(1)	35(1)	35(1)	-7(1)	-6(1)	3(1)
F	25(2)	34(3)	31(3)	2(2)	-2(2)	-5(2)
C	28(4)	19(4)	27(4)	-2(3)	4(4)	-1(3)
B(2)	29(5)	27(6)	24(4)	-3(4)	-7(4)	-2(4)
B(3)	33(5)	8(4)	32(5)	2(4)	1(4)	0(4)
B(4)	27(5)	28(6)	24(5)	-6(4)	4(4)	-4(4)
B(5)	36(5)	14(5)	28(5)	1(4)	7(4)	-2(4)
B(6)	23(4)	21(5)	30(5)	-8(4)	-6(4)	-8(4)
B(7)	31(5)	17(4)	23(4)	0(4)	6(4)	-6(4)
B(8)	37(5)	13(5)	25(4)	0(4)	-6(4)	1(4)
B(9)	32(5)	13(5)	23(4)	-1(4)	-4(4)	-2(4)
B(10)	27(5)	16(4)	25(4)	3(4)	7(4)	-1(4)
B(11)	35(5)	15(5)	23(4)	0(4)	4(4)	0(4)
B(12)	31(5)	15(4)	21(4)	-2(4)	-9(4)	1(4)
C(21)	27(4)	58(7)	25(4)	3(4)	-5(4)	-1(4)
C(22)	38(5)	37(5)	43(6)	-9(5)	-6(5)	2(5)
C(23)	37(6)	57(8)	43(6)	4(6)	-8(5)	-15(6)
C(24)	42(6)	83(10)	19(4)	1(5)	0(4)	-11(6)
C(25)	39(5)	46(7)	42(6)	-18(5)	0(5)	7(5)
C(26)	38(5)	38(6)	35(5)	3(5)	-8(4)	3(4)
C(31)	24(5)	35(6)	35(5)	-13(4)	-4(3)	3(4)
C(32)	31(4)	36(5)	26(4)	4(4)	0(4)	9(4)
C(33)	37(4)	33(4)	24(4)	3(6)	11(6)	-2(3)
C(34)	31(5)	31(5)	31(5)	-9(4)	-3(4)	4(4)
C(35)	39(5)	36(5)	24(4)	5(4)	3(4)	-1(4)
C(36)	50(7)	25(6)	48(7)	10(5)	-1(6)	-3(5)

Table 7. Hydrogen coordinates (x 10^4) and isotropic displacement parameters ($Å^2$ x 10^3) for 1.

	x	y	z	U(eq)
H(0)	-738(58)	-6007(19)	1514(5)	29
H(2)	-116(36)	-4602(40)	8(58)	32
H(3)	-132(35)	-2246(123)	1512(6)	29
H(4)	-38(36)	-4765(36)	2885(58)	32
H(5)	188(3)	-8817(10)	2321(4)	31
H(6)	145(3)	-8757(10)	626(3)	29
H(7)	1587(3)	-6442(6)	95(4)	29
H(8)	1369(3)	-2368(10)	642(3)	30
H(9)	1399(3)	-2345(10)	2369(4)	28
H(10)	1662(30)	-6558(35)	2927(48)	28
H(11)	1755(35)	-9136(125)	1471(6)	29
H(21A)	259(6)	-11133(17)	-756(6)	44
H(22A)	594(6)	-7852(16)	-1108(6)	47
H(23A)	1448(7)	-7430(21)	-2151(7)	55
H(24A)	2277(6)	-9941(21)	-2602(6)	57
H(25A)	2091(7)	-13158(19)	-2100(6)	51
H(26A)	1238(6)	-13649(16)	-1018(6)	44
H(31A)	3478(6)	-8147(18)	669(6)	38
H(32A)	3249(6)	-11338(15)	1053(5)	37
H(33A)	3206(5)	-13927(14)	79(8)	37
H(34A)	3715(6)	-13206(15)	-1148(5)	37
H(35A)	3886(6)	-9979(14)	-1542(6)	40
H(36A)	3633(7)	-7349(18)	-663(7)	49

PART II

Nonclassical Metal Carbonyls: A Theoretical Study

"The first step to wisdom is getting things by their right names."

–Chinese Proverb

CHAPTER 1

Nonclassical Metal Carbonyls

Introduction

Carbon monoxide is one of the most important ligands in transition metal chemistry.[1-5] Its uses range from a ligand for fundamental studies of structure and bonding to a chemical feedstock. Many industrial processes, including hydroformylation, Fischer–Tropsch synthesis, methanol synthesis, acetic acid synthe sis, and the water–gas shift reaction employ CO as a reagent and transition-metal compounds as heterogeneous or homogeneous catalysts and involve the intermediacy of metal carbonyls. Carbon monoxide is used to stabilize transition metals in low, even negative, oxidation states. It is also used as a probe ligand in diverse fields such as surface chemistry, catalysis, solid-state chemistry, organometallic chemistry, and biochemistry.

The classical picture of metal-carbonyl bonding, shown in Figure II.1.1, is well developed and is one of the most enduring paradigms in inorganic chemistry. It involves synergistic bonding, with carbon monoxide acting simultaneously as a σ donor and a π acceptor ligand for *d*-block metals. The literature of metal carbonyl chemistry is so vast that more than 600 review articles on this subject have appeared since 1967. The recent review by Lupinetti, Frenking, and Strauss will provide the reader with an entry

point into this literature.[6] Another important reference is the excellent monograph by the Olivés, which was published in 1984.[1] For a glimpse of the field of metal carbonyl chemistry in its earlier years, the reader can consult some of the oldest available reviews.[2-5]

M←CO σ donation

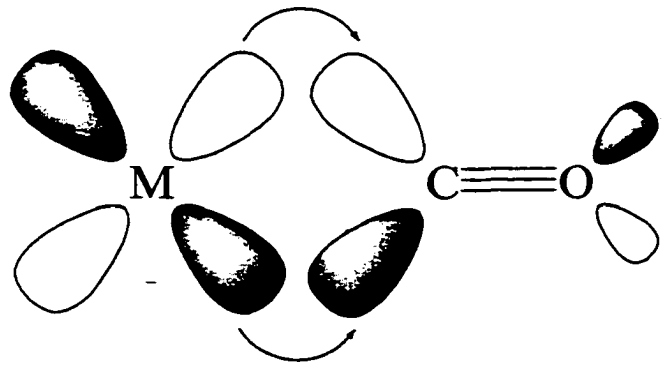

M→CO π backdonation

Figure II.1.1. The classical description of the synergistic bonding in metal carbonyls.

M←CO σDonation

As the carbon end of a CO molecule approaches a metal along the z-axis, the first effects encountered are those of σ donation from the 5σ orbital of CO into empty orbitals on the metal. This OC→metal σ interaction is bonding at long distances (ca. 4Å), because the empty metal orbitals are more diffuse than the occupied metal orbitals, which is particularly true when the metal is positively charged. This donation has the effect of *shortening* the C–O bond and increasing the carbon-oxygen stretching frequency, ν(CO). For example, ν(CO) is 2295 cm^{-1} for CH_3CO^+, 2184 cm^{-1} for HCO^+, and 2168 cm^{-1} for BH_3CO, three species in which σ bonding is the predominant, if not the only, type of bonding.[7-11] *There is, however, an historical controversy in the literature about the nature of the 5σ orbital of carbon monoxide.* The standard textbook explanation states that the HOMO of CO (i.e., the "lone pair" on the carbon atom) is antibonding in the interatomic region.[12,13] Fenske et al.,[14] who showed that the Mulliken population analysis of approximate molecular orbitals was antibonding for the HOMO, were the first to give this explanation. Therefore, as CO donates electron density from this orbital into an empty metal orbital, R(CO) decreases and ν(CO) increases. This finding helped to give a plausible explanation for the experimental results for CO^+ as well: the vibrational frequency (2184 cm^{-1}) and the force constant (19.26 mdyn/Å) of CO^+ are higher than that of CO (2143 cm^{-1} and 18.56 mdyn/Å), and CO^+ has a shorter equilibrium distance (1.1150 Å) than CO (1.12822 Å).[15] If an electron was removed from the HOMO of CO (i.e., $CO \rightarrow CO^+ + e^-$), it would be removed from the 5σ orbital, an antibonding orbital, and the bond order of the C–O bond would increase. Another experimental result which could be explained by assuming an antibonding HOMO for CO was the finding that HCO^+ also has a higher ν(CO) value (2184 cm^{-1}), a larger C–O force constant, *F*(CO),

(21.3 mdyn/Å)[16], and a shorter R(CO) (1.1047 Å) than free CO.[17,18] Once again, the rationale is the same: bonding of the CO molecule to the H^+ requires electron density from the HOMO of CO to be transferred to the empty 1s orbital on the proton.

There is an important theoretical result, however, which speaks against the suggestion that the HOMO of CO is antibonding. Ab initio calculations at the Hartree-Fock level of theory predict a HOMO that is highly localized at the carbon end but is bonding between carbon and oxygen. This result is independent of basis set quality. Calculations at the same level of theory predict that CO^+ and HCO^+ have higher C–O vibrational frequencies than CO, although the HOMO of CO is bonding. There must be another factor besides the nature of the HOMO that strongly influences the C–O bonding interactions. It is argued by some that the explanation for this apparent discrepancy is the charge on the species to which CO is bound. Goldman and Krogh-Jesperson argued that σ bonding does not have a significant effect on the carbon-oxygen force constant but rather, electrostatic effects are the primary reason for larger carbonyl force constants in charged carbonyl complexes than in free CO.[19] This question will be addressed in more detail in Part II, Chapter 3.

M→CO π Backdonation

In addition to being a σ donor, carbon monoxide can also act simultaneously as a π acceptor. Although the amount of σ donation is larger than the amount of π backdonation,[20,21] there is now general agreement that for most transition-metal carbonyl complexes metal→CO π backdonation is more important for M–C bond energy than OC→metal σ donation.[22] This results largely from the fact that the HOMO of CO encounters significant electron repulsion with occupied orbitals on the metal, which counterbalances the bonding interactions of the CO donor orbital with empty orbitals at

the metal.[22] Electron donation from the occupied π orbital of CO to the metal, which has been suggested as an additional source of metal–CO bonding interactions,[13] was found to be insignificant.[20,21]

Charge Effects

In addition to σ and π bonding, there is a purely electrostatic parameter that affects ν(CO) as a function of M–C distance. In a theoretical study by Hush and Williams, it was found that the carbon-oxygen bond in free CO becomes stronger, and ν(CO) rises, if the diatomic molecule is placed in an electric field with the carbon atom facing the direction of increasing positive charge (e.g., towards an electrophilic center).[23] The results of the study are illustrated in Figure II.1.2. An axial electric field affects the dipole moment of CO such that the carbon-oxygen bond is polarized further, resulting in a stronger ionic component. The effect of a point charge on a carbon monoxide molecule or a carbonyl ligand will be examined in depth in Part II, Chapter 2.

High ν(CO) *Carbonyl Compounds*

There is a growing class of metal carbonyl compound, M–C≡O or E–C≡O species (M = metallic element, E = nonmetallic element), with unusually high ν(CO) values, that is, carbonyl compounds with ν(CO) values greater than the ν(CO) = 2143 cm^{-1} of free CO in the gas phase. Examples are ($\nu(CO)_{ave}$ in parentheses) $Cl(CO)(Sb_3F_{16})$ (2256 cm^{-1}),[24] $Cu(CO)_2(AsF_6)$ (2171 cm^{-1}),[25] $Ag(CO)_2(Nb(OTeF_5)_6)$ (2208 cm^{-1}),[26] $Au(CO)_2(Sb_2F_{11})$ (2236 cm^{-1}),[27,28] $Hg(CO)_2(Sb_2F_{11})_2$ (2280 cm^{-1}),[9] $Ir(CO)_6(Sb_2F_{11})_3$ (2268 cm^{-1}),[29] $Rh(CO)_4(1\text{-Et-}CB_{11}F_{11})$ (2167 cm^{-1}),[30] $Cu(CO)_4(1\text{-Et-}CB_{11}F_{11})$ ($\nu(CO)_{asym}$ = 2184 cm^{-1}),[31] and the recently isolated $N(CO)_2(Sb_3F_{16})$ (2327 cm^{-1}).[32] Table II.1.1 is a Periodic Table illustrating all of the elements for which carbonyl

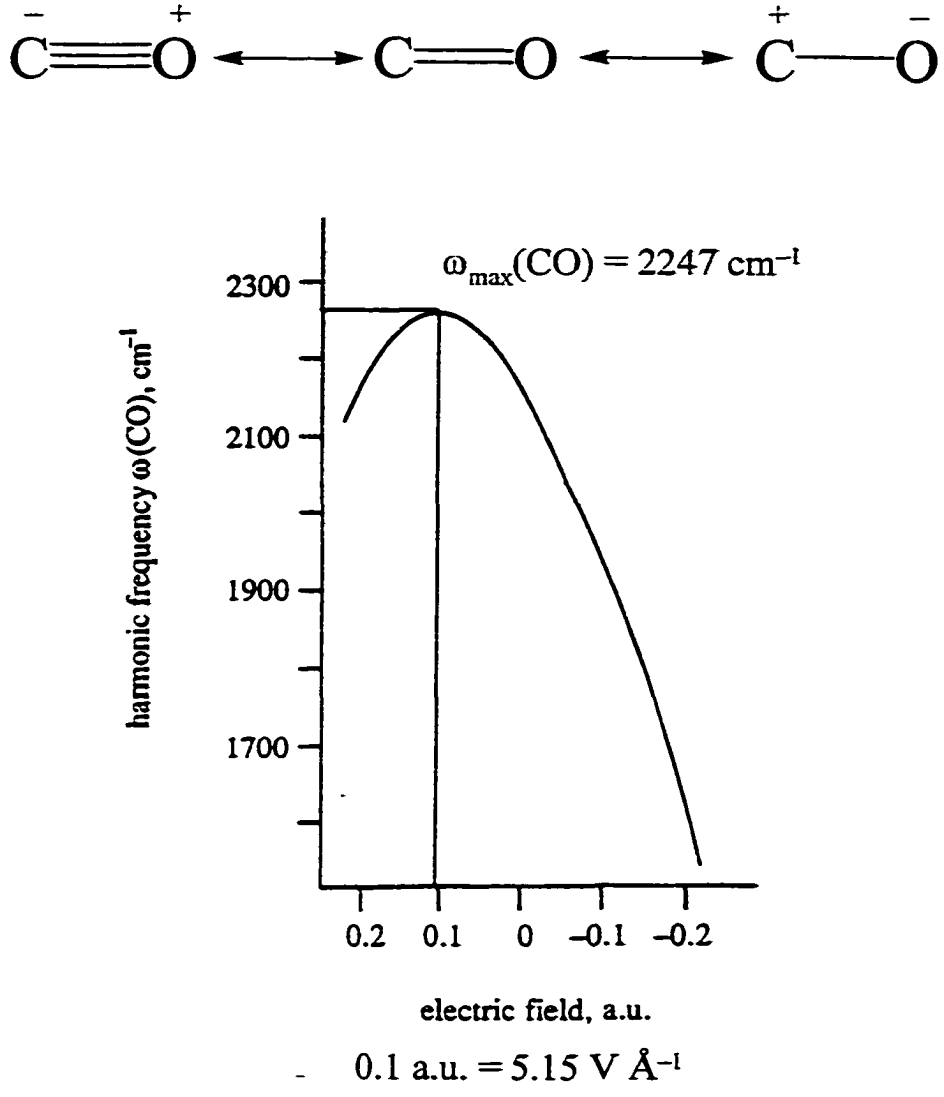

Figure II.1.2. Calculated harmonic carbon-oxygen stretching frequency, ω(CO), for gaseous CO as a function of axial electric field strength (0.1 a.u. = 5.15 V $Å^{-1}$). Values are scaled to the experimental zero-field frequency of CO, ω(CO) 2143 cm^{-1} (ν(CO) = 2143 cm^{-1}). The curve maximum is at ω(CO) = 2247 cm^{-1} or ν(CO) ~ 2220 cm^{-1} (E = 0.1 a.u.). The upper picture illustrates the resonance forms of carbon monoxide, the formal charge of each atom is given above the atom.

Table II.1.1. Periodic Table of Elements that form Nonclassical Carbonyl Complexes[a]

H 2184																	He
Li 2185	Be 2207											B 2167	C 2294	N 2327	O	F	Ne
Na 2172	Mg 2203											Al 2185	Si 2158	P	S	Cl 2256	Ar
K 2153	Ca 2158	Sc 2218	Ti 2212	V 2205	Cr 2181	Mn 2208	Fe 2198	Co 2179	Ni 2200	Cu 2191	Zn 2212	Ga	Ge	As	Se	Br	Kr
Rb 2159	Sr 2181	Y 2184	Zr 2176	Nb	Mo	Tc	Ru 2216	Rh 2167	Pd 2218	Ag 2209	Cd 2209	In	Sn 2176	Sb	Te	I	Xe
Cs 2145	Ba 2178	La 2182	Hf	Ta	W	Re	Os 2211	Ir 2268	Pt 2261	Au 2236	Hg 2280	Tl	Pb 2161	Bi	Po	At	Rn

[a] Numbers in the table are ν(CO) values (cm^{-1}) for one, characteristic example:[6]

s-block

HCO^+, gas phase

Li(CO)(ZSM–5), 226 K

Na(CO)F, Ar/CO matrix, 10 K

K(CO)Cl, 100 face of KCl, 77 K

Rb(CO)(mordenite), 77 K

Cs(CO)(ZSM–5), 226 K

Be(CO)O, 77 K

Mg(CO)O, 001 face of MgO

$Ca(CO)(Cp^*)_2$, toluene

$Sr(CO)F_2$, Ar/CO matrix

Ba(CO)(zeolite–Y), 77 K

groups 3–7

$Sc(CO)O^+$, Ar matrix, 12 K

$Y_2(CO)F_6$, Ar/CO matrix, 10 K

$La(CO)F_3$, Ar/CO matrix, 10 K

$Ti(CO)O_2$, anatase

$Zr(CO)(Cp)_2(COCH_3)^+$, CH_2Cl_2

$V(CO)O^+$, Ar matrix, 12 K

$Cr_2(CO)O_3$, $01\bar{1}2$ face of Cr_2O_3

Mn(CO)(zeolite–Y)

groups 8–10

Fe(CO)(zeolite–Y)

$Ru(CO)_6(Sb_2F_{11})_2$

groups 8–10 (continued)

$Os(CO)_6(Sb_2F_{11})_2$

Co(CO)O

$Rh(CO)_4(1\text{-Et-}CB_{11}F_{11})$

$Ir(CO)_6(Sb_2F_{11})_3$

$Ni(CO)F_2$, Ar/CO matrix, 10 K

$Pd(CO)_2(SO_3F)_2$

$Pt(CO)_4(Sb_2F_{11})_2$

groups 11–12

$Cu(CO)_3(AsF_6)$

$Ag(CO)_2(B(OTeF_5)_4)$

$Au(CO)_2(Sb_2F_{11})$

Zn(CO)O

Cd(CO)(zeolite–Y)

$Hg(CO)_2(Sb_2F_{11})_2$

main group

$BH_3(CO)$, Ne matrix, 10 K

$Al(CO)Me_3$, CO matrix

$CH_3CO(SbF_6)$

$Si(CO)O_2$

$Sn(CO)Cl_2$, Ar matrix

$Pb(CO)Br_2$, Ar matrix

$N(CO)_2(Sb_3F_{16})$

$Cl(CO)(Sb_nF_{5n+1})$ $(n > 2)$

compounds with average ν(CO) values greater than 2143 cm^{-1} have been isolated. A complete review of carbonyl complexes with $\nu(CO) > 2143$ cm^{-1} (as of the end of 1999) is provided by Lupinetti, Frenking, and Strauss.[6]

Despite the recent activity in the area of metal carbonyls with ν(CO) > 2143 cm^{-1},[1,25,26,28,29,33-35] it should be noted that metal carbonyls with $\nu(CO) > 2143$ cm^{-1} have been known since the inception of metal carbonyl chemistry. Previous workers noted the "atypical" nature of metal carbonyls of late *d*-block metal ions and suggested that many such compounds have little or no π backbonding (an idea that will be investigated in detail later in Part II).[36,37] The compound Au(CO)Cl, with $\nu(CO) =$ 2162 cm^{-1}, was first described in the literature in 1925.[38] Even more striking is *cis*-$Pt(CO)_2Cl_2$, with $\nu(CO)_{ave} = 2158$ cm^{-1}. The synthesis of this complex, one of only ~225 reported to date with $\nu(CO) > 2143$ cm^{-1}, was reported by Schützenberger in 1870,[39] two decades before Mond reported the synthesis of $Ni(CO)_4$.[40] History is full of ironies, and the history of chemistry is no exception. The first metal carbonyl complex to be reported in the literature was not the prototype: *cis*-$Pt(CO)_2Cl_2$ turned out to be categorically different than 98–99% of the carbonyl compounds to come.

As illustrated above, the carbon-oxygen bond in carbon monoxide is affected in two distinct ways when bound to a metal (i.e., M or E). In the vast majority of the cases, the carbon oxygen bond becomes weaker, which is manifested in a ν(CO) less than free CO (i.e., $\nu(CO) < 2143$ cm^{-1}). However, in approximately 1–2% of the carbonyl compounds synthesized to date, the carbon-oxygen bond becomes stronger upon bonding with M or E, which is manifested in a ν(CO) greater than free CO. These differences in behavior indicate a fundamental difference in the metal–carbonyl bonding between these two classes of carbonyl compounds, and the names classical ($\nu(CO) < 2143$ cm^{-1}) and nonclassical ($\nu(CO) < 2143$ cm^{-1}) were previously proposed to distinguish between the two classes.[33] In the following section, a more rigorous definition for classical and nonclassical metal carbonyl will be proposed.

The Justification for Two Categories of Metal Carbonyls[6,41]

Listed below are ten statements about transition metal carbonyls that most chemists would agree are unambiguous and valid. These statements are divided into five pairs. It may seem at first that each pair of statements is repetitive, i.e., that each pair is simply two ways of expressing the same concept. However, the important distinction between the *a* Statements (1*a*–5*a*) and the *b* Statements (1*b*–5*b*) is that the former are true for all metal carbonyls while the latter are not true for all metal carbonyls.[41]

1*a*. CO is a σ donor and a π acceptor ligand;

1*b*. M–CO bonds have a significant M←CO σ component and a significant M→CO π component;

2*a*. The π component (π backbonding) involves the transfer of electron density from metal d_π orbitals to CO π* orbitals;

2*b*. C–O distances (R(CO)) are longer and ν(CO) values are lower for metal carbonyls than for the free CO molecule (1.12822 Å and 2143 cm^{-1}, respectively);

3*a*. Adding a donor ligand L to a metal carbonyl complex increases the electron density at the metal center and enhances M←CO π backbonding;

3*b*. Adding a donor ligand L to a metal carbonyl complex results in a stronger, shorter M–CO bond and a weaker, longer C–O bond;

4*a*. Substituting an ancillary ligand L with one that is a stronger σ donor enhances M→CO π backbonding;

4*b*. Substituting an ancillary ligand L with one that is a stronger σ donor results in a stronger, shorter M–CO bond and a weaker, longer C–O bond;

5*a*. The transformation $LM(CO)_n \leftarrow LM(CO)_{n-1} + CO$ results in fewer π-acceptor CO ligands competing for the same metal d_π electron density;

5*b*. The transformation $LM(CO)_n \leftarrow LM(CO)_{n-1} + CO$ results in weaker, longer C–O bonds and lower ν(CO) values.

Support for Statements 1b–5b

First consider typical examples for which the Statements 1*b*–5*b* are true. *M–CO bonds have a significant M←CO σ component and a significant M→CO π component.* The synergistic nature of M–CO bonding, shown in Figure II.1.1 is very well accepted.[42] Even before the application of molecular orbital theory to metal complexes, the unexpectedly (for the time) short Ni–CO distance in $Ni(CO)_4$[43] prompted Pauling to suggest partial double–bond character for the nickel-carbon bonds.[44] This was followed by the now standard Dewar–Chatt–Duncansen molecular orbital model.[45-47] A good example with which to demonstrate the validity of Statement 1*b* is $Cr(CO)_6$. In 1980, both Sherwood and Hall[48] and Bursten, Freier, and Fenske[49] predicted that the amount of Cr→CO π backbonding in $Cr(CO)_6$ was between 33% and 45% of the amount of Cr→CO σ bonding. The recent predicted value of 35% based on a modern DFT charge decomposition analysis of $Cr(CO)_6$ is consistent with these earlier results.[50]

C–O distances (R(CO)) are longer and ν(CO) values are lower for metal carbonyls than for the free CO molecule (1.12822 Å and 2143 cm^{-1}, respectively). The validity of Statement 2*b* is best demonstrated using the tetrahedral complex $Co(CO)_4^-$. The value of $\nu_{asym}(CO)$ for the sodium salt in HMPA solution is 1890 cm^{-1},[51] more than 250 cm^{-1} lower than the 2143 cm^{-1} value for free CO. The R(CO) values for the protonated quinuclidine salt of $Co(CO)_4^-$ (±σ shown in parentheses) range from 1.154(3) to 1.165(3) Å,[52] more than 0.025 Å longer than the 1.12822 Å value for free CO. Note that the structure of [H(quinuclidine)][$Co(CO)_4$] (Figure II.1.3) is one of very few recent structures of metal carbonyls in which R(CO) lengthening was observed to be significant at the ±3σ level of confidence.

Adding a donor ligand L to a metal carbonyl complex results in a stronger, shorter M–CO bond and a weaker, longer C–O bond. Statement 3*b* is demonstrated by examination of the effect of the addition of two weak F^- ion donors to the linear $Pd(CO)_2$

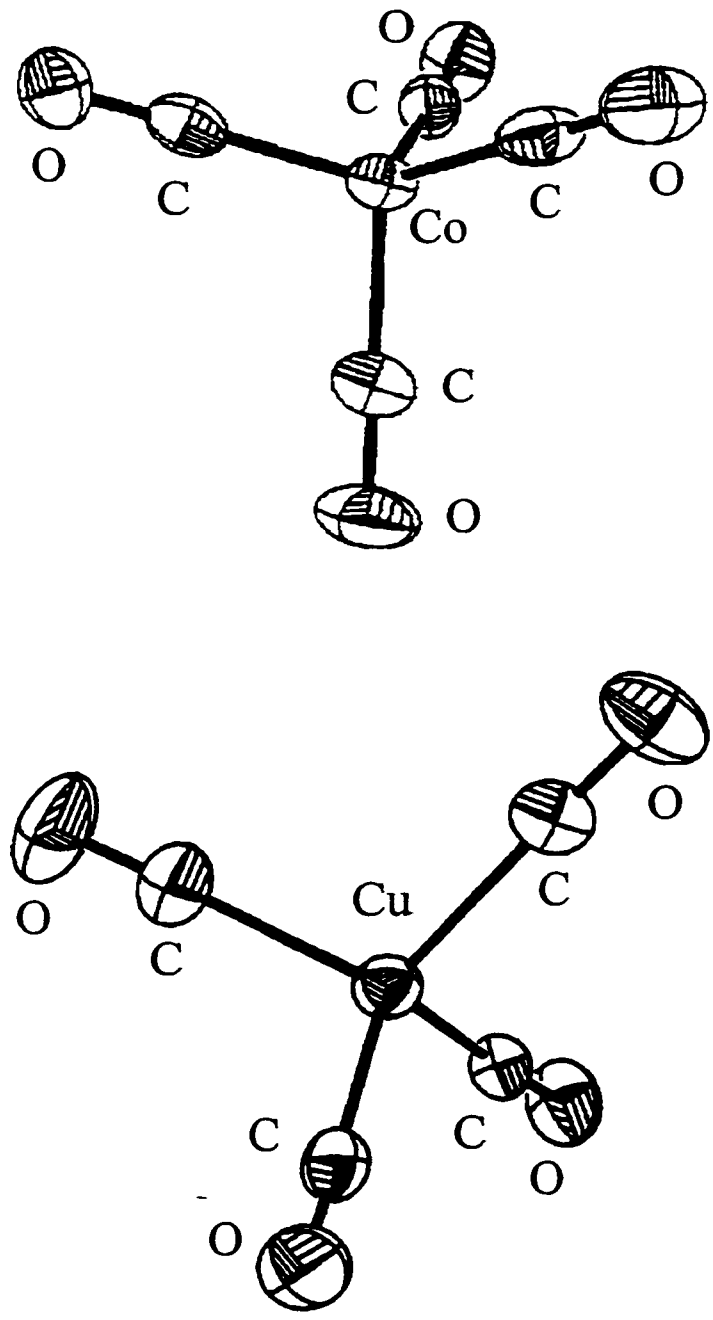

Figure II.1.3. Structures of the $Co(CO)_4^-$ anion in [H(quinuclidine)][$Co(CO)_4$] (reference 59; top) and the $Cu(CO)_4^+$ cation in $Cu(CO)_4$(1-Et-$CB_{11}F_{11}$) (reference 31; bottom). Selected bond distances and angles (deg): Co–C, 1.757(2)–1.777(2); C–O, 1.150(2)–1.153(2); C–Co–C, 107.5(2)–113.6(1); Cu–C, 1.961(3)–1.968(3); C–O, 1.109(4)–1.114(3); C–Cu–C, 104.3(1)–112.1(6); O–C–Cu, 174.8(3)–178.4(3).

moiety, which was studied at the MP2 level of theory.[53] (These experiments will be presented in detail in Part II, Chapter 4.) Even with relatively long Pd–F^- distances of 3 Å, the D_{2h} symmetry complex $[Pd(CO)_2(F)_2]^{2-}$ was predicted to have Pd–C and C–O distances (1.924 and 1.167 Å) that were shorter and longer, respectively, than the corresponding predicted distances in linear $Pd(CO)_2$ (1.942 and 1.156 Å). In harmony with the longer, weaker C–O bonds in $[Pd(CO)_2(F)_2]^{2-}$, the predicted value of $\nu_{sym}(CO)$ decreased by 66 cm^{-1} ($\Delta\nu(CO)_{ave} = -84$ cm^{-1}) on going from linear $Pd(CO)_2$ to D_{2h} $[Pd(CO)_2(F)_2]^{2-}$. Clearly, the F^- σ-donor ligands induce additional π backbonding in $[Pd(CO)_2(F)_2]^{2-}$ relative to $Pd(CO)_2$.

Substituting an ancillary ligand L with one that is a stronger σ donor results in a stronger, shorter M–CO bond and a weaker, longer C–O bond. There are many examples that demonstrate the validity of Statement 4b. Two classic examples are the consequences of substituting three CO ligands in $Cr(CO)_6$ with three σ-donor ligands. The 1.909 Å Cr–CO distance in $Cr(CO)_6$ decreased to 1.839 Å in fac–$Cr(CO)_3(PH_3)_3$[54] and to 1.816 Å in fac–$Cr(CO)_3(NH(C_2H_4NH_2)_2)$.[55] Addition of better σ-donor ligands provides more electron density to the metal center. This allows for better π backdonation, and therefore shorter, stronger M–C bonds and longer C–O bonds (lower ν(CO)).

The transformation $LM(CO)_n \leftarrow LM(CO)_{n-1} + CO$ results in weaker, longer C–O bonds and lower ν(CO) values. Three examples demonstrate the validity of Statement *5b* are $Cr(CO)_6$ ($\nu(CO)_{ave} = 2017$ cm^{-1}) vs. $Cr(CO)_5$ ($\nu(CO)_{ave} < 2000$ cm^{-1}),[56] $CpMn(CO)_3$ ($\nu(CO)_{ave} = 1967$ cm^{-1}) vs. $CpMn(CO)_2$ (ν(CO)ave = 1921 cm^{-1}),[57] and $Fe(OEP)(CO)_2$ ($\nu(CO)_{ave} \geq 2016$ cm^{-1}) vs. Fe(OEP)(CO) (ν(CO) = 1951 cm^{-1}).[58] Here it is assumed that when a π-acceptor ligand is removed from the metal center, the remaining CO ligands have more d_π electron density per CO—fewer π acceptors means more π density for each ligand and, therefore, lower ν(CO) values.

Violations of Statements 1b–5b

Now that examples have been given in support of the five statements listed above, it is appropriate to examine those cases that violate Statements 1*b*–5*b*. For this study, four of the five statements will be examined; Statement 4*b* will not be discussed since to the best of the author's knowledge, neither experimental nor theoretical cases exist that violate this statement.

M–CO bonds have a significant M←CO σ component and a significant M→CO π component. Theoretical studies by Szilagyi and Frenking of the isoelectronic series $M(CO)_6^{x+}$ (M^{x+} = Hf^{2-}, Ta^{-}, W, Re^{+}, Os^{2+}, Ir^{3+}) show that as the charge on the metal increases, the percentage of π backdonation with respect to the total donation/backdonation decreases (42% for Hf^{2-} and 8% for Ir^{3+}). From these calculations, it is obvious that there is very little π backdonation in the $Ir(CO)_6^{3+}$.

C–O distances (R(CO)) are longer and ν(CO) values are lower for metal carbonyls than for the free CO molecule (R(CO) < 1.12822 Å and ν(CO) > 2143 cm^{-1}).[60] There are now greater than 225 M–C≡O and E–C≡O species with ν(CO) > 2143 cm^{-1}.[6] At least six of these have R(CO) values that are significantly smaller than 1.12822 Å. Two examples that violate both criteria of Statement 1*b* are $Pd(CO)_2(SO_3F)_2$ ($\nu(CO)_{ave}$ = 2218 cm^{-1}; R(CO) = 1.102(6), 1.114(6) Å),[61] and $Cu(CO)_4^{+}$ ($\nu_{asym}(CO)$ = 2184 cm^{-1}; R(CO) = 1.109(4)–1.114(3) Å),[31] which is compared with the structure of $Co(CO)_4^{-}$ in Figure II.1.3. Figure II.1.4 displays eight carbonyl species from the literature with R(CO) values shorter than free carbon monoxide (1.12822 Å) at the ±3σ level of confidence. All of these carbonyl containing species have ν(CO) values > 2143 cm^{-1}. Also included in Figure II.1.4, for comparison, are two examples of classical metal carbonyls, $[NEt_4][Cr(CO)_4(NHMeCH_2CO_2)]$[59] and [H(quinuclidine)][$Co(CO)_4$].[59] Despite this comparison it is clear that experimental R(CO) values cannot be used, in general, to reliably compare and contrast different metal carbonyls. In the past, X-ray

structures of metal carbonyls were rarely of sufficient precision that derived R(CO) values were significantly different than 1.12822 Å. This is a consequence of the strength of the CO bond, which is one of the strongest known chemical bonds. The depth and steepness of the CO potential energy well requires that even a significant change in CO bond energy or force constant will result in only a small change in R(CO) relative to $\pm 3\sigma$. A further limitation on experimental R(CO) values is caused by librational motion in crystals that can lead to an underestimation of the true C–O distance. For these reasons, vibrational data are the most reliable experimental characterization technique, therefore, ν(CO) > 2143 cm^{-1} is a useful criterion for determining if a carbonyl complexes is a nonclassical metal carbonyl species. The above data provides compelling evidence that the diatomic molecule CO can respond in two completely different ways when it binds to a metal center. In the vast majority of cases, the response is that R(CO) increases and ν(CO) decreases. This large category of metal carbonyls could be called common, ordinary, or usual; we have chosen to call it classical. Strictly speaking, we should say that metal carbonyls in this category are classical with respect to Statement 2*b*. The other response is that R(CO) decreases and ν(CO) increases, and metal carbonyls in this category are termed nonclassical with respect to Statement 2*b*.

Adding a donor ligand L to a metal carbonyl complex results in a stronger, shorter M–CO bond and a weaker, longer C–O bond. One example of a violation of Statement *3b* is provided by the examination of the effect of the addition of two weak F^- ion donors to the linear $Ag(CO)_2^+$ moiety, which was studied at the MP2 level of theory.[53] (These experiments will be presented in detail in Part II, Chapter 4.) This complex is isoelectronic with $Pd(CO)_2$, discussed above as an example in support of Statement 3*b*, but behaves differently under an identical perturbation—two F– anion 3 Å away from the metal. In the case of the silver(I) dicarbonyl, the D_{2h} symmetry complex $[Ag(CO)_2(F)_2]^-$ was predicted to have Ag–C and C–O distances (2.196 and 1.147 Å) that

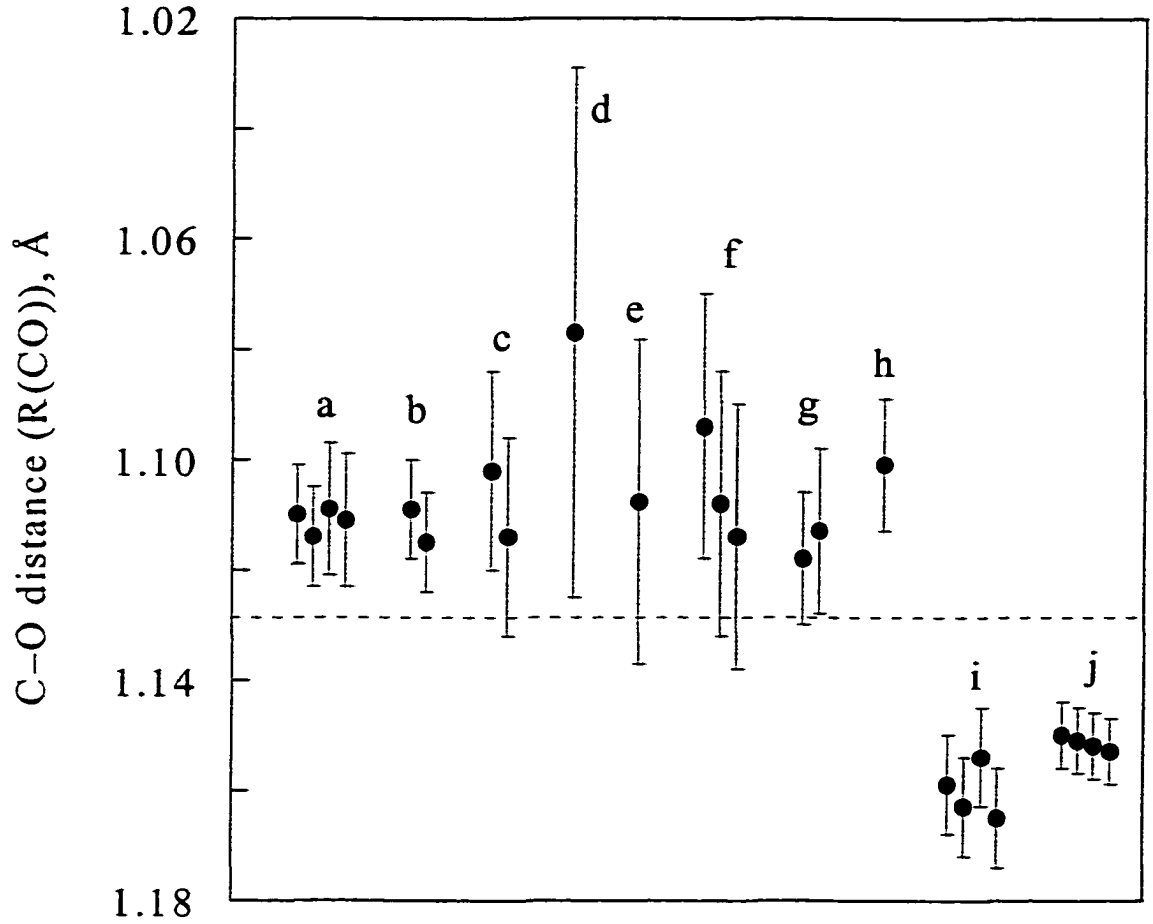

Figure II.1.4. R(CO) values for six nonclassical metal carbonyls (a–f), two salts of p-block carbonyls (g, h), and two classical metal carbonyls (i, j): (a) $[Cu(CO)_4][1\text{-Et-}CB_{11}F_{11}]$ (ref 31); (b) $Cu(CO)_2(1\text{-Bn-}CB_{11}F_{11})$ (ref 31); (c) $Pd(CO)_2(SO_3F)_2$ (ref 62); (d) $Ag(CO)(B(OTeF_5)_4)$ (ref 26); (e) $Au(CO)_2(Sb_2F_{11})$ (ref 27); (f) $Ir(CO)_3(SO_3F)_3$ (ref 63); (g) $[N(CO)_2][Sb_2F_{16}]$ (ref 32); (h) $[(CH_3)_2CHCO][SbCl_6]$ (ref 26); (i) $[NEt_4][Cr(CO)_4(NHMeCH_2CO_2)]$ (ref 52); (j) [H(quinuclidine)][$Co(CO)_4$] (ref 52). The horizontal dotted line represents the distance in free CO (1.12822 Å).[60]

were both longer than the corresponding predicted distances in linear $Ag(CO)_2^+$ (2.160 and 1.142 Å). Since the F^- σ-donor ligands are expected to induce additional π backbonding in $[Ag(CO)_2(F)_2]^-$ relative to $Ag(CO)_2^+$ and since the Ag–C bonds become longer, it can be concluded that there is insignificant π backbonding in $Ag(CO)_2^+$.

The transformation $LM(CO)_n \rightarrow LM(CO)_{n-1} + CO$ results in weaker, longer C–O bonds and lower ν(CO) values. Experimental $\nu_{asym}(CO)$ values for $Cu(CO)_3(AsF_6)$ and $Cu(CO)_2(AsF_6)$ are 2179 and 2164 cm^{-1}, respectively, in harmony with Statement *5b*.[25] In contrast, $\nu_{asym}(CO)$ values for $Ag(CO)_3(Nb(OTeF_5)_6)$ and $Ag(CO)_2(Nb(OTeF_5)_6)$ are 2191 and 2198 cm^{-1}, respectively,[26] and for $Au(CO)_3(Sb_2F_{11})$ and $Au(CO)_2(Sb_2F_{11})$ are 2212 and 2217 cm^{-1}, respectively, in violation of Statement *5b*.[28,64] These differences are shown graphically in Figure II.1.5.[33] In this case too, the same perturbation has produced two different effects, classical (Cu^+) and nonclassical (Ag^+ and Au^+). Note that the copper complexes behave classically with respect to Statement *5b* but nonclassically with respect to Statement *2b*.

What is a Nonclassical Metal Carbonyl?

Based on the five pairs of statements presented above, the most sensible way to label metal carbonyls is as follows: metal carbonyls that conform to Statements *1b–5b* are classical metal carbonyls; any metal carbonyl complex that violates *at least one* of Statements *1b–5b* is a nonclassical metal carbonyl.

For example, are linear d^{10} copper(I) dicarbonyls classical or nonclassical? The answer depends on which statement about metal carbonyls is being considered. Both $Cu(CO)_3(AsF_6)$ and $Cu(CO)_2(AsF_6)$ are nonclassical with respect to Statement *2b* (the ν(CO) values for these two complexes are *higher* than for the free CO molecule), but they are classical with respect to Statement *5b* (the transformation $LM(CO)_n \leftarrow LM(CO)_{n-1} + CO$ *does* result in lower ν(CO) values).

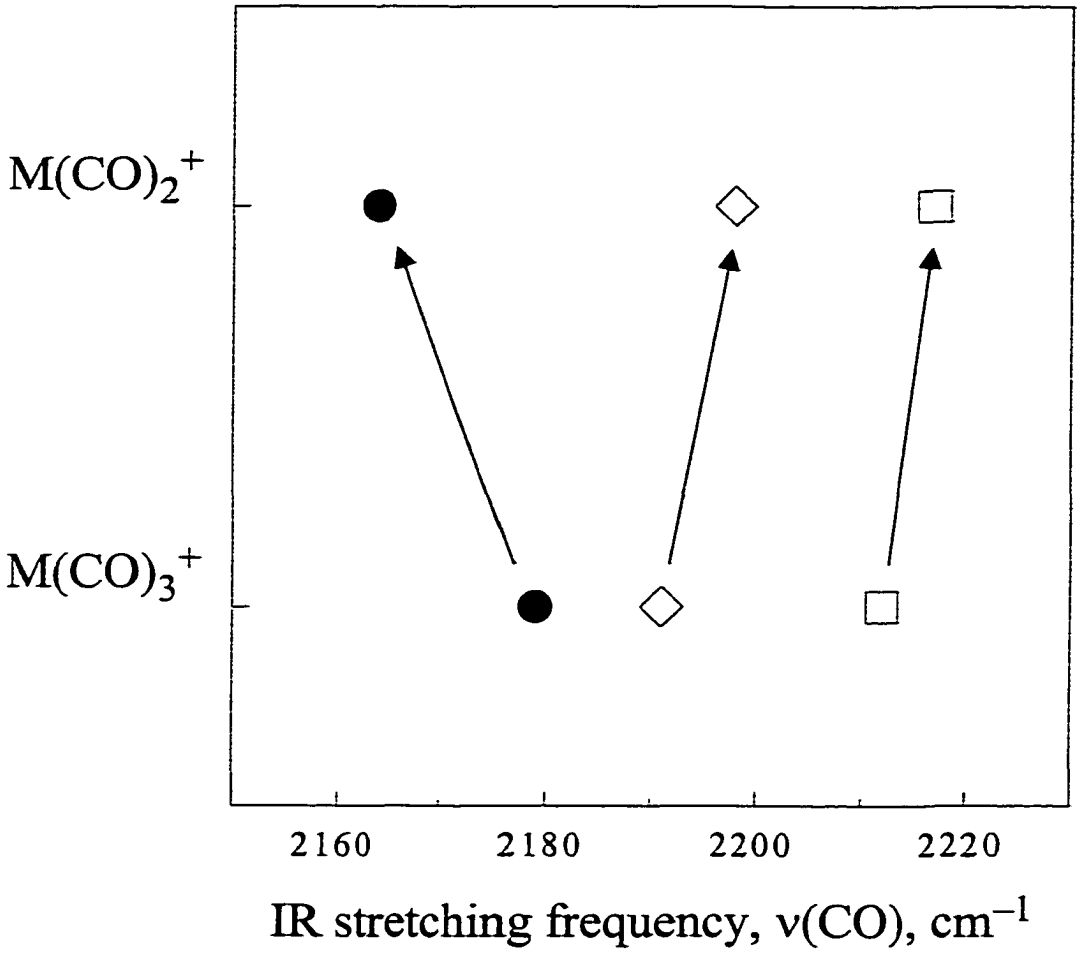

Figure II.1.5. Changes in ν(CO) values, from solid-state infrared spectra, for the transformations $M(CO)_3^+ \rightarrow M(CO)_2^+ + CO$ ($M^+ = Cu^+$, Ag^+, and Au^+). The ν(CO) values for $M(CO)_3^+$ and $M(CO)_2^+$ correspond to the E' normal mode (D_{3h} symmetry) and the Σ_u^+ normal mode ($D_{\infty h}$ symmetry), respectively.

Whether a metal carbonyl complex is investigated experimentally or theoretically the definitions presented above are appropriate. That the phrase *with respect to* is needed to answer the question should be no more disconcerting than the fact that this three-word phrase is also needed to answer questions unambiguously about the stability of compounds. For example, a compound might be thermodynamically *stable* with respect to its constituent elements but *unstable* with respect to disproportionation or with respect to another set of products. As far as a simple question of stability is concerned, the most sensible approach is to designate a compound as unstable if it is unstable with respect to *at least one* set of products, even if it is stable with respect to other possible sets of products.

If a carbonyl complex violates even one of the five pairs of Statements, its designation as nonclassical will serve to alert other scientists that it is an unusual compound and that careful scrutiny of it might be rewarded by new chemical insights and discoveries. Other definitions of "nonclassical metal carbonyl" can and undoubtedly will be conceived and tested by other workers. It is expected that further experimental and theoretical work will lead to new surprises, new insights, and new debates about the metal-carbon bonds in metal carbonyls with $\nu(CO)_{ave}$ values > 2143 cm^{-1}.

Scope of Part II

Part II of this dissertation is a computational work. It will be concerned with the geometric and electronic structures of M–C≡O and E–C≡O species with ν(CO) values greater than 2143 cm^{-1} as well as with the differences between classical and nonclassical metal carbonyl complexes. Chapter 2 will focus on the controversy surrounding the effects of charge on the bonding between the carbon and oxygen in carbon monoxide. Once the effect of charge on a carbonyl ligand is established, Chapter 3 will examine the

geometries of the group 11 and group 12 homoleptic metal carbonyls. A number of high stretching frequency group 11 (and a few group 12) metal carbonyls have been synthesized, isolated, and characterized and sequential bond dissociation energies for the gas phase cations $M(CO)_n^+$ (M = Cu, Ag; n = 1–4) have been experimentally determined. These experimental data allow for the calibration of the computational methods used. These complexes will then be examined in order to determine the electronic factors contributing to the trends in bond energies and geometries seen for these complexes. Finally, in Chapter 4, two theoretical experiments will be presented in which a perturbation is applied to a series of metal carbonyl complexes; in each set of experiments, two different responses occur. These differences provide theoretical support for the distinction between classical and nonclassical carbonyls. It is hoped that this work will give the reader a better understanding of the factors affecting the bonding in metal carbonyl complexes and also convince the reader that two distinctly different classes of metal carbonyl complexes exists—classical and nonclassical—which behave differently under an identical perturbation.

Computational Details

Details of the theoretical experiments performed in the following chapters are described here. Unless otherwise noted (i.e., Part II, Chapter 2), these methods are employed in all of the calculations described.

Basis Sets

All calculations in Part II of this dissertation were carried out using the quasi-relativistic small-core pseudopotentials (ECP) for the metals developed by the Stuttgart

group.[65,66] The basis sets for the valence electrons have at least triple-zeta quality,[65,66] which were augmented by an f-type polarization function in some of the calculations.[67] The standard basis sets 6-31G(d)[68] or TZ2P[69,70] were employed for carbon and oxygen atoms. Table II.1.2 lists basis set combinations I–V, some of which have been used in previous studies.[71,72]

Table II.1.2. Basis Sets Used in This Dissertation

basis	metal valence basis set	C,O
I[a]	(311111/22111/411)	6-31G(d)
II	(311111/22111/411/1)	6-31G(d)
III[b]	(311111/22111/411)	TZ2P
IV	(311111/22111/411/1)	TZ2P
V	(311111/22111/3111/1)	TZ2P

[a] ECP1 in references [71,72]. [b] ECP2 in references [71,72].

Methods

The geometries of all of the metal carbonyl cations were optimized at the MP2 level of theory[73,74] using basis set I (MP2/I), which is the standard method for geometry optimization in this dissertation. *Unless otherwise noted, it will be assumed that the MP2 level of theory was employed using basis set I.* Additional geometry optimizations were carried out for selected complexes at the CCSD(T) level of theory[75-81] and using density functional theory (DFT). The DFT optimizations employed the gradient-corrected

functionals BP86[82,83] and the 3-parameter hybrid functional B3LYP.[82,83] In most cases, M–CO bond energies were calculated using the MP2/I geometries, but the single point energy calculations were performed at the CCSD(T) level of theory (CCSD(T)/I//MP2/I). In Part II, Chapter 3, bond distances and bond energies were also determined at BP86/I and B3LYP/I for selected complexes. Vibrational frequencies were calculated at MP2/I. Unless otherwise noted, the structures discussed in this work are energy minima. The program packages Gaussian 94,[84] Molpro,[85] and ACES II[86] were employed.

Electronic Structure

The nature of the M–C and C–O bonds was examined using three methods: the natural bond orbital (NBO)[87] partitioning scheme; charge decomposition analysis (CDA);[20] and the topological analysis of the electron density distribution.[88] In the CDA method the (canonical, natural or Kohn-Sham) molecular orbitals of the complex are expressed in terms of the MOs of appropriately chosen fragments. In the present cases, the natural orbitals of the MP2/I wavefunctions of $M(CO)_n^{x+}$ are formed as a linear combination of the orbitals of M^{x+} as one fragment and $(CO)_n$ as the second fragment in the geometry of the complex. The orbital contributions are then divided into four parts: (1) mixing of the occupied orbitals of $(CO)_n$ and the unoccupied orbitals of M^{x+} (σ donation, $M^{x+}\leftarrow(CO)_n$); (2) mixing of the unoccupied orbitals of $(CO)_n$ and the occupied orbitals of M^{x+} (π backdonation, $M^{x+}\rightarrow(CO)_n$); (3) mixing of the occupied orbitals of both fragments (repulsive polarization, $M^{x+}\leftrightarrow(CO)_n$); and (4) mixing of the vacant orbitals of the two fragments (residual term). The latter contribution should be ~0 for true closed-shell interactions. For the CDA calculations the program CDA 2.1 was used.[89] Topological analysis of the electron density distribution, $\rho(\mathbf{r})$, the gradient vector field $\nabla\rho(\mathbf{r})$, and the associated Laplacian, $\nabla^2\rho(\mathbf{r})$, were computed using the programs PROAIM, SADDLE, GRID, and GRDVEC.[90]

CHAPTER 2

Theoretical Analysis of the Bonding Between CO and Positively Charged Atoms

Introduction

The classical picture of metal-ligand bonding in transition metal carbonyl complexes given in textbooks of inorganic and transition metal chemistry describes the donor-acceptor bonds in terms of synergistic bonding, where carbon monoxide acts simultaneously as σ donor and π acceptor (Part II, Chapter 1).[13,91-93] Theoretical studies about the nature of the metal–CO bond have shown that the dominant orbital interactions at CO involve the HOMO, which has its major extension at the carbon end (σ donation) and the C–O antibonding LUMO (π–backdonation).[20-22,94-98] This chapter is concerned with two aspects of the bonding in carbonyl compounds: (1) the reason for the increase in the C–O stretching frequency in carbonyl compounds where σ donation is the dominant factor for the bonding interactions, i.e. in nonclassical carbonyls; (2) the relationship between the two components σ donation and π backdonation in metal carbonyl cations M^{+}–CO and the influence of the two different types of interactions upon the C–O bond length.

The results presented in this chapter show that the major reason leading to a change in the C–O force constant and the equilibrium distance of XCO^+ and COX^+ is, in the absence of strong π interactions, the electrostatic effect of X^+ upon CO. This explains why ν(CO) and F(CO) decrease when X^+ approaches CO from the oxygen end, while they increase when X^+ approaches from the carbon end. Goldman and Krogh–Jespersen, have reached a similar conclusion in an independent theoretical study in which they showed that a positive point charge Q^+ at the carbon end of CO has nearly the same effect as a proton.[19] The work presented here complements the important work of these authors by showing the results not only for QCO^+ but also for COQ^+ together with an analysis of the changes in the electronic structure of CO when Q^+ approaches CO from the oxygen or the carbon end. These results are compared with calculated data for HCO^+ and COH^+. It will be shown that the electrostatic effect of the proton on CO, which was suggested by Goldmann and Krogh–Jespersen to be the main reason for the bond shortening and increase of the force constant, operates indirectly by reducing the polarization of the C–O bond orbitals.

Carbonyl cations HCO^+ and COH^+ have been studied theoretically before, but most studies were concerned with the structure and bond energy of the cations.[99-107] In a pioneering study, Hall and Fenske[108] compared calculated orbital populations taken from approximate calculations with experimental vibrational frequency data. Beach and Jolly[109] suggested that the rehybridization of the CO 4σ and 5σ orbitals is responsible for the increase of ν(CO) when CO becomes coordinated to BH_3, but the effect of the π orbitals was not considered. This study focuses on the changes of the properties and electronic structure of CO when it is bonded to an H^+ or a point charge, Q^+.

Additional Methods

The calculations in this chapter required a number of special computational methods not described in Part II, Chapter 1. The Coulomb effect of a positive point charge Q^+ was achieved in two different ways. The first method used a proton with no orbitals. This method was chosen for the geometry optimization and frequency calculations, since it is then possible to use analytical gradients for the geometry optimization. The second method used a true point charge, i.e. a positive charge that has no mass. Both methods were used for the analysis of the electronic structure of QCO^+ and COQ^+. The results were the same.

The internal force constants for the C–O stretching mode, F(CO), were calculated using Equation 1. The F(CO) values obtained resulted from energy changes, relative to the energy minimized geometries in the carbonyl complex (ΔE_{XCO}) and in free CO (ΔE_{CO}), caused by a 0.01 Å extension of the C–O bond. This method is identical to the one used in the study by Goldman and Krogh–Jespersen.[19]

$$F(CO) = (\Delta E_{XCO}/\Delta E_{CO})F(CO) \qquad (II.2.1)$$

The F(CO) value on the right side of Equation 1 is a scaling factor and represents the calculated F(CO) value for free CO at MP2/I, i.e. 18.92 mdyn/Å.

Results and Discussion

In order to estimate the difference between the effect of a proton, H^+, and a positive charge, Q^+, on the energy, the interatomic distance and the vibrational mode of CO, the geometries of linear HCO^+ and QCO^+ were optimized and the vibrational frequencies at fixed H^+–CO and Q^+–CO distances were calculated using intervals between 4.0 and 0.5 Å. Table II.2.1shows the calculated results. Figure II.2.1 shows a plot of the calculated energies of HCO^+ and QCO^+ as a function of the H^+–CO and Q^+–CO distances. The energy minimum of HCO^+ is found at R(HC) = 1.095 Å and at R(CO) = 1.131 Å, which is shorter than the calculated value for free CO (1.151 Å). The shorter C–O bond of HCO^+ compared with free CO is in agreement with the experimental results cited above and with recent theoretical work at the CCSD(T)/ cc–pVQZ level of theory[110], which gave R(HC) = 1.093 Å and R(CO) = 1.109 Å for HCO^+ and 1.131 Å for free CO.

The theoretically predicted H^+–CO bond energy was D_e = 149.2 kcal/mol, which gives, after correcting for zero-point energy contributions (ZPE), a calculated proton affinity of D_o = 142.1 kcal/mol. This is in good agreement with the experimentally observed proton affinity of 141.6 kcal/mol[111] and with one theoretically predicted value at CCSD(T)/cc–pVQZ, D_o = 140.2 kcal/mol.[110] Figure II.2.1 shows that the potential energy curve of Q^+–CO has a shape similar to the energy curve of H^+–CO, however, the well depth of QCO^+ is not as deep as that of HCO^+. The energy minimum for QCO^+ occurred at R(QC) = 1.186 Å and R(CO) = 1.131 Å. The charge stabilization energy of QCO^+ was 72.7 kcal/mol, which is about half that of H^+–CO. It follows that part of the bond energy of the H^+–CO bond is due to electrostatic attraction, but corrections for basis set superposition error, BSSE, were not calculated. It is expected that the majority of the energy difference between H^+–CO and Q^+–CO is due largely to lack of basis set(s) on the Q^+ (i.e., the Q^+ "borrows" basis functions from the carbon and oxygen atoms).

Table II.2.1. Calculated Changes (MP2/I) of HCO^+ and QCO^+ as a Function of the H^+–CO and Q^+–CO Distance[a]

	HCO^+				QCO^+			
R(XC)[b]	R(CO)	ν(CO)	*F*(CO)[b]	E_{rel}	R(CO)	ν(CO)	*F*(CO)[c]	E_{rel}
0.5	1.119	2253	22.44	461.7	1.115	2255	22.46	511.8
0.75	1.126	2204	21.53	–46.1	1.121	2252	22.52	20.2
1.0	1.130	2171	21.25	–144.8	1.127	2163	21.79	–64.2
1.095	1.131	2137	21.16	–149.2	1.130	2069	21.52	–71.0
1.186	1.131	2031	21.03	–146.3	1.131	1898	21.31	–72.7
1.5	1.134	2222	20.62	–116.2	1.136	2249	20.77	–60.6
2.0	1.138	2183	20.12	–67.5	1.141	2185	20.11	–30.7
2.5	1.140	2168	19.80	–35.9	1.144	2163	19.67	–15.1
3.0	1.142	2157	19.58	–17.5	1.146	2152	19.48	–8.4
3.5	1.145	2147	19.38	–8.1	1.147	2145	19.37	–5.2
4.0	1.147	2141	19.29	–4.1	1.147	2140	19.31	–3.5
∞	1.151	2118	18.92	0.0	1.151	2118	18.92	0.0

[a] Distances, R, in Å; stretching frequencies, ν, in cm^{-1}; force constants, *F*, in mdyn/Å; relative energies, E_{rel}, in kcal/mol. [b] X = H^+ or Q^+. [c] Calculated using equation II.2.1, see text.

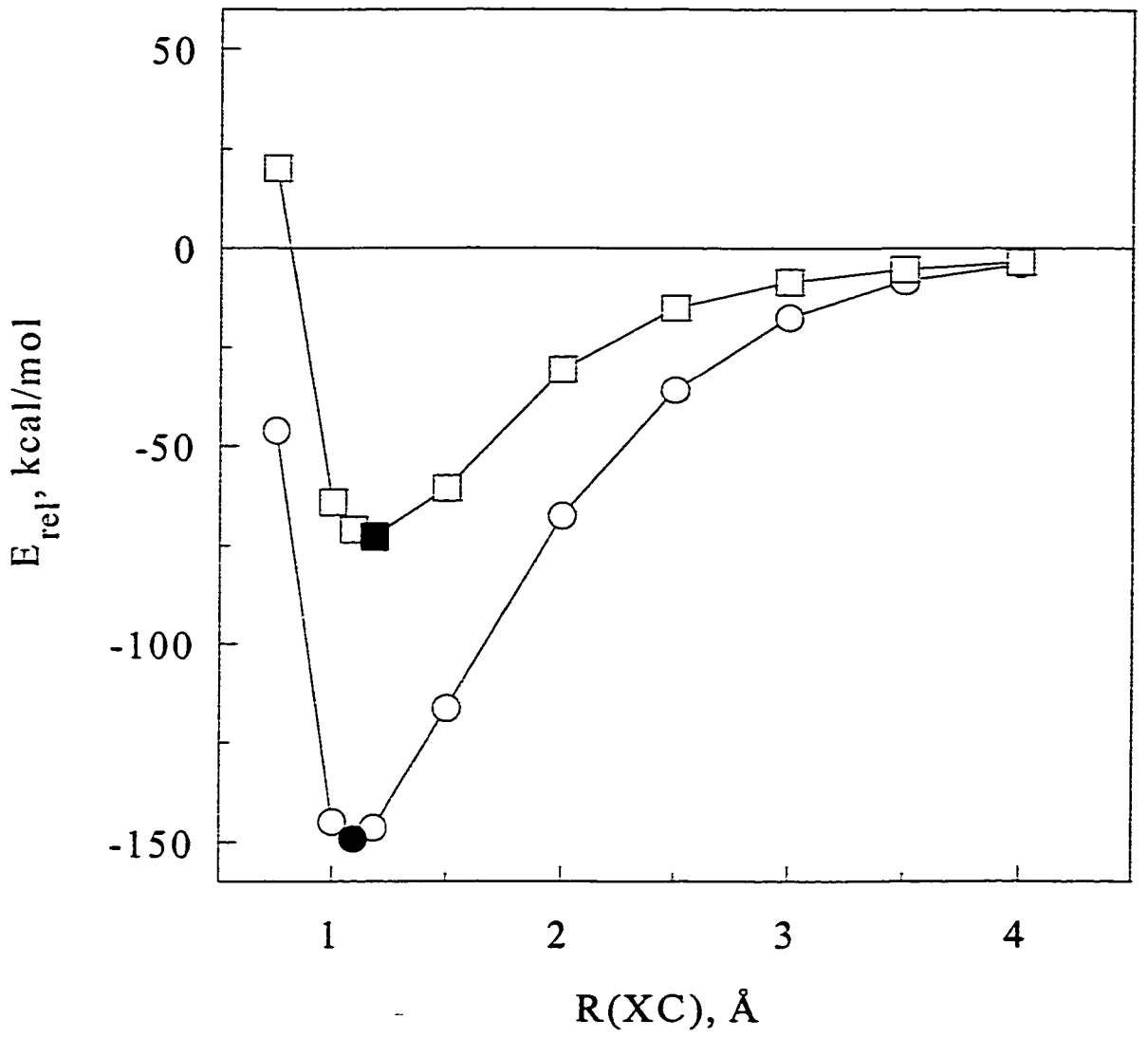

Figure II.2.1. Plot of the calculated energies E_{rel} (kcal/mol) of XCO^+ ($X = H^+$ or point charge Q^+) at various distances X^+–CO. Arrows show the position of the equilibrium structure.

Table II.2.1 shows that the carbon–oxygen distance, R(CO), of HCO^+ and QCO^+ become shorter as the carbonyl approaches the proton or the point charge from the carbon end. Figure II.2.2 is a plot of the C–O distance as a function of $R(H^+–CO)$ and $R(Q^+–CO)$, respectively. The two curves are very similar; in particular, the R(CO) bond shortening of HCO^+ at the equilibrium distance ($\Delta R(CO) = -0.019$ Å) is nearly the same as calculated for QCO^+ using the $R(H^+–CO)$ equilibrium distance ($\Delta R(CO) = -0.020$ Å). The results listed in Table II.2.1 and displayed in Figure II.2.2 show clearly that the C–O bond shortening of HCO^+ is caused, almost exclusively, by the electrostatic effect positive charge.

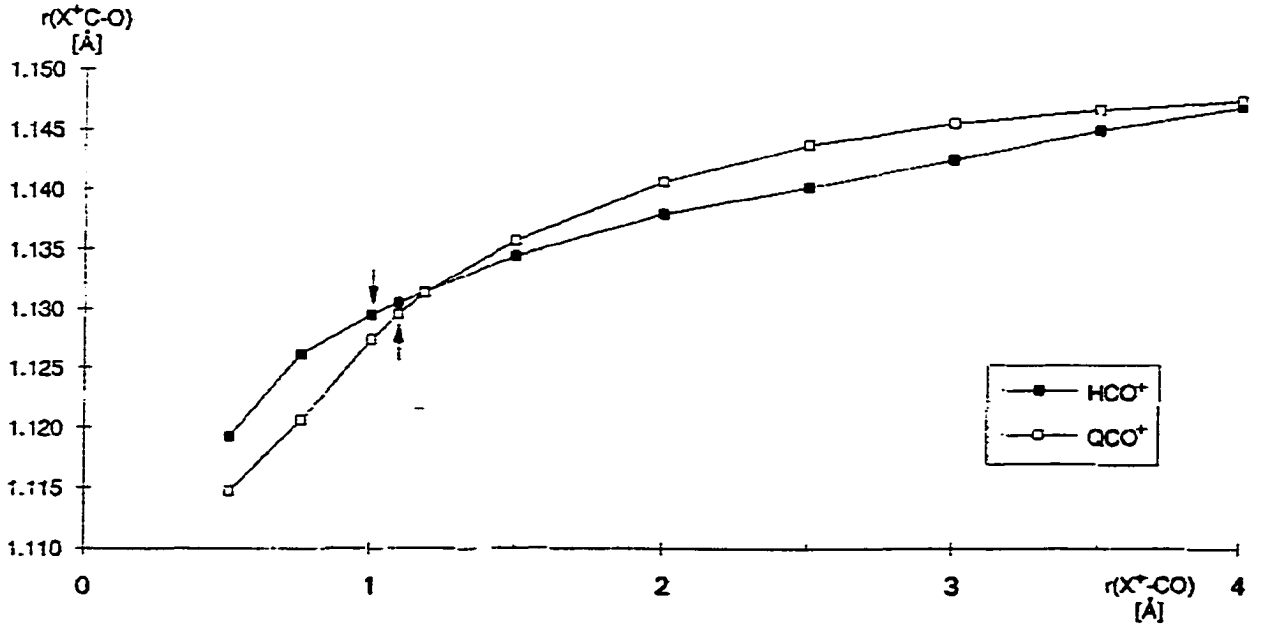

Figure II.2.2. Plot of the calculated C–O distances (Å) of XCO^+ ($X = H^+$ or point charge, Q^+) at various distances $X^+–CO$. Arrows show the position of the equilibrium structure.

A very interesting result is given when the change of the C–O distance of HCO^+ and QCO^+ is compared with the change of the stretching frequency ν(CO) and force constant *F*(CO) (Table II.2.1). The frequency and the force constant increase first, when H^+ or Q^+ approaches the carbon atom. This is expected, because the C–O bond distances decreases. At R(H–CO) = 1.50 Å, the C–O frequency has increased by nearly 100 cm^{-1}. However, when the proton or positive charge is close to the carbon atom, the wavenumber of the C–O mode suddenly decreases. The C–O stretching mode of HCO^+ at the equilibrium geometry (2137 cm^{-1}) is only 12 cm^{-1} higher than for free CO. This behavior is not an artifact of strong anharmonicity effects caused by frequency calculations performed at non-equilibrium geometries. Rather, the relatively low C–O stretching frequency of HCO^+ is caused by strong coupling of the C–O mode with the C–H stretching mode. This has been previously shown. Goldmann and Krogh-Jespersen calculated the vibrational spectrum of HCO^+ where the proton has an artificially increased mass of 500 a.u. The increased mass reduces the coupling of the two stretching modes significantly;[19] the resulting calculated ν(CO) value at the equilibrium geometry was 2369 cm^{-1}. These authors also calculated the harmonic ν(CO) of HCO^+ using the force constant obtained from Equation 1; this gave a hypothetical ν(CO) value of 2248 cm^{-1}.[19] It follows that the C–O stretching frequency of HCO^+ given by experiment or by calculations is not an accurate indicator of the carbon-oxygen bonding in carbonyl complexes, since it is significantly influenced by coupling with the C–H mode.[112] Although the large mass of transition metals lessens the M–C coupling influence on ν(CO) in metal carbonyls, it becomes clear that the C–O stretching frequency should be used with caution when the electronic structure of the X–CO bond is discussed. A more reliable indicator is the C–O bond distance. Since trends in R(CO) can be calculated quite accurately, the remaining discussion will focus only on the CO bond lengths.

In order to further investigate the role of a positive charge on C–O bonding interactions further, changes in R(CO), ν(CO), and *F*(CO) were calculated when a proton

or a positive charge approached CO from the oxygen end. The results are listed in Table II.2.2.

The energy curves displayed in Figure II.2.3 show that the well depth of COQ^+ at the equilibrium distance, R(CO–Q^+) = 1.055 Å, (D_e = 49.8 kcal/mol) is slightly less than half of the stabilization energy of COH^+ (D_e = 102.3 kcal/mol at R(CO–H^+) = 1.007 Å). The two curves are similar to those calculated for HCO^+ and QCO^+ (Figure II.2.1), except that the stabilization energies are lower than in the carbon–coordinated species. It follows that also for the CO–H^+ bond ~50% of the bonding energy is due to electrostatic effects and that ~50% are covalent interactions. The covalent contributions arise from the orbital interactions between the HOMO of CO and the empty 1*s* AO of H^+. Since the HOMO of CO is more localized at the carbon end than at oxygen, HCO^+ is lower in energy than COH^+.

The change in the C–O distance is even more interesting than the energy change along the reaction coordinate. Figure II.2.4 shows that the C–O distance increases when a proton or a positive charge approaches CO from the oxygen end. Only at short CO–X distances does the C–O distance begin to decrease. At the CO–H^+ equilibrium distance (1.007 Å), the C–O distance (ΔR(CO) = +0.018 Å) is nearly the same as that calculated for COQ^+ at the same distance (ΔR(CO) = +0.019 Å; Table II.2.2). It follows that electrostatic effects are also responsible for changes in the C–O distance caused by the proton in COH^+. If the HOMO of CO was antibonding, then the C–O distance in COH^+ would also be shorter than in free CO. It could be argued that, since the HOMO coefficient at the oxygen side of CO is rather small, the proton in COH^+ interacts with CO orbitals that are lower in energy than the HOMO. One CO σ orbital with a large coefficient at the oxygen end of the molecule is the 3σ valence orbital; this orbital is a C–O bonding orbital. It is interesting to note that ν(CO) and *F*(CO) for COH^+ and COQ^+

Table II.2.2. Calculated Changes (MP2/I) of COH^+ and COQ^+ as a Function of the CO–H^+ and CO–Q^+ Distance[a]

	COH^+				COQ^+			
R(OX)[b]	R(CO)	ν(CO)	*F*(CO)[b]	E_{rel}	R(CO)	ν(CO)	*F*(CO)[c]	E_{rel}
0.5	1.158	2033	17.92	422.0	1.156	2087	18.89	482.5
0.75	1.166	1994	17.28	–43.1	1.162	2063	18.56	10.3
1.0	1.168	1973	17.13	–102.3	1.169	1984	17.42	–49.0
1.007	1.168	1971	17.12	–102.3	1.169	1982	17.39	–49.2
1.055	1.169	1957	17.11	–101.3	1.169	1965	17.42	–49.8
1.5	1.169	2005	17.10	–62.3	1.163	2053	18.00	–30.9
2.0	1.164	2030	17.62	–28.0	1.158	2084	18.46	–13.6
2.5	1.158	2068	18.21	–11.6	1.156	2099	18.67	–6.6
3.0	1.155	2096	18.61	–4.9	1.154	2107	18.77	–3.6
3.5	1.153	2109	18.82	–2.4	1.153	2111	18.86	–2.2
4.0	1.153	2114	18.88	–1.4	1.153	2114	18.88	–1.4
∞	1.151	2118	18.92	0.0	1.151	2118	18.92	0.0

[a] Distances, R, in Å; stretching frequencies, ν, in cm^{-1}; force constants, *F*, in mdyn/Å; relative energies, E_{rel}, in kcal/mol. [b] X = H^+ or Q^+. [c] Calculated using equation II.2.1, see text.

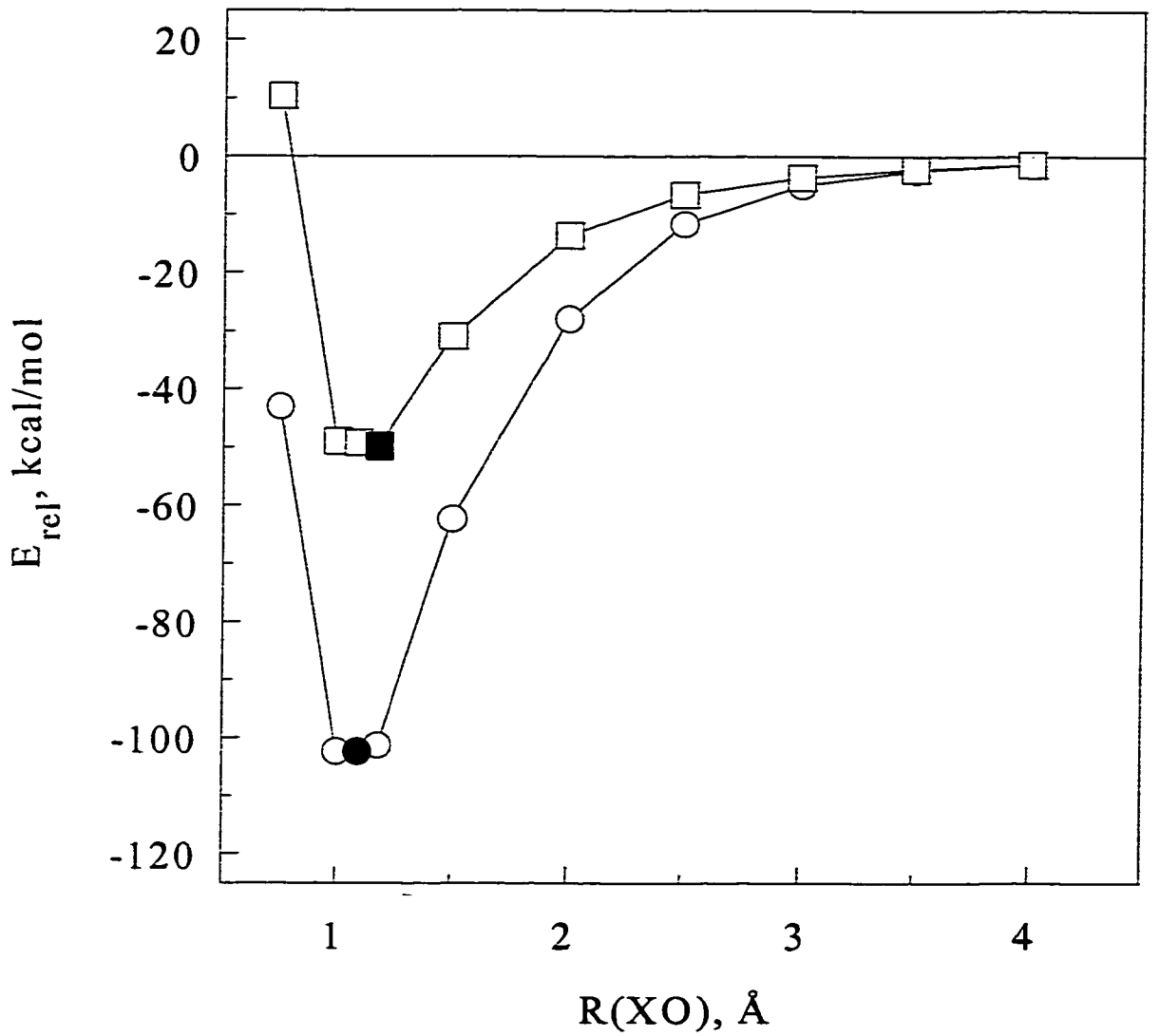

Figure II.2.3. Plot of the calculated energies E_{rel} (kcal/mol) of COX^+ ($X = H^+$ or point charge, Q^+) at various distances CO–X^+. Arrows show the position of the equilibrium structure.

decrease as R(CO) increases, and increase again as R(CO) decreases (Table II.2.2). However, the dramatic lowering of F(CO) at shorter O–X distances indicates that there is significant mode coupling, in CO–H^+ and CO–Q^+, between the two stretching vibrations.

It is illuminating to analyze the alteration in the electronic structure of CO when H^+ or Q^+ approaches the molecule from the carbon or the oxygen end. The calculated atomic partial charges for CO, HCO^+, QCO^+, COH^+ and COQ^+ are shown in Table II.2.3 and Table II.2.4. Because the partitioning of the electronic charge within a molecule is dependent on the method, the atomic charge was calculated using two different partitioning schemes: the NBO method[87] (Table II.2.3) and the topological analysis of the charge distribution (Table II.2.4).[88] Although the absolute values of the changes are clearly different, the trends the same. Both methods predict that, in CO, carbon has a positive charge and oxygen has a negative charge, which leads to electrostatic attraction between the two atoms. The charge separation between the carbon and oxygen atoms decreases when a proton or a positive charge Q^+ is attached to the carbon end. This is reasonable, because the positive charge attached to the carbon atom strengthens its electron attraction (i.e., the effective electronegativity increases), which leads to a charge flow *from* the oxygen atom to the carbon atom. It follows that the shortening of the C–O bond in HCO^+ and QCO^+ cannot be explained by the change in the electrostatic interactions between carbon and oxygen. The same conclusion can be made from the calculated charges of COH^+ and COQ^+. The attachment of H^+ or Q^+ to the oxygen end of the carbonyl increases the effective electronegativity of the oxygen atom, which leads to a higher negative charge at the oxygen atom and a more positive charge at the carbon atom. If the electrostatic attraction between the oxygen atom and the carbon atom is the dominant factor determining the C–O distances, COH^+ and COQ^+ should have a longer C–O bond and HCO^+ and QCO^+ should have a shorter C–O bond than free CO.

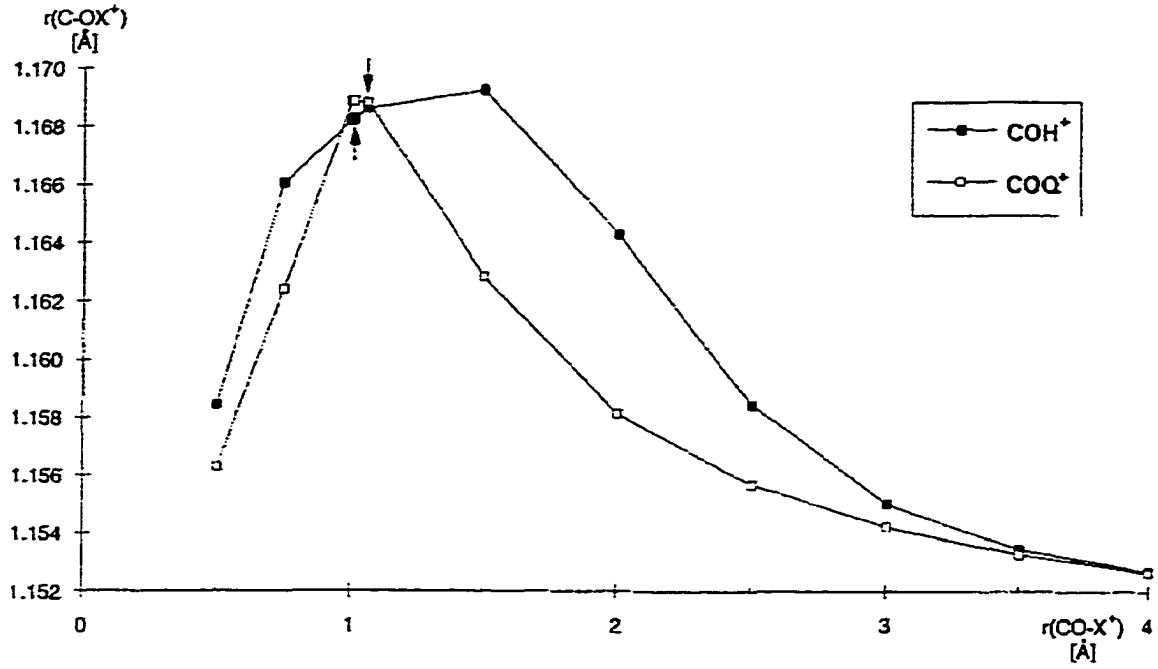

Figure II.2.4. Plot of the calculated C–O distances (Å) of COX^+ (X = H^+ or point charge, Q^+) at various distances CO–X^+. Arrows show the position of the equilibrium structure.

Table II.2.3. Results of the NBO Analysis for the CO Moiety[a]

molecule	q_C	q_O	$q_C - q_O$	q_{CO}	BO	WBI
CO	0.45	–0.45	0.90	0.00	1.44	2.09
HCO^+	0.76	–0.09	0.85	0.67	1.54	2.35
$(HCO^+)^b$	0.76	–0.09	0.85	0.67	1.51	2.34
QCO^+	0.13	–0.13	0.26	0.00	1.52	2.34
COH^+	0.91	–0.61	1.50	0.30	1.24	1.64
COQ^+	0.86	–0.86	1.72	0.00	1.25	1.68

[a] q, atomic partial charges. BO, overlap-weighted natural atomic orbital (NAO) bond order; WBI, Wiberg bond index. [b] Calculated using the R(CO) for free CO (1.151 Å).

Table II.2.4. Results of the Bader Analysis for the CO Moiety[a]

molecule	q_C	q_O	q_C-q_O	q_{CO}	ρ_b	$\nabla^2\rho_b$	R_b	H_b
CO	1.18	–1.18	2.36	0.00	3.05	31.97	0.671	–4.99
HCO^+	1.38	–0.87	2.25	0.51	3.20	34.94	0.665	–5.47
$(HCO^+)^b$	1.34	–0.83	2.17	0.51	3.07	28.32	0.666	–5.25
QCO^+	1.14	–1.14	2.28	0.00	3.20	35.04	0.666	–5.41
COH^+	1.43	–1.24	2.67	0.19	2.64	32.45	0.672	–3.95
COQ^+	1.57	–1.57	3.14	0.00	2.69	30.11	0.672	–4.08

[a] q, atomic partial charges. ρ_b, electron density at the bond critical point in e $Å^{-3}$; $\nabla^2\rho_b$, Laplacian at the bond critical point in e $Å^{-5}$; R_b, position of the bond critical point given by the ration R(b–O)/R(CO); H_b, energy density at the bond critical point hartrees $Å^{-3}$. [b] Calculated using the R(CO) for free CO (1.151 Å).

Then what is the reason for the calculated changes in the C–O bond lengths? The calculated changes in the covalent contribution to the bonding between he carbon atom and the oxygen atom provides the answer. More specifically, the change in the polarization of the molecular orbitals of CO explains the calculated C–O bond *shortening* in HCO^+ and QCO^+ and the bond *lengthening* in COH^+ and COQ^+. Table II.2.5 shows the natural localized orbitals (NLMOs) of the calculated compounds.[113] There are two bonding orbitals in CO, one σ orbital and one degenerate π orbital. Both orbitals are strongly polarized towards the oxygen end of the molecule. The σ orbital has a distribution of 27(C):73(O), and the π orbital has a distribution of 24(C):76(O). There are also two lone-pair orbitals, one at the carbon end and one at the oxygen end of the molecule. The polarization of the bonding orbitals changes significantly when H^+ or Q^+ is attached to CO. The C–O bonding orbitals are *less polarized*[39] in HCO^+ (σ orbital,

32(C):68(O); π orbital, 30(C):70(O)) and in QCO^+ (σ orbital, 31(C):69(O); π orbital, 30(C):70(O)), while they are *more polarized* in COH^+ (σ orbital, 22(C):78(O); π orbital, 15(C):85(O)) and COQ^+ (σ orbital, 23(C):77(O); π orbital, 16(C):84(O)). It is interesting to note that the polarization of the π orbital changes more than the σ orbital. This is reasonable, since the π bond is higher in energy than the σ bond.

It might be argued that the change in the bond polarization of CO is caused by the longer C–O bond in HCO^+ rather than the electrostatic effect of the proton and that the discussion uses a chicken–and–egg argument. In order to investigate this point, the electronic structure of HCO^+ was calculated using the theoretically predicted R(CO) value for free CO (1.151 Å). Table II.2.3 shows that the carbon–oxygen bond order is nearly the same in HCO^+, which has R(CO) fixed at 1.151 Å, and in the fully optimized HCO^+ cation. Table II.2.5 shows that the polarization of the C–O bond orbitals of HCO^+ is the same as in HCO^+. This shows clearly that the driving force for the C–O bond shortening in HCO^+ is the electrostatically induced change of the polarization of the C–O bond orbitals.

It should be noted that the alteration in the bond polarization in QCO^+ and COQ^+ is similar to the bond polarization in HCO^+ and COH^+, respectively. This supports the conclusion that the changes in C–O bond that occur upon bonding of CO to a proton are due to electrostatic interactions. The electrostatic interactions play a paradoxical role, however, because they only manifest themselves indirectly. The electrostatic interactions lead to an opposite change in the polarization of the bonding orbitals of HCO^+ and QCO^+ compared to COH^+ and COQ^+ and, thereby, to a change in the covalent part of the C–O bonding. This is the central mechanism which leads to the *shortening* of the C–O bond in HCO^+ and to the *lengthening* of the C–O bond in COH^+.

The change in the hybridization and in the C–O bond orders support the above conclusions. Relative to free CO, the percentage of s-orbital character at the carbon end of the C–O σ bond increases and the C–O bond orders are higher in HCO^+ and QCO^+,

while the percentage of s-orbital character at the carbon end of the C–O σ bond decreases and the C–O bond orders are lower in COH^+ and in COQ^+ (Table II.2.3 and Table II.2.5). It is the change in the covalent contribution to the C–O bond, which leads to a shorter or longer bond in the C– and O–protonated isomers, respectively. The increased covalency of the C–O bond in HCO^+ and QCO^+ and decreased covalency in COH^+ and COQ^+, as compared with free CO, is also supported by the topological analysis of the electron density distribution (Table II.2.4). The electron density at the CO bond critical points of HCO^+ and QCO^+ is higher than in CO, while The electron density at the CO bond critical points of COH^+ and COQ^+ is lower than in CO. An accumulation of electronic charge has been suggested as an indicator of covalent bonding.[114] In addition, more covalent character in the C–O bonds of HCO^+ and QCO^+ and less covalent bonding in COH^+ and COQ^+ is apparent from the calculated energy density at the bond critical point which are more negative in the former compounds and less negative in the latter than in CO.[115]

Summary and Conclusion

The shortening of the C–O bond length in HCO^+, and the lengthening in COH^+ relative to free CO is caused by the change in the polarization of the bond orbitals due to the positive charge of the H^+ ion. The bonding orbitals of free CO are polarized towards the oxygen atom because oxygen is more electronegative than carbon. Placing a proton or a positive charge at the carbon atom of CO serves to attract electron density from the oxygen atom to the carbon atom; this leads to less polarized σ and π bonds and to a more covalent C–O bond in the HCO^+ molecular ion than in free CO. Placing a proton or a positive charge at the oxygen atom has the opposite effect.

Table II.2.5. NLMO Analysis of the Valance Orbitals at MP2/6-31G(d)[a]

molecule	bond	occupancy	polarization	hybr(C)	hybr(O)
CO	CO(σ)	1.98	27:73	24:75:0.5	44:55:0.7
	CO(π)	1.95	24:76	0:99:0.7	0:100:0.4
	CO(π)	1.95	24:76	0:99:0.7	0:100:0.4
	C(LP)	1.97		78:22:0.0	
	O(LP)	1.98			56:44:0.1
HCO^+	CO(σ)	1.98	32:68	48:58:0.2	40:60:0.5
	CO(π)	1.94	30:70	0:100:0.5	0:100:0.5
	CO(π)	1.94	30:70	0:100:0.5	0:100:0.5
	HC(σ)	1.98	33:67	59:41:0.1	
	O(LP)	1.98			60:40:0.1
$(HCO^+)^b$	CO(σ)	1.97	32:68	48:58:0.2	38:61:0.5
	CO(π)	1.93	30:70	0:100:0.4	0:100:0.5
	CO(π)	1.93	30:70	0:100:0.4	0:100:0.5
	HC(σ)	1.98	33:67	60:40:0.1	
	O(LP)	1.98			62:38:0.1
QCO^+	CO(σ)	1.98	31:69	39:61:0.3	42:57:0.7
	CO(π)	1.94	30:70	0:100:0.4	0:100:0.5
	CO(π)	1.94	30:70	0:100:0.4	0:100:0.5
	C(LP)	1.98		60:40:0.2	
	O(LP)	1.98			58:42:0.1

Table II.2.5. NLMO Analysis of the Valance Orbitals at MP2/6-31G(d)[a] (*continued*)

molecule	bond	occupancy	polarization	hybr(C)	hybr(O)
COH^+	CO(σ)	1.98	22:78	20:80:0.7	55:45:0.3
	CO(π)	1.96	15:85	0:99:1.2	0:100:0.1
	CO(π)	1.96	15:85	0:99:1.2	0:100:0.1
	C(LP)	1.97		82:18:0.0	
	OH(σ)	1.98	86:14		45:55:0.1
COQ^+	CO(σ)	1.98		21:79:0.7	53:47:0.3
	CO(π)	1.96	23:77	0:99:1.1	0:100:0.1
	CO(π)	1.96	16:84	0:99:1.1	0:100:0.1
	C(LP)	1.97	16:84	82:18:0.0	
	O(LP)	1.98			46:54:0.2

[a] polarization, % of occupancy assigned to first and second atom; hybr, % s, p, and d character of the hybrid orbitals; all delocalizations to other atoms are below 0.6%. [b] Calculated using R(CO) for free CO (1.151 Å).

CHAPTER 3

Theoretical Study of the Homoleptic d^{10} Metal Carbonyl Cations $M(CO)_n^{x+}$ ($M^{x+} = Cu^+, Ag^+, Au^+, Zn^{2+}, Cd^{2+}, Hg^{2+}$). Trends in Molecular Geometries and Electronic Structures for n = 1–6

Introduction

The chemistry of cationic, homoleptic, metal carbonyl complexes is an area of intense research activity.[6,33,53,116,117] In addition to their intrinsic interest as "unusual" metal carbonyl species, some nonclassical metal carbonyls, especially those of groups 11 and 12, are of technological importance. Copper(I) and Zn(II) carbonyls may be involved as intermediates in the large-scale industrial transformation of CO to CH_3OH using copper–promoted ZnO catalysts.[118-122] Copper(I) carbonyls may be involved as intermediates in the heterogeneous copper-catalyzed low-temperature water-gas shift reaction,[43] and Cu(I), Ag(I), and Au(I) carbonyls may be homogeneous catalysts in the production of carboxylic acids from alkenes.[123-129] Copper(I) carbonyls are formed when CO is absorbed by supported or soluble Cu(I) salts, processes that are used to remove CO from a variety of industrial gas streams.[130-134] In addition, biochemists have long used CO as a probe ligand for the elucidation of structural and dynamic properties of reduced Cu-containing proteins and enzymes, including hemocyanin and cytochrome *c*

oxidase, although in most of these cases $\nu(CO) < 2143\ cm^{-1}$.[135-139] Perhaps the greatest, if unappreciated, significance of nonclassical metal carbonyls is that they provide a model for the dissociation of CO from a classical metal carbonyl. To the author's knowledge, no one has studied the reactivity of the CO ligand of a classical, catalytic M–CO species as the M–C distance is lengthened from its equilibrium value, thereby decreasing π backbonding. In the discussion in Part II, Chapter 4, it will be demonstrated that many metal carbonyls that are classical at equilibrium are nonclassical during their formation.

Cationic complexes with the general formula $M(CO)_n^{x+}$ that were unknown or thought to be too unstable to exist in condensed phases have been isolated as salts of weakly coordinating anions in the last few years.[6,33,53,116,117,140-144] Some illustrative examples are O_h $Fe(CO)_6^{2+}$, D_{4h} $Pd(CO)_4^{2+}$, $D_{\infty h}$ and C_{2v} $Cu(CO)_2^{+}$, D_{3h} $Cu(CO)_3^{+}$, T_d $Cu(CO)_4^{+}$, and $D_{\infty h}$ $Ag(CO)_2^{+}$, $Au(CO)_2^{+}$, and $Hg(CO)_2^{2+}$.[6,33,53,116,117,140-144] The isolation of $Ir(CO)_6(Sb_2F_{11})_3$ demonstrates that even triply-charged, homoleptic, metal carbonyl complexes can be stable with respect to CO dissociation if the counterion is weakly coordinating.[116] Many cationic, homoleptic, metal carbonyl complexes have unusually high $\nu(CO)$ values. It has been suggested that these species are sufficiently different than the vast majority of metal carbonyls and should be referred to as nonclassical metal carbonyls (see Part II, Chapter 1).[6,33,53]

The cationic, homoleptic, group-11 $M(CO)_n^{+}$ complexes with $n \geq 2$ have been the focus of numerous recent experimental studies ($M^+ = Cu^+$, Ag^+, and Au^+).[6,25,26,28,33,53,116,117,140-149] Although copper(I) monocarbonyls have been known for a very long time,[36,150-154] evidence for the formation of copper(I) polycarbonyls as discrete, isolable compounds has only recently been reported.[25,145-147] A series of seminal studies by Souma and co-workers demonstrated that Cu^+ ions dissolved in very strong acids such as $BF_3 \cdot H_2O$ or HSO_3F can bind up to four CO

ligands at certain temperatures and pressures.[155-157] Armentrout and co-workers later confirmed the existence of the $Cu(CO)_4^+$ cation in the gas phase,[158] and Strauss and co-workers recently determined the structure of a salt containing the T_d $Cu(CO)_4^+$ complex.[145] Salts of the $D_{\infty h}$ complexes $Ag(CO)_2^+$ and $Au(CO)_2^+$ have been isolated,[26,28] and the structure of the silver(I) salt has been reported.[26] The pressure of CO required for the solid-state transformation $M(CO)_2^+ \rightarrow M(CO)_3^+$ varies dramatically from Cu^+ (~ 1 atm, AsF_6^- salt)[25] to Ag^+ (13 atm, $Nb(OTeF_5)_6^-$ salt)[148] to Au^+ (~100 atm, $Sb_2F_{11}^-$ salt).[149] The high pressure needed to form $Au(CO)_3^+$ in the solid-state is very interesting, since the dicarbonyl complex $Au(CO)_2^+$ *does not* lose CO under vacuum and both $Cu(CO)_2^+$ and $Ag(CO)_2^+$ *do* lose CO under vacuum. Apparently, $Au(CO)_3^+$ is the least stable of the three group-11 tricarbonyl cations with respect to loss of a CO ligand even though $Au(CO)_2^+$ is the most stable of the three group-11 dicarbonyl cations with respect to loss of a CO ligand.

The only group-12 carbonyl which has been isolated and well characterized thus far is $Hg(CO)_2^{2+}$,[159,160] although there are reports of Zn^{2+} carbonyl species formed under CO pressure in zinc-substituted zeolites or on the surface of ZnO.[161-164] The $D_{\infty h}$ species $Hg(CO)_2^{2+}$ has the highest average ν(CO) value, 2280 cm^{-1}, of any metal carbonyl ever reported. Table II.3.1 lists homoleptic group-11 and -12 metal carbonyls for which experimental ν(CO) values have been reported. The increase in ν(CO) upon coordination of CO to a late d-block metal cation has been shown to be due to the effect of the positive charge on the orbitals of CO (see Part II, Chapter 2), which become less polarized towards oxygen in the cationic complexes relative to free CO.[19,165,166] Most transition metal carbonyls have average ν(CO) values below 2143 cm^{-1}, the value for free CO.[167] This is because M→CO π backdonation, which is significant for classical metal carbonyls and which involves the transfer of electronic charge from the metal d-π orbitals to the degenerate CO p-π^* orbital, leads

Table II.3.1. Experimental Data for Relevant $M(CO)_n^{x+}$ Complexes[a]

complex	idealized symmetry[b]	ν(CO),[c] cm^{-1} IR	ν(CO),[c] cm^{-1} Raman	R(MC),[d] Å	D_o,[e] kcal mol^{-1}	refs
$Cu(CO)^+$	$C_{\infty v}$	2178			36(2)	25, 158
$Cu(CO)_2^+$	$D_{\infty h}$	2164	2177	1.901(6)		25, 158
$Cu(CO)_2^+$	C_{2v}	2182, 2162		1.965(3)	41(1)	146
$Cu(CO)_3^+$	D_{3h}	2183	2179,2206	2.10(1)	18(1)	25, 158
$Cu(CO)_4^+$	T_d	2184		2.14(5)	13(1)	31, 158
$Ag(CO)^+$	$C_{\infty v}$	2208	2206		21(1)	26, 158
$Ag(CO)_2^+$	$D_{\infty h}$	2196	2220		26(1)	26, 158
$Ag(CO)_3^+$		2191			13(4)	148,158
$Ag(CO)_4^+$					11(+4/–1)	158
$Au(CO)_2^+$	$D_{\infty h}$	2217	2254			28
$Au(CO)_3^+$		2212				64
$Hg(CO)_2^+$	$D_{\infty h}$	2278	2281			159, 160

[a] Only data for salts of highly-fluorinated anions are given. [b] Symmetry determined by X-ray crystallography or by vibrational spectroscopy. [c] From spectra of solid samples; ν(CO) for gaseous CO is 2143 cm^{-1}. [d] Average metal-carbon bond distance; the stated error is the largest esd for the values avereaged. [e] Energy of gas-phase dissociation of a single CO ligand from the complex; from ref 158; the stated errors are one esd.

to a weaker C–O bond. Theoretical analyses of *neutral* transition-metal carbonyls have shown that M→CO π backdonation is more important for the overall M–CO bond than M←CO σ donation.[22] Positively charged metal ions should be weaker π-donors than the corresponding neutral metal atoms since a given M^+ cation has a higher ionization potential than the neutral atom M. It is therefore understandable that M→CO π backdonation in some $M(CO)_n^{x+}$ species may be much less significant than M←CO σ donation and that ν(CO) values of some $M(CO)_n^{x+}$ species may be considerably higher than in related neutral metal carbonyls. A high ν(CO) value, signaling a small or negligible amount of M→CO π backdonation, is one of the criteria distinguishing that distinguishes a nonclassical metal carbonyl from a classical carbonyl (see Part II, Chapter 1).[6,53,143]

One might assume that the lack of π backdonation in nonclassical metal carbonyls would lead to relatively weak M–CO bonds for these "σ-only" species. One might even rationalize that the small number of isolable nonclassical metal carbonyls is related to the presumably weak M–CO bonds. However, theoretical calculations have shown that dissociation of a single CO ligand from $Ir(CO)_6^{3+}$ is more endothermic than dissociation of a single CO ligand from the isoelectronic hexacarbonyl species $W(CO)_6$.[50] Hence, M←CO σ donation and the coulombic attraction between the metal cation and the CO dipole in nonclassical metal carbonyls can result in very strong M–CO bonds. The problem with isolating new *cationic* nonclassical metal carbonyl species is therefore not intrinsically weak M–CO bonds due to the lack of M→CO π backdonation but the displacement of CO ligands by the counteranion(s). It is likely that many new nonclassical metal carbonyls will be discovered as newer and less basic weakly coordinating counteranions come into widespread use.[140-144]

It would be very helpful for future experimental studies if M–CO bond energies of proposed nonclassical metal carbonyl species could be predicted from

accurate ab initio calculations. In previous studies it was shown that calculated CO dissociation energies of transition metal carbonyls at the CCSD(T) level of theory using relativistic effective core potentials were accurate to within ±3 kcal mol^{-1} of experimental values.[21,168-170] In this work, theoretically predicted equilibrium geometries, sequential M–CO bond energies, and an analysis of the M–CO bonding for 36 group-11 and group-12 metal carbonyls $M(CO)_n^{x+}$ (M^{x+} = Cu^+, Ag^+, Au^+, Zn^{2+}, Cd^{2+}, and Hg^{2+}; n = 1–6) will be presented. These results are important in that they will serve as a guide to experimental chemists working in the area of condensed phase nonclassical carbonyls. The relatively high BDEs of the group-12 complexes should serve as an incentive to experimental chemists that Zn^{2+}, Cd^{2+}, and higher n value Hg^{2+} carbonyl complexes can be made. The results are also used to understand the bonding in nonclassical metal carbonyl species as well as to show what level of theory is necessary to achieve a good correspondence with experimental gas-phase M–CO bond energies.

Results and Discussion

Calibration of Methods

Comparison of Theoretical and Experimental Results

Metal–CO and C–O bond distance calculations for the group-11 $M(CO)_n^+$ complexes (n = 1–4) at several levels of theory, including two sets of results from previously published high-level calculations,[35,171] were compared (Table II.3.2). Sequential bond dissociation energies, D_e(M–CO), were calculated for the same twelve

Table II.3.2. Calculated Bond Lengths (Å) for $M(CO)_n^+$ (M = Cu, Ag, Au; n = 1–4)

		$n=1$		$n=2$		$n=3$		$n=4$	
M	Method	R(MC)	R(CO)	R(MC)	R(CO)	R(MC)	R(CO)	R(MC)	R(CO)
Cu	MP2/I	1.891	1.142	1.884	1.142	1.920	1.144	1.932	1.146
	CCSD(T)/I	1.957	1.136	1.942	1.136	1.995	1.138	2.022	1.139
	CCSD(T)/III	1.941	1.122	1.926	1.122				
	MCPF/VTZP[a]	1.941	1.128	1.933	1.128				
	CCSD(T)/ VQZP[b]	1.927	1.120						
	BP86/I	1.834	1.140	1.882	1.139	1.934	1.141	1.965	1.142
	BP86/III	1.831	1.130	1.882	1.128	1.930	1.131	1.964	1.132
	B3LYP/I	1.887	1.126	1.913	1.126	1.973	1.128	2.012	1.129
Ag	MP2/I	2.249	1.142	2.160	1.142	2.238	1.144	2.302	1.145
	CCSD(T)/I	2.272	1.137	2.189	1.137	2.273	1.138	2.342	1.139
	CCSD(T)/III	2.230	1.223	2.170	1.123				
	MCPF/VTZP[a]	2.293	1.130	2.226	1.129				
	BP86/I	2.086	1.138	2.077	1.138	2.146	1.141	2.200	1.142
	BP86/III	2.084	1.127	2.078	1.127	2.149	1.130	2.203	1.131
	B3LYP/I	2.161	1.126	2.126	1.126	2.212	1.128	2.280	1.129
Au	MP2/I	1.976	1.142	2.007	1.142	2.078	1.145	2.137	1.146
	CCSD(T)/I	2.001	1.137	2.030	1.136	2.120	1.139	2.195	1.140
	CCSD(T)/III	1.973	1.123	2.016	1.122				
	BP86/I	1.916	1.141	1.988	1.139	2.063	1.142	2.121	1.143
	BP86/III	1.918	1.130	1.990	1.128	2.066	1.131	2.123	1.132
	B3LYP/I	1.962	1.127	2.011	1.126	2.103	1.129	2.178	1.130

[a] Reference 35. [b] Reference 171.

Table II.3.3. Calculated M–CO Bond Energies (D_e, kcal mol^{-1}) for $M(CO)_n^+$ Complexes (M^+ = Cu, Ag, Au; n = 1–4) at Five Different Levels of Theory

complex	MP2/I// MP2/I	CCSD(T)/I// MP2/I	CCSD(T)/I// CCSD(T)/I	BP86/I// BP86/I	B3LYP/I// B3LYP/I
$Cu(CO)^+$	38.1	32.3	32.9	51.7	43.3
$Cu(CO)_2^+$	43.1	36.2	36.7	47.1	42.6
$Cu(CO)_3^+$	23.4	18.6	19.6	25	20.5
$Cu(CO)_4^+$	22.8	16.5	18	21.7	17.3
$Ag(CO)_+$	23.3	21.8	22	35.2	29.5
$Ag(CO)_2^+$	28.6	26.4	26.6	38.4	33.1
$Ag(CO)_3^+$	13.9	12.6	12.8	16.4	13.8
$Ag(CO)_4^+$	12.3	11.1	11.3	13	11.2
$Au(CO)^+$	40.8	38.3	38.5	61.3	49.9
$Au(CO)_2^+$	51	47	47.3	57.2	51.9
$Au(CO)_3^+$	9.2	6.4	6.9	11.5	7.2
$Au(CO)_4^+$	9.3	6.7	7.3	10.1	7.1

Table II.3.4. Calculated Cu–CO Bond Energies for $Cu(CO)_n^+$ Complexes (n = 1–4) at Different Levels of Theory[a]

complex	geometry optimization	basis set	D_e, kcal mol^{-1}		D_o, kcal mol^{-1}	
			CCSD	CCSD(T)	CCSD	CCSD(T)
$Cu(CO)^+$	MP2/I	I	30.0	32.3	28.6	30.9
	MP2/I	II	31.9	34.5	30.4	33.1
	MP2/I	III	29.3	31.7	27.9	30.3
	MP2/I	IV	31.4	34.3	30.0	32.9
	MP2/I	V	28.9	32.3	27.4	30.9
	CCSD(T)/I	I	31.0	32.9	29.5	31.4
	CCSD(T)/I	V	29.6	32.5	28.2	31.1
	CCSD(T)/III	III	30.3	32.3	28.9	30.9
	CCSD(T)/III	V	29.6	32.6	28.2	31.2
$Cu(CO)_2^+$	MP2/I	I	33.4	36.2	31.6	34.3
	MP2/I	II	35.0	38.1	33.1	36.2
	MP2/I	III	34.1	37.0	32.2	35.2
	MP2/I	IV	35.9	39.1	34.0	37.4
	MP2/I	V	32.2	36.0	30.3	34.2
	CCSD(T)/I	I	34.2	36.7	32.4	34.9
	CCSD(T)/I	V	33.0	36.6	31.1	34.7
	CCDS(T)/III	III	35.0	37.6	33.1	35.7
	CCSD(T)/III	V	32.9	36.5	31.0	34.7

Table II.3.4. Calculated Cu–CO Bond Energies for $Cu(CO)_n^+$ Complexes (n = 1–4) at Different Levels of Theory[a] (*continued*)

complex	geometry optimization	basis set	D_e, kcal mol^{-1}		D_o, kcal mol^{-1}	
			CCSD	CCSD(T)	CCSD	CCSD(T)
$Cu(CO)_3^+$	MP2/I	I	15.9	18.6	14.6	17.3
	MP2/I	II	16.4	19.4	15.1	18.1
	MP2/I	III	14.6	17.7	13.3	16.4
	MP2/I	IV	15.4	18.8	14.0	17.1
	MP2/I	V	14.9	18.6	13.6	17.3
	CCSD(T)/I	I	17.4	19.6	16.1	18.3
	CCSD(T)/I	V	15.9	18.8	14.6	17.5
$Cu(CO)_4^+$	MP2/I	I	13.2	16.5	11.4	14.7
	MP2/I	II	13.9	17.5	12.1	15.8
	MP2/I	III	11.1	14.4	9.3	12.7
	MP2/I	IV	11.8	15.5	10.1	13.7
	MP2/I	V	9.9	14.0	8.1	12.3
	CCSD(T)/I	I	15.4	18.0	13.7	16.2
	CCSD(T)/I	V	12.3	15.5	10.6	13.7

[a] ZPE corrections at MP2/I.

complexes at five levels of theory (Table II.3.3), while D_e(Cu–CO) and D_o(Cu–CO) values were calculated at nine (n = 1, 2) or seven (n = 3, 4) different levels of theory (Table II.3.4).

There are three experimental parameters that can be used to assess the performance of the different theoretical methods: ν(CO) values; M–CO bond distances; and M–CO bond dissociation energies (BDEs). The experimental ν(CO) values and M–CO bond distances listed in Table II.3.1 are solid-state data for salts of $M(CO)_n^{x+}$ complexes with weakly coordinating anions, whereas these theoretical results refer to isolated gas-phase $M(CO)_n^{x+}$ complexes. It has been shown (Part II, Chapter 1; Part II, Chapter 4) that even weak interactions between fluoride ions and the metal centers of $M(CO)_2^{x+}$ complexes (M···F = 3 Å) can change ν(CO) values by up to 57 cm^{-1} and M–CO distances by up to 0.60 Å relative to the homologous isolated $M(CO)_2^{x+}$ species.[53] Therefore, with one exception, comparisons between experimental and theoretical ν(CO) values or M–CO bond distances will not be made in this work (the exception is $Cu(CO)_4^+$ in which M···F interactions are negligible).

On the other hand, the experimental M–CO bond dissociation energies for $Cu(CO)_n^+$ and $Ag(CO)_n^+$ (n = 1–4) listed in Table II.3.1 are gas-phase data, and a comparison with theoretical results is warranted. The experimental results are from a study by Armentrout and co-workers, who measured the bond energies by collision-induced dissociation of CO ligands in a guided-ion-beam tandem mass spectrometer.[158] The most economical level of theory that gave an excellent correlation with the experimental D_o values was CCSD(T)/I//MP2/I. The correlation can be readily seen in Figure II.3.1. A linear least-squares fit to the data, with the requirement that the line pass through the origin, resulted in the following correlation: $D_o(M–CO)_{exp}$ = (1.10 ± 0.03) x $D_o(M–CO)_{theo}$ (R = 0.981). Therefore, the CCSD(T)/I//MP2/I theoretical

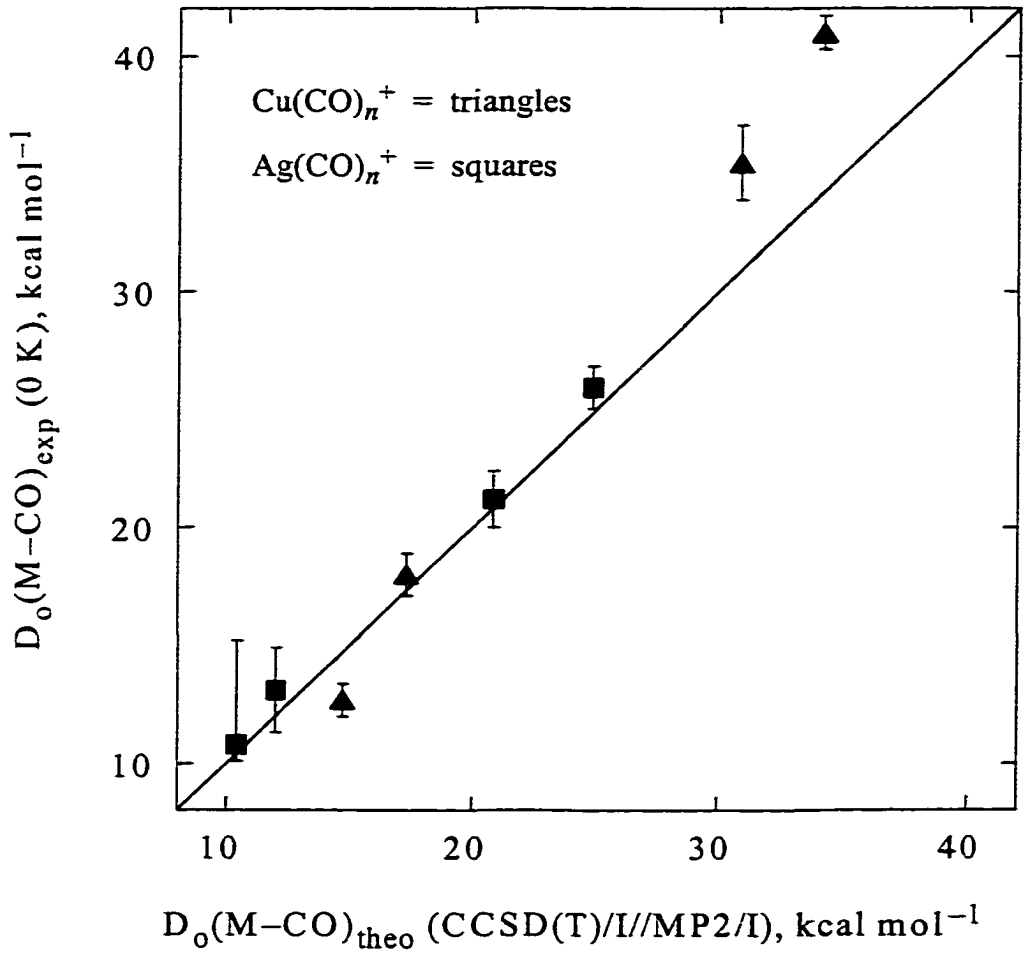

Figure II.3.1. Plot of the experimental sequential M–CO bond energies ($D_o(M–CO)_{exp}$, kcal mol^{-1}) versus the theoretical CCSD(T)/I//MP2/I sequential M–CO bond energies ($D_o(M–CO)_{theo}$, kcal mol^{-1}) for Cu(CO)$_n^+$ (triangles) and Ag(CO)$_n^+$ (squares). A linear least-squares fit to the data, with the requirement that the line pass through the origin, resulted in the following correlation: $D_o(M–CO)_{exp} = (1.10 \pm 0.03) \times D_o(M–CO)_{theo}$ ($R = 0.981$).

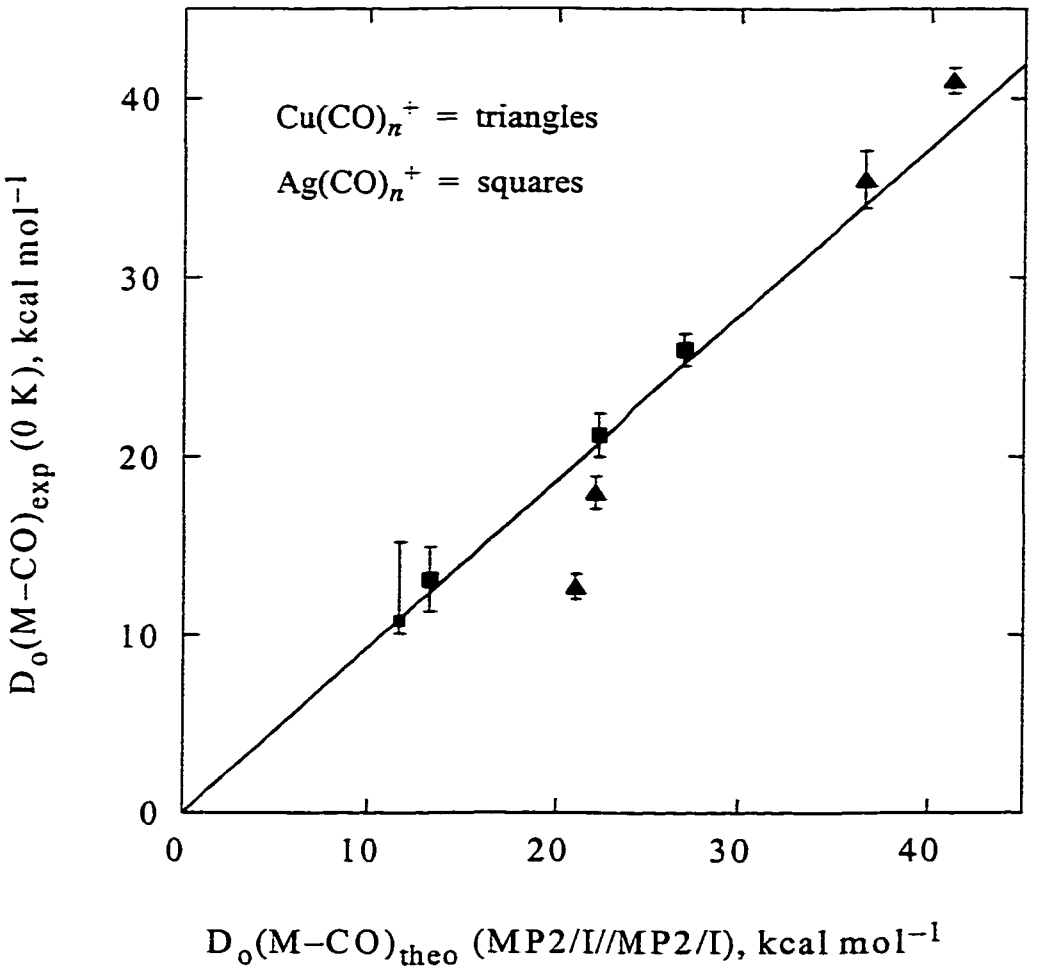

Figure II.3.2. Plot of the experimental sequential M–CO bond energies ($D_o(M-CO)_{exp}$, kcal mol^{-1}) versus the theoretical MP2/I//MP2/I sequential M–CO bond energies ($D_o(M-CO)_{theo}$, kcal mol^{-1}) for $Cu(CO)_n^+$ (triangles) and $Ag(CO)_n^+$ (squares). A linear least-squares fit to the data, with the requirement that the line pass through the origin, resulted in the following correlation: $D_o(M-CO)_{exp} = (0.93 \pm 0.04) \times D_o(M-CO)_{theo}$ ($R = 0.962$).

values are, on average, 10% lower than the experimental values. A similar plot using MP2/I//MP2/I theoretical values (Figure II.3.2) yielded a poorer but still acceptable straight-line correlation, with a slope of 0.93 ± 0.04 and an *R* value of 0.962. Theoretical D_e and D_0 values at the CCSD/I//MP2/I level of theory were consistently lower than CCSD(T)/I//MP2/I values (Table II.3.5). The good correlation between the CCSD(T)/I//MP2/I or MP2/I//MP2/I and experimental D_0 values for $Cu(CO)_n^+$ and $Ag(CO)_n^+$ (n = 1–4) justifies the choice of these two methods for subsequent analyses of bond energies and electronic structures of all the title complexes.

M–CO Bond Distances at Different Levels of Theory

The CCSD(T) method has been found by others to give highly accurate geometries.[172,173] The MP2/I and CCSD(T)/I M–CO bond distances in Figure II.3.3 are quite similar for $M^+ = Ag^+$ and Au^+ (the average difference is 0.034 Å). There is a larger discrepancy for $M^+ = Cu^+$ (the average difference is 0.072 Å). Nevertheless, a plot of CCSD(T)/I//MP2/I D_e(M–CO) values versus CCSD(T)/I//CCSD(T)/I D_e(M–CO) values for the twelve complexes $M(CO)_n^+$ ($M^+ = Cu^+$, Ag^+, Au^+; n = 1–4) (Figure II.3.4) displays a linear correlation through the origin with a slope of 0.98 and a *R* value of 0.999. Therefore, for these homoleptic metal carbonyl cations the MP2/I geometries are quite suitable for energy calculations at the CCSD(T)/I level of theory. Note that the agreement between the MP2/I M–CO distances and the CCSD(T)/III M–CO distances is even better than between MP2/I and CCSD(T)/I (basis set III represents a larger basis set at the C and O atoms relative to basis set I). Our results are in agreement with previous calculations, which showed that (1) MP2 calculated M–CO bond distances for first-row transition-metal carbonyl complexes are significantly shorter than CCSD(T) calculated distances and (2) the two methods give much better agreement for second- and third-row transition-metal carbonyls.[170] Note that the average experimental

Table II.3.5. Calculated M–CO Bond Energies at MP2/I Optimized Geometries and Experimental Dissociation Energies (kcal/mol) of $M(CO)_n$ ($M = Cu^+, Ag^+, Au^+, Zn^{2+}, Cd^{2+}, Hg^{2+}$; $n = 1$–6)

			D_e		D_o		
M	n	sym	CCSD	CCSD(T)	CCSD	CCSD(T)	Exp. (0 K)[†]
Cu^+	1	$C_{\infty v}$	30.0	32.3	28.6	30.9	35.5±1.6
	2	$D_{\infty h}$	33.4	36.2	31.6	34.3	41.0±0.7
	3	D_{3h}	15.9	18.6	14.6	17.3	18.0±0.9
	4	T_d	13.2	16.5	11.4	14.7	12.7±0.7
	5	C_{3v}	4.3	4.7	3.8	4.2	
	6	O_h	-6.2	-9.1	-3.7	-6.6	
Ag^+	1	$C_{\infty v}$	20.6	21.8	19.6	20.8	21.2±1.2
	2	$D_{\infty h}$	24.7	26.4	23.3	24.9	26.0±0.9
	3	D_{3h}	11.6	12.6	10.9	12.0	13.1±1.8
	4	T_d	10.1	11.1	9.5	10.4	10.8 +4.4/-0.7
	5	C_{3v}	4.5	4.9	4.2	4.5	
	6	O_h	3.7	3.5	4.1	3.8	
Au^+	1	$C_{\infty v}$	36.1	38.3	34.7	36.9	
	2	$D_{\infty h}$	45.2	47.0	43.3	45.0	
	3	D_{3h}	4.5	6.4	3.8	5.7	
	4	T_d	5.0	6.7	4.3	5.9	
	5	D_{3h}	6.4	6.1	6.3	6.0	
	6	O_h	-13.9	-14.9	-11.9	-12.9	

Table II.3.5. Calculated M–CO Bond Energies at MP2/I Optimized Geometries and Experimental Dissociation Energies (kcal/mol) of $M(CO)_n$ ($M = Cu^+$, Ag^+, Au^+, Zn^{2+}, Cd^{2+}, Hg^{2+}; $n = 1$–6) (*continued*)

			D_e		D_o		
M	*n*	sym	CCSD	CCSD(T)	CCSD	CCSD(T)	Exp. (0 K)†
Zn^{2+}	1	$C_{\infty v}$	72.9	74.8	71.5	73.3	
	2	$D_{\infty h}$	64.0	65.6	62.3	64.0	
	3	D_{3h}	41.3	42.5	40.0	41.2	
	4	T_d	32.4	33.6	31.1	32.3	
	5	D_{3h}	12.1	12.8	11.4	12.1	
	6	O_h	14.1	14.9	13.4	14.1	
Cd^{2+}	1	$C_{\infty v}$	54.0	55.6	52.8	54.4	
	2	$D_{\infty h}$	50.7	52.2	49.3	50.7	
	3	D_{3h}	32.8	33.9	31.9	32.9	
	4	T_d	27.9	28.9	26.8	27.8	
	5	D_{3h}	15.0	15.7	14.2	14.9	
	6	O_h	15.3	16.1	14.6	15.3	
Hg^{2+}	1	$C_{\infty v}$	67.9	70.0	66.5	68.7	
	2	$D_{\infty h}$	65.3	67.0	63.5	65.2	
	3	D_{3h}	26.7	27.9	26.0	27.2	
	4	T_d	24.2	25.3	23.3	24.4	
	5	D_{3h}	10.6	11.2	10.0	10.7	
	6	O_h	10.2	10.9	9.8	10.5	

† Reference 158. Experimental gas phase values (error bars represent 1σ).

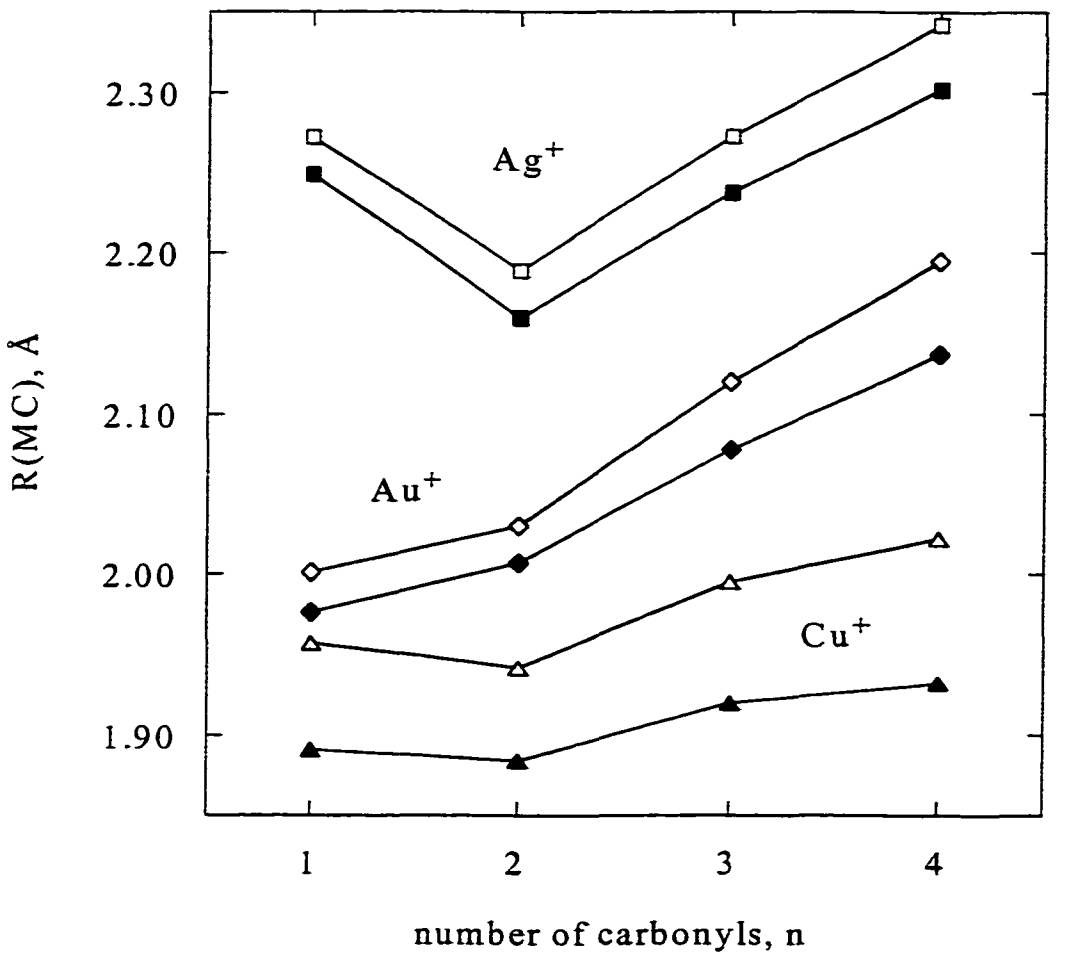

Figure II.3.3. Plot of the calculated MP2/I (solid shapes) and CCSD(T)/I (open shapes) M^{+}–CO bond distances of $M(CO)_n^+$ (Å) versus the number of carbonyl ligands (*n*).

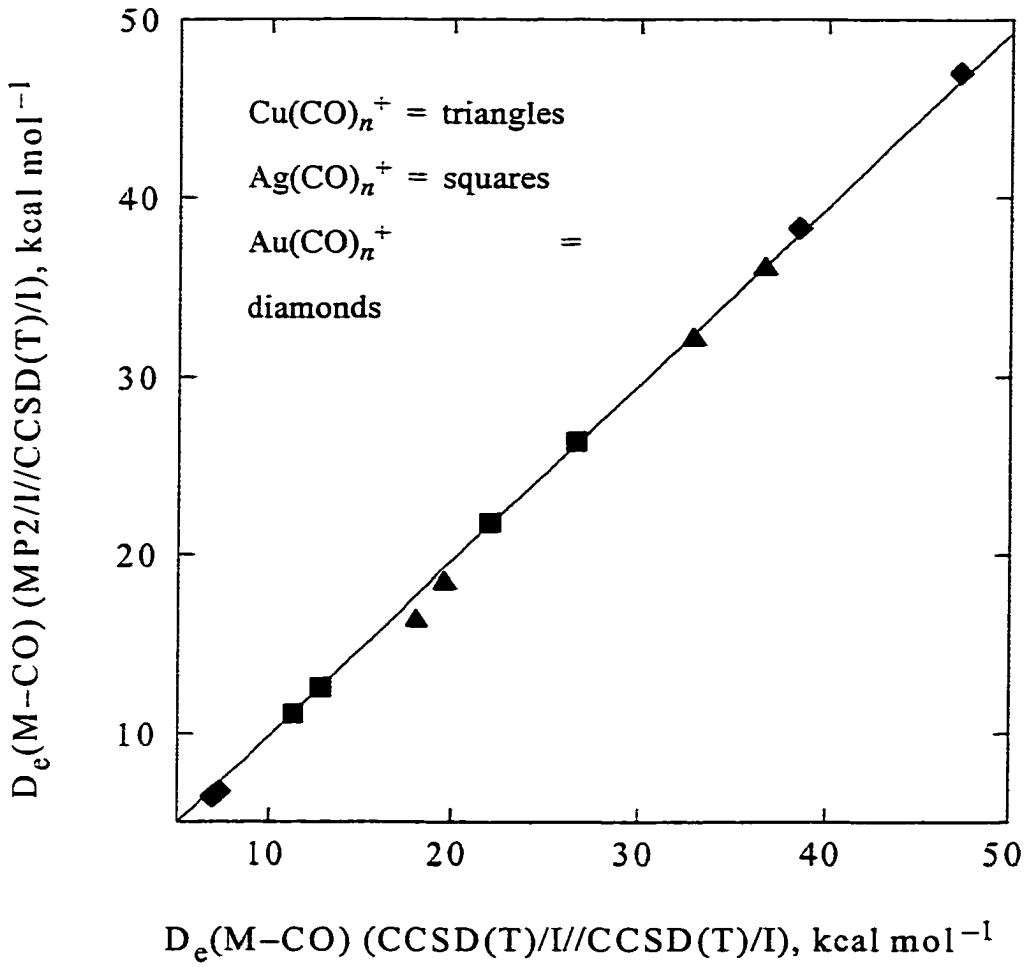

Figure II.3.4. Plot of the theoretical CCSD(T)/I//MP2/I sequential M–CO bond energies (kcal mol^{-1}) versus the theoretical CCSD(T)/I//CCSD(T)/I sequential M–CO bond energies (kcal mol^{-1}) for $Cu(CO)_n^+$ (triangles), $Ag(CO)_n^+$ (squares), and $Au(CO)_n^+$ (diamonds). The linear least-squares fit of the data, with the requirement that the line pass through the origin, has a slope of 0.98 and an *R* value of 0.999.

Cu–CO bond distance in $Cu(CO)_4^+$ is 1.965(3) Å,[145] approximately midway between the MP2/I and CCSD(T)/I values. This comparison is valid because the $Cu(CO)_4^+$ cation experiences minimal interionic contacts with counteranion fluorine atoms (the closest F···Cu or F···CO contacts are > 3.1 Å and 2.9 Å respectively).[145]

Note that the Cu–CO and Ag–CO distances become shorter from the monocarbonyl complexes to the respective dicarbonyl complexes. The DFT methods do not give good agreement with the CCSD(T)/I or MP/2 M–CO distances for any of the monocarbonyl complexes (Table II.3.2). Not only are the DFT monocarbonyl M–CO bond distances consistently shorter than the MP2/I distances, they are also shorter than the DFT dicarbonyl distances for Cu^+ and Ag^+. Nevertheless, the BP86/I and B3LYP/I plots mirror the CCSD(T)/I plots from $M(CO)_2^+$ to $M(CO)_4^+$ for all three metal ions.

M–CO Bond Energies at Different Levels of Theory

The excellent agreement between CCSD(T)/I//MP2/I and CCSD(T)/I//CCSD(T)/I D_e values was noted earlier. The average difference in D_e values due to the different geometries is only 0.5 kcal mol^{-1} (the range of differences is 0.2–1.5 kcal mol^{-1}). The agreement between MP2/I//MP2/I and CCSD(T)/I//CCSD(T)/I D_e values is not as good. In this case, the average difference in D_e values is 3.0 kcal mol^{-1} (the range is 1.0–6.4 kcal mol^{-1}). Similar differences between MP2/I//MP2/I and CCSD(T)/I//CCSD(T)/I D_e values for 34 $(CO)_nM$–L complexes were previously reported, and a correction factor for isostructural compounds which reduced the average difference to 3.9 kcal mol^{-1} was introduced.[174] The dissociation energy trends are displayed in Figure II.3.5. The DFT methods used significantly overestimate the monocarbonyl D_e values, which is consistent with the significant underestimation of M–CO bond distances noted above.

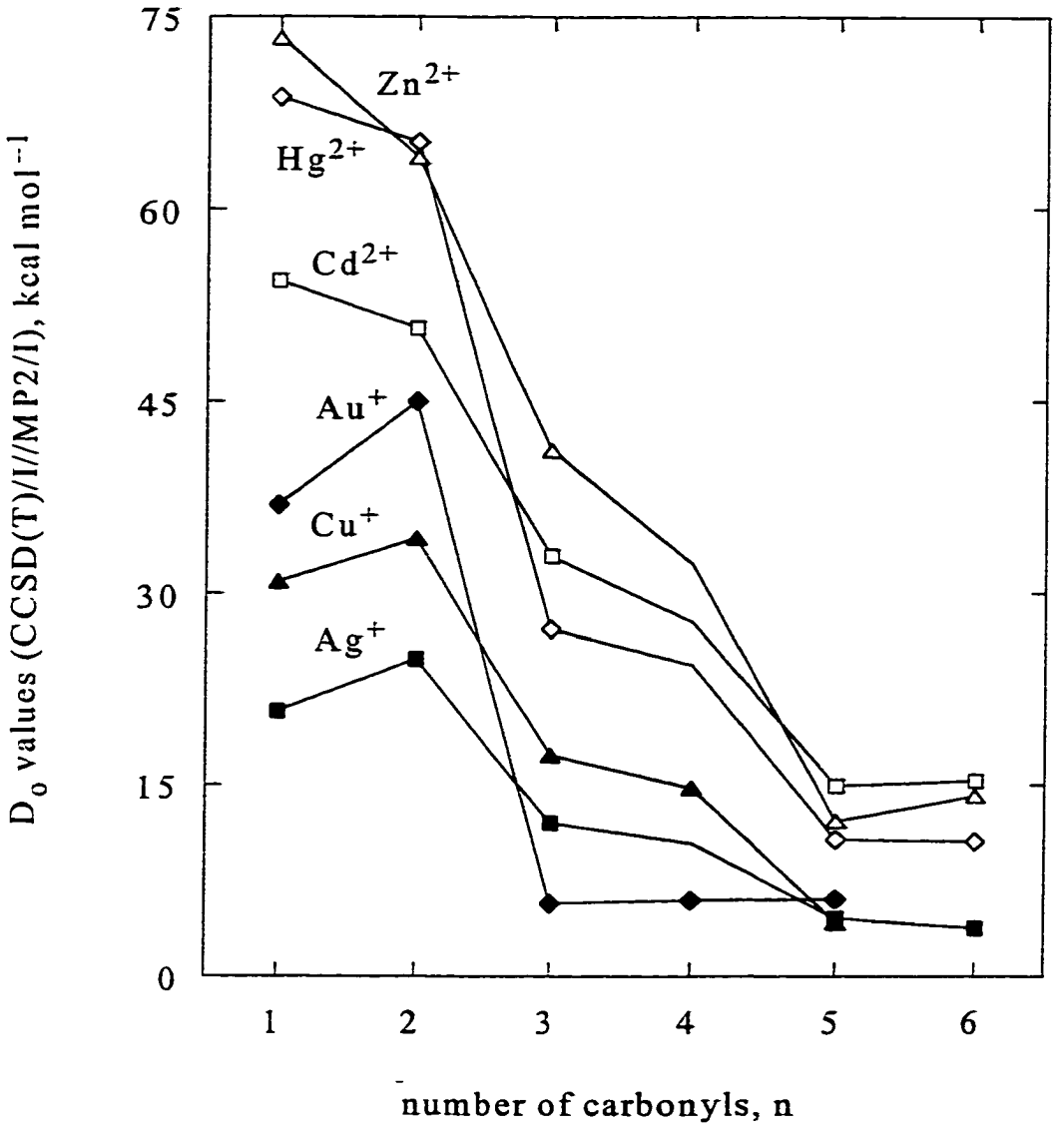

Figure II.3.5. Plot of the theoretical sequential M–CO bond energies (D_o, kcal mol^{-1}) versus number of carbonyl ligands (n) for 34 bound species in this study ($M(CO)_n^{+}$ (solid shapes), $M(CO)_n^{2+}$ (hollow shapes)).

The use of BP86/I//BP86/I and B3LYP/I//B3LYP/I leads to the incorrect prediction (Table II.3.1) that dissociation of a CO ligand from the dicarbonyl complex $Cu(CO)_2^+$ is less endothermic than dissociation of CO from the monocarbonyl complex $Cu(CO)^+$and that the BP86/I//BP86/I D_e value for $Au(CO)^+$ is predicted to be higher than the D_e value for $Au(CO)_2^+$. This is in contrast to the predictions at the MP2/I and CCSD(T)/I levels of theory. Even when the larger basis set III was used, the BP86 method still predicted a lower D_e value for $Cu(CO)_2^+$ than for $Cu(CO)^+$ (Table II.3.2).

Cu–CO Bond Energies with Different Basis Sets

The greatest differences between the eight experimental Cu–CO and Ag–CO D_o values (exp; Table II.3.1) and the CCSD(T)/I//MP2/I D_o values (theo) occur for the bonds between Cu^+ and the first two CO ligands. The CCSD(T)/I//MP2/I D_o values are listed in Table II.3.6. Interestingly, there is very little difference in the bond energies calculated with the smallest basis set, I, and the largest basis set, V (Table II.3.4). At the highest level of theory employed in this study, CCSD(T)/V//CCSD(T)/III using ZPE corrections at MP2/I, the dissociation of a single CO ligand from $Cu(CO)^+$ (D_o = 31.2 kcal/mol) and from $Cu(CO)_2^+$ (D_o = 34.7 kcal/mol) is still found to be 4.3 and 6.3 kcal mol^{-1}, respectively, lower than the experimental values. Another interesting observation is that D_o values calculated using CCSD(T)/V for $Cu(CO)^+$ vary by only 0.3 kcal mol^{-1} and for $Cu(CO)_2^+$ vary by 0.5 kcal mol^{-1} when the bond distances are changed from MP2/I to CCSD(T)/I to CCSD(T)/III optimized values. This suggests that further consideration of the complicated electronics in the linear, period three copper mono- and dicarbonyl systems may be needed. For the purposes of this study, a difference of only 4–6 kcal mol^{-1} in these two (of 34) complexes is of only minor concern.

Table II.3.6. Predicted M–C and C–O Bond Distances (MP2/I) and M–CO Sequential Bond Dissociation Energies (D_e and D_o; CCSD(T)/I//MP2/I)

complex	sym	R(MC), Å [a]	R(CO), Å [a]	D_e,[b] kcal mol^{-1}	D_o,[b,c] kcal mol^{-1}
$Cu(CO)^+$	$C_{\infty v}$	1.891	1.142	32.3	30.9
$Cu(CO)_2^+$	$D_{\infty h}$	1.884	1.142	36.2	34.3
$Cu(CO)_3^+$	D_{3h}	1.920	1.144	18.6	17.3
$Cu(CO)_4^+$	T_d	1.932	1.146	16.5	14.7
$Cu(CO)_5^+$	C_{3v}	1.928, 1.934, 3.687	1.146, 1.146, 1.148	4.7	4.2
$Cu(CO)_5^+$	D_{3h}	1.908, 2.673	1.146, 1.147		
$Cu(CO)_6^+$	O_h	2.290	1.148	–9.1	–6.6
$Ag(CO)^+$	$C_{\infty v}$	2.249	1.142	21.8	20.8
$Ag(CO)_2^+$	$D_{\infty h}$	2.160	1.142	26.4	24.9
$Ag(CO)_3^+$	D_{3h}	2.238	1.144	12.6	12.0
$Ag(CO)_4^+$	T_d	2.302	1.145	11.1	10.4
$Ag(CO)_5^+$	C_{3v}	2.293, 2.346, 3.641	1.145, 1.145, 1.148	4.9	4.5
$Ag(CO)_5^+$	D_{3h}	2.275, 2.851	1.145, 1.147		
$Ag(CO)_6^+$	O_h	2.290	1.148	3.5	3.8
$Au(CO)^+$	$C_{\infty v}$	1.976	1.142	38.3	36.9
$Au(CO)_2^+$	$D_{\infty h}$	2.007	1.142	47.0	45.0
$Au(CO)_3^+$	D_{3h}	2.078	1.145	6.4	5.7
$Au(CO)_4^+$	T_d	2.137	1.146	6.7	5.9
$Au(CO)_5^+$	D_{3h}	2.072, 3.124	1.146, 1.148	6.1	6.0
$Au(CO)_6^+$	O_h	2.578	1.147	–14.9	–12.9

Table II.3.6. Predicted M–C and C–O Bond Distances (MP2/I) and M–CO Sequential Bond Dissociation Energies (D_e and D_o; CCSD(T)/I//MP2/I) (*continued*)

complex	sym	R(MC), Å [a]	R(CO), Å [a]	D_e,[b] kcal mol^{-1}	D_o,[b,c] kcal mol^{-1}
$Zn(CO)^{2+}$	$C_{\infty v}$	2.017	1.140	74.8	73.3
$Zn(CO)_2^{2+}$	$D_{\infty h}$	2.011	1.139	65.6	64.0
$Zn(CO)_3^{2+}$	D_{3h}	2.069	1.141	42.5	41.2
$Zn(CO)_4^{2+}$	T_d	2.108	1.141	33.6	32.3
$Zn(CO)_5^{2+}$	D_{3h}	2.136, 2.372	1.142, 1.144	12.8	12.1
$Zn(CO)_6^{2+}$	O_h	2.299	1.144	14.9	14.1
$Cd(CO)^{2+}$	$C_{\infty v}$	2.255	1.140	55.6	54.4
$Cd(CO)_2^{2+}$	$D_{\infty h}$	2.228	1.140	52.2	50.7
$Cd(CO)_3^{2+}$	D_{3h}	2.301	1.141	33.9	32.9
$Cd(CO)_4^{2+}$	T_d	2.349	1.142	28.9	27.8
$Cd(CO)_5^{2+}$	D_{3h}	2.398, 2.504	1.143, 1.144	15.7	14.9
$Cd(CO)_6^{2+}$	O_h	2.500	1.144	16.1	15.3
$Hg(CO)^{2+}$	$C_{\infty v}$	2.164	1.139	70.0	68.7
$Hg(CO)_2^{2+}$	$D_{\infty h}$	2.126	1.139	67.0	65.2
$Hg(CO)_3^{2+}$	D_{3h}	2.246	1.141	27.9	27.2
$Hg(CO)_4^{2+}$	T_d	2.313	1.142	25.3	24.4
$Hg(CO)_5^{2+}$	D_{3h}	2.318, 2.644	1.142, 1.144	11.2	10.7
$Hg(CO)_6^{2+}$	O_h	2.530	1.144	10.9	10.5

[a] For five-coordinate complexes, the first value given is for equatorial CO ligands and the other values are for axial CO ligands. [b] Dissociation of a single CO ligand from the complex. [c] ZPE corrections from MP2/I.

General Observations

The geometries of all $M(CO)_n^{x+}$ (M^{x+} = Cu^+, Ag^+, Au^+, Zn^{2+}, Cd^{2+}, Hg^{2+}; n = 1–6) cations were optimized at MP2/I, followed by single-point energy calculations at CCSD(T)/I. Table II.3.6 lists the bond distances and D_e and D_0 values (ZPE corrections were made at MP2/I). Figure II.3.5 is graphical representation of the D_0 values for the 34 bound species. These are the first published theoretical treatments for any of these six d^{10} metal ions for $n > 3$. All thirty-six combinations examined are predicted to be bound species except for the hexacarbonyls of Cu^+ and Au^+. Examination of Figure II.3.5 reveals four major features (1) the group-12 complexes always have a larger D_0 than the corresponding group-11 complexes; (2) the group-11 complexes increase from $n = 1$ to $n = 2$; (3) for all complexes, there is a large decrease in D_0 from $n = 2$ to $n = 3$; (4) for the period-5 metals, the decrease in D_0 from $n = 2$ to $n = 3$ is larger than the for other periods. These issues will be discussed in detail below.

All of the mono-, di-, tri-, and tetracarbonyl species were energy minima at their $C_{\infty v}$-, $D_{\infty h}$-, D_{3h}-, and T_d-symmetry conformations, respectively. The energies (CCSD(T)/I//MP2/I) required to bend the C–M–C angles of the group-11 dicarbonyl species from 180° ($C_{\infty v}$) to 120° (C_{2v}) were 8.5, 6.7, and 21.1 kcal mol^{-1} for Cu^+, Ag^+, and Au^+, respectively (the M–C–O angles were fixed at 180°). The recent isolation of a salt of the $Cu(CO)_4^+$ cation, with a predicted gas-phase D_0 value of nearly 15 kcal mol^{-1}, suggests that the twelve group-12 mono-, di-, tri-, and tetracarbonyls may be isolable species because all twelve complexes have D_0 values greater than 20 kcal mol^{-1}. However, isolation of group-12 $M(CO)_n^{2+}$ complexes will probably require the weakest possible counteranions, since each successive addition of CO to an M^{2+} cation in the solid state is a displacement reaction, not just a ligand addition reaction. Details of the

thermodynamic aspects have been discussed elsewhere for the series of compounds $Ag(CO)_n(B(OTeF_5)_4)$ (n = 0–2).[143] Recall that the salt $Hg(CO)_2(Sb_2F_{11})_2$ has been isolated and characterized by single-crystal X-ray diffraction[159,160] and that $Zn(CO)_n^{2+}$ species have been generated in zeolites and on metal-oxide surfaces (n = 1, 2).[161-164]

All of the pentacarbonyl species were energy minima in D_{3h} symmetry except for $Cu(CO)_5^+$ and $Ag(CO)_5^+$. For $Au(CO)_5^+$, the axial Au–CO bond distance is 50% longer than the equatorial Au–CO distance. The group-12 pentacarbonyl axial:equatorial M–CO bond distance ratios are significantly smaller than those of the group-11 pentacarbonyls: 11% for Zn^{2+}; 4% for Cd^{2+}; and 14% for Hg^{2+}. Calculation of Hessian matrices demonstrated that the D_{3h} conformations of $Cu(CO)_5^+$ and $Ag(CO)_5^+$ are higher-order saddle points on their respective potential energy surfaces. Further geometry optimizations led to energy-minimized structures with C_{3v} symmetry and one very long axial Cu–CO or Ag–CO distance. Drawings of these structures are shown in Figure II.3.6. The C_{3v} complexes $Cu(CO)_5^+$ and $Ag(CO)_5^+$ can be considered to be weakly bonded adducts of the respective metal tetracarbonyl with an additional CO ligand. Note that the C_{ax}–M–C_{eq} bond angles involving the strongly bonded axial CO ligand are essentially unchanged from 109.5° and that the average Cu–CO and Ag–CO bond distances for the four strongly bound CO ligands in the pentacarbonyls, 1.930 and 2.306 Å, respectively, are essentially unchanged from the distances in the tetracarbonyls, 1.932 and 2.302 Å, respecitvely. Consistent with the very long distance between the fifth CO ligand and the Cu^+ or Ag^+ ions, the D_o values for $Cu(CO)_5^+$ and $Ag(CO)_5^+$ are both less than 5 kcal mol^{-1}. It is doubtful that these two species will ever be generated unless very low temperatures and very high pressures of CO gas are used.

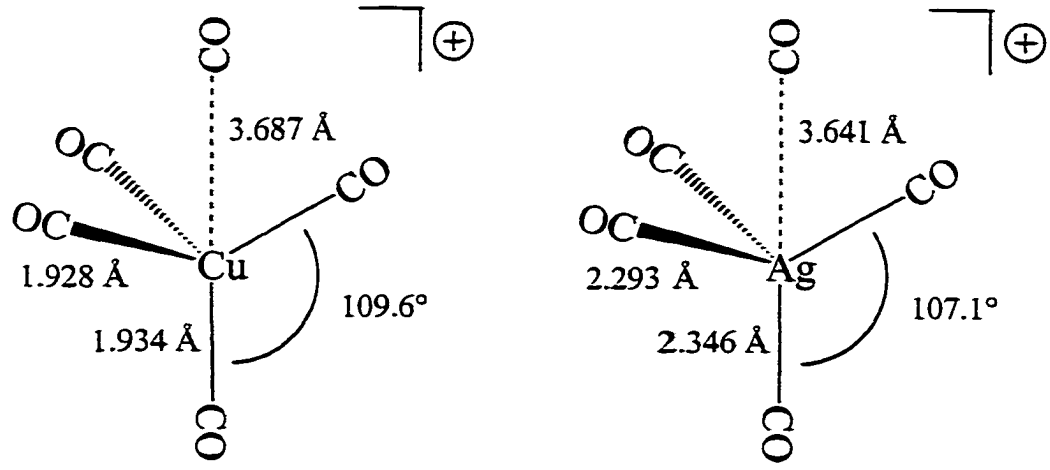

Figure II.3.6. Optimized geometries of $Cu(CO)_5^+$ and $Ag(CO)_5^+$.

Geometry optimizations of the hexacarbonyls were carried out assuming O_h symmetry. Calculation of the Hessian matrices at the MP2/I level showed that the O_h conformations of $Cu(CO)_6^+$ and $Au(CO)_6^+$ are higher-order saddle points on the potential energy surface (each complex had five imaginary frequencies). The octahedral conformations of the other four hexacarbonyl cations, however, are true minima on their respective potential energy surfaces. It is possible that very weakly bonded $Cu(CO)_6^+$ and $Au(CO)_6^+$ species with a symmetry lower than O_h may exist, but this possibility was not pursued.

The D_o values for the group-12 carbonyl complexes are significantly higher than for the corresponding group-11 complexes, in most cases at least twice as high. For example, D_o values for $Zn(CO)_2^{2+}$ and $Cu(CO)_2^+$ are 64.0 and 34.3 kcal mol^{-1}, respectively. As discussed below, there is a large electrostatic contribution to the

metal-carbon bonds in these complexes, and it is, therefore, sensible that doubly charged group-12 metal ions attract dipolar CO ligands much more strongly than singly charged group-11 metal ions. With the exception of $Au(CO)_2^+$, the dicarbonyl complexes of the other five metal ions have shorter M–CO bonds than the corresponding monocarbonyl complexes. For each of the three group-11 metal ions, D_o is higher for the dicarbonyl complex than for the monocarbonyl complex. Significantly, the opposite is true for the group-12 complexes. As a general trend, D_o for $M(CO)_n^{x+}$ decreases as n increases from 2 to 6, but there are several interesting exceptions. The sixth CO ligand is more strongly bound than the fifth CO ligand for Zn^{2+} and Cd^{2+}, and D_o increases slightly from $n = 3$ to $n = 5$ for Au^+.

There is an interesting pattern to the group-11 M–CO bond energies that will be discussed below. The complexes $Au(CO)^+$ and $Au(CO)_2^+$ have much higher D_o values than the Cu^+ or Ag^+ analogues, but $Au(CO)_3^+$ and $Au(CO)_4^+$ are much more weakly bonded than the Cu^+ or Ag^+ analogues. This is consistent with the experimental observation that $Au(CO)_3(Sb_2F_{11})$ is only formed when $Au(CO)_2(Sb_2F_{11})$ is treated with more than 100 atm CO while $Cu(CO)_3(AsF_6)$ and $Ag(CO)_3(Nb(OTeF_5)_6)$ are formed from their respective dicarbonyl precursors at much lower pressures.[25,147,148]

NBO and Wavefunction Topology Analysis

Two questions will now be addressed: What is the nature of the M–CO bonds in the group-11 and -12 metal carbonyl cations? Can the observed patterns in bond distances and bond energies be understood in terms of relatively simple chemical principles? Information about the bonds between the six metal ions and one or more carbonyl ligands were obtained from charge distributions and metal-ion valence

Table II.3.7. NBO Results at the MP2/I level. Calculated Partial Charges at the Metal, q(M), Total OC→Metal Charge Donation Δq; Metal Valence Orbital Population, d(M) and s(M), for the Transition Metal Compounds $M(CO)_n^+$ and $M(CO)_n^{2+}$

M	*n*	q(M)	Δq	d(M)	s(M)
Cu^+	1	0.93	0.07	9.77	0.18
	2	0.67	0.33	9.65	0.55
	3	0.75	0.25	9.61	0.49
	4	0.78	0.22	9.55	0.51
	5	0.78	0.22	9.55	0.51
Ag^+	1	0.95	0.05	9.91	0.09
	2	0.73	0.27	9.80	0.41
	3	0.75	0.25	9.81	0.36
	4	0.73	0.27	9.82	0.38
	5	0.72	0.28	9.82	0.38
	6	0.61	0.39	9.89	0.42
Au^+	1	0.85	0.15	9.72	0.38
	2	0.54	0.46	9.57	0.84
	3	0.74	0.26	9.57	0.61
	4	0.81	0.19	9.57	0.52
	5	0.75	0.25	9.56	0.60

Table II.3.7. NBO Results at the MP2/I level. Calculated Partial Charges at the Metal, q(M), Total OC→Metal Charge Donation Δq; Metal Valence Orbital Population, d(M) and s(M), for the Transition Metal Compounds $M(CO)_n^+$ and $M(CO)_n^{2+}$ (*continued*)

M	*n*	q(M)	Δq	d(M)	s(M)
Zn^{2+}	1	1.82	0.18	9.91	0.19
	2	1.56	0.44	9.88	0.46
	3	1.49	0.51	9.89	0.51
	4	1.43	0.57	9.89	0.55
	5	1.42	0.58	9.89	0.56
	6	1.37	0.63	9.90	0.60
Cd^{2+}	1	1.86	0.14	9.96	0.14
	2	1.63	0.37	9.93	0.40
	3	1.57	0.43	9.94	0.43
	4	1.50	0.50	9.94	0.49
	5	1.46	0.54	9.94	0.52
	6	1.41	0.59	9.95	0.57
Hg^{2+}	1	1.75	0.25	9.92	0.29
	2	1.42	0.58	9.83	0.71
	3	1.44	0.56	9.88	0.61
	4	1.41	0.59	9.89	0.61
	5	1.37	0.63	9.90	0.63
	6	1.31	0.69	9.93	0.68

configurations of the metals calculated using the NBO method[87] and from the electron density distribution.[88] The results of these calculations are listed in Table II.3.7.

The group-11 complexes will be considered first. In the $M(CO)^+$ monocarbonyls, the metal-ion charge is only reduced by 0.07, 0.05, and 0.15 e relative to the bare metal ions Cu^+, Ag^+, and Au^+, respectively. Since there is very little $M^+ \rightarrow CO$ backdonation (see below), this indicates that the bonding between a single CO ligand and all three M^+ metal ions is largely electrostatic in nature. Nevertheless, covalency must also be important, at least for $Au(CO)^+$. This must be true because a purely electrostatic interaction would lead to the incorrect prediction $D_o(Cu(CO)^+) > D_o(Au(CO)^+)$, since the metal charge is higher and the metal-carbon bond is shorter for the copper species. The donation of electron density from the CO ligands to the metal ions is significantly greater in the group-11 dicarbonyl complexes than in the monocarbonyl complexes: 0.33 e for $Cu(CO)_2^+$; 0.27 e for $Ag(CO)_2^+$; and 0.46 e for $Au(CO)_2^+$. These results are consistent with the larger D_o values for the dicarbonyls relative to the monocarbonyls. The lower metal-ion charges should result in a weaker coulombic contribution to the total bond energy (this is true even after accounting for the shorter M–CO bonds in the dicarbonyl species). It follows that the greater D_o values are the result of significant covalent contributions to the M–CO bonds in all three group-11 dicarbonyl complexes.

The foregoing conclusion is supported by the calculated energy densities at the bond critical points, H_b, which are listed in Table II.3.8. It has been show that the value of H_b is a sensitive probe of the type of bonding between two atoms: typical covalent bonds have negative values between –1 and –4 hartree $Å^{-3}$ and closed shell interactions (i.e., electrostatic interactions) have $H_b \sim 0$.[115] For the $Cu(CO)_n^+$ complexes, the monocarbonyl has a small degree of covalent character, –0.219 hartree $Å^{-3}$, which increases by ~10% to –0.239 hartree $Å^{-3}$ upon formation of the dicarbonyl. The set of silver complexes follows the same trend, i.e., an ~70% increase in covalency

Table II.3.8. Results of the Topological Analysis of the Wave Function Calculated at MP2/I for $M(CO)_n^{x+}$ complexes ($n = 1 - 4$)[a]

		ρ_b		$\nabla^2\rho_b$		H_b	
M	*n*	M–C	C–O	M–C	C–O	M–C	C–O
Cu^+	1	0.745	3.113	11.299	33.684	–0.219	–5.180
	2	0.761	3.116	11.204	33.325	–0.239	–5.187
	3	0.692	3.098	11.129	32.563	–0.181	–5.149
	4	0.672	3.089	11.005	31.964	–0.167	–5.132
Ag^+	1	0.453	3.107	6.167	34.571	–0.079	–5.144
	2	0.557	3.109	7.214	34.296	–0.135	–5.154
	3	0.461	3.097	6.453	33.753	–0.083	–5.123
	4	0.402	3.089	5.650	33.333	–0.060	–5.103
Au^+	1	0.943	3.104	8.990	34.236	–0.430	–5.166
	2	0.883	3.110	8.853	33.895	–0.383	–5.177
	3	0.749	3.090	8.421	33.158	–0.275	–5.129
	4	0.658	3.084	7.741	32.864	–0.211	–5.112

Table II.3.8. Results of the Topological Analysis of the Wave Function Calculated at MP2/I for $M(CO)_n^{x+}$ complexes ($n = 1 - 4$)[a] (*continued*)

		ρ_b		$\nabla^2\rho_b$		H_b	
M	*n*	M–C	C–O	M–C	C–O	M–C	C–O
Zn^{2+}	1	0.527	3.465	5.416	36.408	–0.126	–5.747
	2	0.610	3.123	7.017	36.838	–0.162	–5.201
	3	0.531	3.118	6.507	35.911	–0.122	–5.189
	4	0.481	3.115	6.067	35.316	–0.100	–5.177
Cd^{2+}	1	0.468	3.116	5.333	37.131	–0.089	–5.179
	2	0.500	3.120	5.572	36.556	–0.110	–5.189
	3	0.416	3.114	5.099	35.765	–0.066	–5.171
	4	0.373	3.110	4.693	35.252	–0.050	–5.160
Hg^{2+}	1	0.645	3.111	5.929	38.520	–0.194	–5.169
	2	0.705	3.121	6.271	37.289	–0.242	–5.197
	3	0.537	3.113	5.836	36.349	–0.130	–5.170
	4	0.464	3.106	5.335	35.626	–0.092	–5.154

[a] Electron density ρ_b (e $Å^{-5}$), Laplacian Concentration $\nabla^2\rho_b$ (e $Å^{-5}$), energy density H_b (hartree $Å^{-3}$) at the bond critical point.

from –0.079 (n = 1) to –0.135 hartree Å^{-3} (n = 2). Interestingly, the gold complexes do not follow this trend. The Au–C bond in $Au(CO)^+$ has a largest amount of covalent character of all the group-11 or -12 complexes studied, –0.430 hartree Å^{-3}. The covalency of the gold-carbon bonds in $Au(CO)_2^+$ is predicted to be about 11% less than for the unique gold-carbon bond in $Au(CO)^+$. The degree of covalency for all of the silver complexes is less than that of the homologous copper or gold species.

One explanation for such behavior was recently by Bauschlicher et al., who found a similar trend in the sequential bond energies of $Cu(H_2O)_n^+$ (n = 1–4).[175] They attributed the rather high bond energy of $Cu(H_2O)_2^+$ to favorable 4s–3dσ hybridization, which removes metal-ion electron density from the bonding axis and thereby enhances charge donation from σ-donor ligands along this axis (the bonding axis is the z axis and dσ is d_{z^2}). This is shown schematically in Figure II.3.7. This effect can be described as the polarization by a Lewis base of the isotropic charge distribution of the valence shell of a spherical d^{10} metal-ion into a disk-shaped valence-electron distribution that lies in the plane perpendicular to the bonding axis. This in turn facilitates the approach of a second Lewis base *trans* to the first. Since a majority of the energy cost for the hybridization is paid during the formation of the first metal–ligand bond, the second D_0 value is higher than the first. Consequently, the large decrease in D_0 from n = 2 to n = 3 can be attributed to the loss of this very favorable 4s–3dσ hybridization.[175] A similar, albeit qualitative, analysis was used by Armentrout et al. to explain the bond energy sequences for the series of gas-phase complexes $Cu(CO)_n^+$ and $Ag(CO)_n^+$.[158] Note that this explanation is essentially the basis for understanding the prevalence of two-coordination in the chemistry of Ag^+, Au^+, and Hg^{2+} and has been an enduring paradigm in inorganic chemistry for many years.[20,158,176,177]

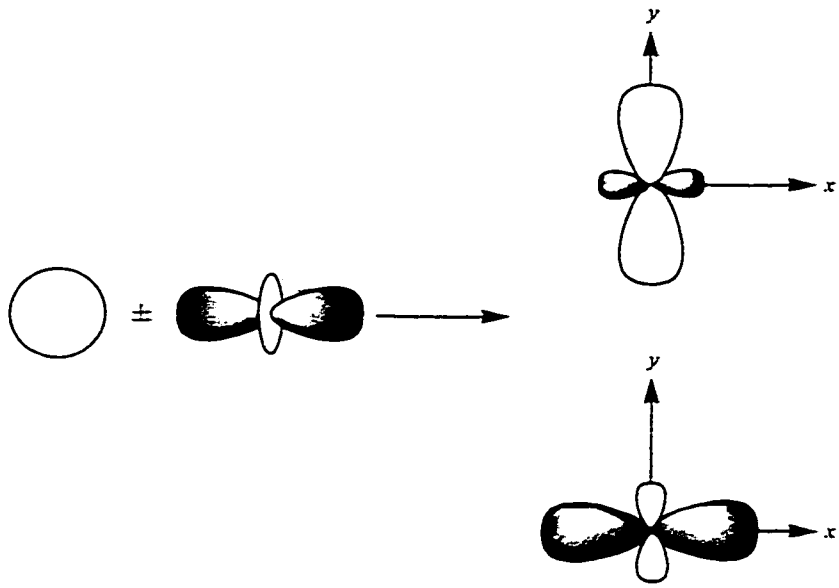

Figure II.3.7. Schematic representation of the s-dσ hybridization leading to charge polarization at the (d^{10}) metal which favors the approach of CO along the x axis.

The calculated metal-ion electron populations listed in Table II.3.7 support the s–dσ hybridization model. The d^{10} configurations of the M^+ cations clearly become distorted in the $M(CO)^+$ monocarbonyls via s-dσ hybridization: the electronic charge in the metal-ion valence s orbitals is larger than the amount of charge donated to the metal ion by the CO ligand. For example, the CO ligand in $Au(CO)^+$ transfers 0.15 unit of electronic charge to the gold ion, but the gold 6s orbital in the complex contains 0.38 unit of charge. The "excess" metal-ion s-orbital charge is equal to the decrease in metal-ion d-orbital charge. The increase in M^+←CO charge donation on going from $M(CO)^+$ to $M(CO)_2^+$ is clearly greater than the decrease in the metal d-orbital population, confirming that 4s–3dσ hybridization makes $M(CO)^+$ a better acceptor (i.e., a better Lewis acid) than M^+. Therefore, it appears that the decrease in electron-electron repulsion between the metal-ion dσ and CO 5σ orbitals along the bonding axis in $Au(CO)_2^+$ more than compensates for the weaker coulombic

attraction and the loss of covalency relative to the monocarbonyl complex of Au^+. The gold valence s orbital in $Au(CO)_2^+$ has a population of 0.84 e, whereas it is only 0.55 e in $Cu(CO)_2^+$ and 0.41 e in $Au(CO)_2^+$. The large decrease in D_o for $Au(CO)_3^+$ relative to $Au(CO)_2^+$ can be attributed to loss of the favorable 4s–3dσ hybridization. As discussed earlier, bending the C–Au–C framework of the dicarbonyl complex from 180° to 120° (a distortion necessary for tricarbonyl formation) is significantly more endothermic (21.1 kcal mol^{-1}) than the corresponding distortion for the copper and silver dicarbonyl species (≤ 8.5 kcal mol^{-1}).

Similarities in distortion energies are the key to understanding the pattern of D_o values for the group-12 carbonyl complexes, in which the M–CO bonds are significantly less covalent, and therefore more ionic, than the M–CO bonds in the group-11 homologs (e.g., H_b values for $Au(CO)^+$ and $Hg(CO)^{2+}$ are –0.430 and –0.194 hartree $Å^{-3}$, respectively). For each of the three group-12 metal ions, the D_o values are very similar for $n = 1$ and 2, for $n = 3$ and 4, and for $n = 5$ and 6 (e.g., 68.7 and 65.2 kcal mol^{-1} for $Hg(CO)^{2+}$ and $Hg(CO)_2^{2+}$, 27.2 and 24.4 kcal mol^{-1} for $Hg(CO)_3^{2+}$ and $Hg(CO)_4^{2+}$, and 10.7 and 10.5 kcal mol^{-1} for $Hg(CO)_5^{2+}$ and $Hg(CO)_6^{2+}$, respectively). Figure II.3.8 displays the results of MP2/I//MP2/I calculations of $-D_e$ values, reorganizational energies (E_r), and $-D_e'$ values for the $Cd(CO)_n^{2+}$ complexes; the numerical results for all eighteen Zn^{2+}, Cd^{2+}, and Hg^{2+} complexes are given in Table II.3.9. The distortions are geometry changes from the ground-state $Cd(CO)_n^{2+}$ structure to the structure of the frozen $Cd(CO)_n^{2+}$ fragment that would result from removing one CO ligand from the ground-state $Cd(CO)_{n+1}^{2+}$ structure. The $-D_e'$ values result from adding a CO ligand to the frozen $Cd(CO)_n^{2+}$ fragments to give the $Cd(CO)_{n+1}^{2+}$ complexes. Since the four distortion energies in Figure II.3.8 are virtually the same, one can analyze the four $-D_e'$ values as follows. The new CO ligand that approaches the vacant coordination site of the distorted $Cd(CO)_2^{2+}$ and $Cd(CO)_3^{2+}$ complexes

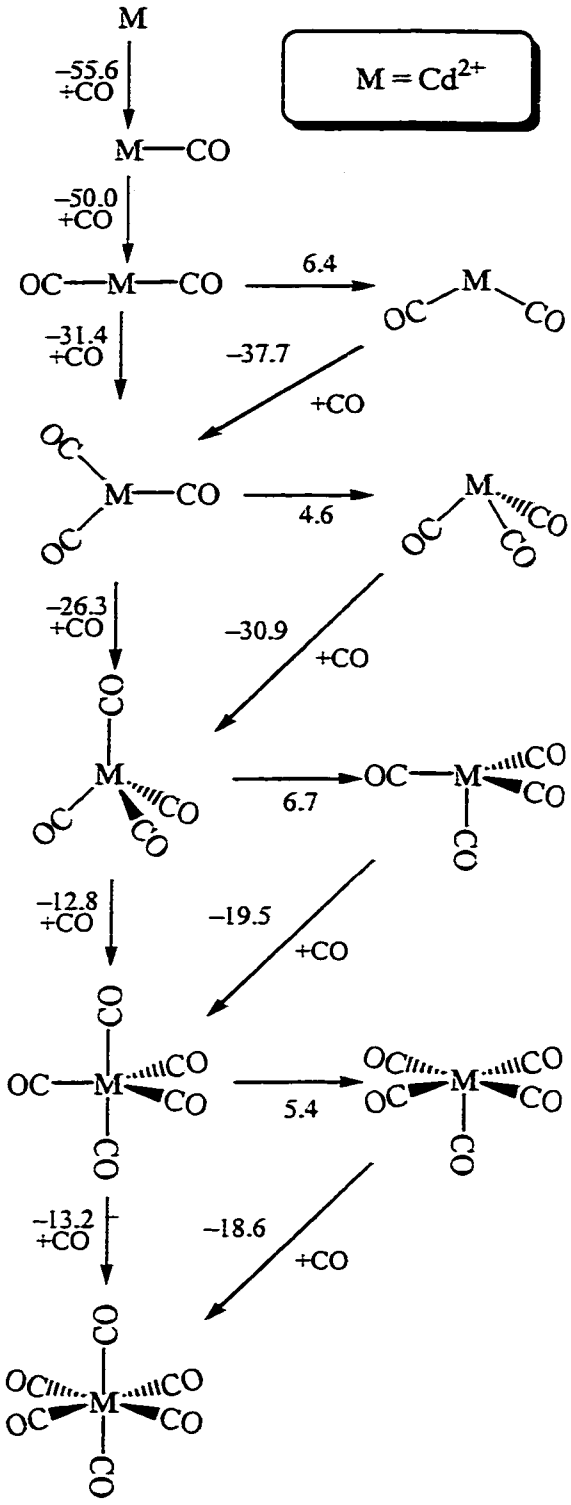

Figure II.3.8. Schematic representation of sequential bond dissociation energies ($-D_e$), reorganizational energies (E_r), and carbonyl binding energies ($-D_e'$) for $Cd(CO)_n^{2+}$. The energies (kcal mol^{-1}) are calculated at the MP2/I//MP2/I level of theory.

Table II.3.9. Sequential Bond Dissociation Energies ($-D_e$), Reorganizational Energies (E_r), and Carbonyl Binding Energies ($-D_e'$) at the MP2/I//MP2/I Level of Theory for $[M(CO)_n]^{2+}$ (M = Zn, Cd, Hg; n = 1-6)

M	$-D_{e(01)}$	$-D_{e(12)}$	E_r	$-D_{e(23)}'$	$-D_{e(23)}$	E_r	$-D_{e(34)}'$	$-D_{e(34)}$	E_r	$-D_{e(45)}'$	$-D_{e(45)}$	E_r	$-D_{e(56)}'$	$-D_{e(56)}$
Zn^{2+}	-78.9	-69.9	7.8	-53.0	-45.2	7.1	-43.3	-36.2	10.1	-24.0	-13.9	8.9	-25.2	-16.3
Cd^{2+}	-57.8	-54.7	6.4	-42.4	-36.1	4.6	-35.7	-31.0	6.7	-24.2	-17.5	5.4	-23.4	-18.0
Hg^{2+}	-72.1	-70.6	16.5	-46.5	-29.9	9.2	-36.8	-27.6	6.7	-19.4	-12.7	8.7	-21.0	-12.3

experiences steric and electronic repulsions from an array of bound CO ligands at angles of either 120° or 109.5°, respectively. According to a simple electrostatic attraction and repulsion model, similar bond angles should lead to similar $-D_e'$ values. The values for the tricarbonyl (–42.4 kcal mol^{-1}) and the tetracarbonyl (–35.7 kcal mol^{-1}) are indeed similar; they are considerably different from the pair of $-D_e$ values for the monocarbonyl and dicarbonyl complexes, –57.8 and –54.7 kcal mol^{-1}, respectively (note that $-D_e = -D_e'$ for mono- and dicarbonyl complexes since no distortion is necessary). Similarly, a new CO ligand approaching either the distorted tetra- and pentacarbonyl complex experiences an array of bound CO ligands at 90° from the vacant site. This leads to a pair of similar $-D_e'$ values, –24.2 and –23.4 kcal mol^{-1}, that are considerably less negative than the previous two $-D_e'$ values. The charge distributions and the electronic configurations of the group-12 metal ions in the complexes listed in Table II.3.7 show an interesting if not expected phenomenon. The d sub-shell populations are closer to 10 than for the group-11 complexes, and the Δq and s(M) values are virtually the same for a given metal ion and a given value of *n*. This indicates that the CO ligands are donating electron density into the empty metal s orbital with little or no d orbital participation. Only in the case of $Hg(CO)_2^{2+}$ is there appreciable covalency (i.e., a H_b value greater than –0.2 hartree $Å^{-3}$). Curiously, the D_o values for the group-12 dicarbonyl complexes are all smaller than for the respective monocarbonyl complexes even though the M–C distances for the dicarbonyl complexes are shorter than for the monocarbonyl complexes. For all three metal ions, H_b increases in magnitude from $M(CO)^{2+}$ to $M(CO)_2^{2+}$, so there is a situation in which the more covalent M–CO bonds in $M(CO)_2^{2+}$ are shorter but are also weaker than the M–CO bonds in $M(CO)^{2+}$.

Donor/Acceptor Behavior of the CO Ligands

The effect of $M^{x+} \rightarrow CO$ π backdonation (π-backbonding) in the 34 bound metal carbonyl cations was investigated using the CDA method.[29] The results are listed in Table II.3.10. The positive charge on the metal ions should diminish $M^{x+} \rightarrow CO$ π backdonation relative to d^{10} carbonyl complexes with neutral or anionic central metals (e.g., $Ni(CO)_4$, $Co(CO)_4^-$, or $Fe(CO)_4^{2-}$). This is because π backdonation and ionization of a gaseous metal atom or ion are both related to the ability of the metal to retain its valence d electrons. For example, the second ionization energy of Cu (20.3 eV) is much larger than the first ionization energy of Ni (7.6 eV).

The absolute magnitudes of the CDA backdonation and donation values are less meaningful than the ratio of the two values (i.e., b/d). It has been shown that CDA b/d ratios can be used to classify ligands in terms of their relative donor and acceptor strengths.[29] Here a constant ligand, CO, was used so the calculated b/d ratios can be analyzed in terms of properties of the metal ions. Note first that b/d increases in the order $Ag^+ < Cu^+ < Au^+$ for all four values of n. Therefore, the trend in b/d values down the coinage-metal triad mirrors the trend in D_o values for $n = 1$ and 2. In addition, the b/d ratio is greater for $Cu(CO)_2^+$ and $Ag(CO)_2^+$ than for the respective monocarbonyl derivatives, although b/d is smaller for $Au(CO)_2^+$ than for $Au(CO)^+$.

The copper and silver CDA results are consistent with the NBO analysis: the M–CO bonds in $Cu(CO)_2^+$ and $Ag(CO)_2^+$ are more covalent than in $Cu(CO)^+$ and $Ag(CO)^+$, respectively. Even though this trend is not followed by the gold complexes, the Au–CO bonds in $Au(CO)^+$ and $Au(CO)_2^+$ have b/d ratios twice as large as any of the copper and silver complexes and therefore are more covalent than any of the M–CO bonds in any of the copper and silver complexes. However, covalency is only

Table II.3.10. MP2/I Charge Decomposition Analysis (Per CO) of the Metal-Ligand Interaction for $M(CO)_n$ ($M = Cu^+, Ag^+, Au^+, Zn^{2+}, Cd^{2+}, Hg^{2+}$; $n = 1–4$) where M is the Acceptor and $(CO)_n$ is the Donor

M	n	backdonation (M→CO)	donation (M←CO)	repulsion (M↔CO)	residual Δ	b/d
Cu^+	1	0.060	0.537	–0.047	–0.018	0.112
	2	0.058	0.463	–0.022	–0.022	0.125
	3	0.058	0.528	–0.039	–0.016	0.110
	4	0.056	0.549	–0.037	–0.029	0.103
Ag^+	1	0.013	0.327	–0.080	0.002	0.040
	2	0.025	0.359	–0.065	–0.080	0.070
	3	0.020	0.328	–0.079	–0.002	0.061
	4	0.016	0.326	–0.071	–0.001	0.049
Au^+	1	0.109	0.425	–0.131	0.024	0.256
	2	0.084	0.356	–0.066	–0.009	0.236
	3	0.067	0.362	–0.138	0.014	0.185
	4	0.056	0.392	–0.122	0.012	0.142

Table II.3.10. MP2/I Charge Decomposition Analysis (Per CO) of the Metal-Ligand Interaction for $M(CO)_n$ ($M = Cu^+, Ag^+, Au^+, Zn^{2+}, Cd^{2+}, Hg^{2+}$; $n = 1$–4) where M is the Acceptor and $(CO)_n$ is the Donor (*continued*)

M	*n*	backdonation (M→CO)	donation (M←CO)	repulsion (M↔CO)	residual Δ	b/d
Zn^{2+}	1	0.001	0.561	–0.021	–0.014	0.002
	2	0.003	0.581	–0.021	–0.017	0.004
	3	0.002	0.522	–0.027	–0.007	0.004
	4	0.001	0.478	–0.027	–0.008	0.002
Cd^{2+}	1	-0.003	0.405	–0.047	0.013	-0.007
	2	0.001	0.376	–0.041	0.000	0.003
	3	0.001	0.382	–0.042	0.005	0.002
	4	0.001	0.369	–0.039	0.001	0.002
Hg^{2+}	1	0.006	0.459	–0.070	0.013	0.013
	2	0.012	0.403	–0.051	–0.005	0.030
	3	0.006	0.428	–0.068	0.005	0.014
	4	0.004	0.409	–0.064	0.001	0.010

significant in the linear $Au(CO)^+$ and $Au(CO)_2^+$ species, since the very effective s–dσ hybridization is lost in the more highly ligated complexes. This is evident from the relatively small decrease in b/d on going from $Au(CO)^+$ to $Au(CO)_2^+$ (8%) and the much larger decrease in b/d on going from the dicarbonyl to the tricarbonyl (22%).

There are two reasons why covalent bonding in $Au(CO)^+$ and $Au(CO)_2^+$ is particularly strong. First, relativistic effects lead to shrinkage of the s orbitals and to expansion of the d orbitals. This allows for more effective $M^+ \rightarrow CO$ π backdonation, which is indeed more important in the gold carbonyl cations than in the copper and silver carbonyl cations. The second reason is the lower $d^9s^1 \leftarrow d^{10}$ promotion energy for Au^+ (1.86 eV) relative to Cu^+ (2.72 eV) and Ag^+ (4.86 eV),[43] which makes s–dσ hybridization very effective for Au^+. The CDA results also indicate that there is a doubling of the donor-acceptor repulsion term on going from $Au(CO)_2^+$ to $Au(CO)_3^+$. This may also cause D_o to be much lower for $Au(CO)_3^+$ than for the tricarbonyl cations of copper and silver.

The higher D_o value of a $Cu(CO)_n^+$ complex relative to the corresponding $Ag(CO)_n^+$ complex might be due, in part, to the difference in the ionic radii of Cu^+ and Ag^+, which are 0.96 and 1.26 Å, respectively.[44] Since the M–CO bonds in the copper and silver carbonyl cations are largely ionic and therefore coulombic in nature, the larger radius of Ag^+ results in weaker bonds. Although the radius of Au^+, at 1.37 Å, is even larger,[44] the strong covalent contribution makes up for the weaker ionic contribution and results in stronger M–CO for $n = 1$ or 2. Note that the Au↔CO repulsion for $n = 3$ and 4 () is larger than for any of the Cu^+ or Ag^+ species, and this also explains the weak bonding of $Au(CO)_n^+$ for $n = 3$–5. The surprising stability of $Ag(CO)_6^+$ may be due to the right balance between the Ag^+–CO coulombic attraction and the repulsion among the carbonyl ligands, which appears to be more favorable compared to the copper and gold hexacarbonyls.

The $d^9s^1 \leftarrow d^{10}$ promotion energies for Zn^{2+}, Cd^{2+}, and Hg^{2+}, 9.68, 9.97, and 5.31 eV, respectively,[43] are much higher than those of the group-11 monocations. This is undoubtedly the reason for poor s–dσ mixing and hence the lack of covalency in the M–CO bonds of the $M(CO)_n^{2+}$ complexes. Furthermore, the CDA calculations indicate a virtual lack of π backdonation in the $M(CO)_n^{2+}$ complexes, consistent with the very high third ionization energies of the group-12 metals. The D_o value for any given $M(CO)_n^{2+}$ complex is, in general, twice as large as for the $M(CO)_n^{+}$ complex when the two metal ions are in the same period and *n* is constant. As we have seen, the most important contribution to the M–CO bond energies is ion-dipole electrostatic attraction. The metal ion charges in the group-12 complexes are twice as large as in the group-11 charges (Table II.3.7), and doubling the charge of an ion results in the doubling of the energy of interaction between the ion and a fixed dipole.

The conventional wisdom among metal carbonyl chemists is that an increase in π backbonding leads to a stronger M–CO bond. For example, experimental M–CO D_o values increase from $Cu(CO)_n^{+}$ to $Ni(CO)_n$ to $Co(CO)_n^{-}$,[8,45] as shown in Figure II.3.9, and most chemists would attribute this to an increase in π-backbonding. The present results suggest that a decrease in π backbonding does not always yield a weaker M–CO bond. As Figure II.3.9 clearly shows, the complexes with the least π backbonding, $Zn(CO)_n^{2+}$, are predicted to have, in general, the strongest M–CO bonds of the period 4 d^{10} carbonyl complexes shown in the Figure.

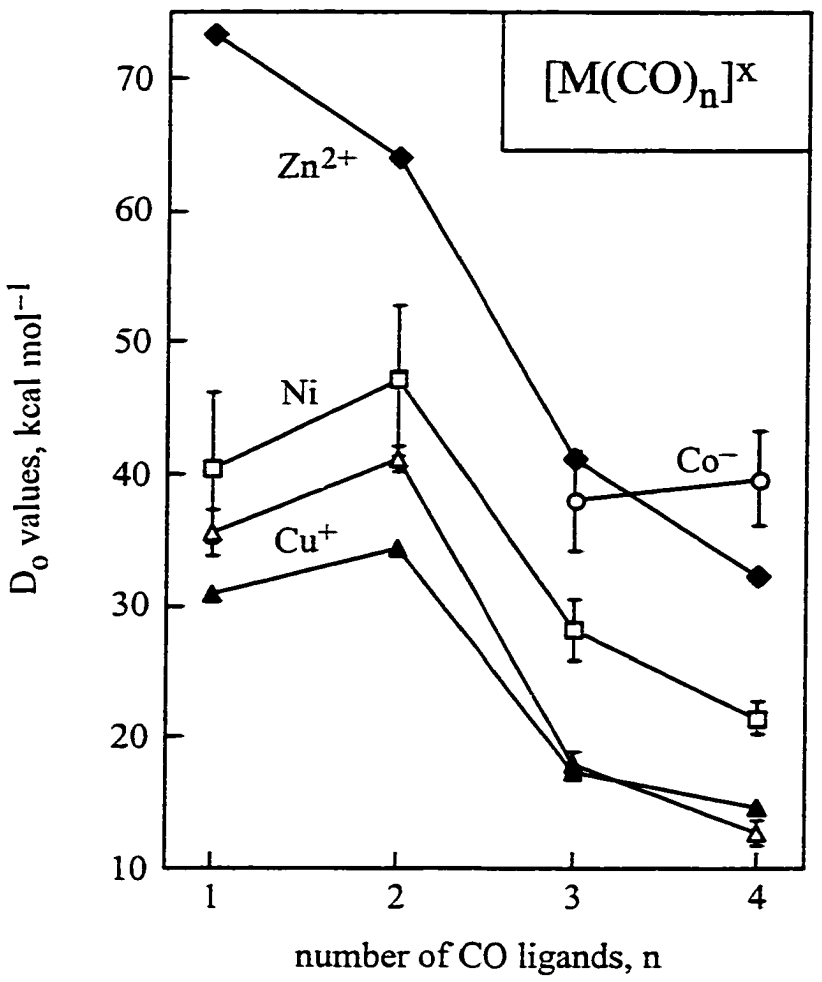

Figure II.3.9. Plot of the sequential M–CO bond energies (D_o, kcal mol^{-1}) versus number of carbonyl ligands (n) for $Co(CO)_n^-$ (experimental, hollow circles), $Cu(CO)_n^+$ (theoretical, solid triangles), $Cu(CO)_n^+$ (experimental, hollow triangles), $Ni(CO)_n$ (experimental, hollow squares), and $Zn(CO)_n^{2+}$ (theoretical, solid diamonds).

Conclusions

The results of this study can be summarized as follows:

1. All $M(CO)_n^{2+}$ (m = Zn, Cd, Hg; n =1–6) group 12 metal-ion carbonyls are energy minima in their highest possible symmetries. The group 11 complexes $Cu(CO)_n^+$ and $Au(CO)_n^+$ are predicted to be bound species for n = 1–5 only, whereas $Ag(CO)_n^+$ species are energy minima for n = 1–6.

2. The theoretically predicted bond dissociation energies at CCSD(T)/I//MP2/I are in good agreement with experimental results. BP86/I and B3LYP/I give BDEs which are too high. Both DFT methods have problems predicting the correct BDE trend between the mono and dicarbonyl species.

3. In the group 12 species $M(CO)_n^{2+}$, the bond strengths follow the trend $M = Zn^{2+} > Hg^{2+} > Cd^{2+}$. For each metal, the strength of the M–CO bonds is similar for n = 1 and 2, intermediate for n = 3 and 4, and weak for n = 5 and 6.

4. For a given value of n, the group 11 cations, $M(CO)_n^+$, all have weaker M–CO bonds than the corresponding group 12 dications. The dicarbonyls, $M(CO)_2^+$, have higher BDEs than the monocarbonyls, $M(CO)^+$. For n = 1 and 2, the trend in bond strengths is $M = Cu^+ > Au^+ > Ag^+$, whereas Au+ has the weakest bonds for n = 3 and 4.

5. The bonding pattern for the cationic metal carbonyls can be explained by the nature of the M^{x+} interactions.. The group 12 carbonyl complexes, $M(CO)_n^{2+}$, exhibit mainly coulombic M^{2+}–CO interactions. Covalent contributions are, in general, quite small, except for $Hg(CO)^{2+}$ and $Hg(CO)_2^{2+}$. Covalent contributions aresignificant for the M^+–CO bonds of he group 11 metal carbonyl complexes, $M(CO)_n^+$, particularly for $Au(CO)^+$ and $Au(CO)_2^+$. The favorable σ–d_σ hybridization at the metal center is the reason for the BDE trend $M(CO)_2^+ > M(CO)^+$. The analysis of the M^{x+}–CO interactions in all of the $M(CO)_n^{x+}$ complexes shows that there is little to no $M^{x+} \rightarrow CO$ π backdonation in these species.

CHAPTER 4

One Perturbation, Two Behaviors: Theoretical Experiments Supporting the Classical/Nonclassical Distinction

Overview

The following chapter will use theoretical experiments to illustrate the fundamental differences between classical and nonclassical carbonyls. The different behaviors of metal carbonyl complexes will be probed by examining the response of a metal carbonyl complex to perturbation in one of two ways. In the first computational experiment, the effect of adding two fluoride ions (σ donors) to a series of $M(CO)_n^x$ (n = 2, 3; x = –1, 0, 1, 2) cations will be examined. In the second computational experiment, the M–C bond in a series of $M(CO)_n^+$ (n = 1, 2) complexes will be compressed and lengthened from the equilibrium geometry. The effect of this perturbation on the C–O bond distance will be explored.

Fluoride Ion Perturbation

Introduction

Adding a donor ligand L to a metal carbonyl complex results in a stronger, shorter M–CO bond and a weaker, longer C–O bond. In order to probe this statement (Statement 3*b* of Part II, Chapter I), a computational experiment was performed in which two donor fluoride ions were placed 3 Å away from a metal center in a series of metal carbonyl complexes, $M(CO)_n^x$, as shown in Figure II.4.1.[53] The objective of this study was to create a set of homologous $M(CO)_n^x$ and $[M^x(CO)_n(F)_2]^{x-2}$ complexes and to examine the effect of changing the metal on the M–C and C–O bond distances and stretching frequencies. The pair of F^- ions was added to each $M(CO)_n^x$ complex so that the M···F^- vectors were orthogonal to the M–C vectors. The geometries of the $[M^x(CO)_n(F)_2]^{x-2}$ fragments were constrained as shown in Figure II.4.1: $[M^x(CO)_2(F)_2]^{x-2} \equiv D_{2h}$ symmetry; $[M^x(CO)_3(F)_2]^{x-2} \equiv D_{3h}$ symmetry. The hard base F^- was selected to model the weak M···F^- interactions that exist in crystals of $Ag(CO)_2(B(OTeF_5)_4)$[26,178] and $Hg(CO)_2(Sb_2F_{11})_2$[160] (Figure II.4.2) and are presumed to exist in other late-transition-metal dicarbonyl species such as $Cu(CO)_2(AsF_6)$ and $Au(CO)_2(Sb_2F_{11})$. Notably, one of the three unique $Ag(CO)_2^+$ cations in $Ag(CO)_2(B(OTeF_5)_4)$ interacts with two fluorine atoms from different $B(OTeF_5)_4^-$ anions (Figure II.4.2) such that the centrosymmetric $[Ag(CO)_2(F)_2]$ moiety is planar with Ag···F = 3.02(1) Å and F–Ag–C = 70.4(9)° (the sum of van der Waals radii for silver and fluorine is ~3.2 Å),[7,21] i.e., with fluorine geometries similar to the computational experiments being performed. Since the objective of this study was to create a set of homologous complexes in which one feature (i.e., the metal center) could be changed, it does not matter that some of the $[M(CO)_2(F)_2]$ moieties in this study are unknown species at the time of this writing.

(M^x = Rh^-, Pd^0, Cu^+, Ag^+, Au^+, Zn^{2+}, Cd^{2+}, and

Figure II.4.1. Geometries of the $[M(CO)_n(F)_2]^{x-2}$ complexes examined.

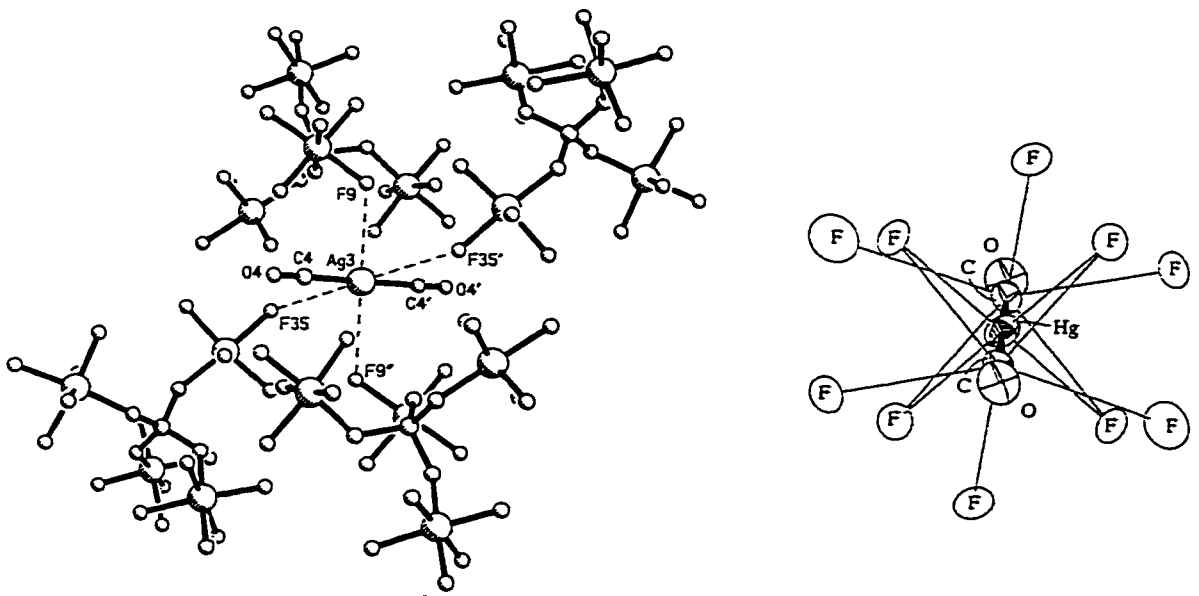

(a) (b)

Figure II.4.2. Structures of (a) $Ag(CO)_2(B(OTeF_5)_4)$ (refs 26,178) and (b) $Hg(CO)_2(Sb_2F_{11})_2$ (ref 160) showing metal···fluorine interactions. The structure of $Ag(CO)_2(B(OTeF_5)_4)$ (a) shows one of the centrosymmetric $Ag(CO)_2^+$ cations and four $B(OTeF_5)_4^-$ anions. Selected distances (Å) and angles (deg): Ag3···F9, 2.96(1); Ag3···F35, 3.09(2); C4–Ag3–F9, 92.1(7); C4–Ag3–F35, 67.2(7); F9–Ag–F35, 109.3(4). Selected interatomic distances (Å) and angles (deg) for $Hg(CO)_2(Sb_2F_{11})_2$: Hg···F, 2.595(5), 2.691(4); C···F, 2.65(1)–3.00(1); O···F, 2.82(1)–2.92(1).

In general, the addition of a fluoride ion (or any coordinating base) to a metal carbonyl complex will decrease the effective charge on the metal center. Such a decrease will affect the three aspects of metal-carbonyl bonding: (1) charge effects; (2) σ donation; (2) π backdonation. A decrease in the charge on the metal center will decrease the M···CO electrostatic interaction and will also decrease the amount of M←CO σ donation. These effects will cause both the M–C σ bond and the C–O bond to be lengthened. Decreased metal positive charge will also facilitate an increase in M→CO π donation; this will shorten the M–C π bonds and lengthen the C–O bonds. In all cases, addition of two F^- ions to the metal in a metal carbonyl complex will lengthen the C–O bond, while there are two competing effects at work to determine whether the M–C bond increases or decreases. These effects are summarized Table II.4.1. If there is significant π backdonation, as in classical metal carbonyls (cf. Part II, Chapter I), the effect of π backdonation will dominate the bonding interactions in the carbonyl complex and the M–C bond will become shorter. If there is insignificant π backdonation, as in nonclassical metal carbonyls (cf. Part II, Chapter I), σ donation will dominate the bonding interactions in the carbonyl complex and the M–C bond will become longer. Therefore, this experiment can be used as a way to differentiate *classical* and *nonclassical* metal carbonyl complexes.

Table II.4.1. Effects of a Base on the Three Aspects of M^+–CO Bonding

	electrostatic	σ donation	π backdonation
R(MC)	↑	↑	↓
R(CO)	↑	↑	↑

The results of the fluoride ion perturbation on the isoelectronic d^{10} $M(CO)_2^x$ and $M(CO)_3^x$ complexes are presented in Table II.4.2 and Table II.4.3, respectively. The changes in M–C and CO bond distances upon addition of the fluoride ions are shown in Table II.4.4and Table II.4.5. As anticipated, the addition of two fluoride ions 3 Å from the metal center increased in the C–O bond length in all cases, but the same ligand-field perturbation had two different effects on the M–C bond. For the $M(CO)_2^x$ species, the perturbation *decreased* the M–C bond length in $Rh(CO)_2^-$, $Pd(CO)_2$, $Pt(CO)_2$, $Cu(CO)_2^+$, and $Au(CO)_2^+$ but *increased* the M–C bond length in $Ag(CO)_2^+$, $Zn(CO)_2^{2+}$, $Cd(CO)_2^{2+}$, and $Hg(CO)_2^{2+}$. For $M(CO)_3^x$ complexes, the perturbation *decreased* the M–C bond length in all of the complexes studied except $Cd(CO)_3^{2+}$ and $Hg(CO)_3^{2+}$. A decrease in M–C bond length suggests that the M–CO bonds in these complexes are *stronger* than in the parent complexes. Therefore in these ten d^{10}-complexes the fluoride-ion perturbation resulted in an increase in M→CO π backdonation, which more than offset the decrease in M←CO σ donation and in M···CO electrostatic interaction. The increase in M–C bond length for $[Ag(CO)_2(F)_2]^+$, $[Zn(CO)_2(F)_2]^{2+}$, $[Cd(CO)_2(F)_2]^{2+}$, $[Hg(CO)_2(F)_2]^{2+}$, $[Cd(CO)_3(F)_2]^{2+}$, and $[Hg(CO)_3(F)_2]^{2+}$ indicates that the metal-carbonyl bonds in these species are *weaker* than in the parent complexes. In these complexes the increase in M→CO π backdonation was not large enough to offset the weakening of the M←CO σ donation or the decrease in M···CO electrostatic interactions.

To better understand the implications of the data just presented, two case studies, using the metal complexes with and without the pair of F^- ions at 3 Å, will be examined. The first is a comparison of the group-10 complexes $Cu(CO)_2^+$ and $Ag(CO)_2^+$; the second is a comparison of the isoelectronic period-5 series $M(CO)_2$, where M = Rh^-, Pd, Ag^+, and Cd^{2+}. In the $Cu(CO)_2^+$ the effects on metal-carbon and carbon-oxygen are

Table II.4.2. Calculated Distances and Symmetric Carbon–Oxygen Stretching Frequencies for the D_{2h} species $[M(CO)_2(F)_2]^{x-2}$ (M^x = Rh^-, Pd^0, Cu^+, Ag^+, Au^+, Zn^{2+}, Cd^{2+}, and Hg^{2+})[a]

M^x	R(MF), Å	R(MC), Å	R(CO), Å	ν_{sym}(CO), cm^{-1}
Rh^-	∞	1.901	1.182	2019
Rh^-	3	1.797	1.241	1817
Pd^0	∞	1.942	1.156	2112
Pd^0	3	1.924	1.167	2046
Cu^+	∞	1.884	1.142	2196
Cu^+	3	1.850	1.148	2164
Ag^+	∞	2.160	1.142	2184
Ag^+	3	2.196	1.147	2152
Au^+	∞	2.007	1.142	2201
Au^+	3	1.983	1.148	2164
Zn^{2+}	∞	2.011	1.140	2187
Zn^{2+}	3	2.046	1.142	2182
Cd^{2+}	∞	2.228	1.140	2185
Cd^{2+}	3	2.365	1.143	2176
Hg^{2+}	∞	2.126	1.139	2195
Hg^{2+}	3	2.725	1.148	2138

[a] Calculated ν(CO) = 2118 cm^{-1} for the free CO molecule; calculated R(CO) = 1.151 Å for the free CO molecule.

Table II.4.3. Calculated Distances and Symmetric Carbon–Oxygen Stretching Frequencies for the D_{3h} species $[M(CO)_3(F)_2]^{x-2}$ (M^x = Rh^-, Pd^0, Cu^+, Ag^+, Au^+, Zn^{2+}, Cd^{2+}, and Hg^{2+})[a]

M^x	R(MF), Å	R(MC), Å	R(CO), Å	ν_{sym}(CO), cm^{-1}
Rh^-	∞	1.904	1.181	1971
Rh^-	3	1.897	1.191	1835
Pd^0	∞	1.964	1.158	2092
Pd^0	3	1.935	1.169	2037
Cu^+	∞	1.920	1.144	2171
Cu^+	3	1.866	1.150	2145
Ag^+	∞	2.239	1.144	2168
Ag^+	3	2.206	1.149	2142
Au^+	∞	2.078	1.145	2164
Au^+	3	2.023	1.151	2131
Zn^{2+}	∞	2.069	1.141	2181
Zn^{2+}	3	2.052	1.142	2183
Cd^{2+}	∞	2.302	1.141	2178
Cd^{2+}	3	2.352	1.144	2176
Hg^{2+}	∞	2.246	1.141	2179
Hg^{2+}	3	2.321	1.144	2170

[a] Calculated ν(CO) = 2118 cm^{-1} for the free CO molecule; calculated R(CO) = 1.151 Å for the free CO molecule.

Table II.4.4.[a] Effect of Two Fluoride Ions on R(CO) and R(MC) in $[M(CO)_2(F)_2]^{x-2}$

Group 9	Group 10	Group 11	Group 12
		Cu^+	Zn^{2+}
		$\Delta R(CO) = +0.006$	$\Delta R(CO) = +0.002$
		$\Delta R(MC) = -0.034$	$\Delta R(MC) = +0.035$
Rh^-	Pd^0	Ag^+	Cd^{2+}
$\Delta R(CO) = +0.059$	$\Delta R(CO) = +0.011$	$\Delta R(CO) = +0.005$	$\Delta R(CO) = +0.003$
$\Delta R(MC) = -0.104$	$\Delta R(MC) = -0.018$	$\Delta R(MC) = +0.036$	$\Delta R(MC) = +0.136$
		Au^+	Hg^{2+}
		$\Delta R(CO) = +0.006$	$\Delta R(CO) = +0.009$
		$\Delta R(MC) = -0.024$	$\Delta R(MC) = +0.599$

[a] $\Delta R(AB) = (R(AB)$ for $M\cdots F^- = 3$ Å$) - (R(AB)$ for $M\cdots F^- = \infty)$; AB = CO or MC

Table II.4.5.[a] Effect of Two Fluoride Ions on R(CO) and R(MC) in $[M(CO)_3(F)_2]^{x-2}$

Group 9	Group 10	Group 11	Group 12
		Cu^{+}	Zn^{2+}
		$\Delta R(CO) = +0.006$	$\Delta R(CO) = +0.001$
		$\Delta R(MC) = -0.054$	$\Delta R(MC) = -0.017$
Rh^{-}	Pd^{0}	Ag^{+}	Cd^{2+}
$\Delta R(CO) = +0.010$	$\Delta R(CO) = +0.011$	$\Delta R(CO) = +0.005$	$\Delta R(CO) = +0.003$
$\Delta R(MC) = -0.007$	$\Delta R(MC) = -0.029$	$\Delta R(MC) = +0.033$	$\Delta R(MC) = +0.136$
		Au^{+}	Hg^{2+}
		$\Delta R(CO) = +0.006$	$\Delta R(CO) = +0.003$
		$\Delta R(MC) = -0.055$	$\Delta R(MC) = +0.075$

[a] $\Delta R(AB) = (R(AB)$ for $M\cdots F^{-} = 3$ Å$) - (R(AB)$ for $M\cdots F^{-} = \infty)$; AB = CO or MC

$\Delta R(CO)$ = 0.006 Å and $\Delta R(MC)$ = –0.034 Å; in the case of the silver(I) complex, $\Delta R(CO)$ = 0.005 Å and $\Delta R(MC)$ = 0.036 Å. The virtual equivalence of $\Delta R(CO)$ for these two systems provides no indication that the metal-carbon bonds respond so differently to the same chemical perturbation. However, based on the $\Delta R(MC)$ values, it certainly seems appropriate to place the parent complexes in different categories, classical for $Cu(CO)_2^+$ and nonclassical for $Ag(CO)_2^+$. Note that $Cu(CO)_2^+$ is classical by the $\Delta R(MC)$ definition even though the calculated value of $\nu_{sym}(CO)$, at 2195 cm^{-1}, is much higher than the calculated value for free CO, 2118 cm^{-1} (the experimental values for $\nu_{sym}(CO)$ and $\nu_{asym}(CO)$ for $Cu(CO)_2(AsF_6)$ are 2177 and 2164 cm^{-1}, respectively).[25]

It is important to note that these results should be used only to interpret the magnitude of *changes* in the amounts of σ and π bonding for a given system, not the absolute amounts of σ and π bonding in a given complex. The fact that $\Delta R(MC)$ is negative for $Cu(CO)_2^+$ and positive for $Ag(CO)_2^+$ means that these two complexes should be categorized as classical and nonclassical metal carbonyl complexes, respectively. These results do not indicate that there is zero π backbonding in $Ag(CO)_2^+$, only that charge and σ effects outweigh any π effects. The behavior of $Cu(CO)_2^+$ (classical) and $Ag(CO)_2^+$ (nonclassical), as probed by the fluoride-ion perturbation, is consistent with other theoretical[165] and experimental[179] results.

Finally, let us compare the four d^{10} period-5 complexes $Rh(CO)_2^-$, $Pd(CO)_2$, $Ag(CO)_2^+$, and $Cd(CO)_2^{2+}$. The monotonic trends in R(CO) at R(M···F) = ∞ (1.182, 1.156, 1.142, and 1.140, respectively), $\nu_{sym}(CO)$ at R(M···F) = ∞ (2019, 2112, 2184, and 2185 cm^{-1}, respectively), $\Delta R(CO)$ (0.059, 0.011, 0.005, and 0.003 Å, respectively), and $\Delta\nu_{sym}(CO)$ (–202, –66, –32, and –9 cm^{-1}, respectively) mask the more significant result that $\Delta R(MC)$ is *negative* for $Rh(CO)_2^-$ and $Pd(CO)_2$ but *positive* for $Ag(CO)_2^+$ and $Cd(CO)_2^+$. These results are illustrated graphically in Figure II.4.3. The "smooth correlation" in R(CO) and ν(CO) values is smooth only because weakening the

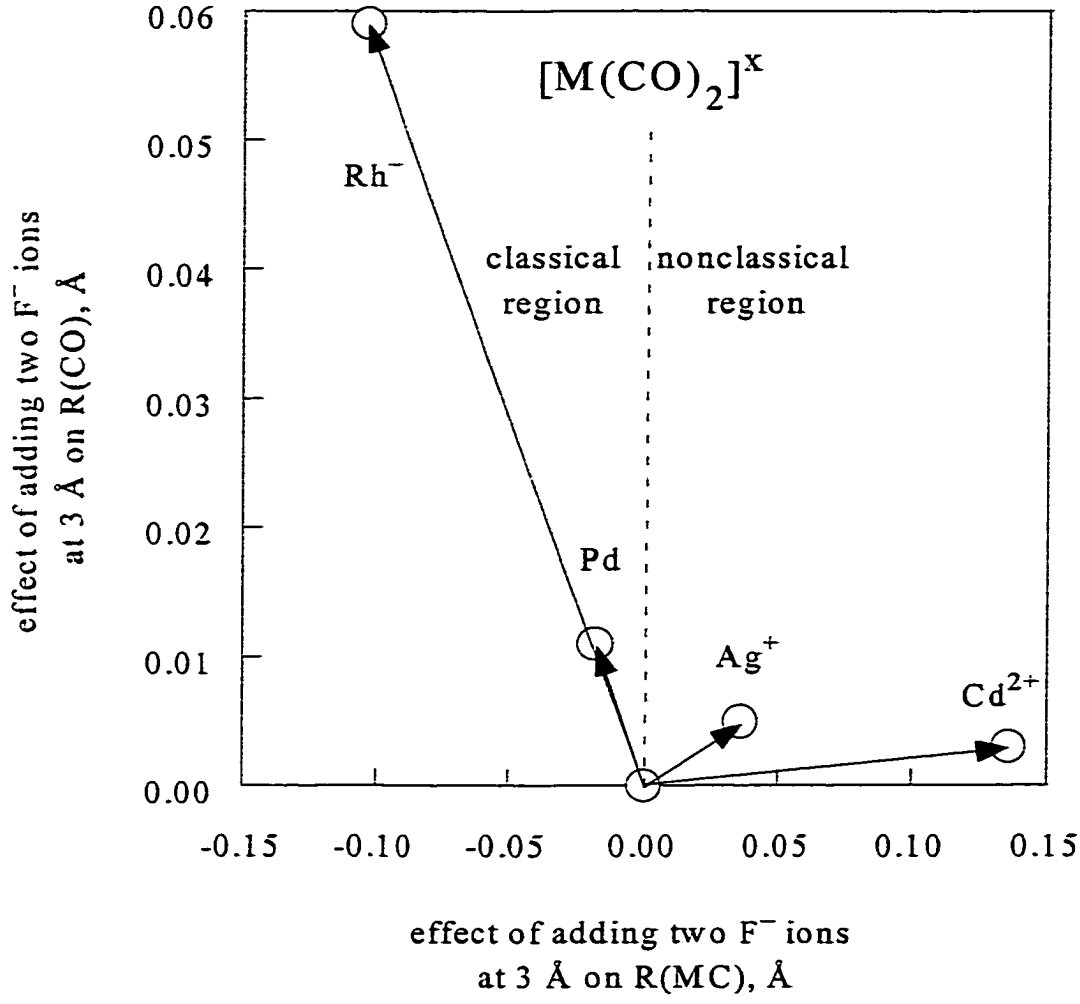

Figure II.4.3. The effects of adding to F^- ions to linear d^{10} $M(CO)_2^x$ complexes. Note that there is a monotonic trend for $\Delta R(CO)$ but a discontinuity (dotted line) between Pd and Ag^+.

M←CO σ bond and strengthening the M→CO π bond *both* cause R(CO) to increase and ν(CO) to decrease regardless of whether the complex is classical or nonclassical.

The distinction between classical and nonclassical metal carbonyls based on ΔR(MC) (or Statement 3*b*) is unequivocal, non-arbitrary, and chemically relevant. In the former category, the change in M→CO π backbonding due to the fluoride-ion perturbation has a larger effect on R(MC) than the offsetting but less significant change in M←CO σ bonding or the change in the ionic component of the M–CO bond. In the latter category, the opposite is true. However, this appropriate definition will be difficult for the experimentalist to apply routinely.

Metal Carbonyl Bond Formation Experiment

Introduction

In a landmark theoretical study by Sherwood and Hall the simple dissociation reaction of one carbonyl ligand from a $Cr(CO)_6$ molecule was examined in an effort to probe the effects of π backdonation of the M–C bonding:[180]

$$(CO)_5Cr\text{–}CO \rightarrow (CO)_5Cr\cdots CO \rightarrow (CO)_5Cr + CO$$

When the unique Cr–C bond was stretched by 0.25 Å from the equilibrium Cr–C distance of 1.80 Å, the Cr–C π-bond overlap became negligible. Lengthening the bond further resulted in the complete disappearance of π backdonation. The bond between the chromium atom and the dissociating CO ligand became purely σ in character. In addition, the C–O bond became *shorter and stronger* than in free CO. A plot of the

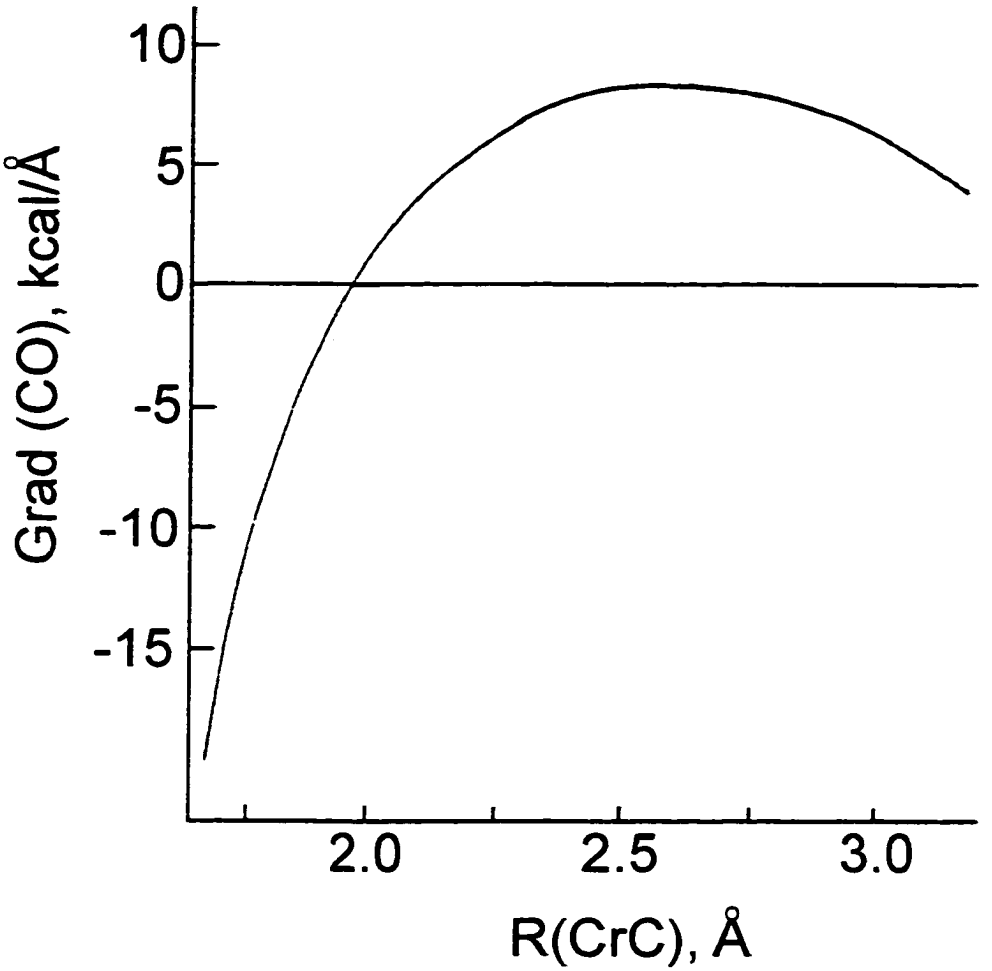

Figure II.4.4. Plot of gradient of the unique carbonyl versus the chromium carbon bond distance of the unique carbonyl in $(OC)_5Cr\cdots CO$. Zero corresponds to free CO. Negative values indicate a longer C–O bond than in free CO; positive values indicate a shorter bond than in free CO.

gradient of the dissociating CO ligand (i.e., the force on the C–O bond) versus the Cr···CO distance, taken from Sherwood and Hall's paper, is reproduced here in Figure II.4.4.

These results suggest that the carbon-oxygen bond length, bond strength, and consequently ν(CO) do not change monotonically as CO approaches a metal atom or a metal surface. First, the C–O bond becomes shorter (i.e., stronger) as carbon lone pair atoms interact with the metal. This study supports the idea that σ effects (charge, polarization, etc.) begin to occur at long distances (see Part II, Chapter 1). As the carbonyl ligand approaches sufficiently close to the metal, M–C π backbonding begins to occur, lengthening (i.e., weakening) the carbon-oxygen bond. This is shown in the scheme below:

$L_nM + CO$	$\rightarrow$	$L_nM\cdots CO$	$\rightarrow$	$L_nM–CO$
$\nu(CO) = 2143\ cm^{-1}$		$\nu(CO) > 2143\ cm^{-1}$		$\nu(CO) < 2143\ cm^{-1}$
$R(CO) = 1.12822$ Å		$R(CO) < 1.12822$ Å		$R(CO) > 1.12822$ Å

The curves in Figure II.4.5 are qualitative adaptations of Sherwood and Hall's results,[33] in which the various effects are deconvoluted from one another. The top curve maps the hypothetical behavior of a carbonyl ligand as it approaches a metal/non-metal where only σ donation and charge effects are present. One example of this behavior is given by the behavior of the CO in the HCO^+ cation as the H^+–C bond distance is varied (Part II, Chapter 4). The bottom curve maps the behavior of a carbonyl ligand as it approaches a hypothetical metal that is only capable of π backdonation and where no charge or σ effects affect the ligand. Note that this situation is purely hypothetical and does not exist in reality. The middle curve in Figure II.4.5, is the resultant of adding the upper and lower curves; this curve is topologically congruent to Sherwood and Hall's plot in Figure II.4.4.

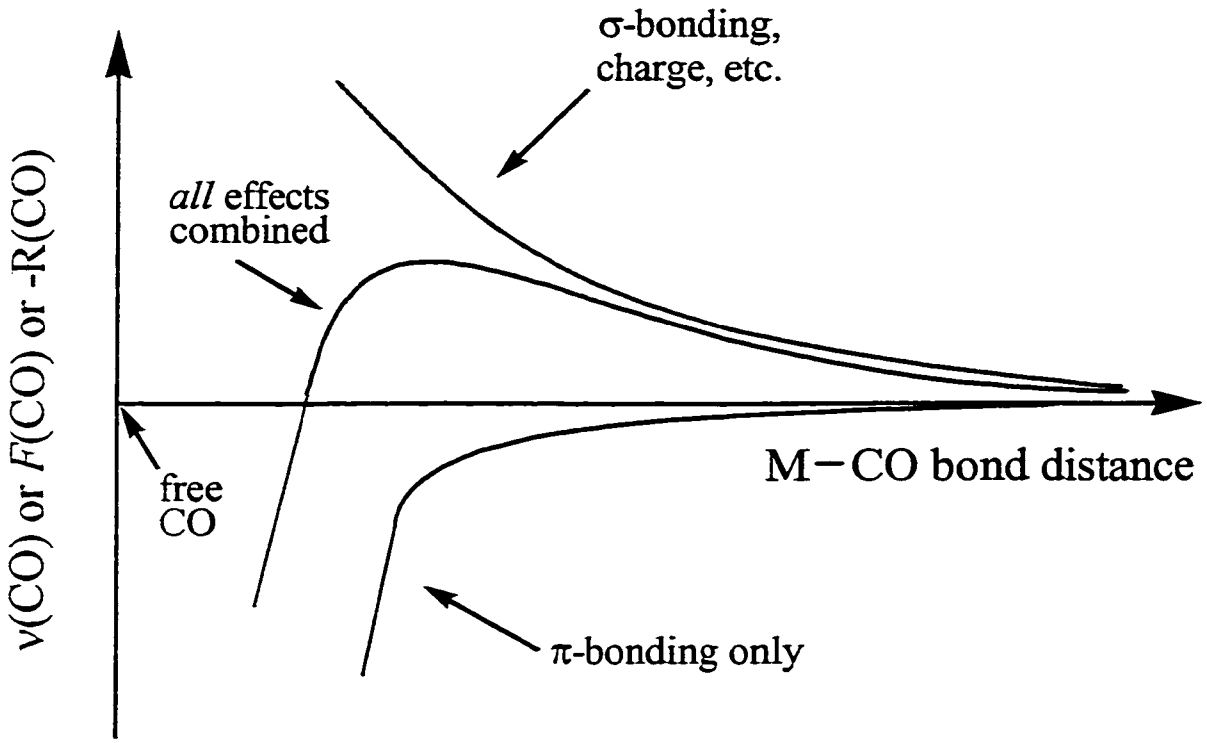

Figure II.4.5. Hypothetical plots of ν(CO) or *F*(CO) or –R(CO) vs. R(MC) for a generic metal carbonyl complex. The middle curve is the mathematical sum of the upper and lower curves.

In reality, most metal carbonyl complexes have a significant amount of π backdonation (as deduced from their ν(CO) < 2143 cm^{-1}). These species would be expected to lie on a point below the free CO line on the middle curve of Figure II.4.5. It should be noted here that each metal carbonyl complex would be expected to have it own unique curve. Accordingly, this model predicts that two complexes with different bonding characteristics can have the same unusually high ν(CO) value. Figure II.4.6 divides the middle curve from Figure II.4.5 into to regions based on the turning point of the curve ($\partial R(CO)/\partial R(MC) = 0$, $\partial \nu(CO)/\partial \nu(MC) = 0$). The same perturbation (stretching the metal-carbon bond) performed on each of these complexes will cause two distinctly different results: The complex on the left experiences an increase in ν(CO) (i.e., a decrease in R(CO)); the complex on the right experiences a decrease in ν(CO) (i.e., an increase in R(CO)). These two complexes have been categorized as *classical* and *nonclassical* metal carbonyl complexes, respectively. So, a ν(CO) > 2143 cm^{-1} can occur for two distinguishable situations, either (i) negligible or relatively minor M→CO π backbonding (i.e., *nonclassical* behavior) or (ii) π backbonding that is *significant* (i.e., classical behavior) *but insufficient* to lower ν(CO) below 2143 cm^{-1}.[2]

These differences in behavior (based on Statement 1*b* in Part II, Chapter 1) are the focus of this theoretical experiment; the group-11 cationic mono- and polycarbonyls were examined in a fashion similar to that used by Sherwood and Hall.[180] The major difference between the experiments presented in this dissertation and Sherwood and Hall's experiment is whereas they the held the geometry of the remaining $Cr(CO)_5$ fragment constant (i.e., distances and angles as in $Cr(CO)_6$), all of the ligands in this work were allowed to equilibrate in response to a given perturbation. The group-11 $M(CO)_n^+$ (n = 1–4) complexes were chosen for two reasons: (1) these complexes have been synthesized experimentally and have ν(CO) > 2143 cm^{-1}; (2) copper and silver have been shown to behave differently in similar situations (cf. violations of Statement 5*b*).

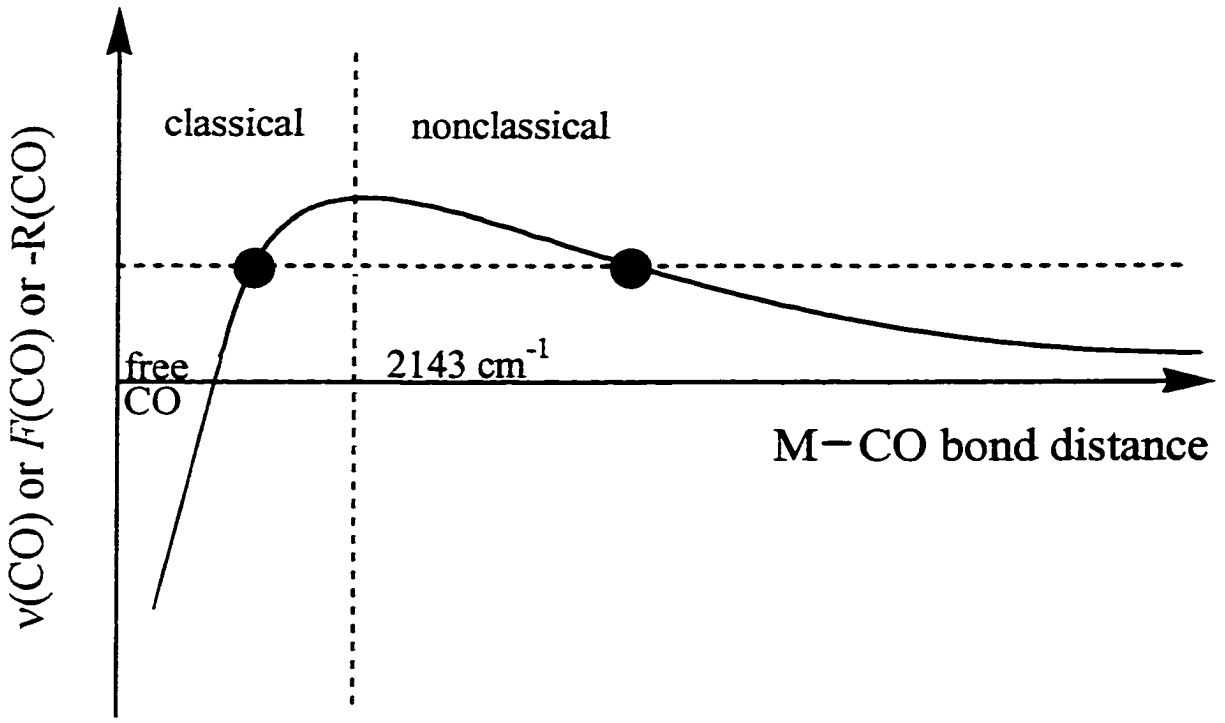

Figure II.4.6. Separation of classical and nonclassical metal carbonyls based on their position relative to the ν(CO) vs. R(MC) curve maximum. The circles represent equilibrium geometries for hypothetical classical and nonclassical metal carbonyls. Note that both complexes have the same ν(CO) value, which is greater than 2143 cm^{-1}. The difference in R(MC) values for the two complexes is not to scale.

Results and Discussion

Monocarbonyls

In this part of the experiment, the effect of compressing the M–C bond on the carbon-oxygen bond length for a monocarbonyl complex, $M(CO)^+$, is examined. The results of the experiment for the group 11 monocarbonyls (M = Cu, Ag, Au) are listed in Table II.4.6. Figure II.4.7 and Figure II.4.8 show plots of MP2-calculated C–O distances as a function of R(MC). The curves for the monocarbonyl species look like the curves describes above.

At long metal–carbonyl separations (i.e., 4.0 Å) the C–O bond distance is already shorter than for CO in the gas phase by about 0.004 Å in all cases. The almost identical bond lengths for the three complexes is not surprising since any effects at this distance must be caused by dipole effects identical to those discussed in Part II, Chapter 2 for a charge interacting with a carbon monoxide; the C–O bond should become less polar, regardless of the particular metal ion present. As the CO continues to approach a metal cation, the C–O bond continued to get shorter; at longer M–C distances, the C–O distance for $Au(CO)^+$ is shorter than the C–O distance of either $Cu(CO)^+$ or $Ag(CO)^+$. For example, at 3.0 Å the C–O bond is 0.0005 Å shorter in $Au(CO)^+$ than in the other two complexes. There is no significant M→CO π backdonation occurring at this distance, and the dipole effects caused by charge would be expected to be roughly equal; therefore, the difference in C–O bond distance must be due to a difference in the amount of σ donation. Even at 2.5 Å metal-carbon separation, R(CO) for $Au(CO)^+$ is longer than the copper or silver analogues despite the larger *b/d* ration for the gold complex. These results are supported by the more facile removal of electron density from the bonding region (s-dσ hybridization) for Au^+ than for Cu^+ or Ag^+ (cf. Part II, Chapter 3).

Table II.4.6. Bond Distances and CDA Results for $M(CO)^+$ Complexes (M = Cu, Ag, Au) at Variable Metal–Carbon Distances[a]

M	R(MC),Å	R(CO), Å	donation *d*	backdonation *b*	repulsion *r*	*b/d*
Cu^+	1.75	1.1437	0.535	0.100	-0.068	0.187
	1.8909	*1.1420*	*0.537*	*0.060*	*-0.047*	*0.112*
	2.00	1.1415	0.500	0.036	-0.034	0.072
	2.15	1.1412	0.447	0.019	-0.025	0.043
	2.25	1.1416	0.408	0.012	-0.021	0.029
	2.50	1.1426	0.322	0.004	-0.013	0.012
	3.00	1.1447	0.206	0.001	-0.005	0.005
	3.50	1.1463	0.135	0.000	-0.002	0.000
	4.00	1.1474	0.087	0.000	0.000	0.000
Ag^+	1.75	1.1457	0.453	0.161	-0.259	0.355
	1.85	1.1439	0.417	0.105	-0.205	0.252
	2.00	1.1424	0.380	0.055	-0.147	0.145
	2.05	1.1421	0.361	0.040	-0.126	0.111
	2.15	1.1420	0.342	0.024	-0.099	0.070
	2.2494	*1.1421*	*0.327*	*0.013*	*-0.077*	*0.040*
	2.35	1.1423	0.314	0.009	-0.060	0.029
	2.50	1.1428	0.302	0.002	-0.042	0.007
	3.00	1.1447	0.235	0.000	-0.010	0.000
	3.50	1.1462	0.166	0.000	-0.002	0.000
	4.00	1.1473	0.112	0.000	0.000	0.000

Table II.4.6. Bond Distances and CDA Results for $M(CO)^+$ Complexes (M = Cu, Ag, Au) at Variable Metal–Carbon Distances[a] (*continued*)

M	R(MC),Å	R(CO), Å	donation *d*	backdonation *b*	repulsion *r*	*b/d*
Au^+	1.75	1.1474	0.486	0.246	-0.202	0.506
	1.85	1.1445	0.452	0.171	-0.166	0.378
	1.9757	*1.1423*	*0.425*	*0.109*	*-0.133*	*0.256*
	2.00	1.1420	0.413	0.094	-0.122	0.228
	2.15	1.1409	0.387	0.049	-0.090	0.127
	2.25	1.1409	0.374	0.031	-0.074	0.083
	2.50	1.1418	0.338	0.008	-0.045	0.024
	3.00	1.1442	0.243	0.000	-0.014	0.000
	3.50	1.1460	0.166	0.000	-0.003	0.000
	4.00	1.1472	0.116	0.000	0.000	0.000

[a] Italicized values are equilibrium values.

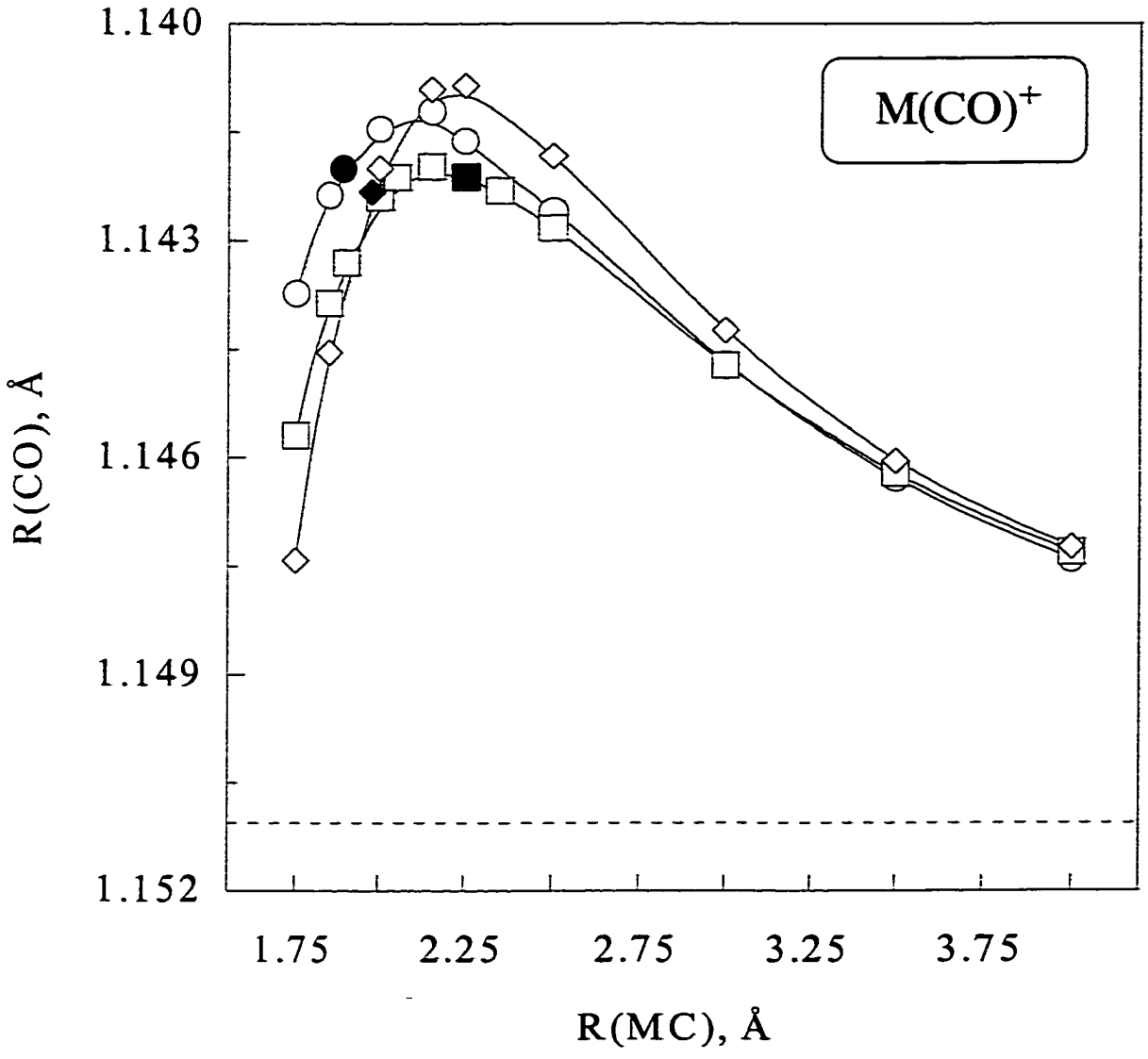

Figure II.4.7. Plots of R(CO) versus R(MC) for the monocarbonyls $Cu(CO)^+$ (circles), $Ag(CO)^+$ (squares), and $Au(CO)^+$ (diamonds) (MP2/I level of theory). Filled data points represent equilibrium geometries. The dotted line represents the calculated R(CO) value for free CO (1.151 Å). The solid lines are for visual reference. Note that the y-axis is reversed.

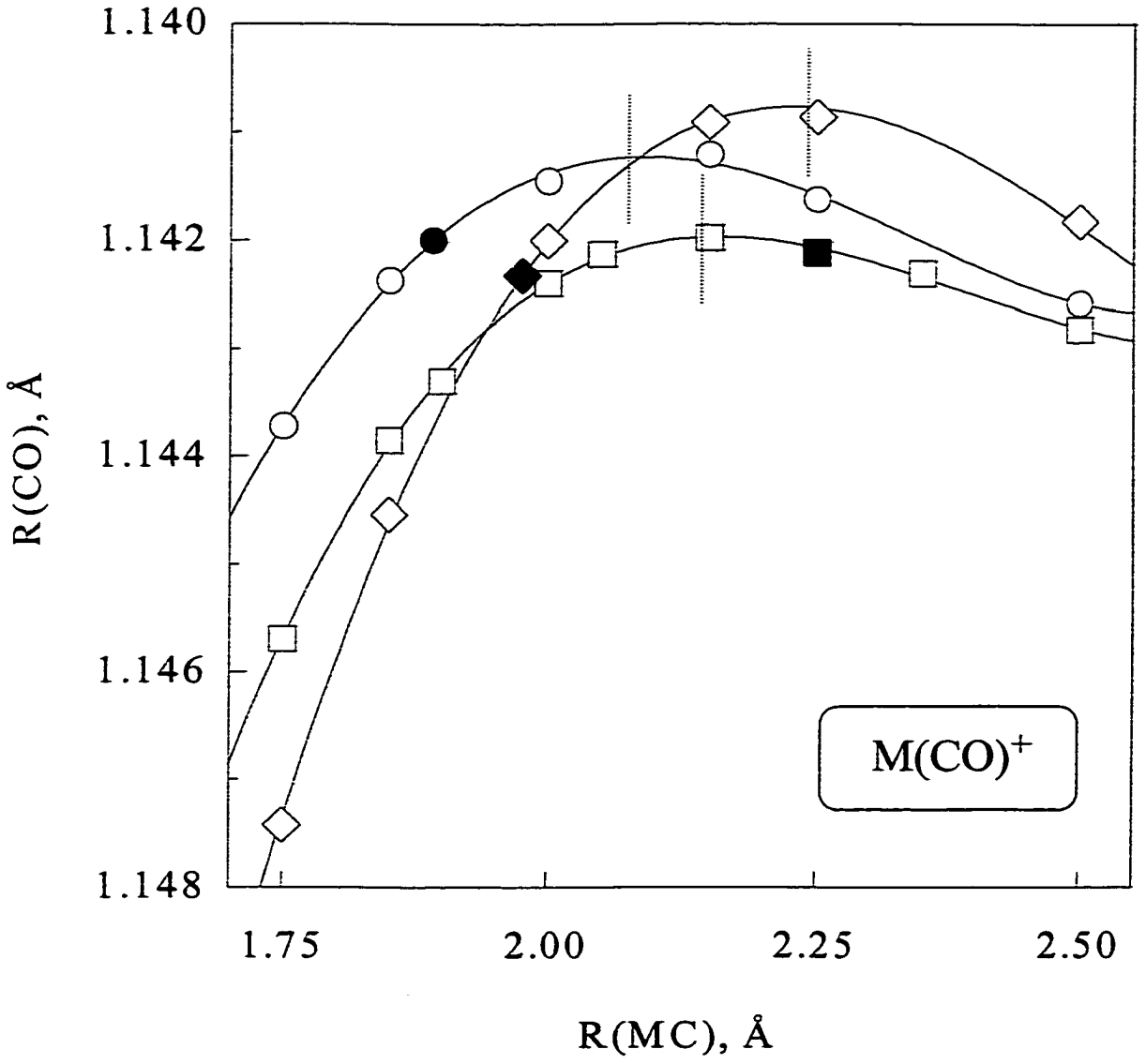

Figure II.4.8. Enlarged view of the turning-point region of Figure II.4.7. Plots of R(CO) versus R(MC) for the monocarbonyls $Cu(CO)^+$ (circles), $Ag(CO)^+$ (squares), and $Au(CO)^+$ (diamonds) (MP2/I level of theory). Filled data points represent equilibrium geometries; the dotted vertical lines mark the curve turning points. The theoretical value for free CO is 1.511 Å. Note that the y-axis is reversed.

The plots for $Cu(CO)^+$, $Ag(CO)^+$ and $Au(CO)^+$ have turning points for R(CO) at nearly the same metal$^+$–CO distance: $R(CuC)_{equil}$ = 2.091 Å, $R(AgC)_{equil}$ = 2.139, and $R(AuC)_{equil}$ = 2.227 Å (a spread of only 0.136 Å). This is a remarkable result since the three metal cations have quite different equilibrium M^+–CO distances (Table II.4.6). The M^+–CO equilibrium bond distances of $Cu(CO)^+$ and $Au(CO)^+$ are shorter than the turning point of R(CO), while the equilibrium Ag^+–CO distance is longer than the turning point. Nevertheless, the shortening of the C–O bond at the equilibrium geometry is nearly the same for the three $M(CO)^+$ species (0.0091 Å for $Cu(CO)^+$, 0.0089 Å for $Ag(CO)^+$, 0.0088 Å for $Au(CO)^+$). The CDA results for $M(CO)^+$, also listed in Table II.4.6, shed light on the nature of the M^+–CO bonds. First, note that the absolute numbers of the calculated charge donation have little meaning when comparing different species; it is the ratio of the two donor-acceptor components that is significant. At the M^+–CO equilibrium distances the ratio is 0.26 for $Au(CO)^+$, 0.11 for $Cu(CO)^+$, and 0.04 for $Ag(CO)^+$, indicating significant $Au^+ \rightarrow CO$ π backdonation, some $Cu^+ \rightarrow CO$ π backdonation, but negligible $Ag^+ \rightarrow CO$ π backdonation.

To understand these differences in metal–carbonyl bonding, the CDA results for $Au(CO)^+$ will be examined more closely. Figure II.4.9 shows plots of M←CO donation (open circles), M→CO backdonation (open squares; these are displayed as the negative of the value listed in Table II.4.6), and the sum of the donation and backdonation (d+b) for $Ag(CO)^+$ and $Au(CO)^+$. These plots are similar in shape to the curves in Figure II.4.5, i.e., the individual effects of M←CO σ donation and M→CO π backdonation have been deconvoluted. It can be seen that at long distances the donation of electron density from the CO to the metal dominated the bonding picture; significant backdonation does not begin to occur before 2.5 Å. This is consistent with the poor metal d_π–CO π^* overlap at long distances. At R(MC) < 2.5 Å the backdonation begins to influence the d+b curve and by 2.25 Å the M→CO backdonation is large enough to outweigh M←CO donation.

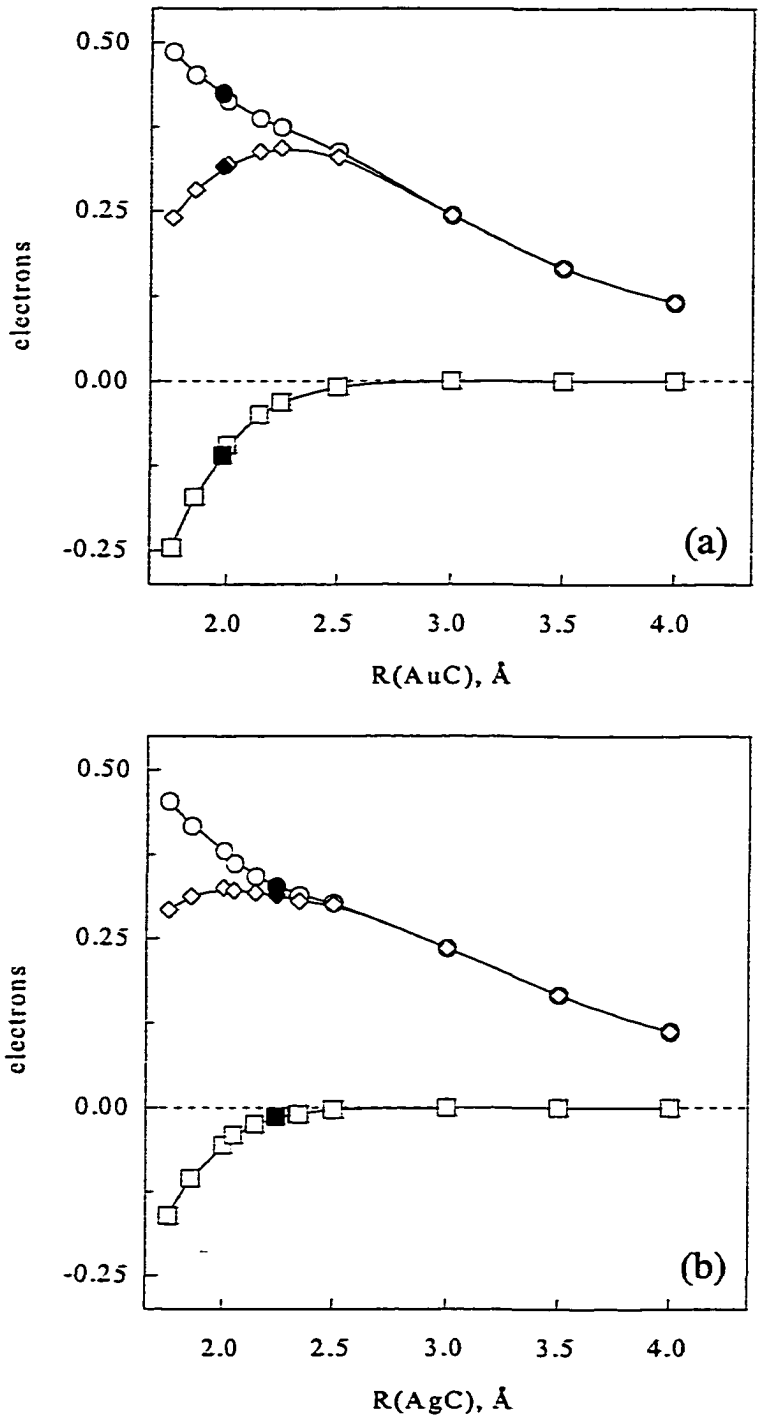

Figure II.4.9. Plots of CDA results versus M–C bond length for the(a) $Au(CO)^+$ and (b) $Ag(CO)^+$. The open circles represent M→CO donation; the open squares represent the negative of M←CO backdonation; the open diamonds represent the absolute value of the sum of donation minus backdonation. The shaded shapes represent equilibrium values. The dotted line marks the zero point. The solid lines are for visual aid.

The equilibrium Au–C bond distance (solid shapes) occurs at a position on the curve where backdonation effects outweigh donation effects. The overall trends presented for $Au(CO)^+$ also hold for the silver(I) case, however, the equilibrium R(AgC) distance occurs at a position on the curve where donation effects outweigh backdonation effects.

In summary, an infinitesimal increase in R(MC) from the equilibrium distance (Table II.4.6) results in a *shortening* of the C–O bond in $Cu(CO)^+$ and $Au(CO)^+$ but a *lengthening* of the C–O bond in $Ag(CO)^+$. The same perturbation has produced two different effects. In all cases, stretching the M–C bond causes a decrease in M→C π backdonation, which will cause the C–O bond to become shorter, and a decrease in M←C σ donation, which will cause the C–O bond to become longer. Since both effects occur when an M–C bond is stretched, the behavior of the C–O bond should give an indication of which effect plays the greater role in the M–CO bonding. In this case, π backdonation plays the dominant role in the Cu^+–CO and Au^+–CO bonding, while the σ donation plays the dominant role in Ag^+–CO bonding. The Cu^+–CO and Au^+–CO complexes adhere to Statement 1*b*; they are therefore called *classical* metal carbonyls. The silver(I) monocarbonyl cation violates Statement 1*b*; Ag^+–CO is therefore called *nonclassical* metal carbonyl.

Dicarbonyls

For the linear dicarbonyl complexes $M(CO)_2^+$ (M = Cu, Ag, Au), there are two possibilities for examining the effect varying the M–C bond length has on R(CO). One approach is to vary parametrically both M–C distances together (i.e., so that the CO ligands are always equidistant from the metal center), while the other is to vary only one M–C distance allowing the rest of the complex to equilibrate. A pictorial representation of each experiment is given in Figure II.4.10.

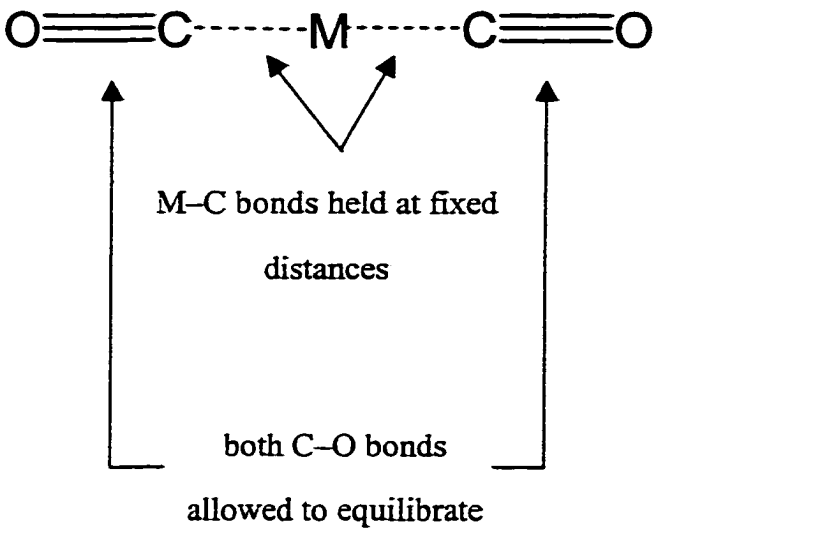

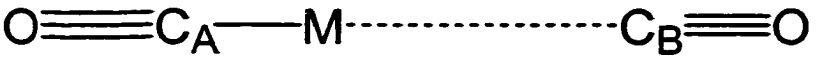

Figure II.4.10. Pictorial representation of the symmetric (top) and asymmetric (bottom) M–C bond compression experiment. Note that in the asymmetric experiment the M–C_B distance is held at fixed distances and *not* allowed to equilibrate, while the M–C_A, C_A–O, and C_B–O bonds are allowed to equilibrate at each M–C_B distance.

In the first approach, the two equivalent M–C bonds are parametrically compressed from infinite distance; only the C–O bonds are allowed to equilibrate with respect to the C–M–C geometry at each step. This will be called the symmetric experiment. In the second approach, one of the carbonyl ligands is held at fixed M–C distances. At each distance, both of the C–O bonds and the M–C bond from the monocarbonyl ($M–C_A$) are allowed to equilibrate. This experiment will be called the asymmetric M–C bond compression experiment.

The results of the symmetric experiment are listed in Table II.4.7. Plots of the C–O bond lengths as a function of M–C distance are shown in Figure II.4.11, and an enlarged view of the turning-point region is shown in Figure II.4.12. The behavior of the complexes represented in these graphs is the same for $M(CO)_2^+$ as it is for $M(CO)^+$. The R(CO) values for all three metals in $M(CO)^+$ at 4.0 Å are the same (± 0.0001 Å), and the dicarbonyl values at 4.0 Å are the same as the values for the monocarbonyls at 4.0 Å. This again reinforces the idea that the C–O bond shortening is due to electrostatic effects. Examination of the equilibrium geometries reveals that stretching the M–C bonds in $Cu(CO)_2^+$ and $Au(CO)_2^+$ cause the C–O bond to become *shorter*, while stretching the M–C bonds in $Ag(CO)_2^+$ cause the C–O bond to become *longer*. The rational is the same as for the monocarbonyl examples: there is a significant amount of M→CO π backdonation in $Cu(CO)_2^+$ and $Au(CO)_2^+$, while there is little to none in $Ag(CO)_2^+$ Therefore, $Cu(CO)_2^+$ and $Au(CO)_2^+$ are *classical* metal carbonyl complexes, while $Ag(CO)_2^+$ is a *nonclassical* metal carbonyl complex.

Table II.4.7. Bond Distances and CDA Results for $M(CO)_2^+$ Complexes (M = Cu, Ag, Au) at Variable Metal–Carbon Distances

M	R(MC),Å	R(CO), Å	donation *d*	backdonation *b*	repulsion *r*	*b/d*
Cu^+	*1.8840*	*1.1418*	*0.463*	*0.058*	*-0.022*	*0.125*
	2.00	1.1414	0.470	0.037	-0.011	0.078
	2.10	1.1414	0.452	0.025	-0.006	0.054
	2.25	1.1418	0.406	0.014	-0.005	0.034
	2.50	1.1428	0.328	0.007	-0.005	0.020
	3.00	1.1449	0.219	0.003	-0.004	0.011
	4.00	1.1475	0.089	0.000	-0.001	0.000
	5.00	1.1488	0.034	0.000	0.000	0.000
Ag^+	2.00	1.1424	0.396	0.052	-0.097	0.130
	2.10	1.1421	0.373	0.033	-0.075	0.089
	2.13	1.1421	0.366	0.029	-0.070	0.078
	2.1596	*1.1421*	*0.359*	*0.025*	*-0.065*	*0.070*
	2.20	1.1422	0.350	0.021	-0.059	0.059
	2.25	1.1422	0.340	0.017	-0.053	0.049
	2.50	1.1431	0.300	0.006	-0.031	0.018
	3.00	1.1449	0.238	0.001	-0.009	0.004
	4.00	1.1474	0.115	0.001	-0.001	0.004
	5.00	1.1487	0.050	0.000	0.000	0.000

Table II.4.7. Bond Distances and CDA Results for $M(CO)_2^+$ Complexes (M = Cu, Ag, Au) at Variable Metal–Carbon Distances (*continued*)

M	R(MC),Å	R(CO), Å	donation *d*	backdonation *b*	repulsion *r*	*b/d*
Au^+	1.90	1.1431	0.359	0.123	-0.099	0.341
	2.00	1.1419	0.357	0.086	-0.068	0.241
	2.0067	*1.1419*	*0.356*	*0.084*	*-0.066*	*0.236*
	2.10	1.1413	0.353	0.059	-0.046	0.167
	2.20	1.1410	0.350	0.041	-0.034	0.116
	2.25	1.1410	0.348	0.034	-0.030	0.096
	2.50	1.1418	0.329	0.013	-0.022	0.040
	3.00	1.1444	0.249	0.001	-0.011	0.004
	4.00	1.1473	0.120	0.001	-0.001	0.004
	5.00	1.1487	0.051	0.000	0.000	0.000

[a] Italicized values are equilibrium values. [b] The values for *d*, *b*, and *r* listed in the table and are half of the calculated values for $(CO)_n$ as a donor (*d*/2, *b*/2, *r*/2) and M^+ as an acceptor.

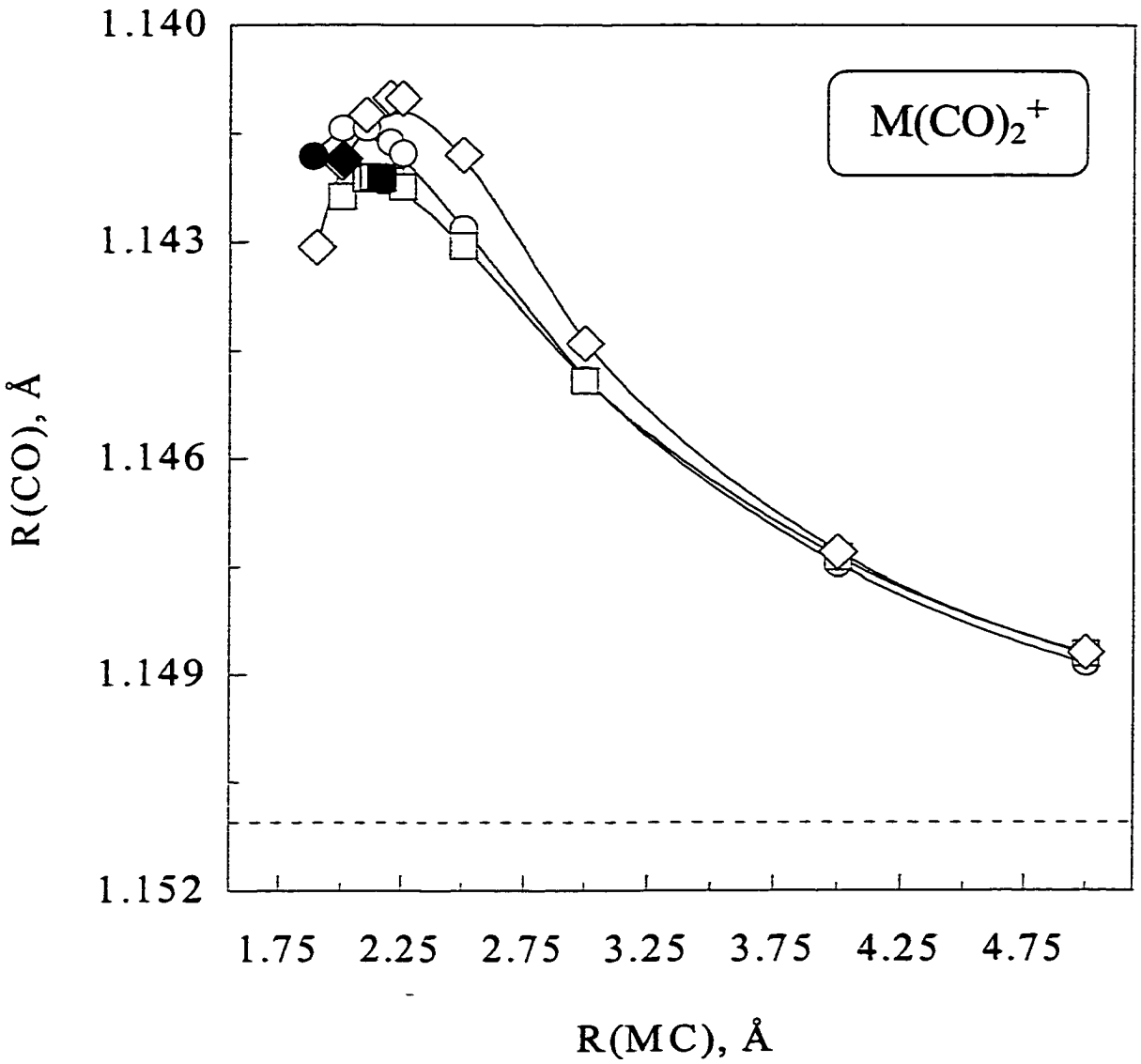

Figure II.4.11. Plots of R(CO) versus R(MC) for the dicarbonyls $Cu(CO)_2^+$ (circles), $Ag(CO)_2^+$ (squares), and $Au(CO)_2^+$ (diamonds) (MP2/I level of theory). Filled data points represent equilibrium geometries. The dotted line represents the calculated R(CO) value for free CO (1.151 Å). The solid lines are for visual reference. Note that the y-axis is reversed.

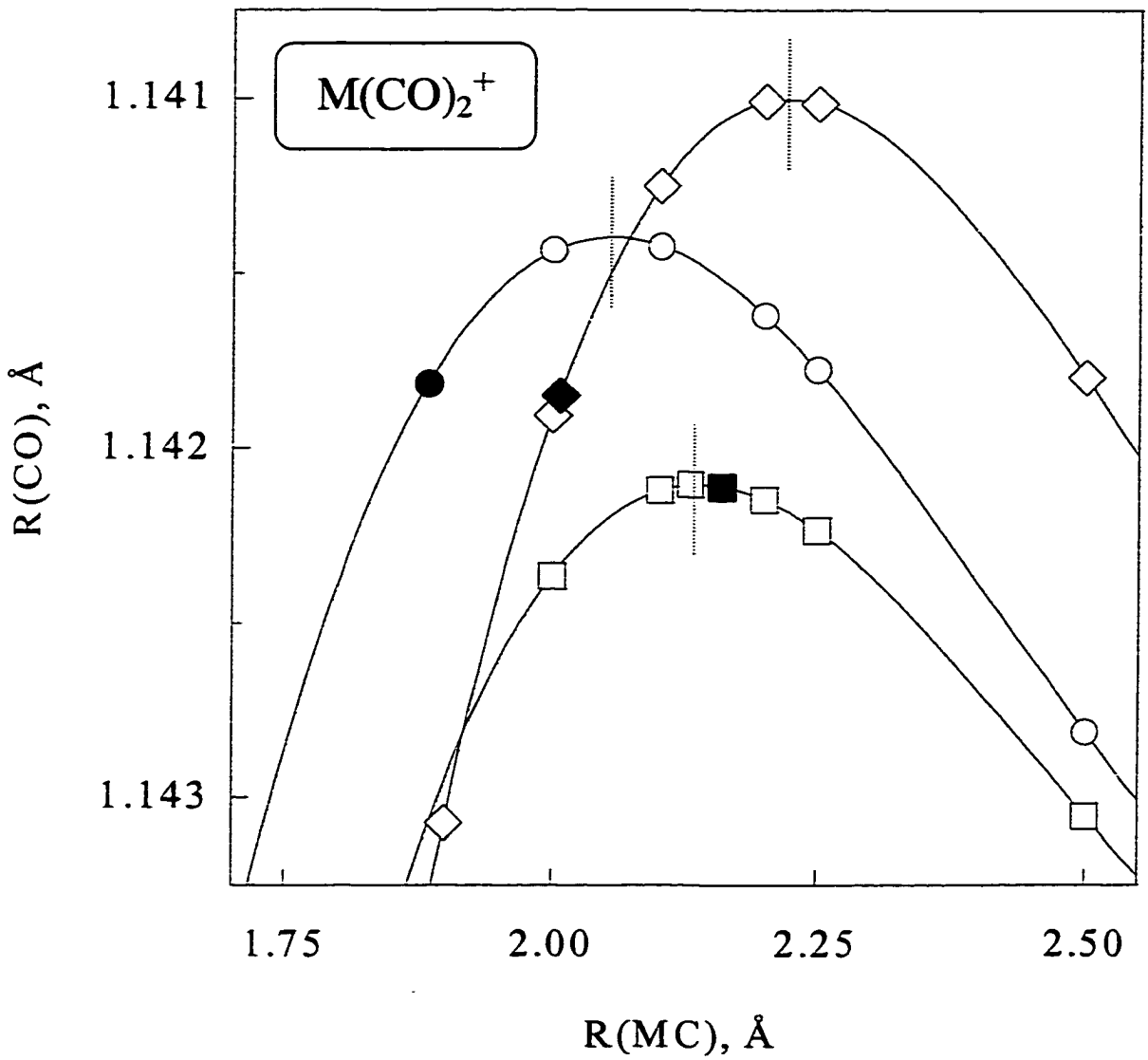

Figure II.4.12. Enlarged view of the turning-point region of Figure II.4.11. Plots of R(CO) versus R(MC) for the dicarbonyls $Cu(CO)_2^+$ (circles), $Ag(CO)_2^+$ (squares), and $Au(CO)_2^+$ (diamonds) (MP2/I level of theory). Filled data points represent equilibrium geometries; the dotted vertical lines mark the curve turning points. The theoretical value for free CO is 1.511 Å. Note that the y-axis is reversed.

While the preceding symmetric experiment is useful for examining the nonclassical nature of a metal dicarbonyl complex, it is unrealistic; the asymmetric M–C bond compression experiment is a better model for examining bond changes in a carbonyl ligand(s) of a dicarbonyl complex as the complex is being formed (i.e., from the monocarbonyl complex). While this experiment is more realistic, it is also more complex. In the symmetric experiment, the only variable was R(CO) as a function of R(MC); for the asymmetric experiment, there are four different variables: the behavior of two different C–O bonds, $R(C_AO)$ and $R(C_BO)$, as a function of $R(MC_B)$; the behavior of $R(MC_A)$ as a function of $R(MC_B)$; and the behavior of $R(C_AO)$ as a function of $R(MC_A)$.

The results for each metal are listed in Table II.4.8. Figure II.4.13a and Figure II.4.13b illustrates the behavior of the approaching carbonyl ligand (C_BO) as a function of the $M–C_B$ distance. The behavior of this approaching carbonyl is, in both cases, similar to that presented above for the monocarbonyl and symmetric dicarbonyl experiments: the equilibrium R(MC) occurs after the turning point of the curve. Figure II.4.14a is a plot of the behavior of the bound $Cu–C_A$ and $C_A–O$ bonds as the second carbonyl ligand (C_BO) approaches, and Figure II.4.14b is a plot of the behavior of the bound $Au–C_A$ and $C_A–O$ bonds as the second carbonyl approaches. Examination of the $M–C_A$ behavior for both metals reveals that this bound metal-carbon bond becomes shorter until $R(M–C_B) \sim 2.4$ Å for Cu^+ and ~2.65 Å for Au^+. At shorter distances, $R(MC_A)$ becomes increasingly long. The bound carbonyl ligand behaves in a manner opposite to that of the metal-carbon bond: R(CO) increases until $R(M–C_B) = 2.4$ Å for Cu^+ and ~2.65 Å for Au^+; $R(MC_A)$ decreases after the turning-point distances.

Table II.4.8. R(MC) and R(CO) values for $OC_A–M^+\cdots C_BO$ complexes (M = Cu, Ag, Au)[a]

M	$R(MC_B)$, Å	$R(C_BO)$, Å	$R(MC_A)$, Å	$R(C_AO)$, Å
Cu	*1.8840*	*1.1418*	*1.8840*	*1.1418*
	2.00	1.1411	1.8704	1.1423
	2.10	1.1410	1.8632	1.1426
	2.25	1.1412	1.8580	1.1429
	2.40	1.1417	1.8573	1.1430
	2.50	1.1422	1.8584	1.1430
	2.75	1.1433	1.8636	1.1429
	3.00	1.1444	1.8697	1.1427
	3.50	1.1461	1.8792	1.1424
	4.00	1.1473	1.8842	1.1423
	5.00	1.1488	1.8881	1.1421
Ag	*2.1596*	*1.1421*	*2.1596*	*1.1421*
	2.2596	1.1422	2.1624	1.1422
	2.30	1.1422	2.1642	1.1422
	2.40	1.1425	2.1701	1.1423
	2.50	1.1429	2.1773	1.1423
	2.60	1.1432	2.1850	1.1423
	2.6596	1.1435	2.1898	1.1423
	2.70	1.1436	2.1929	1.1423
	2.80	1.1440	2.2005	1.1423
	3.1596	1.1453	2.2224	1.1423
	3.50	1.1463	2.2342	1.1422
	4.00	1.1474	2.2415	1.1422
	5.00	1.1488	2.2469	1.1421

Table II.4.8. R(MC) and R(CO) values for OC_A–M^+···C_BO complexes (M = Cu, Ag, Au)[a] (*continued*)

M	$R(MC_B)$. Å	$R(C_BO)$, Å	$R(MC_A)$, Å	$R(C_AO)$, Å
Au	*2.0067*	*1.1419*	*2.0067*	*1.1419*
	2.15	1.1408	1.9752	1.1426
	2.20	1.1406	1.9674	1.1429
	2.25	1.1406	1.9608	1.1430
	2.40	1.1409	1.9477	1.1434
	2.50	1.1412	1.9431	1.1436
	2.60	1.1417	1.9410	1.1436
	2.75	1.1424	1.9410	1.1436
	3.00	1.1436	1.9455	1.1434
	3.50	1.1456	1.9577	1.1430
	4.00	1.1470	1.9658	1.1427
	5.00	1.1486	1.9721	1.1425

[a] Italicized values are equilibrium values.

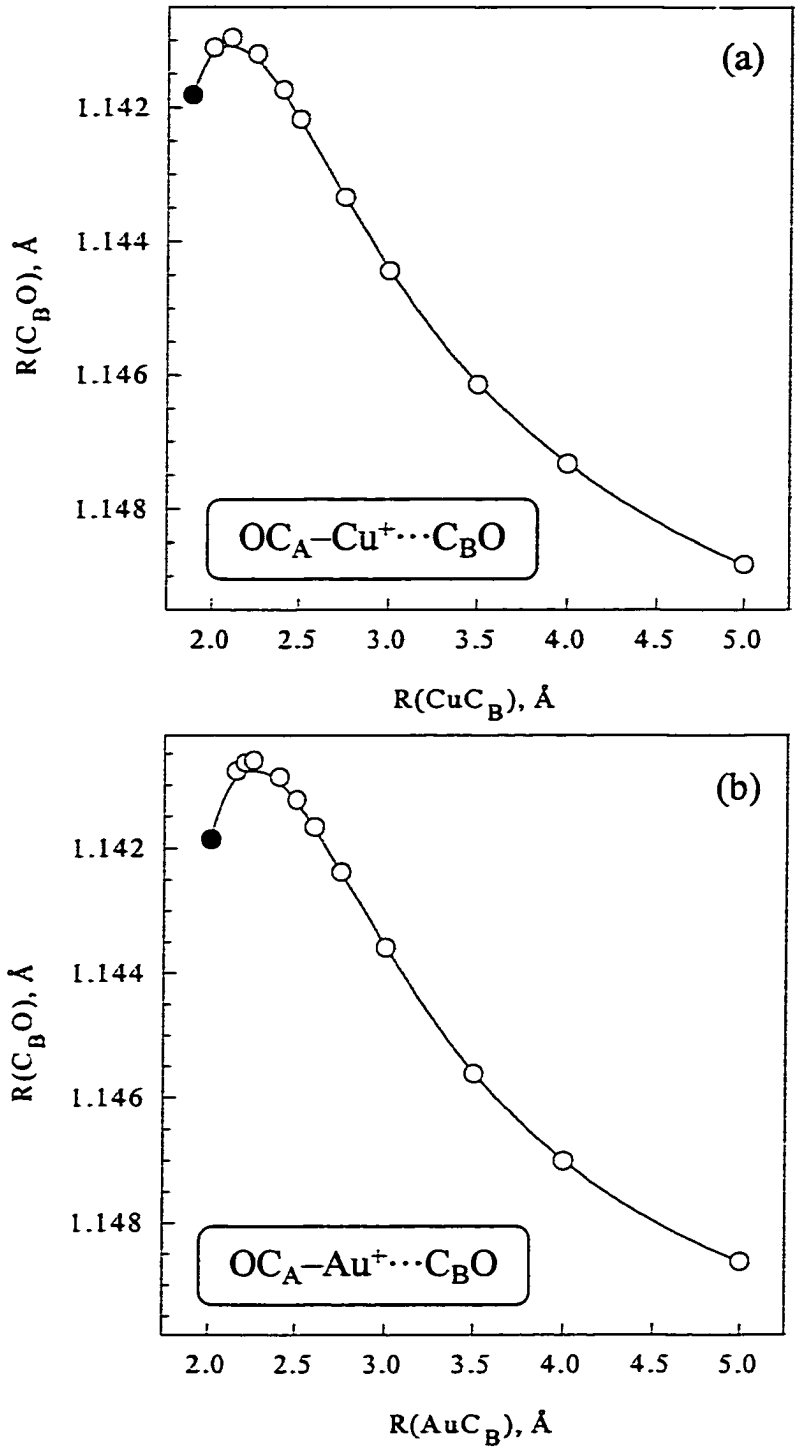

Figure II.4.13. Plots of $R(C_BO)$ versus $R(MC_B)$ for (a) the $OC–Cu^+\cdots CO$ complex and (b) $OC–Au^+\cdots CO$ complex (MP2/I level of theory). Filled data points represent equilibrium geometries. The calculated R(CO) value for free CO is 1.151 Å. The solid lines are for visual reference. Note that the y-axis is reversed.

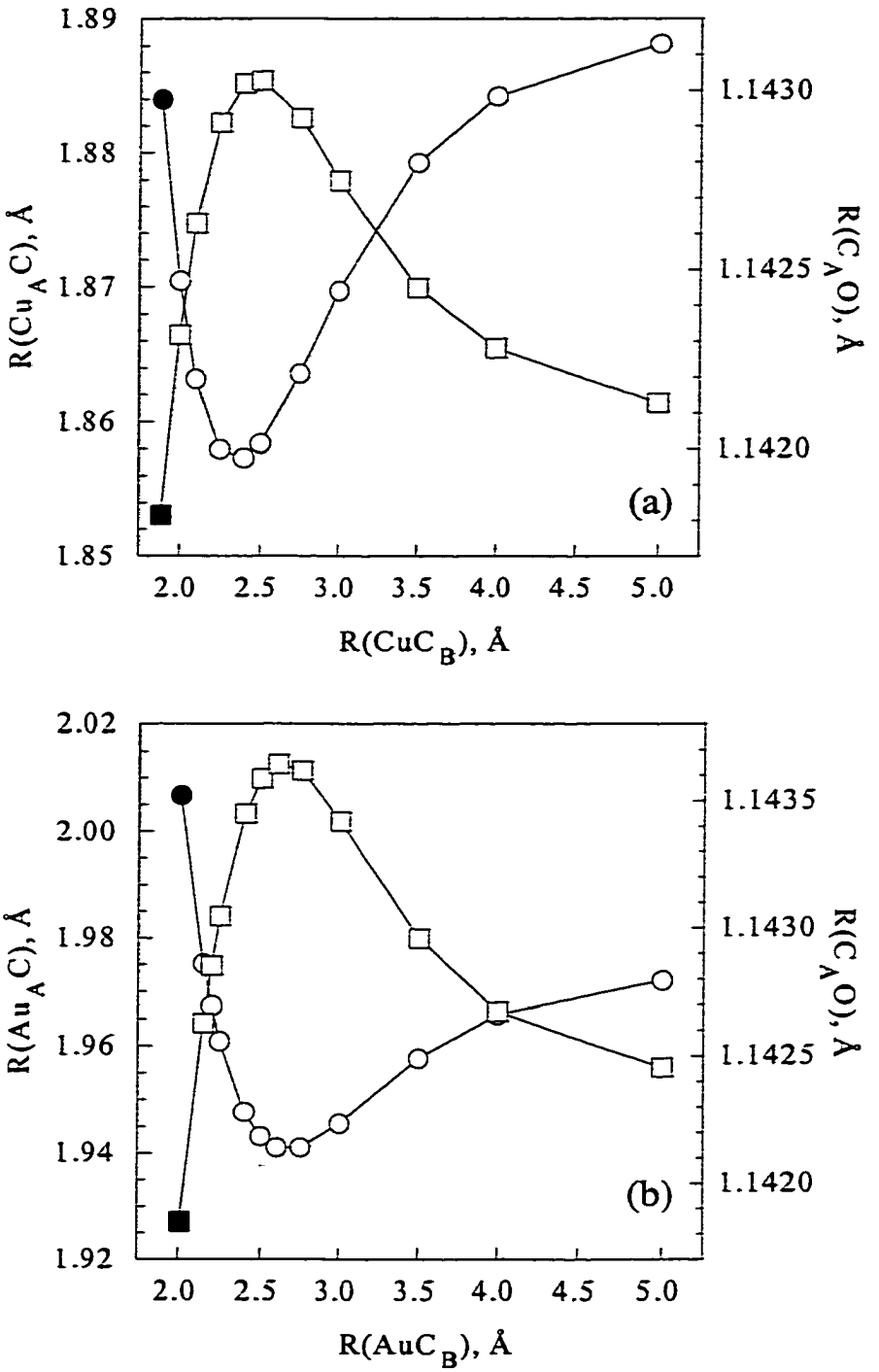

Figure II.4.14. Plots of $R(MC_A)$ and $R(C_AO)$ versus $R(MC_B)$ for (a) the OC–Cu^+···CO complex and (b) OC–Au^+···CO complex (MP2/I level of theory). Filled data points represent equilibrium geometries. The calculated R(CO) value for free CO is 1.151 Å. The solid lines are for visual reference. Note that the y-axis is reversed.

This behavior can be explained in terms of M→CO backdonation and M←CO donation. As the second carbonyl ligand approaches the monocarbonyl complex, the donation form this carbonyl as well as the polarization neutralization caused by the dipolar carbonyl decreases the amount of $M\leftarrow C_AO$ donation (because of decrease in charge on the metal) and causes the bound carbonyl to become more polar. Both of these effects are expected to lengthen the $R(C_AO)$ bond. At the same time, the decrease in charge on the metal will induce an increase in $M\rightarrow C_AO$ backdonation. This effect will lengthen the C–O bond. The decrease in M←CO donation should weaken the M–C bond causing it to become longer, but the increase in M→CO backdonation should cause $R(MC_A)$ to decrease. Qualitatively, the fact that the M–C bond initially decreases as the second CO ligand approaches indicates that M→CO backdonation plays the dominant role in the metal-carbon bonding for these two complexes.

As the R(MC) reaches a minimum, R(CO) reaches a maximum. It was shown above that, for both Cu^+ and Au^+, the $M(CO)^+$ and $M(CO)_2^+$ complexes have a significant amount of M→CO backdonation at the equilibrium geometries. At the turning point distances, the approaching carbonyl ligand has a significant effect on the reorganization of the electrons along the bonding axis. This causes M←CO effects to increase (due to better s-dσ hybridization; cf. Part II, Chapter 3) shortening the C–O bond; this effect should also shorten the M–C bond by creating a stronger σ bond. However, as the $R(MC_B)$ distance decreases, the metal d_π electron density must be shared between two carbonyl ligands instead of one. This weakens the M–C_A bond (less double bond character) and decreases C–O (less density from the metal into the π^* orbitals on CO). This bonding description adequately explains the behavior of the bound C–O bond. To explain this behavior of the M–C_A bond, the assumption again be made that M→CO has a larger effect on M–C bond length (an bond strength) than M←CO does for these two complexes.

The results for $OC–Ag^{+}\cdots CO$ are illustrated in Figure II.4.15 through Figure II.4.17. Figure II.4.15 shows the behavior of the approaching carbonyl (C_BO) as a function of the Ag–C_B distance. The behavior of this carbonyl mimics that seen in the monocarbonyl and symmetric dicarbonyl experiments and is not significantly different than the behavior of R(C_BO) as a function of R(AgC_B) in the Cu^{+} and Au^{+} cases. The equilibrium R(AgC) occurs after the turning point of the curve. Figure II.4.16 is a plot of the behavior of the bound Ag–C_A and C_A–O bonds as the second carbonyl approaches. Examination of the Ag–C_A bond behavior reveals that it becomes monotonically shorter as the second carbonyl ligand approaches. Despite the decrease in Ag–C_A distance, the C–O bond first becomes longer and then, after reaching a maximum R(CO) value, becomes shorter. Figure II.4.17 is an alternate representation of this information. In this plot, R(C_AO) is plotted as a function of R(Ag_AC). Here it can be seen that the carbonyl bond in the dicarbonyl complex is shorter than in the monocarbonyl, but this change is not monotonic. An explanation for this behavior centers on the lack of M→CO backdonation. If is assumed that there is very little backdonation in the silver(I) system, then the bonding behavior must arise from M←CO donation and charge effects. As the second carbonyl ligand approaches the monocarbonyl, the donation from this carbonyl ligand to the metal, as well as the polarization neutralization caused by the dipolar carbonyl decreases the amount of M←C_AO donation (because of decrease in charge on the metal) and causes the bound carbonyl ligand to become more polar. Both of these effects are expected to lengthen the R(C_AO) bond; these same effects should increase the Ag–C_A bond. These behaviors are identical to the effects described for the copper and gold systems.

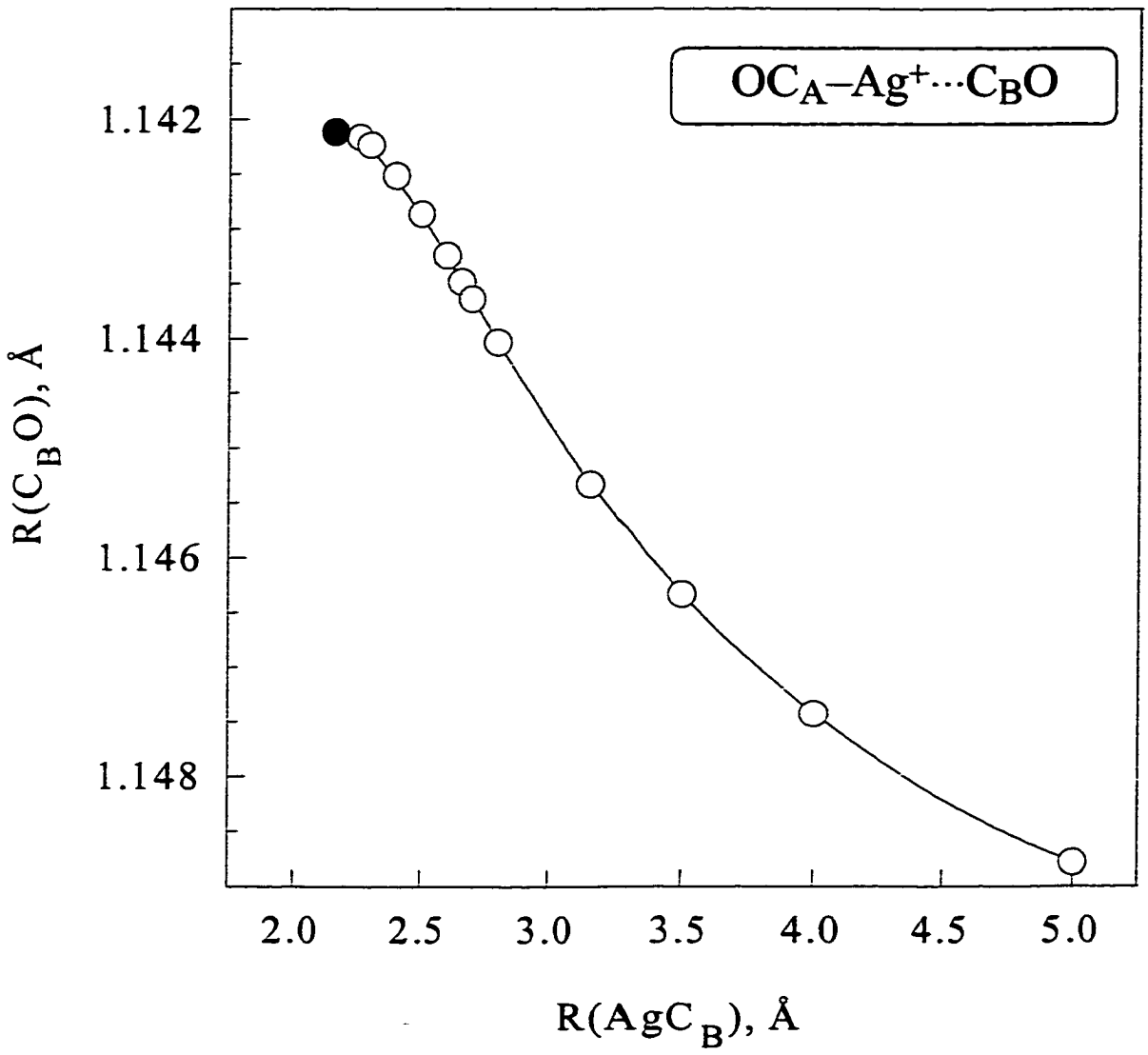

Figure II.4.15. Plot of $R(C_BO)$ versus $R(MC_B)$ for the $OC–Ag^+\cdots CO$ complex. Filled point represent equilibrium geometries. The calculated R(CO) value for free CO is 1.151 Å. The solid lines are for visual reference. Note that the y-axis is reversed.

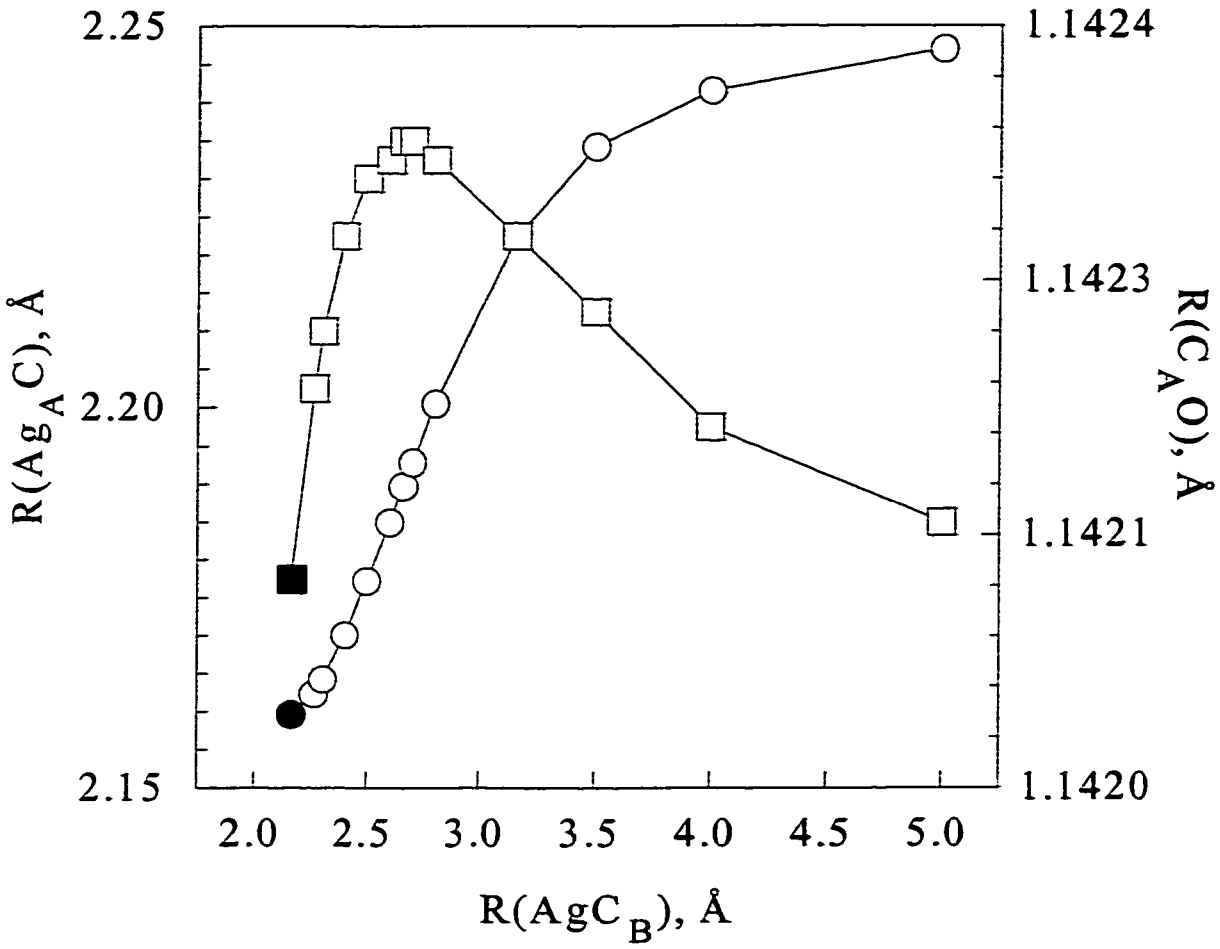

Figure II.4.16. Plots of $R(MC_A)$ and $R(C_AO)$ versus $R(MC_B)$ for the $OC–Ag^+\cdots CO$ complex (MP2/I level of theory). Filled data points represent equilibrium geometries. The calculated R(CO) value for free CO is 1.151 Å. The solid lines are for visual reference. Note that the y-axis is reversed.

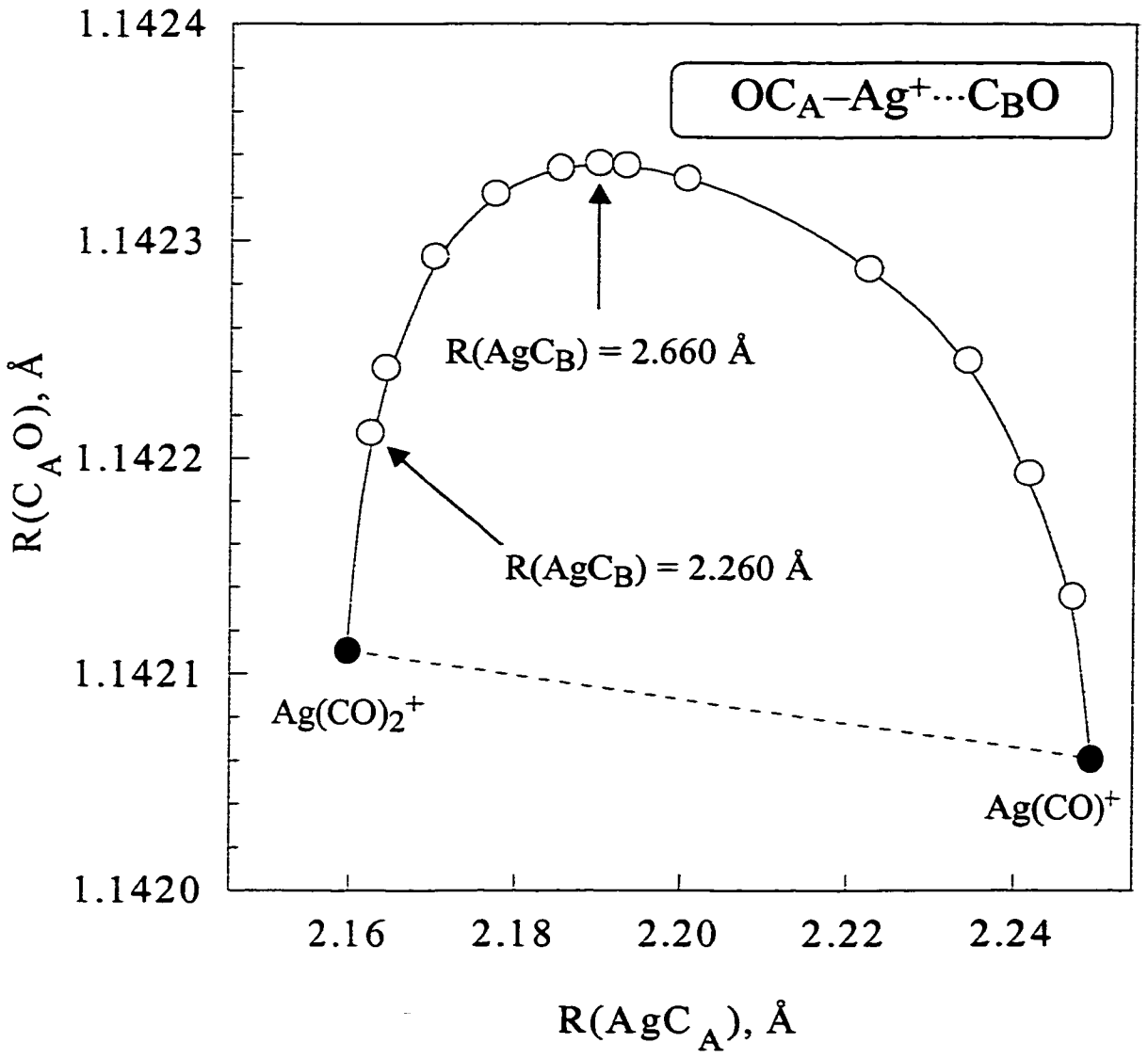

Figure II.4.17. Plot of $R(C_AO)$ versus $R(MC_A)$ for the $OC–Ag^+\cdots CO$ (MP2/I level of theory). Filled data points represent equilibrium geometries. The calculated R(CO) value for free CO is 1.151 Å. The solid lines are for visual reference. Note that the y-axis is reversed.

At 2.66 Å, the R(CO) for the bound carbonyl ligand begins to decrease even though the Ag–C_A bond continues to get shorter. This is in sharp contrast to the Cu^+ and Au^+ systems. At this point the Ag←CO donation and charge effects must begin to have a greater effect on the Ag–C bonding than the Ag→CO effects. As above, the approaching carbonyl ligand is having a significant effect on the reorganization of the electrons along the bonding axis. This increase in Ag←CO donation due to reorganization of electrons allows R(AgC_A) to continue to decrease, and causes R(C_AO) also decreases. From the turning point until equilibrium, donation effects outweigh any backdonation effects that might exist. At approximately 0.1 Å from the equilibrium geometry (R(Ag–C_B) = 2.16 Å) (Figure II.4.17), π backdonation effects on the approaching carbonyl ligand begin to increase. This distance is consistent with the distances at which M→CO backdonation begins to have a significant effect in the $M(CO)^+$ and $M(CO)_2^+$ (symmetric) systems discussed above. This is also consistent with the equilibrium CDA results which show a larger *b/d* ratio for $Ag(CO)_2^+$ than for $Ag(CO)^+$ (but less than either $Cu(CO)_2^+$ or $Au(CO)_2^+$). The large decrease in R(C_AO) from R(AgC_B) = 2.26 Å to equilibrium is caused by the increased Ag←C_AO donation and the removal of available d_π electron density away from the Ag→C_AO side of the complex toward the Ag→C_BO side of the complex.

The OC–Cu^+···CO and OC–Au^+···CO systems behave fundamentally differently than the OC–Ag^+···CO system. As in the $[M^x(CO)_2(F)_2]^{x-2}$ experiment described earlier, the behavior of the C–O bond masks the fact that the M–C bonding in the two examples is different: the copper(I) and gold(I) systems are dominated by M→CO backdonation effects; the behavior of the silver(I) system is dominated by M←CO donation/charge effects. This experiment is yet another example in support of the need for two distinct classes of metal carbonyls. For now the interpretation of these results is speculative. Future work should focus on the examination of the electronic structures of

these systems by topological electron distribution studies, natural bond orbital experiments, and charge decomposition analysis methods. It is logical, based on the quantitative studies of the $M(CO)^+$ and $M(CO)_2^+$ (symmetric) systems discussed above, that the ideas presented here will be supported in the future by further, more thorough, theoretical investigations.

Conclusions

In this chapter, two different theoretical experiments were presented that probe the nature of the bonding interactions in metal carbonyl complexes. In each case, a perturbation was applied to a series of metal carbonyl complexes: in the first experiment, the perturbation consisted of two F^- ions placed orthogonal to the M–CO vectors of a metal carbonyl complex at a distance of 3 Å from the metal center; in the second set of experiments, the perturbation consisted of compression or stretching of the M–C bond(s) of a metal carbonyl complex. Although these are two distinctly different theoretical experiments, they both support the idea that there is a fundamental difference between classical and nonclassical carbonyl complexes. In the first experiment, the fluoride ions caused the M–CO bond become shorter (the normal, usual, classical case) or to become longer (abnormal, unusual, nonclassical case). In the second set of experiments, when the metal–CO bond of a metal carbonyl was stretched, the C–O bond became shorter (normal, usual, classical case) in some case and longer (abnormal, unusual, nonclassical case) in others. There is one underlying explanation for the behaviors observed in each experiment: all classical metal carbonyls have M→CO π backdonation sufficient to compete with M←CO σ donation and charge effects. As a result, π backdonation plays a significant role in the M–C and C–O bonding in these species. Conversely, nonclassical metal carbonyls have neither enough M→CO π backdonation to compete sufficiently

with M←CO σ donation and charge effects nor enough to affect significantly the M–C and C–O bonding in these species. Once again, it has been shown that there is a need for two separate classifications for metal carbonyl complexes—classical and nonclassical.

References for Part II

1. Henrici-Olivé, G.; Olivé, S. *The Chemistry of the Catalyzed Hydrogenation of Carbon Monoxide*; Springer-Verlag: Berlin, 1984.

2. Blanchard, A. A. *Chem. Rev.* **1937**, *21*, 3.

3. Blanchard, A. A. *Chem. Rev.* **1940**, *26*, 409.

4. Welch, A. J. E. *Rep. Progr. Chem.* **1941**, *38*, 71.

5. Anderson, J. S. *Quart. Rev. Chem. Soc.* **1948**, *1*, 331.

6. Lupinetti, A. J.; Frenking, G.; Strauss, S. H. *Progress in Inorganic Chemistry, submitted 1999.*

7. Gates, P. N.; Steele, D. *J. Mol. Struct.* **1968**, 349.

8. Davies, P. B.; Hamilton, P. A.; Rothwell, W. J. *J. Chem. Phys.* **1984**, *81*, 1598.

9. Foster, S. C.; McKellar, A. R. W.; Sears, T. J. *J. Chem. Phys.* **1984**, *81*, 578.

10. Bethke, G. W.; Wilson, M. K. *J. Chem. Phys.* **1957**, *26*, 1118.

11. Jones, L. H.; Taylor, R. C.; Paine, R. T. *J. Chem. Phys.* **1979**, *70*, 749.

12. Albright, T. A.; Burdett, J. K.; Whangbo, M. H. *Orbital Interactions in Chemistry*; Wiley: New York, 1985.

13. Elschenbroich, C.; Salzer, A. *Organometallics*; VCH: New York, 1992.

14. DeKock, R. L.; Sarapu, A. C.; Fenske, R. F. *Inorg. Chem.* **1971**, *10*, 38.

15. Herzberg, G. *Molecular Spectra and Molecular Structure. Volume I-Spectra of Diatomic Molecule*; Krieger Publishing Company: Malabar, 1989.

16. Hirota, E.; J., E. *J. Mol. Spectrosc.* **1988**, *127*, 524.

17. Woods, R. C. *Phil. Trans. R. Soc.* **1988**, *A324*, 141.

18. Berry, R. J.; Harmony, M. D. *J. Mol. Spectrosc.* **1988**, *128*, 176.

19. Goldman, A. S.; Krogh-Jespersen, K. *J. Am. Chem. Soc.* **1996**, *118*, 12159-12166.

20. Dapprich, S.; Frenking, G. *J. Phys. Chem.* **1995**, *99*, 9352.

21. Ehlers, A. W.; Dapprich, S.; Vyboishchikov, F. S.; Frenking, G. *Organometallics* **1996**, *15*, 105.

22. Davidson, E. R.; Kunze, K. L.; Machado, F. B. C.; Chakravorty, S. J. *Acc. Chem. Res.* **1993**, *26*, 628, and further references cited in this work.

23. Hush, N. S.; Williams, M. L. *J. Mol. Spectrosc.* **1974**, *50*, 349.

24. Bernhardt, E.; Willner, H.; Aubke, F. *Angew. Chem., Int. Ed.* **1999**, *38*, 823.

25. Rack, J. J.; Webb, J. D.; Strauss, S. H. *Inorg. Chem.* **1996**, *35*, 277-8.

26. Hurlburt, P. K.; Rack, J. J.; Luck, J. S.; Dec, S. F.; Webb, J. D.; Anderson, O. P.; Strauss, S. H. *J. Am. Chem. Soc.* **1994**, *116*, 10003-14.

27. Seppelt, K., *personal communication to S. H. Strauss*, 1999.

28. Willner, H.; Schaebs, J.; Hwang, G.; Mistry, F.; Jones, R.; Trotter, J.; Aubke, F. *J. Am. Chem. Soc.* **1992**, *114*, 8972-80.

29. Bach, C.; Willner, H.; Wang, C.; Rettig, S. J.; Trotter, J.; Aubke, F. *Angew. Chem., Int. Ed.* **1996**, *35*, 1974.

30. Lupinetti, A. J.; Strauss, S. H., *unpublished results.*

31. Ivanova, S. M.; Ivanov, S. V.; Miller, S. M.; Anderson, O. P.; Solntsev, K. A.; Strauss, S. H. *Inorg. Chem.* **1999**, *38*, 3756-3757..

32. Bernhardi, I.; Drews, T.; Seppelt, K. *Angew. Chem.* **1999**, , in press.

33. Strauss, S. H. *Chemtracts–Inorg. Chem.* **1997**, *10*, 77-103.

34. Weber, L. *Angew. Chem., Int.. Ed.* **1994**, *33*, 1077-1078; *Angew. Chem.* **1994**, *106*, 1131-1133.

35. Barnes, L. A.; Rosi, M.; Bauschlicher, C. W. *J. Chem. Phys.* **1990**, *93*, 609-624.

36. Bruce, M. I. *J. Organomet. Chem.* **1972**, *44*, 209.

37. Calderazzo, F.; Dell'Amico, D. B. *Pure Appl. Chem.* **1986**, *58*, 561.

38. Manchot, W.; Gall, H. *Chem. Ber.* **1925**, *58*, 2175.

39. Schützenberger, P. *Comptes Rendues Hebd. Seances Acad. Sci.* **1870**, *70*, 1134.

40. Mond, L. *J. Chem. Soc.* **1890**, *57*, 749.

41. Strauss, S. H. *Chem. Soc., Dalton Trans.* **1999**, 0000.

42. Elschenbroich, C.; Salzer, A. *Organometallics*, VCH, New York, 1992. (b) Cotton, F.A.; Wilkinson, G. *Advanced Inorganic Chemistry*, Wiley, New York, 1980. (c) Gerloch, M.; Constable, E.C. *Transition Metal Chemistry*, VCH, New York, 1994. (d) Constable, E.C. *Metals and Ligand Reactivity*, VCH, New York, 1996.,

43. Brockway, L. O.; Cross, P. C. *J. Chem. Phys.* **1935**, *3*, 828.

44. Pauling, L. *The Nature of the Chemical Bond*; 3rd ed.; Cornell Univ. Press: Ithaca, NY, 1960, pp 332.

45. Dewar, M. J. S. *Bull. Soc. Chim. Fr.* **1951**, *18*.

46. Chatt, J.; Duncanson, L. A. *J. Chem. Soc.* **1953**, 2929.

47. Orgel, L. E. *An Introduction to Transition-Metal Chemistry*; Wiley: New York, 1960.

48. Sherwood, D. E.; Hall, M. B. *Inorg. Chem.* **1980**, *19*, 1805.

49. Bursten, B. E.; Freier, D. G.; Fenske, R. F. *Inorg. Chem.* **1980**, *19*, 1810.

50. Szilagyi, R. K.; Frenking, G. *Organometallics* **1997**, *16*, 4807.

51. Ellis, J. E. *Adv. Organometal. Chem.* **1990**, *31*, 1.

52. Brammer, L.; Mareque Rivas, J. C.; Zhao, D. *Inorg. Chem.* **1998**, *37*, 5512.

53. Lupinetti, A. J.; Frenking, G.; Strauss, S. H. *Angew. Chem., Int. Ed.* **1998**, *37*, 2113-2116.

54. Huttner, G.; Schelle, S. *J. Crystallogr. Mol. Struct.* **1971**, *1*, 69.

55. Cotton, F. A.; Richardson, D. C. *Inorg. Chem.* **1966**, *5*, 1851.

56. Seder, T. A.; Church, S. P.; Weitz, E. *J. Am. Chem. Soc.* **1986**, *108*, 4721.

57. Black, J. B.; Boylen, M. J.; Braterman, P. S. *J. Chem. Soc., Dalton Trans.* **1981**, 673.

58. Strauss, S. H.; Holm, R. H. *Inorg. Chem.* **1982**, *21*, 863-8.

59. Ellis, J. E.; Beck, W. *Angew. Chem., Int. Ed.* **1995**, *34*, 2489-2491; *Angew. Chem.* **1995**, *107*, 2695-2697.

60. Herzberg, G. *Molecular Spectra and Molecular Structure. I. Spectra of Diatomic Molecules*; 2nd ed.; Van Nostrand: Princeton, 1950.

61. Wang, C.; Willner, H.; Bodenbinder, M.; Batchelor, R. J.; Einstein, F. W. B.; Aubke, F. *Inorg. Chem.* **1994**, *33*, 3521.

62. Hwang, G.; Wang, C.; Bodenbinder, M.; Willner, H.; Aubke, F. *J. Fluorine Chem.* **1994**, *66*, 159-66.

63. Wang, C.; Lewis, A. R.; Batchelor, R. J.; Einstein, F. W. B.; Willner, H.; Aubke, F. *Inorg. Chem.* **1996**, *35*, 1279.

64. Rack, J. J. Ph.D. Dissertation, Colorado State University,, 1996.

65. Dolg, M.; Wedig, U.; Stoll, H.; Preuss, H. *J. Chem. Phys.* **1987**, *86*, 866.

66. Andrae, D.; Häussermann, U.; Dolg, M.; Stoll, H.; Preuss, H. *Theor. Chim. Acta* **1990**, *77*, 123.

67. Ehlers, A. W.; Böhme, M.; Dapprich, S.; Gobbi, A.; Höllwarth, A.; Jonas, V.; Köhler, K. F.; Stegmann, R.; Veldkamp, A.; Frenking, G. *Chem. Phys. Lett.* **1993**, *208*, 111.

68. Hehre, W. J.; Ditchfield, R.; Pople, J. A. *J. Chem. Phys.* **1972**, *56*, 2257.

69. Dunning, T. H., Jr. *J. Chem. Phys.* **1971**, *55*, 716.

70. Dunning, T. H., Jr. *J. Chem. Phys.* **1989**, *90*, 1007.

71. Jonas, V.; Thiel, W. *J. Phys. Chem.* **1995**, *102*, 8474.

72. Jonas, V.; Thiel, W. *J. Phys. Chem.* **1996**, *105*, 3636.

73. Møller, C.; Plesset, M. S. *Phys. Rev.* **1934**, *46*, 618.

74. Binkley, J. S.; Pople, J. A. *Int. J. Quantum Chem.* **1975**, *9*, 229.

75. Cizek, J. *J. Chem. Phys.* **1966**, *45*, 4256.

76. Cizek, J. *Adv. Chem. Phys.* **1966**, *14*, 35.

77. Pople, J. A.; Krishnan, R.; Schlegel, H. B.; Binkley, J. S. *Int. J. Quantum Chem.* **1978**, *14*, 545.

78. Bartlett, R. J.; Purvis, G. D. *Int. J. Quantum Chem.* **1978**, *14*, 561.

79. Purvis, G. D.; Bartlett, R. J. *J. Chem. Phys.* **1982**, *76*, 1910.

80. Noga, J.; Bartlett, R. J. *J. Chem. Phys.* **1987**, *86*, 7041.

81. Raghavachari, K.; Trucks, G. W.; Pople, J. A.; Head-Gordon, M. *Chem. Phys. Lett.* **1989**, *157*, 479.

82. Becke, A. D. *J. Chem. Phys.* **1993**, *98*, 5648.

83. Stevens, P. J.; Devlin, F. J.; Chablowski, C. F.; Frisch, M. J. *J. Phys. Chem.* **1994**, *98*, 11623.

84. Gaussian 94: Frisch, M. J.; Trucks, G. W.; Schlegel, H. B.; Gill, P. M. W.; Johnson, B. G.; Robb, M. A.; Cheeseman, J. R.; Keith, T. A.; Petersson, G. A.; Montgomery, J. A.; Raghavachari, K.; Al-Laham, M. A.; Zakrzewski, V. G.; Ortiz, J. V.; Foresman, J. B.; Cioslowski, J.; Stefanov, B. B.; Nanayakkara, A.; Challacombe, M.; Peng, C. Y.; Ayala, P. Y.; Chen, W.; Wong, M. W.; Andres, J. L.; Replogle, E. S.; Gomberts, R.; Martin, R. L.; Fox, D. J.; Binkley, J. S.; Defrees, D. J.; Baker, I.; Stewart, J. J. P.; Head-Gordon, M.; Gonzalez, C.; Pople, J. A. Gaussian Inc., Pittsburgh, PA 1995,

85. MOLPRO is a package of ab initio programs written by Werner, H.-J. and Knowles, P. J., with contributions from Almlöf, J.; Amos, R. D.; Deegan, M. J. O.; Elbert, S. T.; Hampel, C.; Meyer, W.; Peterson, K. A.; Pitzer, R. M.; Stone, A. J.; and Taylor, P. R,

86. ACES II is a package of ab initio programs written by Stanton, J. F.; Gauss, J.; Watts, J. D.; Lauderdale W. J.; and Bartlett, R. J,

87. Reed, A. E.; Curtiss, L. A.; Weinhold, F. *Chem. Rev.* **1988**, *88*, 899.

88. Bader, R. F. W. *Atoms in Molecules. A Quantum Theory*; Oxford University Press: Oxford, 1990.

89. CDA 2.1 is a program written by Dapprich, S. and Frenking, G. It is available via anonymous ftp server: ftp.chemie.uni-marburg.de (/pub/cda).,

90. Biegler-König, F. W.; Bader, R. F. W.; Ting-Hua, T. *J. Comput. Chem.* **1982**, *3*, 317.

91. Cotton, F. A.; Wilkinson, G. *Advanced Inorganic Chemistry*; Wiley: New York, 1980.

92. Gerloch, M.; Constable, E. C. *Transition Metal Chemistry*; VCH: New York, 1994.

93. Constable, E. C. *Metals and Ligand Reactivity*; VCH: New York, 1996.

94. Sherwood, D. E.; Hall, M. B. *Inorg. Chem.* **1983**, *22*, 93.

95. Williamson, R. L.; Hall, M. B. *Int. J. Quantum Chem.* **1987**, *21S*, 503.

96. Li, J.; Schreckenbach, G.; Ziegler, T. *J. Am. Chem. Soc.* **1995**, *117*, 486.

97. Ziegler, T.; Tschinke, V.; Ursenbach, C. *J. Am. Chem. Soc.* **1987**, *109*, 4825.

98. Blomberg, M. R. A.; Siegbahn, P. E. M.; Lee, T. L.; Rendell, A. P.; Rice, J. E. *J. Chem. Phys.* **1991**, *95*, 5898.

99. Ferrari, A. M.; Ugliengo, P.; Garrone, E. *J. Chem. Phys.* **1996**, *105*, 4129.

100. Su, Y.-N.; Tsai, M.-S.; Chu, S.-Y. *Int. J. Quantum Chem.* **1996**, *59*, 487.

101. Nandi, P. K.; Sannigrahi, A. B. *J. Mol. Struct. THEOCHEM* **1994**, *113*, 99.

102. Grice, S. T.; Harland, P. W.; Maclagan, R. G. A. R. *J. Chem. Phys.* **1993**, *99*, 7619.

103. Puzzarini, C.; Tarroni, R.; Palmieri, P.; Carter, S.; Dore, L. *Mol. Phys.* **1996,** *87*, 879.

104. Weis, B.; Yamashity, K. *J. Chem. Phys.* **1993**, *99*, 9512.

105. Szulejko, J. E.; McMahon, T. B. *J. Am. Chem. Soc.* **1993**, *115*, 7839.

106. Smith, B. J.; Radom, L. *J. Am. Chem. Soc.* **1993**, *115*, 4885.

107. Komornicki, A.; Dixon, D. A. *J. Chem. Phys.* **1992**, *97*, 1087.

108. Hall, M. B.; Fenske, R. F. *Inorg. Chem.* **1972**, *11*, 1619.

109. Beach, D. B.; Jolly, W. L. *Inorg. Chem.* **1985**, *24*, 567.

110. Martin, J. M. L.; Taylor, P. R.; Lee, T. J. *J. Chem. Phys.* **1993**, *99*, 286.

111. Adams, N. G.; Smith, D.; Tichy, M.; Javhery, G.; Twiddy, N. D.; Ferguson, E. E. *J. Chem. Phys.* **1989**, *91*, 4037.

112. This is also obvious by analyzing the components of the calculated C-O stretching mode of HCO^+, which have strong contributions from the movement of the proton.

113. The change of the polarization of the molecular orbitals can also be given for the canonical orbitals. The use of localized orbitals facilitates the discussion, because only two orbitals, one s and one degenerate p orbital needs to be considered.

114. Reference 88, page 290.

115. Cremer, D.; Kraka, E. *Angew. Chem.* **1984**, *96*, 612; *Angew. Chem. Int. Ed.* **1984**, *23*, 627.

116. Willner, H.; Aubke, F. *Angew. Chem.* **1997**, *109*, 2506; *Angew. Chem., Int. Ed. Engl.* **1997**, *36*, 2402.

117. Aubke, F.; Wang, C. *Coord. Chem. Rev.* **1994**, *137*, 483-524.

118. Solomon, E. I.; Jones, P. M.; May, J. A. *Chem. Rev.* **1993**, *93*, 2623.

119. Waugh, K. C. *Cataysis Today* **1992**, *15*, 51.

120. Guczi, L. *Studies in Surface Science and Catalysis, Vol. 64: New Trends in CO Activation*, 1991.

121. Blanchard, A. A. *Chem. Rev.* **1937**, *21*, 3.

122. Blanchard, A. A. *Chem. Rev.* **1940**, *26*, 409.

123. Kawasaki, H.; Nakamoto, Y.; Yamamoto, A.; Kato, T.; Yamada, T. *Sekiyu Gakkaishi* **1994**, *37*, 529.

124. Souma, Y. *Osaka Kogyo Gijutsu Shikensho Hokoku* **1979**, 1.

125. Souma, Y. *Shokubai Gakkai* **1987**, *29*, 317.

126. Souma, Y.; Sano, H. *Bull. Chem. Soc. Japan* **1976**, *49*, 3296.

127. Xu, Q.; Imamura, Y.; Fujiwara, M.; Souma, Y. *J. Org. Chem.* **1997**, *62*, 1594.

128. Bregault, J. M.; Jarjour, C.; Yolou, S. *J. Mol. Catal.* **1978**, 225.

129. Tsuda, T.; Isegawa, Y.; Saegusa, T. *J. Org. Chem.* **1972**, *37*, 2670.

130. Peng, X. D.; Golden, T. C.; Pearlstein, R. M.; Pierantozzi, R. *Langmuir* **1995**, *11*, 534.

131. Kumar, R.; Kratz, W. C.; Guro, D. E.; Golden, T. C. *Process Technol. Proc.* **1994**, *11*, 383.

132. Su, C.; Che, Y.; Duannu, Q.; Wang, Y. *Huanjing Kexue* **1994**, *15*, 38.

133. Gholap, R. V.; Chaudhari, R. V. *Can. J. Chem. Eng.* **1992**, *70*, 505.

134. Koschel, J.; Pfennig, A.; Henschke, M.; Hartmann, H. *Energy Fuels* **1991**, *5*, 729.

135. Dyer, R. B.; Peterson, K. A.; Stoutland, P. O.; Woodruff, W. H. *Biochemistry* **1994**, *33*, 500.

136. Hosler, J. P.; Kim, Y.; Shapleigh, J.; Gennis, R.; Alben, J.; Ferguson-Miller, S.; Babcock, G. *J. Am. Chem. Soc.* **1994**, *116*, 5515.

137. Hazes, B.; Magnus, K. A.; Bonaventura, C.; Bonaventura, J.; Dauter, Z.; Kalk, K. H.; Hol, W. G. *J. Protein Sci.* **1993**, *2*, 597.

138. Lowery, M. D.; Solomon, E. I. *Inorg. Chim. Acta* **1992**, 198-200, 233, and references therein.

139. Blackburn, N. J.; Strange, R. W.; Reedijk, J.; Volbeda, A.; Farooq, A.; Karlin, K. D.; Zubieta, J. *Inorg. Chem.* **1989**, *28*, 1349.

140. Reed, C. A. *Acc. Chem. Res.* **1998**, *31*, 133.

141. Lupinetti, A. J.; Strauss, S. H. *Chemtracts–Inorg. Chem.* **1998**, *11*, 565.

142. Seppelt, K. *Angew. Chem., Int. Ed.* **1993**, *32*, 1025.

143. Strauss, S. H. *Chem. Rev.* **1993**, *93*, 927.

144. Bockmann, M. *Angew. Chem., Int. Ed.* **1992**, *31*, 1181.

145. Ivanova, S. M.; Ivanov, S. V.; Miller, S. M.; Anderson, O. P.; Solntsev, K. A.; Strauss, S. H. *Inorg. Chem.* **1999**, *38*, 3756-3757.

146. Polyakov, O. G.; Ivanova, S. M.; Gaudinski, C. M.; Miller, S. M.; Anderson, O. P.; Strauss, S. H. *Organometallics* **1999**, *13*, 3769-3771.

147. Rack, J. J.; Strauss, S. H. *Catal. Today* **1998**, *36*, 99.

148. Rack, J. J.; Moasser, B.; Gargulak, J. D.; Gladfelter, W. L.; Hochheimer, H. D.; Strauss, S. H. *J. Chem. Soc., Chem. Commun.* **1994**, 685-6.

149. Strauss, S. H.; et al., *unpublished results*.

150. Karlin, K. D.; Tyeklár, Z.; Farooq, A.; Haka, M. S.; Ghosh, P.; Cruse, R. W.; Gultneh, Y.; Hayes, J. C.; Toscano, P. J.; Zubieta, J. *Inorg. Chem.* **1992**, *32*, 1436.

151. Pasquali, M.; Floriani, C. ; Karlin, K. D. Z., J., Ed.; Adenine Press: Guilderland, NY, 1983, pp 311.

152. Wagner, O. H. *Z. Anorg. Chem.* **1931**, *196*, 364.

153. Berthelot, M. *Ann. Chim. Phys.* **1856**, *346*, 477.

154. Leblanc, F. C. *R. Acad. Sci. Paris* **1850**, *30*, 483.

155. Souma, Y.; Kawasaki, H. *Catal. Today* **1997**, *36*, 91.

156. Souma, Y.; Iyoda, J.; Sano, H. *Inorg. Chem.* **1976**, *15*, 968.

157. Souma, Y.; Sano, H. *Chem. Lett.* **1973**, 1059.

158. Meyer, F.; Chen, Y.-M.; Armentrout, P. *J. Am. Chem. Soc. 1995* **1995**, *117*, 4071.

159. Bodenbinder, M.; Balzer-Joellenbeck, G.; Willner, H.; Batchelor, R. J.; Einstein, F. W. B.; Wang, C.; Aubke, F. *Inorg. Chem.* **1996**, *35*, 82-92.

160. Willner, H.; Bodenbinder, M.; Wang, C.; Aubke, F. *J. Chem. Soc., Chem. Commun.* **1994**, 1189-1190.

161. Lin, J.; Jones, P.; Guckert, J.; Solomon, E. I. *J. Am. Chem. Soc.* **1991**, *113*, 8312.

162. Hussain, G.; Sheppard, N. *Spectrochim. Acta* **1987**, *43A*, 1631.

163. Ghiotti, G.; Boccuzzi, F.; Scala, R. *J. Catal.* **1985**, *92*, 79.

164. Huang, Y. Y. *J. Catal.* **1980**, *61*, 461.

165. Lupinetti, A.; Fau, S.; Frenking, G.; Strauss, S. H. *J. Phys. Chem. A* **1997**, *101*, 9551-9559.

166. Jonas, V.; Thiel, W. *Organometallics* **1998**, *17*, 353.

167. Huber, K. P.; Herzberg, G. *Constants of Diatomic Molecules*; Van Nostrand-Reinhold: New York, 1979.

168. Ehlers, A. W.; Frenking, G. *J. Am. Chem. Soc.* **1994**, *116*, 1514.

169. Ehlers, A. W.; Frenking, G. *Organometallics* **1995**, *14*, 423.

170. Frenking, G.; Antes, I.; Böhme, M.; Dapprich, S.; Ehlers, A. W.; Jonas, V.; Neuhaus, A.; Otto, M.; Stegmann, R.; Veldkamp, A.; Vyboishchikov, S. F. in *Reviews in Computational Chemistry*, Vol. 8; Lipkowitz, K. B . Boyd, D. B. Eds.; VCH: New York, 1996; Vol. 8, pp 63-144.

171. Bauschlicher, C.; W., J. *Chem. Phys. Lett.* **1994**, *229*, 577.

172. Lee, T. J.; Scuseria, G. E. ; Langhoff, S. R., Ed.; Kluwer Academic Publishers: Dordrecht, 1995, pp 47-108.

173. Thomas, J. R.; DeLeeuw, B. J.; Vacek, G.; Crawford, T. D.; Yamaguchi, Y.; Schaefer III, H. F. *J. Chem. Phys.* **1993**, *99*, 403.

174. Dapprich, S.; Pidun, U.; Ehlers, A. W.; Frenking, G. *Chem. Phys. Lett.* **1995**, *242*, 521.

175. Bauschlicher, C. W., Jr.; Langhoff, S. R.; Partridge, H. *J. Chem. Phys.* **1991**, *94*, 2068.

176. Dunitz, J. D.; Orgel, L. E. *Adv. Inorg. Chem. Radiochem.* **1960**, *2*, 1.

177. Phillips, C. S. G.; Williams, R. J. P. *Inorganic Chemistry (Part II)*; Oxford University Press: Oxford, 1966, pp 484.

178. Hurlburt, P. K.; Rack, J. J.; Dec, S. F.; Anderson, O. P.; Strauss, S. H. *Inorg. Chem.* **1993**, *32*, 373-4.

179. Rack, J. J.; Strauss, S. H. *Catal. Today* **1997**, *36*, 99-106.

180. Sherwood, D. E.; Hall, M. B. *Inorg. Chem.* **1983**, *22*, 93-100.

APPENDIX II.A

Character Tables for Selected Point Groups

C_{2v}	E	C_2	$\sigma_v(xz)$	$\sigma'_v(xz)$		
A_1	1	1	1	1	z	x^2, y^2, z^2
A_2	1	1	−1	−1	R_z	xy
B_1	1	−1	1	−1	x, R_y	xz
B_2	1	−1	−1	1	y, R_x	yz

C_{3v}	E	$2C_3$	$3\sigma_v$		
A_1	1	1	1	z	x^2+y^2, z^2
A_2	1	1	−1	R_z	
E	2	−1	0	(x, y) (R_x, R_y)	(x^2-y^2, xy) (xz, yz)

D_{3h}	E	$2C_3$	$3C_2$	σ_h	$2S_3$	$3\sigma_v$		
A_1'	1	1	1	1	1	1		$x^2 + y^2, z^2$
A_2'	1	1	−1	1	1	−1	R_z	
E'	2	−1	0	2	−1	0	(x, y)	$(x^2 - y^2, xy)$
A_1''	1	1	1	−1	−1	−1		
A_2''	1	1	−1	−1	−1	1	z	
E''	2	−1	0	2	1	0	(R_x, R_y)	(xy, yz)

T_d	E	$8C_3$	$3C_2$	$6S_4$	$6\sigma_d$		
A_1	1	1	1	1	1		$x^2+y^2+z^2$
A_2	1	1	1	−1	−1		
E	2	−1	2	0	0		$(2z^2-x^2-y^2, x^2-y^2)$
T_1	3	0	−1	1	−1	(R_x, R_y, R_z)	
T_2	3	0	−1	−1	1	(x, y, z)	(xy, xz, yz)

O_h	E	$8C_3$	$6C_2$	$6C_4$	$3C_2$ $(=C^2_4)$	i	$6S_4$	$8S_6$	$3\sigma_h$	$6\sigma_d$		
A_{1g}	1	1	1	1	1	1	1	1	1	1		$x^2+y^2+z^2$
A_{2g}	1	1	−1	−1	1	1	1	1	1	−1		
E_g	2	−1	0	0	2	2	0	−1	2	0		$(2z^2-x^2-y^2,$ $x^2-y^2)$
T_{1g}	3	0	−1	1	−1	3	1	0	−1	−1	(R_x, R_y, R_z)	
T_{2g}	3	0	1	−1	−1	3	−1	0	−1	1		(xy, xz, yz)
A_{1u}	1	1	1	1	1	−1	−1	−1	−1	−1		
A_{2u}	1	1	−1	−1	1	−1	1	−1	−1	1		
E_u	2	−1	0	0	2	−2	0	1	−2	0		
T_{1u}	3	0	−1	1	−1	−3	−1	0	1	1	(x, y, z)	
T_{2u}	3	0	1	−1	−1	−3	1	0	1	−1		

$C_{\infty v}$	E	$2C_\infty{}^\Phi$	...	$\infty\,\sigma_v$		
$A_1 \equiv \Sigma^+$	1	1	...	...	z	x^2+y^2, z^2
$A_2 \equiv \Sigma^+$	1	1	...	–1	R_z	
$E_1 \equiv \Pi$	2	$2\cos\Phi$	...	0	(x, y); (R_x, R_y)	(xy, yz)
$E_2 \equiv \Delta$	2	$2\cos2\Phi$	...	0		x^2-y^2, xy
$E_3 \equiv \Phi$	2	$2\cos3\Phi$	...	0		
...	...	...	...	...		

$D_{\infty h}$	E	$2C_\infty{}^\Phi$	...	$\infty\sigma_v$	i	$2S_\infty{}^\Phi$	...	∞C_2		
$\Sigma_g{}^+$	1	1	...	1	1	1	...	1		x^2+y^2, z^2
$\Sigma_g{}^-$	1	1	...	–1	1	1	...	–1	R_z	
Π_g	2	$2\cos\Phi$	...	0	2	$-2\cos\Phi$	...	0	(R_x, R_y)	(xy, yz)
Δ_g	2	$2\cos2\Phi$	...	0	2	$2\cos2\Phi$	...	0		$(x^2-y^2$, xy)
...	...	...	...	...	...	...	...	...		
$\Sigma_u{}^+$	1	1	...	1	–1	–1	...	–1	z	
$\Sigma_u{}^-$	1	1	...	–1	–1	–1	...	1	(x, y)	
Π_u	2	$2\cos\Phi$	...	0	–2	$2\cos2\Phi$	...	0		
Δ_u	2	$2\cos2\Phi$	...	0	–2	$-2\cos2\Phi$	...	0		
...	...	...	...	...	...	...	...	...		